

---

# Group 14 and 15 elements as building blocks for low dimensional functional nanostructures

---

Dissertation von Sandeep Yadav aus Uttar Pradesh, Indien

October 2017, Darmstadt



TECHNISCHE  
UNIVERSITÄT  
DARMSTADT

Fachbereich Chemie  
Eduard-Zintl-Institut für  
Anorganische und Physikalische  
Chemie

---

**Sandeep Yadav, M. Tech.**

Dissertation

Gruppe 14 und 15 Elemente als Bausteine für niederdimensionale funktionelle Nanostrukturen

Group 14 and 15 elements as building blocks for low dimensional functional nanostructures

Eingereicht: 04. October 2017

**Prof. Dr. rer. nat. Jörg J. Schneider**

Fachbereich Chemie

Eduard-Zintl-Institut für Anorganische und Physikalische Chemie

Technische Universität Darmstadt

Alarich-Weiss-Straße 12

64287 Darmstadt

---

# **Group 14 and 15 elements as building blocks for low dimensional functional nanostructures**

Dem Fachbereich Chemie

der Technischen Universität Darmstadt

zur Erlangung des akademischen Grades eines

Doctor rerum naturalium (Dr. rer. nat.)

genehmigte

Dissertation

vorgelegt von

**Sandeep Yadav, M. Tech.**

aus Uttar Pradesh, Indien

<b>Referent :</b>	<b>Prof. Dr. rer. nat. Jörg J. Schneider</b>
<b>Korreferent:</b>	<b>PD Dr.-Ing. habil. Oktay Yilmazoglu</b>
<b>Tag der Einreichung:</b>	<b>04. October 2017</b>
<b>Tag der mündlichen Prüfung:</b>	<b>27. November 2017</b>

**Darmstadt 2017**

**D 17**

---

Sandeep Yadav

Datum: 04.10.2017

Carl-Ulrich-straße 12

64297 Darmstadt

### **Erklärung**

Ich erkläre hiermit, dass ich meine Dissertation selbstständig und nur mit den angegebenen Hilfsmitteln angefertigt habe.

Sandeep Yadav

---

Sandeep Yadav

Datum: 04.10.2017

Carl-Ulrich-straße 12

64297 Darmstadt

### **Erklärung**

Ich erkläre hiermit, noch keinen Promotionsversuch unternommen zu haben.

Sandeep Yadav

---

## PUBLICATIONS

1. O. Yilmazoglu, S. Al-Daffaie, H. L. Hartnagel, R. Joshi, **S. Yadav**, J. J. Schneider, C. Nick, C. Thielemann “CNT photocathodes based on GaAs high-frequency photoswitches”, *IEEE Xplore*, (2012), DOI: 10.1109/IVNC.2012.6316840.
2. M. Pashchanka, **S. Yadav**, T. Cottre, J. J. Schneider “Bright interference colour tuning in alumina/metallic Pt/Pd, Cr and Al hybrid materials”, *Nanoscale*, (2014), 6, 12877-12883, DOI: 10.1039/C4NR03167A.
3. C. Nick, **S. Yadav**, R. Joshi, J.J. Schneider, C. Thielemann “Growth of Cortical Neurons Grown on Randomly Oriented and Vertically Aligned Dense Carbon Nanotube Networks”, *Beilstein J. Nanotechnol.*, (2014), 5, 1575-1579, DOI:10.3762/bjnano.5.169.
4. Y. Wang, **S. Yadav**, T. Heinlein, V. Konjik, H. Breitzke, G. Buntkowsky, J. J. Schneider, K. Zhang “Ultra-light nanocomposite aerogels of bacterial cellulose and reduced graphene oxide for specific absorption and separation of organic liquids”, *RSC Advances*, (2014), 4, 21553-21558, DOI: 10.1039/C4RA02168A.
5. D. J. Babu, **S. Yadav**, T. Heinlein, G. Cherkashinin, J. J. Schneider “Selective functionalization of vertically aligned carbon nanotube arrays using CO<sub>2</sub> plasma”, *J. Phys. Chem. C.*, (2014), 118, 12028-12034, DOI: 10.1021/jp5027515.
6. C. Nick, **S. Yadav**, R. Joshi, J.J. Schneider, C. Thielemann “A three-dimensional microelectrode array composed of vertically aligned ultra-dense Carbon Nanotube Networks”, *Appl. Phys. Lett.*, (2015), 107, 013101, DOI: 10.1063/1.4926330
7. E. Alam, **S. Yadav**, J. J. Schneider, T. Gambaryan-Roisman “Imbibition of water into heat treated polydimethylsiloxane substrates”, *Colloids and Surfaces A*, (2016), 521, 69-77 DOI: 10.1016/j.colsurfa.2016.09.017.
8. H. Kaur, **S. Yadav**, K. Srivastava, N. Singh, J.J. Schneider, O.P. Sinha, V.V. Agrawal, R. Srivastava “Large area fabrication of semiconducting phosphorene by Langmuir Blodgett assembly”, *Nature Sci. Rep.*, (2016), 6, 34095, DOI: 10.1038/srep34095.
9. O. Yilmazoglu, **S. Yadav**, D. Cicek, J.J. Schneider “A nano-microstructured-artificial-hair-cell-type sensor based on topologically graded 3D carbon nanotube bundles”, *Nanotechnology*, (2016), 27, 365502, DOI: 10.1088/0957-4484/27/36/365502.
10. D. J. Babu, F. G. K uhl, **S. Yadav**, D. Markert, M. Bruns, M. J. Hampe, J. J. Schneider “Adsorption of pure SO<sub>2</sub> on nanoscaled graphene oxide”, *RSC Advances*, (2016), 6, 36834-36839, DOI: 10.1039/C6RA07518E.

- 
11. B. Koerbitzer, P. Krauss, C. Nick, **S.Yadav**, J. J. Schneider, C. Thielemann “Substrate effects on graphene electrodes for stimulation of neuronal cells”, *2D Mater.*, (2016), 3, 024004, DOI: 10.1088/2053-1583/3/2/024004.
  12. H. Kaur, **S. Yadav**, K. Srivastava, N. Singh, R. Shyam, J.J. Schneider, O.P. Sinha, R. Srivastava “High yield synthesis and chemical exfoliation of Two dimensional layered belt like Hafnium Disulfide” *Nano Research*, (2017), DOI: 10.1007/s12274-017-1636-x.

## **PATENTS**

1. Patent No. DE102014018878B3- SPRING SENSOR ELEMENT (Issued in Germany).  
Patent No. US20160178459 A1- SPRING SENSOR ELEMENT (Pending USA).
2. Arrangement of carbon nanotubes and a process of their preparation (Pending).

## **CONFERENCE**

1. O. Yilmazoglu, **S. Yadav**, D. Cicek, J.J. Schneider, Nanostructured spring element sensor, Hannover messe 2016, April 25 – 29, 2016 (Poster presentation).

---

## ACKNOWLEDGEMENT

I express my sincere gratitude towards **Prof. Dr. Jörg J. Schneider** for his patience and continuous support during my Ph.D. work. He was always open for my new ideas and even supported me through developing these ideas to a complete work. I learned a lot from him on the research level and even on a personal level.

I deeply thank **PD Dr.-Ing. habil. Oktay Yilmazoglu** for the collaborative work in which I was involved together with **M.Sc. Deniz Cicek** which added a lot to my work in the Ph.D thesis and even offered me to have a patent. I also thank him for the fruitful discussions which pushed my work forward.

For further collaborative work I want to thank **Prof. Dr.-Ing. Christiane Thielemann** and **Dr.-Ing. Nick Christoph** for the studies on vertically aligned carbon nanotubes and its application in microelectrode arrays. I would also like to thank **Prof. Dr. rer. nat. Markus Biesalski**, **Prof. Kai Zhang** and **Dr. Yonggui Wang** for enabling the work of graphene oxide and bacterial cellulose composite as well as **Dr. Ritu Srivastav**, **M. Sc. Harneet Kaur** and **Dr. Om Prakash Sinha** for the collaborative work on field-effect transistors. Special thanks also go to **Prof. Dr. rer. nat. Robert Stark** and **Asma Siddique** for the HEK cell growth work and to **Dr. Suman Narayan** for the contact angle measurements done in that work.

I am indebted to **Dr. Jörg Engstler** and **Ulrike Kunz** for TEM measurements, **Dr. Rudolf Hoffmann** for TGA measurements, **Prof. Dr. Barbara Albert** for enabling me to work in the solid state chemistry lab, **Dr. Kathrin Hofmann** for the XRD measurements, **Dr. Christina Birkel** for the help with the microwave synthesis, **Dr. Dennis Henge** and **Jutta Kilschautzky** for the help in the ampule preparation, **Dr. Chittaranjan Das** and **Dipl.-Ing. Karl Kopp** for XPS measurements, **Mohamed Ehsanul Alam** for AFM measurements, **Prof. Dr.-Ing. Manfred J. Hampe** and **Dipl.-Ing. Frank Kühl** for SO<sub>2</sub> adsorption measurements, finally **Prof. Bastian J. M. Etzold** and **Konrad Krois** for supercapacitor work.

I am grateful to my recent and former coworkers **Dr. Mathias Nowotny**, **Dr. Hermann Tempel**, **Dr. Julia Patzsch**, **Dr. Mikhail Pashchanka**, **Dr. Ravi Joshi**, **Dr. Divya Puthusseri**, **Dr. Deepu J. Babu**, **Dr. Peter Krauß**, **Ute Schmidt**, **Silvio Heinschke**, **Ildiko Balog**, **Berit Körbitzer**, **Bilge Gündüz**, **Jan Krausmann**, **Shawn Sanctis**, **Jonathan Stott**, **Tobias Wombacher**, **Sherif Okeil**, **Tim Herdt** and **Nico Koslowski** for producing a nice and enjoyable working atmosphere as well as for providing help during my work for the Ph.D.



---

I am always grateful to my family members **Smt. Vidya Yadav, Shri Ashok Kumar Yadav, Smt. Ragini Yadav, Rajesh Yadav, Rita Latocha, Tabea Latocha,** and **Klaus Voelkel** for making my life joyful and for their continuous support throughout my life. Without their presence in my life I never would have been in that position now. May the soul of my grandparents **Shri Ramkaran Yadav and Shri Satiram Yadav** rest in peace as they were my backbone in this life. They grew me up to what I am now and always encouraged me to go on in this life no matter what happens.

I hope I did not forget anyone but if I have, it is not for the lack of appreciation.

---

## DEDICATION

*To my beloved wife, Akanksha ( for your patience, encouragement, trust & support) and precious daughter, Aavya the greatest gift I have ever gotten in my life.*

---

## Zusammenfassung

Kohlenstoffnanoröhren stellen ein interessantes Allotrop von Kohlenstoff dar, die eine breite Palette von Anwendungen haben können, da sie außergewöhnliche mechanische, elektrische und thermische Eigenschaften aufweisen. Dies macht CNTs zu einem interessanten Nanomaterial für verschiedene Anwendungen, von mechanischen Sensoren bis hin zu elektrischen Mikroelektroden und sogar biologischen Anwendungen aufgrund ihrer biologischen Kompatibilität.

Neben den hervorragenden Materialeigenschaften ist die Verwendung einer speziellen Strukturierung dieser Materialien definierter Orientierung von großer Bedeutung. Damit kann man morphologisch reproduzierbare Materialien erhalten, die für Anwendungen besser geeignet ist. Daher wird in dieser Arbeit das kontrollierte Wachstum von vertikal ausgerichteten Kohlenstoffnanoröhren (VACNTs) betrachtet.

VACNTs werden auf Si/SiO<sub>2</sub>-Substraten unter Verwendung einer wasserunterstützten chemischen Dampfabscheidungstechnik synthetisiert. Durch diese Technik werden hochkristalline, reine und mehrwandige CNTs mit weniger Schichten und einer vertikalen Orientierung zum Substrat erhalten. Die Parameter für das Wachstum wurden optimiert, um auch VACNTs mit unterschiedlichen Höhen in einem Syntheseschritt zu ermöglichen. Diese Strukturierung dient dazu, einen nanomikrostrukturierten haarzellartigen Sensor zu erhalten, der beispielsweise als ein mechanischer Sensor dreidimensionale Kräfte durch den wechselnden Kontaktwiderstand zwischen benachbarten CNT-Bündeln unterschiedlicher Höhe messen kann.

Wegen der hervorragenden elektrischen Eigenschaften zusammen mit der stark erhöhten Oberfläche der vertikal ausgerichteten VACNTs wurden sie mit ungeordneten CNTs für Mikroelektrodenanwendungen verglichen. Dabei wird der Vorteil der vertikalen Ausrichtung in der dramatischen Abnahme der elektrischen Impedanz und der enormen elektrischen Kapazitätserhöhung gegenüber planaren Elektroden deutlich. Diese Mikroelektroden wurden in Hinblick auf biologische Anwendungen getestet. Speziell wurde das Wachstum kortikaler Neuronen untersucht.

Während CNTs eindimensionale Systeme darstellen, wurden auch zweidimensionale kohlenstoffbasierte Materialien, wie Graphenoxid und reduziertes Graphenoxid, untersucht und sowohl für die Gasadsorption als auch als Flüssigkeitsabsorptionsmittel in Kombination mit bakterieller Cellulose in Form von Aerogelen verwendet.

Zum Schluss wurde Phosphoren, als Beispiel für ein zweidimensionales Material, das eng mit Graphen in seiner Struktur verwandt ist, synthetisiert. Phosphoren, obwohl strukturell ähnlich mit Graphen, besitzt im Gegensatz zu Graphen eine Bandlücke, die es zu einem interessanten Material für Feldeffekt-Transistoren macht, wie in dieser Arbeit ebenfalls gezeigt wird.

---

## Abstract

Carbon nanotubes (CNTs) are an interesting allotrope of carbon which can have a wide range of applications as they have extraordinary mechanical, electrical and thermal properties. All this makes CNTs an interesting nanomaterial for different applications ranging from mechanical sensors to electrical microelectrodes and even biological applications due to their biological compatibility.

Beside the excellent material properties, the use of special structuring of these materials is of great importance. The random orientation of CNTs cannot be controlled which usually leads to irreproducible material which is not suitable for real world applications. Therefore, the controlled growth of vertically aligned carbon nanotubes (VACNTs) is considered in this work.

VACNTs have been grown on Si/SiO<sub>2</sub> substrates using a water-assisted chemical vapor deposition technique. By this technique highly crystalline, pure, low-layer multiwalled CNTs with a vertical orientation to the substrate are obtained. The parameters for the growth are optimized and even structuring of the VACNTs is possible obtaining VACNTs with different heights in one synthesis step. This structuring is used to construct a nano-microstructured artificial-hair-cell-type sensor as an example for a mechanical sensor which can measure three-dimensional forces by the changing contact resistance between neighboring CNT bundles of different heights.

Because to the excellent electrical properties together with the highly-increased surface area due to the vertical alignment of VACNTs, they are compared to randomly oriented CNTs for microelectrode applications. In this, the advantage of vertical alignment becomes clear in the dramatic decrease in impedance and enormous increase in capacity. These microelectrodes are then tested for biological applications for which the compatibility and growth pattern of cortical neurons on VACNTs is studied.

While CNTs represent one-dimensional systems, also two-dimensional materials related to carbon such as graphene oxide and reduced graphene oxide are studied and used for gas-adsorption as well as liquids absorbents in combination with bacterial cellulose in the form of aerogels.

Finally, phosphorene as an example of a two-dimensional material closely related to graphene is synthesized. Phosphorene, although structurally similar to graphene, it has a band gap in contrast to graphene which makes it an interesting material field-effect transistor devices as shown in this work.

---

## INDEX

<b>I</b>	<b>INTRODUCTION</b>	<b>1</b>
I.1	Carbon nanotubes	1
I.2	Hybridization of carbon	2
I.3	Structure of carbon nanotubes	3
I.4	Methods of preparation	4
I.4.1	Arc-discharge method	4
I.4.2	Laser ablation method	5
I.4.3	Chemical vapor deposition method	6
I.4.4	Floating catalyst method	7
I.5	Growth mechanism of carbon nanotubes	8
I.5.1	Vapor-solid-solid (VSS) growth mechanism	8
I.5.2	Vapor-liquid-solid (VLS) growth mechanism	11
I.6	Characterizations	11
I.6.1	Raman spectroscopy	11
I.6.2	X-ray photoelectron spectroscopy	14
I.6.3	Scanning electron microscopy	17
I.6.4	Transmission electron microscopy	18
I.6.5	X-ray diffraction	20
I.6.6	Thermogravimetric analysis	21
<b>I.7</b>	<b>Objective and motivations</b>	<b>22</b>
<b>II</b>	<b>SYNTHESIS, CHARACTERIZATION, PROPERTIES AND APPLICATIONS OF VERTICALLY ALIGNED CARBON NANOTUBES</b>	<b>23</b>
II.1	Introduction	23
II.2	Water assisted chemical vapor deposition technique	24
II.3	Growth mechanism of water assisted chemical vapor deposition	26
II.4	Unique properties of carbon nanotubes	28
II.4.1	Electrical properties	28
II.4.2	Thermal properties	28
II.4.3	Biological properties	29
II.4.4	Mechanical properties	30

<b>II.5</b>	<b>Results and discussion</b>	32
II.5.1	Characterizations of VACNTs grown over Al (10 nm) and Fe (1.6 nm)	33
II.5.2	Characterizations of VACNTs grown over Al <sub>2</sub> O <sub>3</sub> (30 nm) and Fe (1.2 nm)	35
II.5.3	Application of VACNTs in microelectrode arrays	37
II.5.4	Application of VACNTs in neuron growth	44
II.5.5	A nano-microstructured artificial-hair-cell-type sensor based on topologically graded 3D carbon nanotube bundles	50
II. 6	Conclusions	60
<b>III</b>	<b>SYNTHESIS, CHARACTERIZATIONS AND APPLICATIONS OF GRAPHENE OXIDE</b>	62
III.1	Introduction	62
III.2	Preparation of graphene oxide	63
III.3	Reduction of graphene oxide	65
III.4	Applications of graphene oxide	70
III.5	Results and discussion	73
III.6	Functional application of graphene oxide	81
III.7	Conclusions	87
<b>IV</b>	<b>PHOSPHORENE AND ITS APPLICATIONS</b>	88
IV.1	Introduction	88
IV.2	Phosphorene	90
IV.3	Results and discussions	92
IV.4	Study towards selective functional properties of phosphorene	96
IV.4.1	Gas sensor	96
IV.4.2	Field-effect-transistor	99
IV.4.3	Human embryonic kidney cell growth	103
IV.5	Conclusions	104
<b>V</b>	<b>SUMMARY AND OUTLOOK</b>	105
<b>VI</b>	<b>EXPERIMENTAL SECTION</b>	107
VI.1	Characterization techniques	107
V1.2	Thin film deposition units	107

---

VI.2.1	Electron beam (e-beam) evaporation unit	107
VI.2.2	Atomic layer deposition (ALD) unit	108
VI.2.3	Catalytic chemical vapor deposition (CVD) unit	109
VI.3	Vertically aligned carbon nanotubes	110
VI.3.1	Deposition of aluminium and iron	110
VI.3.2	Growth of VACNTs	110
VI.3.3	Deposition of aluminium oxide	118
VI.3.4	Growth of VACNTs	120
VI.4	Graphene oxide and reduced graphene oxide	123
VI.4.1	Synthesis of graphene oxide	123
VI.4.2	Exfoliation of graphene oxide	124
VI.4.3	Reduction of graphene oxide	124
VI.5	Black phosphorus	126
VI.5.1	Bismuth flux method	126
VI.5.2	Chemical vapor transport reaction	128
VI.5.3	Exfoliation of black phosphorus	129
<b>VII</b>	<b>REFERENCES</b>	<b>130</b>

---

## ABBREVIATIONS

AHCTS	Artificial-hair-cell-type sensor
ALD	Atomic layer deposition
BET	Brunauer-Emmett-Teller
BP	Black phosphorus
C <sub>h</sub>	Chiral vector
CNS	Central nervous system
CNTs	Carbon nanotubes
CVD	Chemical vapor deposition
DNA	Deoxyribonucleic acid
DWCNTs	Double-walled carbon nanotubes
e-beam	Electron-beam
FET	Field-effect-transistor
GO	Graphene oxide
MWCNTs	Multi-walled carbon nanotubes
NLDFT	Non-linear density functional theory
PNS	Peripheral nervous system
rGO	Reduced graphene oxide
RIE	Reactive Ion Etching
RNA	Ribonucleic acid
SEM	Scanning electron microscopy
SWCNTs	Single-walled carbon nanotubes
TEM	Transmission electron microscopy
TGA	Thermogravimetric analysis
VACNTs	Vertically aligned carbon nanotubes
XPS	X-ray photoelectron spectroscopy
XRD	X-ray diffraction



## I INTRODUCTION

This chapter starts with an introduction to carbon nanotubes. Then various synthesis methods, and characterizations carbon nanotubes are discussed.

### I.1 Carbon nanotubes

Carbon nanomaterials are found useful in variety of applications due to their unique properties. Figure I.1 shows different types of carbon nanomaterials. Carbon nanotubes (CNTs) are one of the allotropes of carbon. They have cylindrical structures with at least a single closed end. CNTs are classified as single-walled carbon nanotubes (SWCNTs), double-walled carbon nanotubes (DWCNTs) and multi-walled carbon nanotubes (MWCNTs) based on the number walls present in it <sup>[1]</sup>. Depending on the diameter and chirality of the helical CNTs, they can be either metallic or semiconducting <sup>[2-4]</sup>.

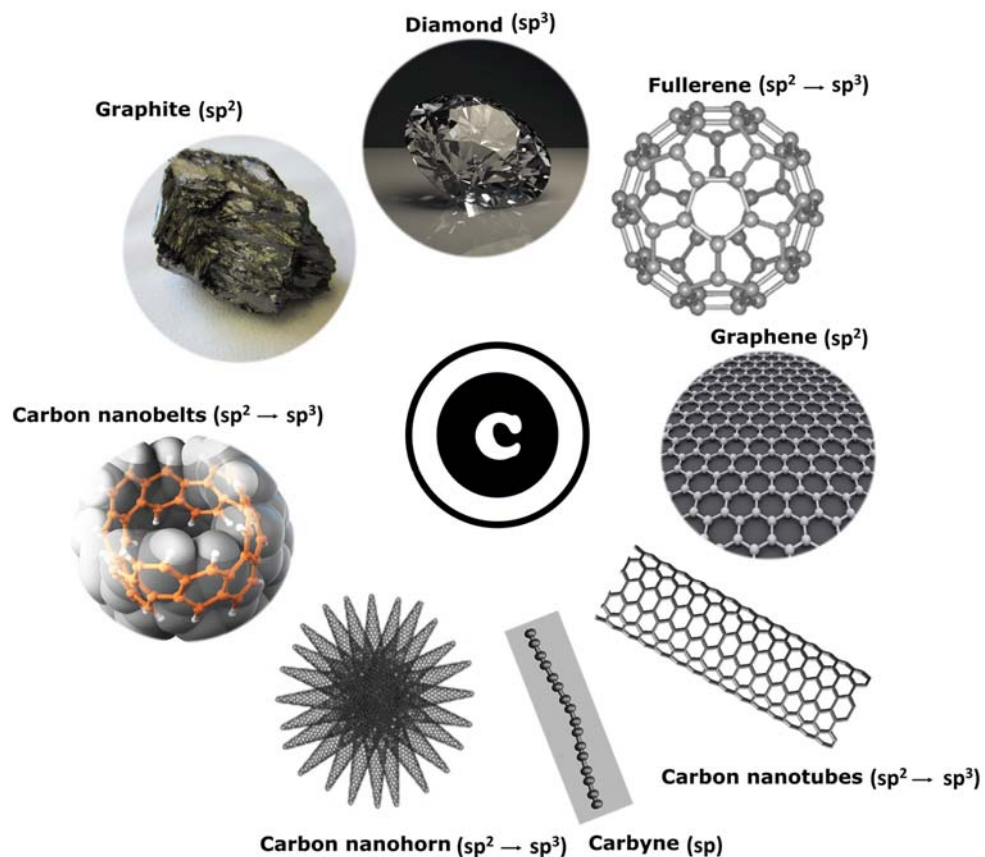


Figure I.1 Different kinds of carbon nanomaterials (Graphite, Diamond, Fullerene <sup>[5]</sup>, Graphene <sup>[6]</sup>, Carbyne <sup>[7]</sup>, Carbon nanohorn <sup>[8]</sup>, Carbon nanobelts <sup>[9]</sup>).

---

The tubular structures of carbon atoms (CNTs) are hundred times stronger than stainless steel and at the same time six times lighter (normalized to its weight). The current-carrying capacity of CNTs are 1000 times higher than that of copper and their thermal stability is up to about 4000 K. CNTs are hard as diamond but their thermal conductivity is two times that of the diamond [10]. CNTs have a Young's modulus of ~1TPa and a tensile strength of ~63GPa [10]. Current research has not offered best cost effective methods of producing CNTs with well-defined superlative properties in large scale quantities. This problem emanates from the limited understanding of how these carbon nanotubes grow. There are pending answers in regards to the CNTs growth mechanisms [11].

CNTs have unique mechanical, electrical, thermal, optical and other properties, which are suitable for various applications. The properties of CNTs depend on their structure in terms of diameter, number of walls, chiral angle and length. CNTs are widely applied in solar cells [12], conductive films [13], sensors [14-15], purification systems [16], transistors [17-18], fuel cells [19], displays [20], memories [21], super capacitors [22], separation membranes and filters [23] etc.

Graphene has densely organized carbon atoms which take the form of a regular  $sp^2$  – bonded and hexagonal pattern like honeycomb, which forms the basic pattern for other allotropes, CNTs inclusive. Understanding of collective mechanism for the growth of CNT forests have led to wafer-scale production of vertically aligned carbon nanotubes (VACNTs) and there is an anticipation of large-scale production of the same [24]. VACNTs arrays are interestingly being used in a wide variety of applications such as energy storage devices [25-26], solar cells [27], field emission device [28], electrical interconnects [29], membranes [30] and thermal interface materials [31].

Carbon nanotubes are the rolled form of a single layer of graphite. Sumio Iijima of NEC is remembered for discovering carbon nanotubes in 1991 as a byproduct of fullerene ( $C_{60}$ ) synthesis by electron microscopy [32]. Carbon nanotubes are nowadays prepared through various methods such as arc-discharge technique [33], laser ablation [33-34], plasma enhanced chemical vapor deposition technique [35-36] and chemical vapor deposition [37]. Denser and thicker linear nanotube arrays are grown through chemical vapor deposition technique [36]. Particular applications demand these carbonic nanomaterials to be extracted in certain forms (non-aggregated or in strands). The commonly used separation methods include electrophoresis [38], centrifugation [39], chromatography [40] etc.

## **1.2 Hybridization of carbon**

Carbon has the electronic configuration  $1s^2, 2s^2, 2p^2$ . In graphite, one of the 2s electrons hybridize with two 2p electrons to give three  $sp^2$  orbital at  $120^\circ$  to each other in a plane. The remaining  $p_z$  orbital arranged at  $90^\circ$  to this plane. The  $sp^2$  orbitals form the strong  $\sigma$  bonds between carbon atoms

in the graphite planes, while the  $p_z$  or  $\pi$ -orbitals provide the weak van der Waals bonds between the planes. The overlap of  $\pi$  orbitals on adjacent atoms in a given plane provides the electron bond network which gives graphite its relatively high electrical conductivity [11]. Figure I.2 shows the schematic of the  $sp^2$  hybridization in graphene.

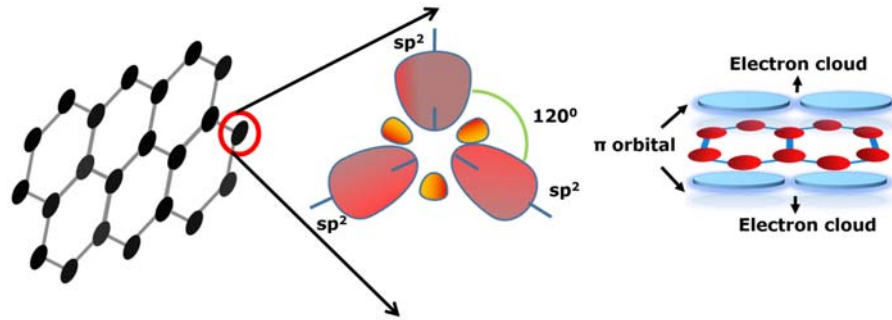


Figure I.2  $sp^2$  hybridized crystal structure of graphene.

### I.3 Structure of carbon nanotubes

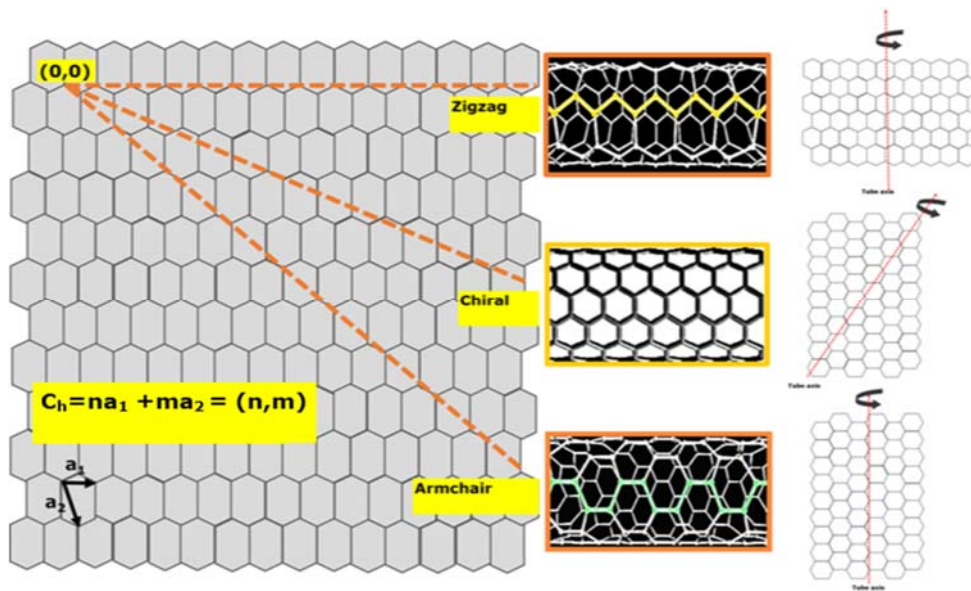


Figure I.3 Armchair, zigzag and chiral carbon nanotube specified using  $(n,m)$ .

Carbon nanotube can be specified in terms of the tube diameter,  $d_t$  and chiral angle,  $\theta$ . The chiral vector can be expressed in terms of the integers  $(n,m)$  and the basis vectors  $\mathbf{a}_1, \mathbf{a}_2$  of the honeycomb lattice.

---

$$\mathbf{C}_h = n\mathbf{a}_1 + m\mathbf{a}_2 \quad (\text{I.1})$$

(n, 0) represents zigzag carbon nanotubes, (n, n) for armchair carbon nanotubes and all other (n, m) represents chiral carbon nanotubes (figure I.3).

The expression for the tubule diameter and chiral angle is provided below

$$d_t = \frac{|\mathbf{C}_h|}{\pi} = \frac{a_{c-c}\sqrt{3(n^2+nm+m^2)}}{\pi} \quad (\text{I.2})$$

$$\theta = \tan^{-1} \frac{\sqrt{3}m}{2n+m} \quad (\text{I.3})$$

where  $a_{c-c}$  is the distance between nearest carbon atoms, which is 1.42 Å in graphite,  $|\mathbf{C}_h|$  is the length of the chiral vector.

Most of the experimentally observed carbon nanotubes are multiwalled consist of capped concentric layers and the interlayer spacing is ~3.5 Å. Each tube can be specified using chiral vector in terms of (n, m) or by tube diameter and chiral angle. Because of the different number of carbon atoms in each layer, ABAB stacking cannot be observed in carbon nanotubes like graphite [1, 4].

## I.4 Methods of preparation

Various methods used for the synthesis of carbon nanotubes are arc-discharge, laser ablation, chemical vapor deposition and floating catalyst method.

### I.4.1 Arc-discharge method

The arc discharge setup consists of a furnace, a stainless steel vacuum chamber, graphite electrodes, a water cooled trap and high voltage power supply. Initially, carbon arc discharge method was used to produce C<sub>60</sub> fullerenes [41]. CNTs were first synthesized through arc-vaporization of two graphite rods placed end to end, separated by approximately 1mm, in an enclosure that is usually filled with inert gas at low pressure (figure I.4). A direct current of 50 to 100 A, driven by a potential difference of approximately 20 V, creates a high temperature arc discharge between the two electrodes. The arc provides high temperature which is needed to vaporize carbon atoms into a plasma (>3000°C) [10]. Graphite rods doped with iron [42] and cobalt [43-44] are used for the production of single walled carbon nanotubes. Multiwalled carbon nanotubes are synthesized by arc discharge in liquid nitrogen and water [45]. Large scale production of SWCNTs over Ni-Y catalyst using arc discharge under helium atmosphere is reported [46].

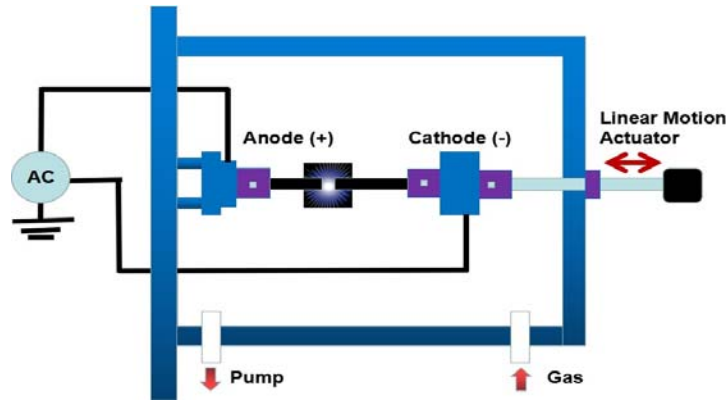


Figure I.4 Schematic of the arc discharge set up.

### I.4.2 Laser ablation method

Laser ablation technique is a method for the synthesis of high purity CNTs. Figure I.5 shows a schematic of laser ablation set-up. In this method, graphite target is evaporated by a laser beam in an inert atmosphere and under high temperatures. The flowing inert gas sweeps the carbon species produced by the laser from the high temperature zone to water cooled conical copper collector. The quality and quantity of the product is determined by the reaction temperature <sup>[10]</sup>. SWCNTs are produced by adding transition metals such as Fe, Ni or Co to the graphite target <sup>[34, 47-48]</sup>. Growth temperature, catalyst composition, laser power, size distribution, average diameter of the nanotube is varied based on nature and pressure of the gas used in the set up. <sup>[10, 35, 49-50]</sup>. CO<sub>2</sub> laser system operating in a continuous wave mode is used to get high yields of SWCNTs <sup>[51]</sup>. Average diameter of the SWNTs increases with increasing laser power <sup>[35, 52]</sup>.

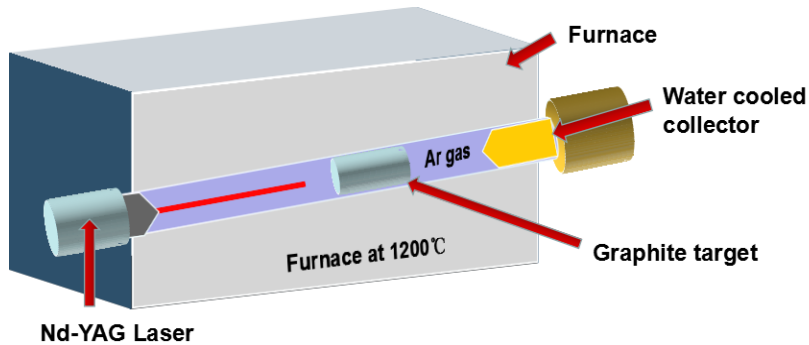
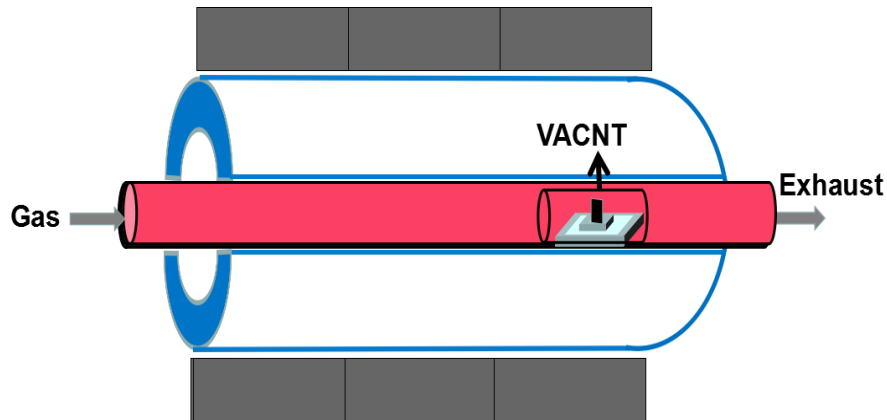


Figure I.5 Schematic of the laser ablation set up.

### I.4.3 Chemical vapor deposition method

In chemical vapor deposition (CVD) method, CNTs are synthesized by decomposing the carbon precursor on the surface of the catalyst particles. Two types of CVD methods used for synthesizing CNTs are thermal CVD and plasma enhanced CVD. In plasma enhanced CVD, CNTs are formed at relatively low temperature and the size of the catalyst particles controls the diameter of the CNTs. These methods are the most preferred technique for the large scale production of CNTs. In CVD method, carbon source is taken in the gas phase and resistive heating is employed to pass energy to gaseous molecules of carbon<sup>[10]</sup>. The most commonly used sources of carbon includes carbon monoxide<sup>[53]</sup>, methane<sup>[54-55]</sup>, ethane<sup>[56]</sup>, ethylene<sup>[57]</sup>, acetylene<sup>[58]</sup>, xylene<sup>[59]</sup>, ethanol<sup>[60]</sup> etc. The steps involved in the synthesis of CNTs by CVD are preparation of the catalyst and the decomposition of the carbon precursor gas over the catalyst under suitable conditions. Fe, Co and Ni is widely used as the catalyst for the growth of CNTs because of their high carbon solubility at high temperature and high carbon diffusion rate. Moreover, high melting point and low vapour pressure of these metals offer wide range of temperature window for wide range of carbon precursors<sup>[61]</sup>.



*Figure I.6 Schematic of catalytic chemical vapor deposition unit.*

Figure I.6 shows the schematic of a chemical vapor deposition unit. Hydrocarbon vapor is passed through a tube furnace containing a catalyst material for about 15-60 minutes and at sufficient temperatures of about 600-1200 °C in order to decompose hydrocarbon. The system is cooled to room temperature and the CNTs which have grown over the catalyst are collected. The setup hence will depend on the state carbon precursors, whether in gaseous state or in liquid form. The reactants are vaporized by a bubbler if liquid carbon precursors are used. A carrier gas is then used to transport the vaporized reactants into the CVD reactor. The gas may be inert such as N<sub>2</sub> or Ar or reactive such

---

as hydrogen. The CNT growth in the CVD is affected by three main parameters which are the catalyst used, the hydrocarbon used and the growth temperature. Low temperatures between 600 and 900 °C lead to formation of MWCNTs whereas higher temperatures about 900-1200 °C favour growth of SWCNTs. This implies that the formation of SWCNTs requires higher energy. The nanotube diameter is dictated by the particle size of the catalyst. This means that controlling metal nanoparticles sizes can control the diameter of the growing CNTs. Uniform CNT deposits can be realized if thin films of catalysts are used and coated onto various substrates [10, 61].

Plasma-enhanced chemical vapor deposition technique as well as thermal CVD technique can be used to produce VACNTs also. The applied electric field in plasma enhanced CVD method affects the alignment of CNTs during growth. The entire CNTs are submerged in the electric field, which is normal to the substrate. Absence of electric field resulted randomly oriented CNTs [62]. Vertically aligned CNTs can be grown on substrate using thermal CVD by employing crowding effect [62-63]. High growth yield is an important factor in vertical alignment because van der Waals force in between the neighbouring CNTs cause them to align vertically on substrate with densely distributed catalyst particles. Indeed, less number of catalyst sites results low growth yield of CNTs which leads to randomness in CNT orientation. This confirms that the crowding effect is the alignment mechanism for densely packed CNT arrays [62].

Water assisted chemical vapor deposition is another method for the growth vertically aligned carbon nanotubes on substrate [64]. Water is added to the CVD reactor in order to enhance the lifetime and activity of the catalyst. The resultant nanotubes are superdense like a forest millimeter-tall and are aligned normal to the substrate. The purity is about 99.98%. Analysis of the kinetics of the supergrowth is important in understanding the effect of water. Time evolution of the forests height at a fixed condition was examined and modelled. Catalysts lose their activity in a similar fashion of radioactive decay. Growth rate is expressed by the equation (I.4) [65]

$$H(t) = \beta\tau_0(1 - e^{-t/\tau_0}) \quad (I.4)$$

where H is the height of the CNT forest,  $\beta$  is the initial growth rate and  $\tau_0$  is the characteristic catalyst life time.

#### **I.4.4 Floating catalyst method**

This method was used in the production of aligned carbon nanotubes using ferrocene as a catalyst precursor and acetylene as a carbon precursor. The synthesis is performed at high temperature of

about 850 ° in double stage CVD apparatus (figure I.7). The grown aligned CNTs are then purified through acid treatment and air oxidation. The produced CNTs possess various length and their diameters range between 15–20 nm. This method has the advantages such as simple, low cost precursors are used in yielding high purity aligned CNTs and avoids preparation of catalyst. They are free from contaminated amorphous carbon. This method can be transformed to continuous process [66]. Array of aligned multiwalled carbon nanotubes are grown by pyrolysis of the floating catalyst precursor, iron(III) chloride in a toluene/*N,N*-dimethylamino acetate solution at 600–850 °C hot H<sub>2</sub> atmosphere [67].

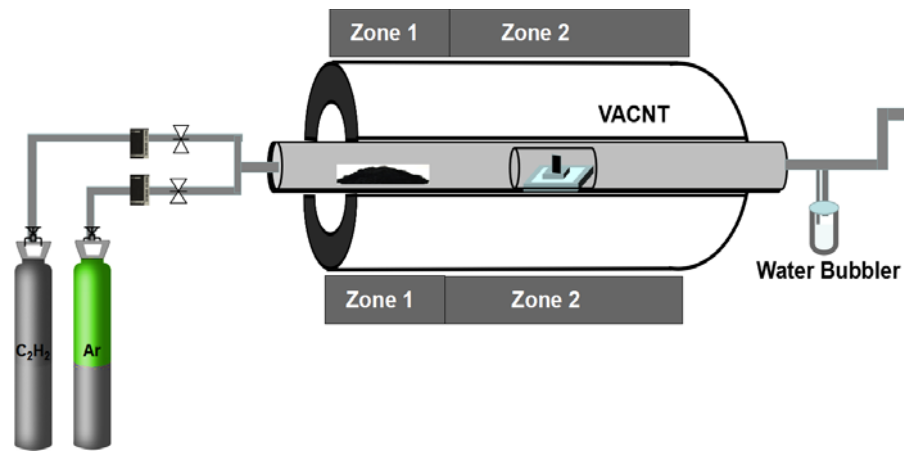


Figure I.7 Schematic of double stage CVD apparatus for floating catalyst method.

## 1.5 Growth mechanism of carbon nanotubes

CNT growth occurs mainly either by vapor-liquid-solid (VLS) mechanism or by vapor-solid-solid (VSS) mechanism [10, 61, 68].

### 1.5.1 Vapor-solid-solid (VSS) growth mechanism

This method involves four steps. The 1<sup>st</sup> step is the formation of nano-sized metallic particles on a substrate. The particles can be deformed by the annealing of a very thin metallic film. Laser ablation can also be used to achieve the same goal. The 2<sup>nd</sup> step is the decomposition of the hydrocarbon gas passing over the metal catalyst particle. This is done to discharge carbon and hydrogen which then dissolve in the catalyst particle. The 3<sup>rd</sup> step is accomplished by diffusing carbon through the metal particle and then carbon precipitation. If the catalyst is over coated and deactivated, termination of nanotube growth happens. Graphite or any other substrate is used to support the metal catalyst. The catalyst can float or be supported over the substrate. Deposition takes place on half of the spheres or



pear shaped catalyst surface, more specific on the lower curvature side. The diffusion of carbon happens along the concentration gradients and its precipitation takes place on the opposite half, below or around the bisecting diameter. There is no precipitation at the apex hemisphere which explains the hollow cores of the filaments. Base or root growth through supported metals forms filaments which result from extrusion. The nanotubes grow upward from the surfaces of the metal particles. The figure I.8 shows the schematics of root growth mechanism.

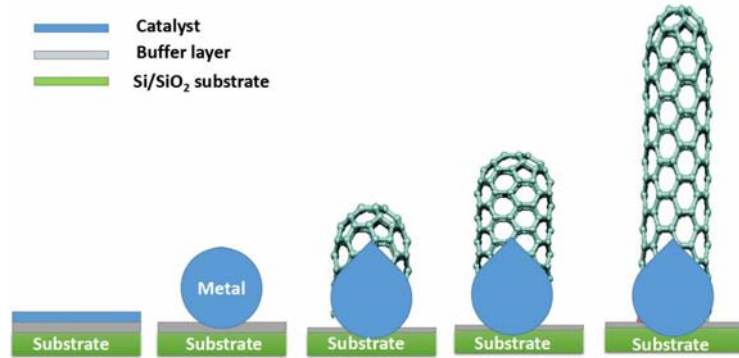


Figure I.8 Schematic of the root growth of VACNT.

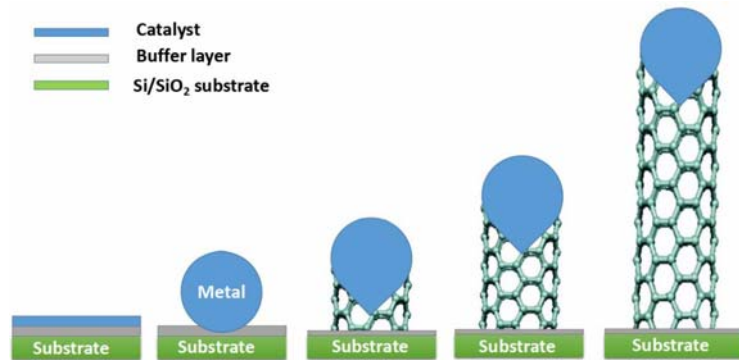
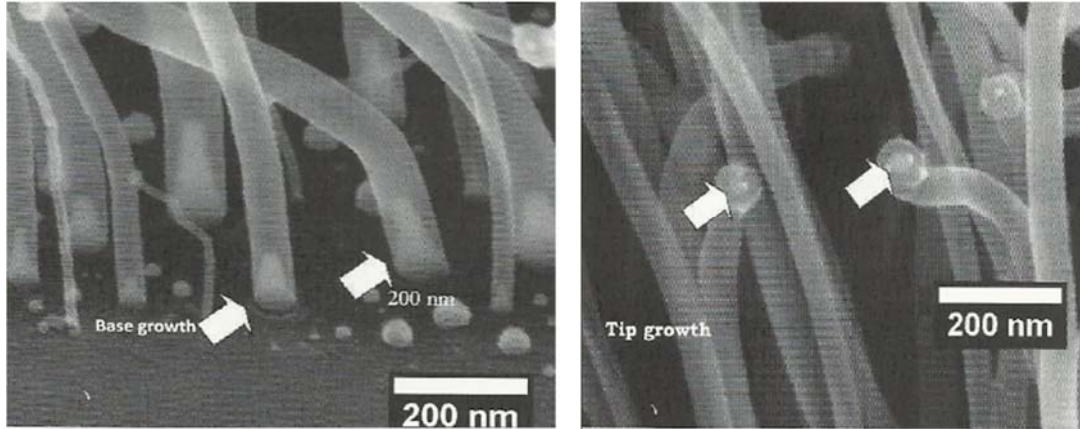


Figure I.9 Schematic of the tip growth of VACNT.

In the catalyst system, this method asserts that the metallic particle strongly interacts with the catalyst support and hence it is not possible to separate the formed graphite layer at the interface of the metal support. Tip growth happens when the particles detach and move at the head of the growing nanotube. Figure I.9 shows the schematic of the tip growth mechanism. Diffusion and osmotic pressure pushes the catalyst particle upwards leading to carbon deposition on the graphite structure located beneath of the catalyst. If the carbon deposits are not removing from the surfaces of the

metallic particles, the surface of the metal will be encapsulated by carbon and make the catalyst inactive. The figure I.10 shows scanning electron microscopy (SEM) image of CNTs and metal particles at the base and tips of the nanotubes.



*Figure I.10 SEM images of base growth and tip growth [10].*

The base-tip growth mechanism is a combination of tip growth and base growth mechanisms. The decomposition of hydrocarbon takes place freely on the surface of the metallic particle to yield carbon and hydrogen. At this temperature, the metal particle is melted into liquid state but not in solid form. The carbon concentration in the metal particles increases until the super saturation point is reached. At this point, the carbon atoms are forced to gather around the surface of the metallic particle. Growth is initiated when first graphite layer is formed. The liquid particle is elongated by a stretching force, breaking the liquid metallic particle into two parts. The growth is much initiated by the bottom parts having strong adhesion to the support. The metallic particles at the top of the tips are fully encapsulated by a graphite layer and hence the metallic particles at the CNT tips are deactivated from taking part in any reaction.

Diameter of the SWCNTs and MWCNTs formed depend on the size of the catalyst particle. The root growth demonstrates the strong catalyst and substrate used in the interaction and the tip growth shows there is a weak interaction between the catalyst and the substrate used. Another mechanism for the growth of CNT is named as the sealed nanotube grown by CVD [69]. In this method, the inner layer and the open tip growth are sealed first through decreasing the concentration of the carbon atoms followed by sealing of the outer layers of the nanotube. Open tip growth is generally applied in the growth of CNTs but the inner and the outer layers of the tube can be sealed simultaneously and stop the growth of the CNTs [10].

## I.5.2 Vapor-liquid-solid (VLS) growth mechanism

Vapor-liquid-solid (VLS) growth mechanism takes place in three major stages which are nucleation, precipitation and finally carbon deposition. In the arc discharge technique, the evaporation of the metal is carried out together with the carbon, forming carbon metal alloy particles on the surfaces of the cathode. The melting point of the alloy is low and the temperatures at the surface of the cathode are high, which leads to presumption that the alloy particles are in liquid state. Metal carbon compound soot is formed in a carbon rich atmosphere, hence the alloy particles in liquid state contain more carbon than its solubility limit in a solid phase. Liquid alloy particles start segregating the carbon particles on their surfaces when the cathode temperature decreases <sup>[10]</sup>.

## I.6 Characterizations

Several advanced techniques are currently used for CNT characterization, including electron microscopy (scanning electron microscopy and transmission electron microscopy), Raman spectroscopy, X-ray photoelectron spectroscopy, X-ray diffraction and thermogravimetric analysis.

### I.6.1 Raman spectroscopy

Raman spectroscopy provides information about molecular vibrations that can be used for sample identification and quantitation. A photograph of the Raman spectrometer and a schematic of its working principle is shown in figure I.11.

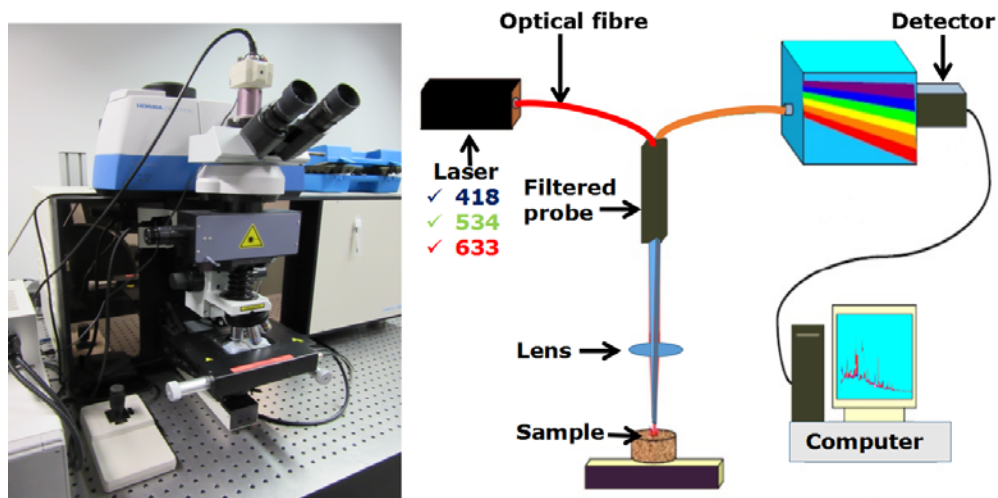


Figure I.11 Optical image of measurement setup (left) and working principle of the instrument (right).

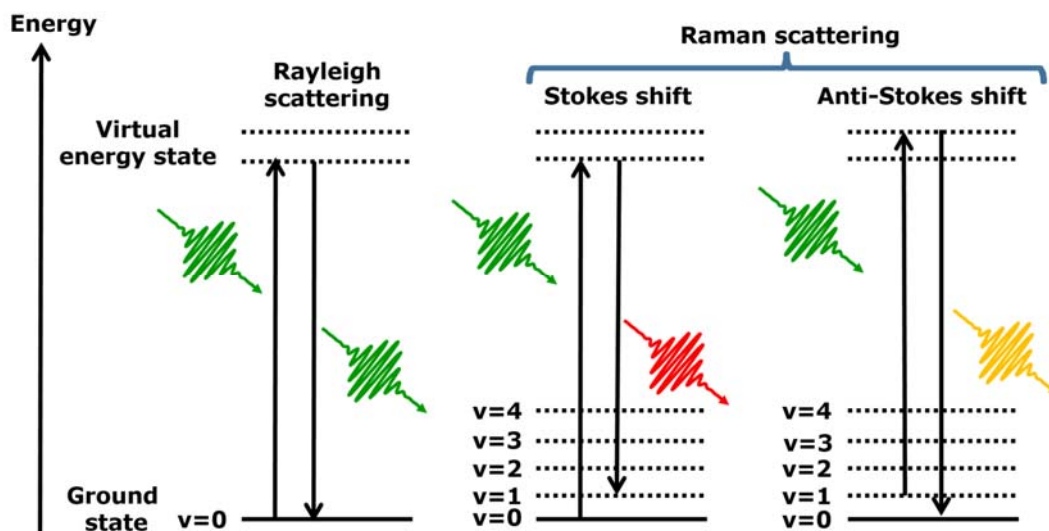


Figure I.12 Energy level diagram showing **Rayleigh**, **Stokes** (Raman) and **anti-Stokes** (Raman).

The technique involves shining a monochromatic light source (i.e. laser) on a sample and detecting the scattered light. The majority of the scattered light is of the same frequency as the excitation source; this is known as **Rayleigh** or elastic scattering. A very small amount of the light energy is scattered (ca.  $10^{-6}$  times the incident light intensity) due to interactions between the incident electromagnetic waves and the vibrational energy levels of the molecules in the sample. As a result, the emitted photons will be shifted to lower energy, i.e., light with a lower frequency. This shift is designated the **Stokes shift**. The difference in energy between the original state and the final state corresponds to a vibrational mode far from the excitation wavelength. If the process starts from a vibrationally excited state  $v=1$  and relaxes to the ground state  $v=0$ , then the emitted photons will be shifted to higher frequency which is designated the **anti-Stokes shift**. **Anti-Stokes-Raman** scattering is mostly weaker than **Stokes-Raman** scattering as most molecules are initially in their ground state. Hence **Stokes-Raman** scattering is mainly measured in Raman spectroscopy <sup>[70-71]</sup>. Figure I.12 shows the Energy level diagram showing **Rayleigh**, **Stokes** and **anti-Stokes** lines.

### **Raman spectra of carbon nanotubes**

Raman spectroscopy is one of the most eloquent, fast and non-destructive analysis tools for characterization of nanocarbonic materials and their position, width, and relative intensity of bands are modified according to the carbon forms <sup>[72-73]</sup>. Raman spectra of carbon nanotubes are very interesting because of its resonance phenomenon and sensitivity to tube assembly. Due to strong excitation the resonance Raman behavior in carbon nanotubes is unusual in that both the incident

and the scattered photon have the possibility to resonate. For this reason the frequencies on the **anti-Stokes** side may not be the same as those on the **Stokes** side [74]. The remarkable Raman features in CNTs (figure I.13) are the radial breathing modes (RBMs), the higher frequency D (disordered), G (graphitic), and G' (second-order Raman scattering from D-band variation) modes.

The Radial Breathing Mode (RBM) is one of the most important characteristic in the Raman spectrum of carbon nanotubes which is generally observed between 100 cm<sup>-1</sup> and 250 cm<sup>-1</sup> or sometime between 350 cm<sup>-1</sup> and 425 cm<sup>-1</sup> for extremely low diameter carbon nanotubes. The frequency of RBM mode is inversely proportional to the nanotube diameter (d<sub>t</sub>) [75-77].

$$\omega_{\text{RBM}} (\text{cm}^{-1}) = 224 (\text{cm}^{-1}) / d_t (\text{nm}) \quad (\text{I.5})$$

In Raman spectrum G-band representing tangential shear mode of carbon atoms in graphite like materials. This band is located near 1580-1590 cm<sup>-1</sup> corresponds due to C-C stretching.

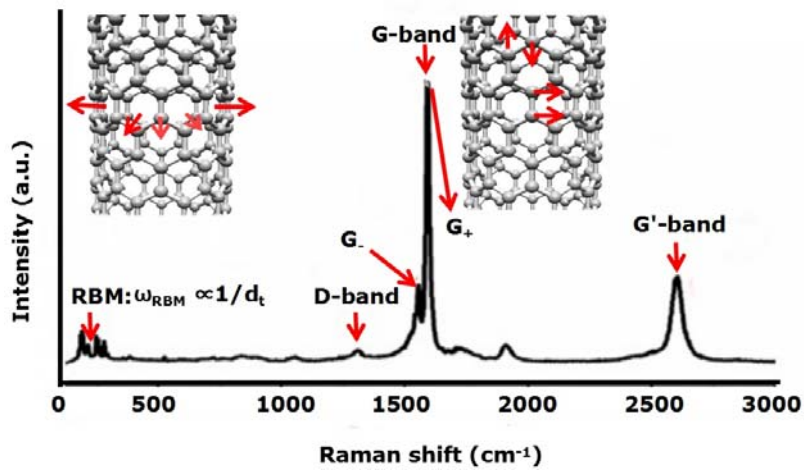


Figure I.13 Raman spectra for SWCNT showing important features like RBM mode, D-band and G-band. [75]

CNTs, this band has two major contributions, G<sub>+</sub> and G<sub>-</sub>. The G-band is the primary Raman active mode in graphite and it provides a good representation of the sp<sup>2</sup> bonded carbon that is present in planar sheet configurations which include the sp<sup>2</sup> bonded carbon of carbon nanotubes. The shape of the G-band and its frequency profile can be used to estimate whether the CNT is metallic or semi-conducting or roughly estimate the nanotube diameter [75, 78]. The D-band is considered as disorder band in graphitic materials and located between 1330 and 1360 cm<sup>-1</sup>. But still there is controversy regarding consideration for using D-band as defect characterization. Normally in high D-band

observed in the characterization of multiwalled carbon nanotubes (MWNT) and if it appears in SWNT considered a defect in the tube. The ratio between intensity of D-band and G-band can directly provide a measure of structural quality of CNTs [79].

G'-band or 2D-band is an intrinsic property of the carbon nanotubes and graphite. Frequency of G'-band is twice of D-band and found around 2500-2900  $\text{cm}^{-1}$ . G'-band does not require an elastic defect-related scattering process. It is observable for defect-free  $\text{sp}^2$  carbons and show a dependence on the chirality and diameter of nanotubes and on laser excitation energy [80].

### I.6.2 X-ray photoelectron spectroscopy

X-ray photoelectron spectroscopy (XPS) is a surface sensitivity method to determine the elemental composition and chemical nature of the surface. The XPS is also known as Electron Spectroscopy for Chemical Analysis (ESCA) due to its ability to distinguish different chemical components of element on the surface. In 1954 Kai Siegbahn at Uppsala University developed the XPS system where he was able to measure the elements present in NaCl [81]. However, the potential application comes into research recognition after Kai Siegbahn's publication about comprehensive study of XPS. In the XPS techniques the surface is illuminated with monochromatic light to strike out the electrons from the surface with characteristic kinetic energy. In laboratory based XPS system the X-ray sources of Al  $K\alpha$  or Mg  $K\alpha$  source with energy 1486.6 eV and 1253.6 eV respectively are used. A schematic of X-ray photoemission process and XPS system is shown in figure I.14.

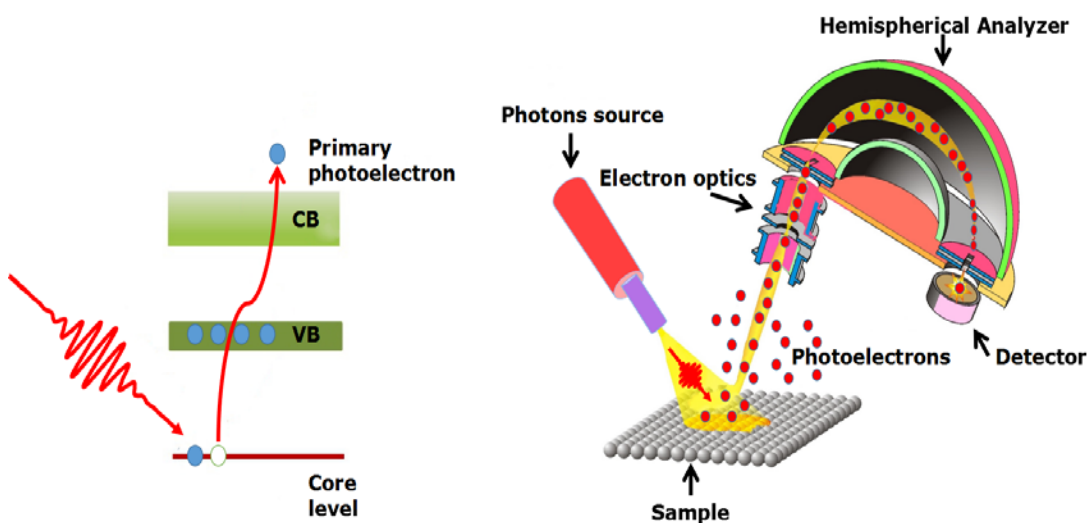


Figure I.14 Schematic diagram of X-ray photoemission process and the XPS system [82].

---

The XPS is surface analytical technique based on the concept of photoelectric effect discovered by Albert Einstein in 1905. In the process of XPS the material is illuminated with monochromatic X-ray photons of energy  $h\nu$  ( $h$  is the Planck's constant and  $\nu$  is the frequency of light). The incident X-ray will excite the electrons from the sample from different core levels of the element and these electrons will be emitted with different kinetic energy ( $E_K$ ). The kinetic energy of the emitted electrons will be detected and converted into binding energy ( $E_B$ ) of electrons by the analyzer. Empirically the relation between  $h\nu$ ,  $E_K$  and  $E_B$  can be give as in following equation

$$E_B = h\nu - E_K - \phi \quad (1.6)$$

where  $\phi$  is the work function of material.

The binding energy for different core levels are different for specific elements which make the XPS as tool to analyze different elements present in the material. However, there are other effects such as final state effect also contributes further identification of elements and chemical states of the elements. The spin orbit splitting in core level spectra are the result of final state effect in photoemission process of XPS. The spin orbit splitting is observed for orbital such as p, d and f having non-zero angular momentum quantum numbers. The spin-orbit splitting is represented by total angular momentum quantum number  $j$  and is given by  $j = l \pm s$  where  $l$  and  $s$  are orbital and spin quantum number. For example, the spin-orbit splitting for p-orbital is given by  $3/2$  ( $j=1+1/2$ ) and  $1/2$  ( $j=1-1/2$ ). The spin-orbit splitting gives rise to the branching ratio of the two peaks and the ratio is given by the multiplicity  $m = 2j + 1$ . This means for p-orbital the intensity ratio of  $p_{3/2}$  to  $p_{1/2}$  will be 1:2.

The final state effect also responsible for another secondary emission of electrons known as Auger electrons. After emission of core electron, the core holes are filled by the electrons from next level and the excess of energy is transferred to electron which emits with the same kinetic energy of that is being transferred to it. The Auger electrons are distinguishable from the photoemitted electron as the binding energy of the Auger peaks keep on changing with different photon energy. The XPS technique can be used for various surface science application such as elemental analysis, chemical analysis, quantitative elemental analysis, depth profiling, interface study etc. In the present work the XPS is used for only elemental and chemical analysis, therefore will focus on these two parts.

### ***Elemental analysis***

The XPS is vastly used of elemental analysis as the binding energy of each core levels are different

from each other in different elements. The different binding energy of core levels of different elements make it possible to identify the presence of different elements in a material.

The presence of different elements in a sample can be quantify by core level peak intensities. The intensities of different peaks can be quantified by considering the integral area under the curve and the sensitivity factor <sup>[83]</sup> for individual elemental core level peak. The intensity of the core level peak depends of the density of the atoms "n" present in the x-ray illuminated area and the atomic sensitivity factor "S". The intensity "I" of the peak is given by

$$I = n/S \tag{I.7}$$

The atomic ratio of different elements present in the sample can be given as bellow:

$$A_x = \frac{I_x/S_x}{\sum_x I_x/S_x} \tag{I.8}$$

A detail analysis of core level can inform about the chemical state of the respective elements present in the sample. The peak broadening, peak shift or appearance of shoulder peak could be due to the different chemical states of the element. However, the different chemical state is not only the solo cause of above effects in peaks shape. The change in shape of core level peak could be due to the

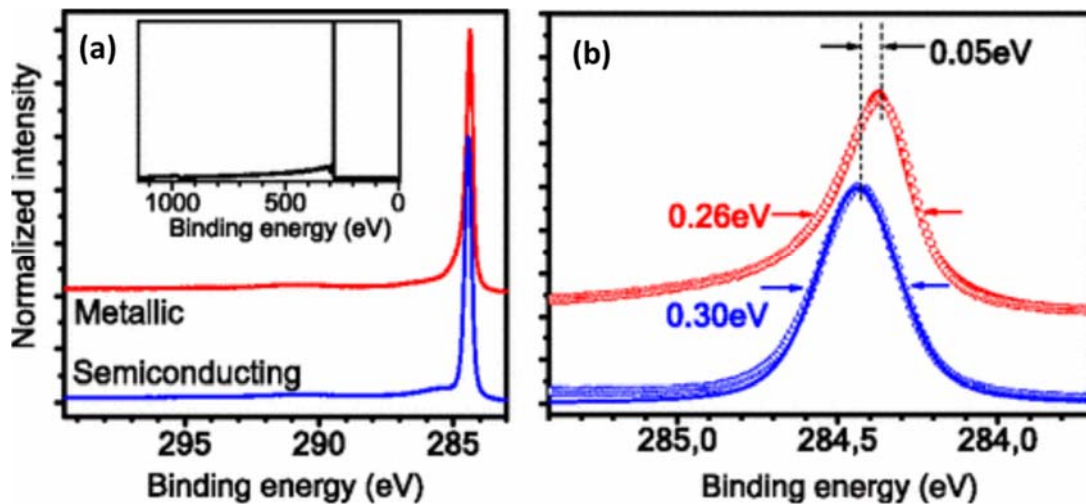


Figure I.15 (a) C1s photoemission of metallic SWCNT (upper curve) and semiconducting SWCNT(lower curve) as conducted at 400 eV photon energy. The inset shows a PES survey scan up to 1200 eV (b) The C1s line of the metallic and semiconducting SWCNT on an expanded scale <sup>[84]</sup>.



chemical shift, charging of the sample and/or the surface potential. Here I would like to mostly focus on change in peak shape due to the chemical shifts. The chemical shift in core level peaks is related to its oxidation states and also surrounding elements.

The stoichiometry and purity is investigated using the PES survey scan up to 1200 eV (inset of figure I.15 (a)). No oxygen contamination as well as catalyst impurity is observed. The High resolution C1s spectra shown in figure I.15 (b) indicated a downshift of 0.05 eV in the binding energy of metallic SWNTs which can be attributed to difference in the chemical potentials [84].

### I.6.3 Scanning electron microscopy

Due to the limitations of microscopy with light ( $\geq 400$  nm) which are limited by the physics of light to 500x or 1000x magnification and a resolution of 0.2 micrometers researcher developed scanning electron microscope (SEM) [85]. A stream of electrons is formed in high vacuum (by electron guns). This stream is accelerated towards the specimen while is confined and focused using metal apertures and magnetic lenses into a thin, focused, monochromatic beam. The sample is irradiated by the beam and interactions occur inside the irradiated sample, affecting the electron beam. These interactions and effects are detected and transformed into an image (figure I.16) [86].

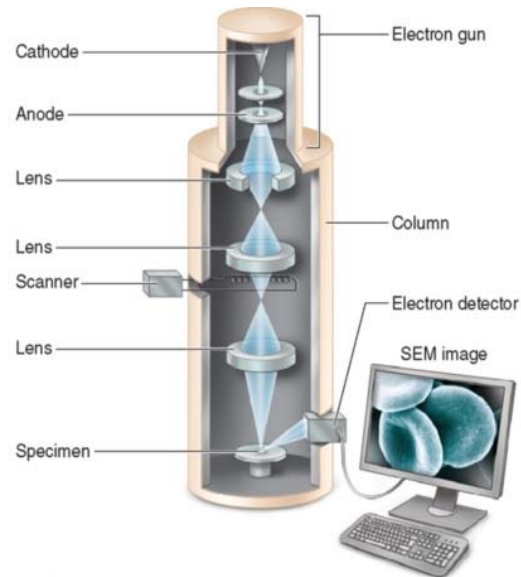


Figure I.16 Photograph and schematic of the scanning electron microscope [87].

Scanning electron microscopy (SEM) used for observation of specimen surface. Topological morphological and compositional information can be gather by SEM and is one of the essential tool

for characterizing bulk as well as nanomaterials [88]. When sample is irradiated with electron beam, secondary electron release from the sample surface and contains information about the surface topography, elemental composition and conductivity. Generally, morphology of carbon nanotubes observed by secondary electron imaging (SEI) compared to secondary electron, back scattered electron, cathodoluminescence or characteristic X-rays [62]. Figure I.16 illustrate SEI schematically, SEM uses focussed ion beam of very high energy electrons (20–40 keV) and when this electron hits the solid sample generate variety of signals. This signal including secondary electron (produce SEM images), back-scattered electron, photons (used for elemental analysis), visible light and heat. SEM is a non-destructive method and the same sample is possible to analyze time and again [89]. The alignment of VACNT bundles provided directly by SEI is shown in figure I.17.

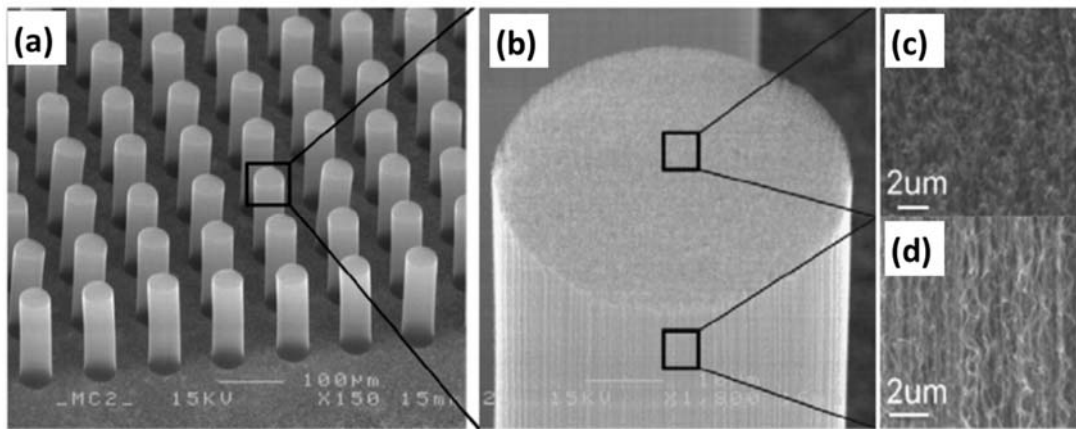


Figure I.17 Scanning electron microscopy images of (a) VACNT bundles grown on Au film (b) a VACNT bundle, (c) Top view of the VACNT bundle and (d) side wall of the VACNT bundle [90].

#### I.6.4 Transmission electron microscopy

Transmission electron microscope operates on the same basic principles as the light microscope but uses electrons instead of light. Figure I.18 shows beam of electrons passes through the sample and scattered by electrostatic potential set up by the constituent elements in the specimen. After passing through the specimen they pass through the electromagnetic objective lens which focuses all the electrons scattered from one point of the specimen into one point in the image plane [91-92].

Transmission electron microscopy (TEM) plays a very importance role on the discovery of CNTs. TEM firstly shows the direct proof of the hollow properties of CNTs. Later TEM, especially high resolution TEM (HRTEM) has been widely employed to study the structures of the CNTs, including the diameter, length, number of walls, etc. [62]. TEM has an unparalleled ability to provide structural & chemical information over a range of length scales down to the level of atomic dimensions.

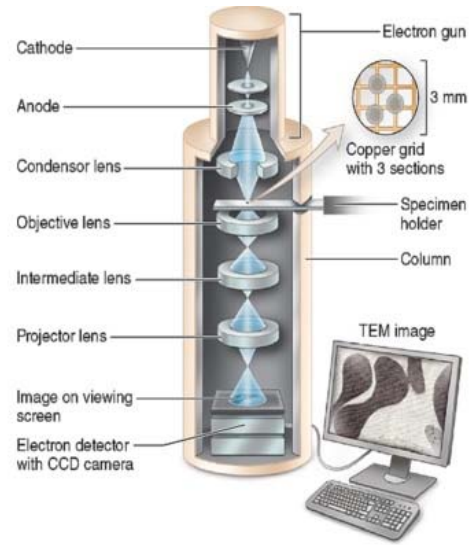


Figure I.18 Photograph and schematic of Transmission electron microscope [87]

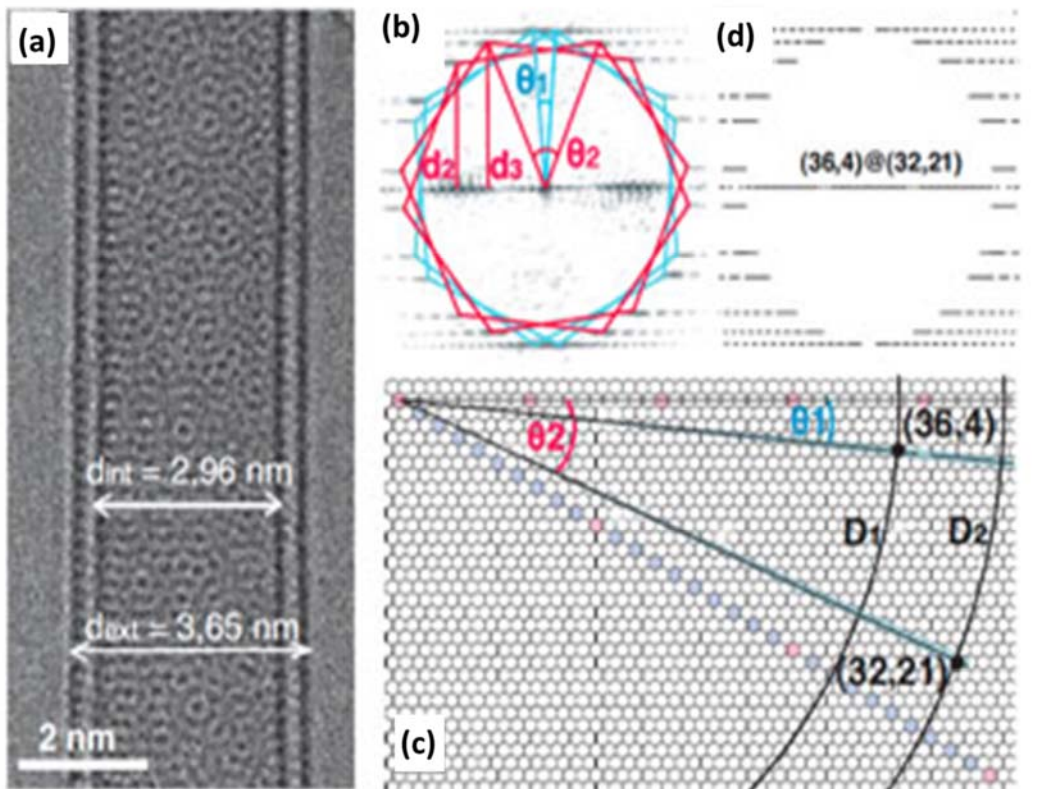


Figure I.19 (a) Experimental HRTEM image of a DWCNT, (b) determination of chiral angles of inner and outer tube from the layer lines spacings present in the FFT of the experimental image, (c) identification of the geometrical solutions of Hamada indexes of inner and outer tubes corresponding to the diameter and chiral angles values and (d) check of the best solution fitting the diffraction pattern [93].

---

It has developed into an indispensable tool for scientists who are interested in understanding the properties of nanostructured materials and manipulating their behavior [94]. Transmission electron microscopy (TEM) as a powerful instrument for characterization of nanostructured materials, in particular, nanotubes. Various nanotubes such as typical MWCNTs, high-crystalline MWCNTs, The parameters of nanotubes such as length, diameter, number of walls, statistical distribution of diameter and atomic structures including lattice parameter information, and exact crystallographic description of crystal can be obtained by TEM [95].

Figure I.19 (a) shows the HRTEM images of a DWNT with inner diameter and outer diameter determined from the fringes profile. Figure I.19 (b-d) explains the determination of chiral angles of inner and outer tube from the layer lines spacings present in the FFT of the experimental image, identification of the geometrical solutions of Hamada indexes of inner and outer tubes corresponding to the diameter and chiral angles values and the best solution fitting the diffraction pattern.

### I.6.5 X-ray diffraction

X-rays, discovered by W. Röntgen in 1895 and widely used to reveal various information on the materials, including crystal structure, phase transition, crystalline quality, orientation, and internal stress [96]. The atomic planes of a crystal cause an incident beam of X-rays to interfere with one another as they leave the crystal. The phenomenon is called X-ray diffraction. It is impossible to examine powder diffraction without Bragg's Law. The interaction of the incident rays with the sample produces constructive interference (and a diffracted ray) when conditions satisfy Bragg's Law

$$n\lambda=2d \sin \theta \quad (I.9)$$

where  $\lambda$  is the wavelength of the radiation

$n$  is an integer, referred to as the order of diffraction, and is often unity

$d$  is the inter-planar spacing involved and

$\theta$  is the angle between the incident (or diffracted) ray

This law relates the wavelength of electromagnetic radiation to the diffraction angle and the lattice spacing in a crystalline sample. These diffracted X-rays are then detected, processed and counted [97].

X-ray diffraction profile is not useful to differentiate microstructural details between the CNTs and the graphite structure but can help to determinate the sample purity [72, 98]. The diffraction peak

of (002) shown in XRD patterns (figure I.20 (b)) indicated that high crystallinity of CNTs.

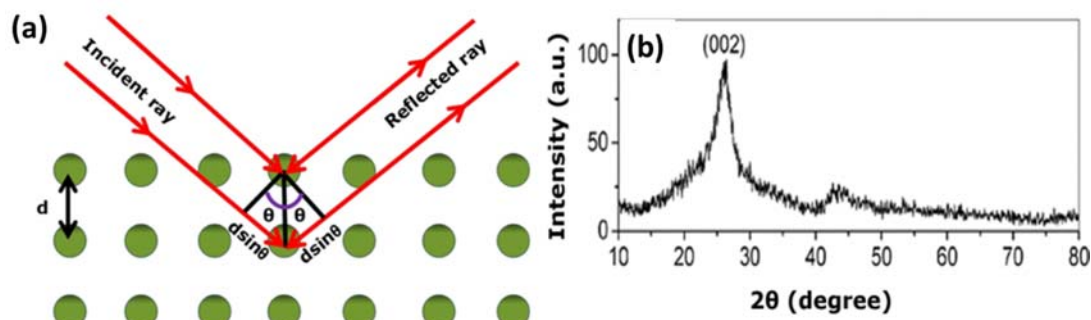


Figure I.20 (a) Schematic of principle of X-ray diffraction and (b) XRD pattern of MWNTs <sup>[99]</sup>

### I.6.6 Thermogravimetric analysis (TGA)

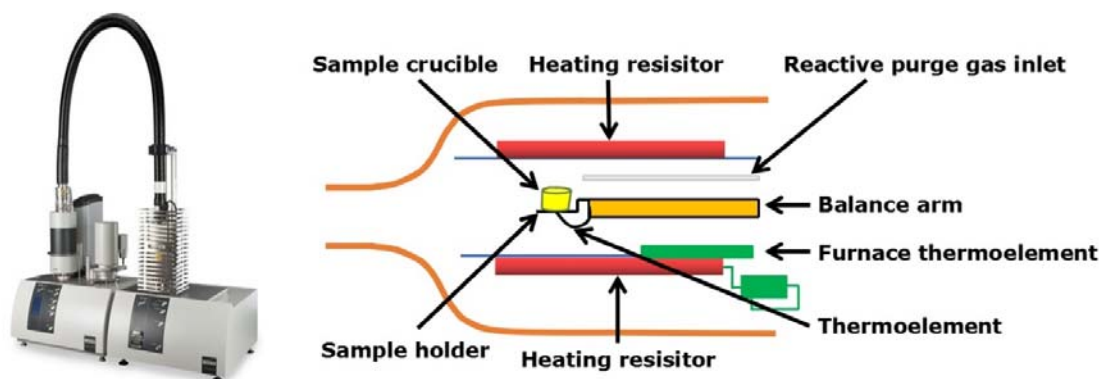


Figure I.21 NETZSCH thermal analysis instruments and furnace component <sup>[100]</sup>.

Thermoanalytical techniques are advanced and important tools for characterizing solids and liquids with respect to their thermal behavior. TGA measures the decrease in sample mass as a function of annealing temperature in a given environment (air, N<sub>2</sub>, He, Ar etc.). The plot of weight loss against temperature is called thermogram is the basic principle of TGA <sup>[101]</sup>. CNTs generally have higher decomposition temperatures than adsorbed molecules and amorphous carbon, TGA data can be used to estimate CNT purity and the presence and concentration of organic molecules attached to CNT sidewalls. Metal impurities can also be assayed by examining the residual sample mass when all of the organics have been volatilized <sup>[102]</sup>.

---

## **I.7 Objective and motivations**

Vertically aligned carbon nanotubes can have many advantages over randomly oriented CNTs when it comes to sensor and electrode applications. The vertical alignment offers a dramatically increased surface area over randomly oriented CNTs. At the same time the perpendicular alignment to the underlying surface resembles structures which can be found in the nature in a wide range of organisms. This enables the use of VACNTs as biomimetic structures for designing sensors as artificial-hair-cell-type sensors which imitate cilia hairs found in sensory organs. Change in resistance due to the bending of VACNTs by different forces can only be realized by designing flexible and elastic one-dimensional nanostructures which are well-oriented. This shows the great advantage of using VACNTs in that area.

Thus it was important to be able to synthesize high-quality VACNTs with good vertical alignment and to be able to fully control their growth in order to obtain structured samples completely composed of VACNTs. This could then enable a variety of applications which cannot be achieved by randomly oriented CNTs as well as other nanomaterials.

Moving from one-dimensional carbon nanomaterials as represented by CNTs, graphene-related two-dimensional nanomaterials offer other advantages when it comes to specific applications with functionalities. While graphene is a zero band gap semiconductor other two-dimensional nanomaterials which have a graphene-related structure as phosphorene contain a band-gap which can be also easily tuned. This enables its effective use in field-effect transistor. The problem is mainly obtain a few-layered phosphorene material allows to be used in field-effect transistor devices. Therefore, the aim of this work is able to achieve a large area fabrication of clean semiconducting phosphorene and its application in a field-effect transistor device.

---

## II SYNTHESIS, CHARACTERIZATION, PROPERTIES AND APPLICATIONS OF VERTICALLY ALIGNED CARBON NANOTUBES

This chapter begins with a brief introduction to vertically aligned carbon nanotubes. Further synthesis, characterization, properties and applications of vertically aligned CNTs are discussed.

### II.1 Introduction

Carbon nanotubes received great attention in many of the applications due to their excellent electrical mechanical and electrical properties. CNTs can be vertically arranged in regular arrays with bundle diameter and spacing of the order of microns <sup>[103]</sup>. Controlled growth of CNTs from an array of closely packed catalysts and utilize the crowding effect make them self-aligned called forests <sup>[104]</sup>. VACNTs are more homogeneous than their counterparts, due to their diameters which enables them promising in micro/nanoelectronics applications <sup>[105]</sup>, well-defined large surface areas makes this material easy to be incorporated into devices <sup>[106]</sup>. VACNTs arrays can be transferred into various substrates of particular interest which offer multi-functional advantages in controlled surface modification and efficient device construction <sup>[107-108]</sup>. Superlong vertically-aligned carbon nanotubes (SLVACNTs) are advantageous compared to their shorter counterparts. Their millimeter-order length offers unique properties electronic, thermal and other physical properties via individual nanotubes over large scale productions. They are used in applications such as in sensors <sup>[109-111]</sup> membranes <sup>[30, 112]</sup>, multifunctional composites <sup>[113-116]</sup> nanoelectronics <sup>[117-119]</sup>, field emission <sup>[120]</sup>, scanning probe arrays <sup>[121]</sup>, photonic crystals <sup>[122]</sup> and neural networks <sup>[123]</sup>.

Arc discharge <sup>[124-125]</sup>, laser ablation <sup>[126-128]</sup> and chemical vapor deposition which are already used for the synthesis of non-aligned CNTs <sup>[58, 129-130]</sup>. Chemical vapor deposition is widely used in vertically aligned carbon nanotube synthesis because it is easy to set up and lower cost. In 1996, Li et al. synthesized aligned carbon nanotubes by decomposition of acetylene on Fe embedded silica using CVD technique <sup>[131]</sup>. In 1998, Ren et al. synthesized aligned carbon nanotubes on nickel-coated glass below 666 °C by plasma-enhanced hot filament chemical vapor deposition <sup>[132]</sup>. In 1999, Huang et al. synthesized micropatterns of aligned carbon nanotubes perpendicular to the substrate <sup>[133]</sup>. In 2000, aligned carbon nanotubes were grown by applying the electric field <sup>[134]</sup>. The mechanism behind the synthesis of aligned CNTs by CVD are described by Fan et al. <sup>[135]</sup>. During CNT growth, carbon precursors are catalytically decomposed on the catalyst surface at specific temperature. As supersaturation occurs, nanotube grows off on densely packed catalyst and extends open space along the direction perpendicular to substrate. Each nanotube interact with neighbouring nanotubes via van der Waals forces to form large bundles. Currently, the leading methods used in the synthesis of VACNTs are the ferrocene-catalyzed growth of aligned MWNTs <sup>[136-138]</sup> and (super)-growth of

ultrahigh-aligned SWNTs on the catalytic system composed of thin aluminium/aluminium oxide and iron metal layers [139-141].

## II. 2 Water assisted chemical vapor deposition technique

Amorphous carbon accumulation on the catalyst degrades its catalytic activity [142]. Activity and life time of the catalyst can be enhanced by the addition of the weak oxidizer (water vapour) during synthesis. Water can oxidize the amorphous carbon and clean the catalyst. Hata et al. reported the growth of dense and vertically aligned SWNT forests with millimeter-scale height (2.5 mm) in 10 minutes growth time using water assisted chemical vapor deposition method [64].

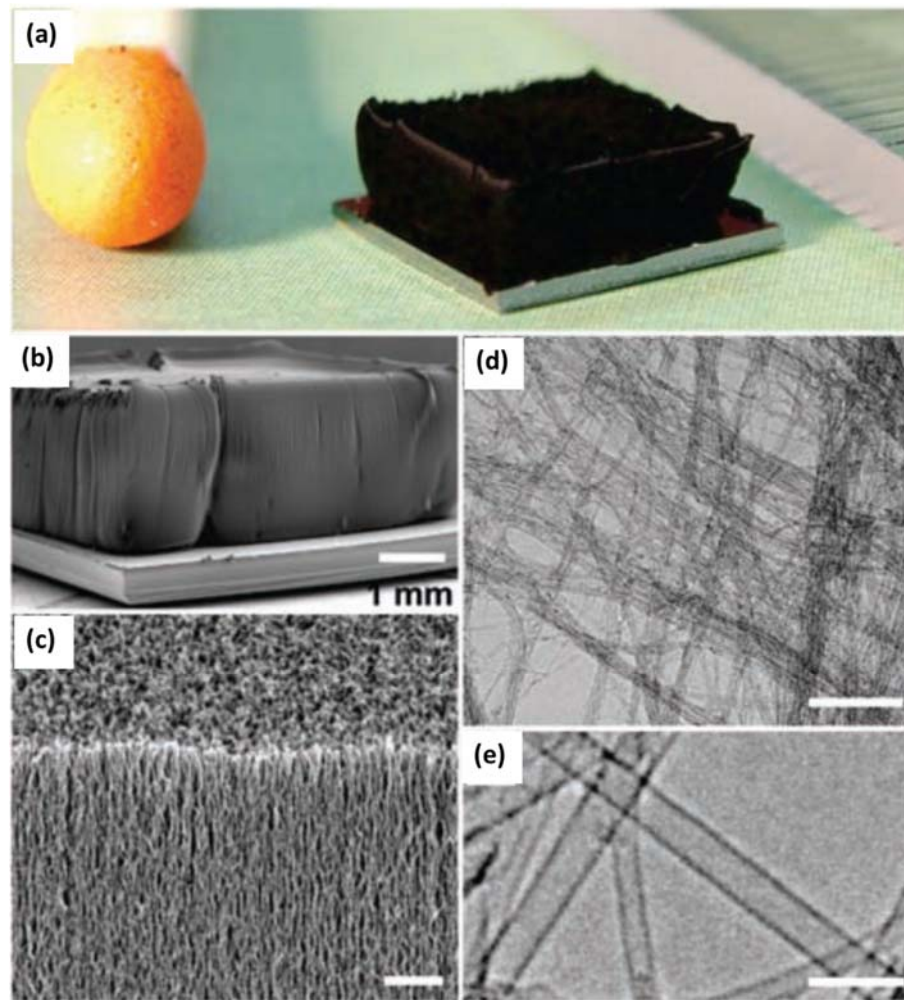


Figure II.1 SWNT forest synthesized using water-assisted chemical vapor deposition technique. (a) Photograph of a 2.5-mm-tall SWNT forest on a 7-mm by 7-mm silicon wafer. Matchstick on the left and ruler with millimeter markings on the right is placed for size reference, (b) Scanning electron microscopy (SEM) image of the same SWNT forest. Scale bar, 1 mm, (c) SEM image of the SWNT forest ledge. Scale bar, 1  $\mu\text{m}$ , (d and e) Low resolution TEM and HRTEM images of the nanotubes. Scale bar, 100 nm and 5 nm [64].



Figure II.1 (a,b and c) shows the photograph and SEM images of SWNT forests. Figure II.1 (d and e) shows the TEM and HRTEM images of the SWNTs. Effect of water as a catalyst enhancer for the supergrowth of vertically aligned carbon nanotubes is reported by Futaba et al. [143]. The catalyst activity was about  $84\pm 6\%$ . Amama et al. demonstrated that Ostwald ripening of the catalyst can be inhibited using water, which enhance the catalyst life time [144]. Yamada et al. investigated and elucidated the effect of water on the catalyst for SWNT synthesis through analyzing the structure and composition of individual catalysts exposed to normal growth conditions, water ambient, and water-assisted growth. They have shown that the water clean the catalyst surface and reactivated efficiently by removing the carbon coating through oxidation hence high catalytic activity, long lifetime and high growth rate can be achieved [145]. Yamada et al. synthesized catalyst free vertically aligned double walled carbon nanotubes forest with millimeter-scale height using water assisted chemical vapor deposition technique [146]. They could grow DWNT forest of 2.2 mm in height on a 20x20 mm Si substrate. Chen et al. used water as the catalyst enhancer for the growth of single walled carbon nanotube forests [147]. Hasegawa et al. reported the growth of millimeter tall SWNT forests with and without water. Water addition widens the window for the rapid growth of millimeter-tall SWCNTs especially at high  $C_2H_2$  partial pressures [148].

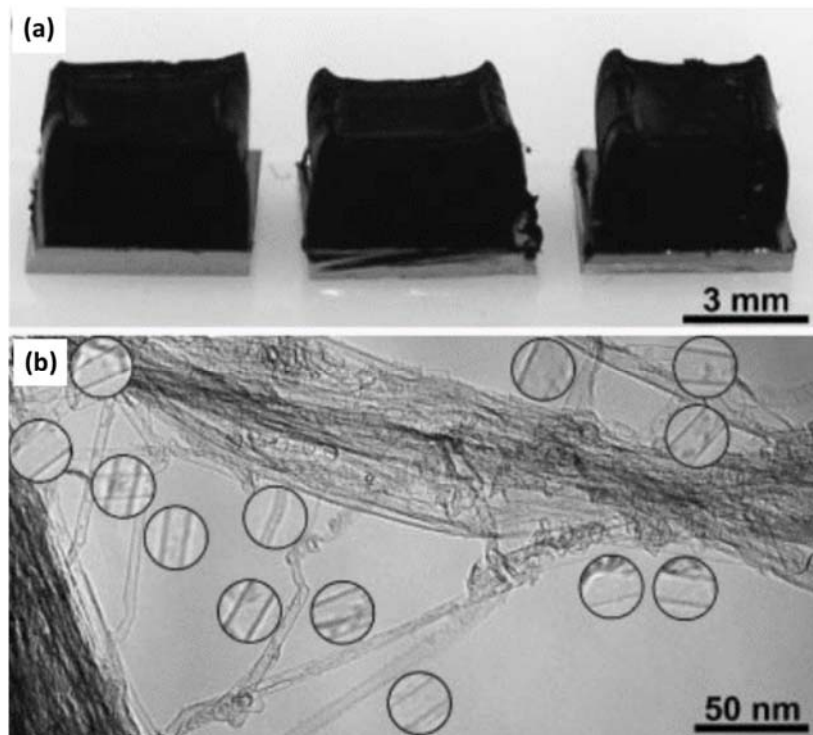


Figure II.2 (a) Photographs of the carbon nanotube forests grown on  $Fe/Al_2O_x$  for 30 minutes with Fe thickness as 0.45 nm, 0.5 nm and 0.55 nm, (b) TEM image of the carbon nanotubes grown using 0.5 nm Fe thickness [149].

---

Noda et al. synthesized carbon nanotube forests over  $\text{Al}_2\text{O}_3/\text{Fe}$  catalyst [149]. Figure II.2 (a and b) shows the photograph and TEM image of the vertically aligned SWCNTs grown on  $\text{Al}_2\text{O}_3/\text{Fe}$  catalyst. Water vapor is the commonly used oxidizer agent but general oxygen-containing compounds like ethers or alcohol may be used too. Alcohol may be used to alternatively synthesize VACNTs because the oxygen is incorporated into the carbon feedstock molecule, the relative levels of carbon and oxygen is fixed. It serves as a source of carbon and it has an advantage in that the alcohol is a weak oxidizer [150-152]. For example, for the HiPco process, the carbon/oxygen ratio is fixed at 1:1 [53].

VACNTs can be prepared by floating catalyst CVD method. Here pyrolysis of organometallic precursors like metallocenes lead to growth of CNTs. It does not require separate catalyst hence it is called as floating catalyst CVD method. The growth of the CNT takes place on a substrate placed in the high-temperature zone where vaporization and sublimation of the catalyst precursor happens. During this floating stage, CNT growth starts from metal particles deposited on substrates or even on the walls of the reactor, which then follows tip or base growth mechanism. Both conductive and non-conductive substrates can be used to grow well-aligned 3D structured CNT architectures in this technique. The growth of the CNTs is performed in double-step. Synthesis is performed after the preparation and distribution of catalytic nanoparticles with controlled size [153-157].

### **II.3 Growth mechanism of water assisted chemical vapour deposition**

Physical vapor deposition techniques such as thermal evaporation, electron beam evaporation, atomic layer deposition and sputtering is widely used to deposit thin films. A thin films of Fe and aluminium [57], Fe and  $\text{Al}_2\text{O}_3$  [149] is used for the growth of vertically aligned carbon nanotubes. Joshi et al. studied the the morphology and composition of the catalyst using high-resolution scanning transmission electron microscopy (STEM) and chemical composition using spectroscopic and diffraction measurements. During the deposition of iron over aluminium, an intermetallic layer forms at the interface and this layer grows thicker upon heating. Aluminum atoms migrate to dissolve into Al/Fe interface and the iron atoms at the top agglomerate to form small nano particles. At the melting point of aluminum (660 °C), Al rich inter metallic phase of iron and aluminum formed hence particle with iron core surrounded by metallic mixture of Al and Fe morphology is obtained [158].

Amama et al. studied the morphology of the catalayst annealed in presence of  $\text{H}_2$  and  $\text{H}_2$  and  $\text{H}_2\text{O}$  (Figure II.3), the difference observed was attributed to Ostwald ripening.  $\text{Al}_2\text{O}_3$  was deposited over the substrate (boron doped silicon) by ALD and Fe was deposited using e-beam evaporation. Ripening of the catalyst observed in when it is annealed in presence of hydrogen but the catalyst remain stable when annealed in  $\text{H}_2$  and  $\text{H}_2\text{O}$  [144].

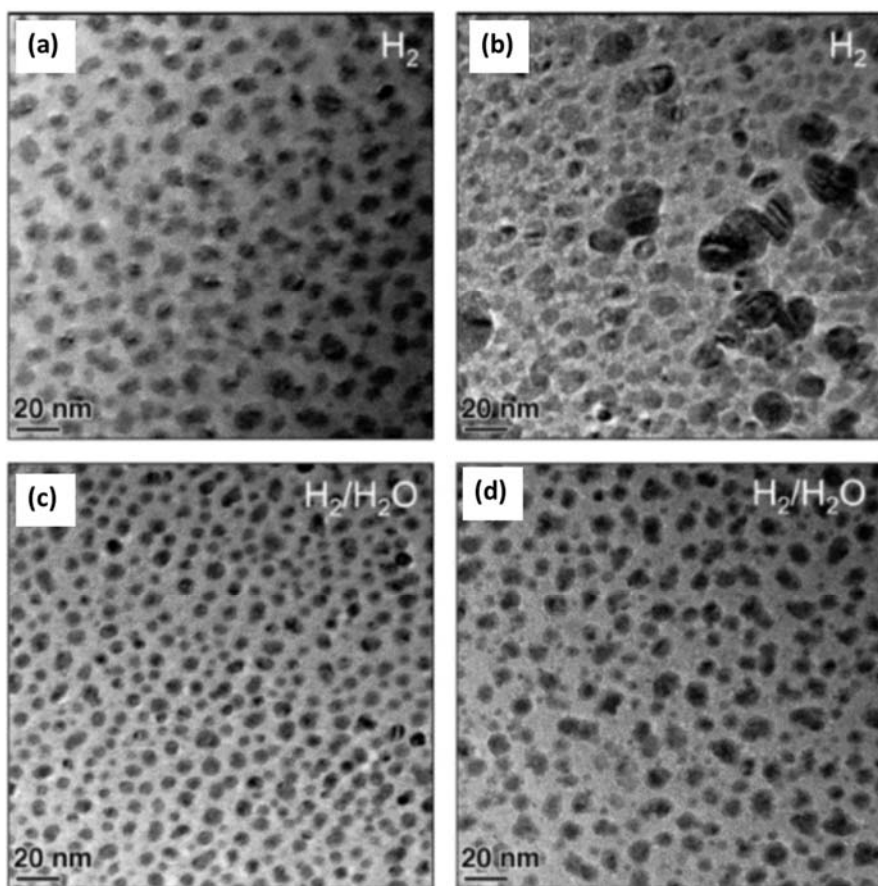


Figure II.3 TEM images of catalyst nanoparticles on the substrate after annealing in  $H_2$  for (a) 30 s and (b) 5 min, and in  $H_2/H_2O$  for (c) 30 s and (d) 5 min <sup>[144]</sup>.

A possible mechanism for supergrowth of VACNTs was explained by Noda et al. contains the following steps. Adsorption  $C_2H_4$  or its derivatives onto aluminum oxides, the surface diffusion from aluminum oxides to Fe nanoparticles, and the segregation as nanotubes from Fe nanoparticles for the growth of CNTs.  $H_2O$  vapor cleans and keeps aluminum oxide surface reactive by removing the carbon byproducts. Addition of water upto certain level enhance the growth rate but more water degrades the nanotube quality <sup>[149]</sup>. Hasegawa and Noda explained the growth mechanism of SWNT forests as follows. Carbon sources decomposes into carbon atoms on the catalyst particle and thereafter the carbon atoms diffuse through/over the catalyst particle and precipitate at the edge of the CNT. Attachment of carbon atom in regular sites of CNT edge leads to grow CNTs while attachment of carbon atom in irregular sites of CNT edge yield disordered structures. Removal of

---

disordered carbon by oxidation with water along with the precipitation/attachment of carbon yields sustainable CNT growth <sup>[148]</sup>.

## **II.4 Unique properties of carbon nanotubes**

The structure of a carbon nanotube is formed by a layer of carbon atoms that are bonded together in a hexagonal mesh. This one-atom thick layer of carbon is called graphene, and it is wrapped in the shape of a cylinder and bonded together to form a carbon nanotube they can have remarkably high aspect ratios. Nanotubes can have a single outer wall of carbon, or they can be made of multiple walls. Carbon nanotubes have a range of mechanical, electric, thermal, and structural properties that can change based on the physical design of the nanotube <sup>[159-160]</sup>.

### **II.4.1 Electrical properties**

Carbon nanotubes have interestingly unique electrical properties. A single sheet of graphite is a semimetal. This means that it has intermediate characteristics between semiconductors and metals <sup>[161]</sup>. The carbon atoms in a rolled graphite sheet into a nanotube line up around the tube's circumference and the electrons' quantum mechanical wave functions also match up. Theoretically, metallic nanotubes carry an electrical current density of  $4 \times 10^9$  A/cm<sup>2</sup>, a value which is about a thousand times higher than that of metals like copper <sup>[162]</sup>. Depending on radius and chirality, a single walled carbon nanotube (SWCNT) can be either metallic or semiconducting. The (n, m) SWCNT is classified as a metal when  $(2n+m)/3$  is an integer; otherwise, it is a semiconductor <sup>[163]</sup>. In single walled carbon nanotubes electron transport occurs only along the axis of the tube. Single walled nanotubes can convey electrical signals at speeds up to 10 GHz when used as interconnects on semi-conducting devices. Nanotubes also have a constant resistivity <sup>[164]</sup>.

### **II.4.2 Thermal properties**

Carbon nanotube exhibits ballistic conduction and are hence expected to be good thermal conductors along the tube because of their carbon-carbon chemical bonding <sup>[163]</sup>. There is a prediction that CNTs will at room temperature be capable of transmitting up to  $6000 \text{ W}\cdot\text{m}^{-1}\cdot\text{K}^{-1}$  compared to copper which is known to be a good metal with tremendous thermal conductivity which transmits up to  $385 \text{ W}\cdot\text{m}^{-1}\cdot\text{K}^{-1}$  at room temperature <sup>[165]</sup>. Carbon nanotubes thermally stable up to  $2800^\circ\text{C}$  in vacuum and about  $750^\circ\text{C}$  in air <sup>[166]</sup>. The thermal expansion of carbon nanotubes is expected to be largely isotropic. Conventional graphite fibers have a different exhibition in that they are very strongly anisotropic. This may be of great benefit for carbon-carbon composites. It is highly anticipated that low-defect CNTs will have very low thermal expansion coefficients <sup>[4]</sup>.

---

### II.4.3 Biological properties

Numerous investigations have been conducted in investigating the adverse biological effects of carbon nanomaterials in biomedicine especially diagnosis, therapy and drug delivery. Cell is the basic structural, functional and biological unit of living organism. Cell uptake is the crucial step in interaction of cells with carbon nanomaterials. Adsorption of biomolecules on nanomaterials in a physiological environment influence their interaction with cells and cellular organelles.

The biological properties of CNTs are correlated with their nano-sized dimension, large reactive surface area (theoretically 1300 m<sup>2</sup>/g) as well as the high surface energy. These nanoparticles exhibit bioactivity that does not happen to micron-size particles made of the same material. Iodinated and platinated and helical double-stranded Deoxyribonucleic acid (DNA) is evenly found on the surfaces of nanotubes. They are employed as probes in DNA visualization. Through sonication, single and double-stranded DNA and ribonucleic acid (RNA) can aid on the dispersion of single-walled carbon nanotubes in water. On the surface of SWNTs there are non-covalent  $\pi$ - $\pi$  stacking of the nucleic acid bases which are responsible for non-specific interaction. There are also hydrophilic sugar-phosphate backbones of the nucleic acids which face outward from the sidewalls<sup>[167]</sup>. Bioactive and biological species like carbohydrates, proteins and nucleic acids can be conjugated with CNTs. The biological functions can be affected by the interactions between biomolecules and CNTs which in turn affect the conformational changes in the particles. Covalent and non-covalent surface functionalization produces CNTs which are soluble in water<sup>[168]</sup>.

The interaction between carbon nanotubes and cells varies with cell type and CNT characteristics. Interfacing nanomaterials with neural systems helps to repair damaged central nervous system tissue and to unravel brain functions. Characterization of the interaction of nanomaterials with brain cells and their circuitry brings new opportunities to implement nanotechnology in nervous system. Several groups used carbon nanotubes as the substrate for neuron growth<sup>[169]</sup>. Mattson et al. developed methods for the growth of embryonic rat-brain neurons on carbon nanotubes. Nanotubes coated with bioactive molecule 4-hydroxynonenal exhibit extensive branching of neurons compared to pristine carbon nanotubes<sup>[170]</sup>. Arrangement of neurons and glia cells on carbon nanotubes islands were investigated. It has been observed that both neurons and glial cells adhere on CNT mats. The immunofluorescent image in figure II.4 (a) shows overlapping neurons (red) and glia cells (green). Glia cells and neurons have distinct morphology. Moreover, Glia cells are mostly separated (figure II.4 (b) and (c)), tends to spread over the surface whereas neurons are more compact and bulky (figure II.4 (a)). Neuronal cells can intertwine, bend and curl on rough surface. The results suggest that a mechanical effect can contribute to the attachment of neuronal cells and processes to porous surfaces<sup>[171]</sup>.

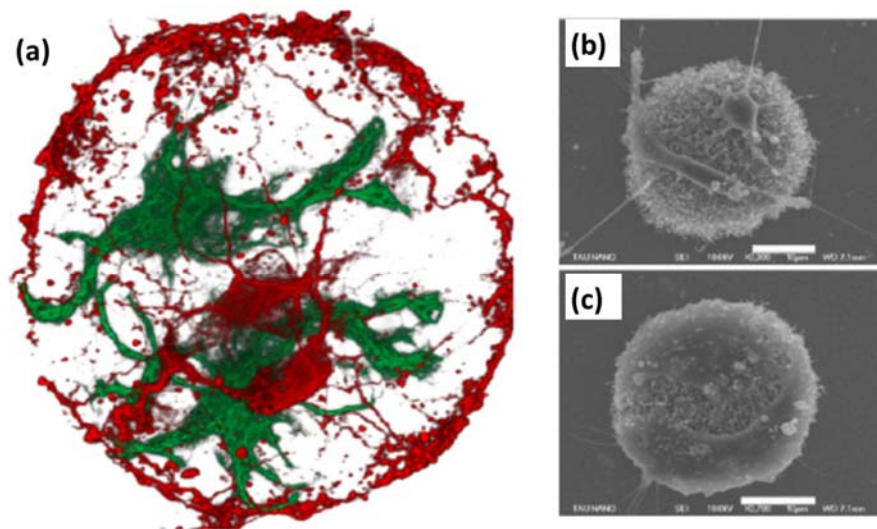


Figure II.4 Rat neurons and glia cells on CNT islands. (a) A three-dimensional rendering of an immunofluorescence staining image of neuronal class III  $\beta$ -tubulin (red indicates neurons) and GFAP (green indicates glia cells), (b and c) HRSEM images of neurons and glia cells on top of a CNT island [171].

#### II.4.4 Mechanical properties

Mechanical properties of CNTs are extensively investigated by several groups. CNTs are stable against deformation due to the strong bonding of  $sp^2$  hybridized carbon atoms in curved graphene sheet [172]. The Young's modulus of SWNTs is of the order of 1 TPa [173-174] and that for individual DWCNTs, TWCNTs, and CNT ropes consisting of only two DWCNTs were measured by tensile loading in the range of 0.73–1.33 TPa [175]. Tensile strength and Young's modulus of individual DWNT bundles possess an average values of 6 GPa and 80 GPa respectively [176]. Tensile strength of SWNT bundles and a single SWNT measured are  $7.5 \pm 0.8$  GPa and  $22.2 \pm 2.2$  GPa respectively [177]. The average Young's modulus and tensile strength of aligned MWNT ropes measured is about  $0.45 \pm 0.23$  TPa and  $1.72 \pm 0.64$  GPa respectively [178].

Highly transparent stretchable conductors were fabricated by embedding SWCNT films in poly(dimethylsiloxane) (PDMS) can be used as interconnects for stretchable electronics and electrodes in optoelectronics [179]. Liu et al. fabricated highly stretchable and transparent conductors using cross stacked super aligned carbon nanotube films [180]. CNT ribbons directly drawn from well aligned CNT forests are embedded in PDMS is used as stretchable conductors. Results shows that the material exhibits stable conductivity under linear tensile strain up to 100% after the first several cycles of stretching/releasing [181].

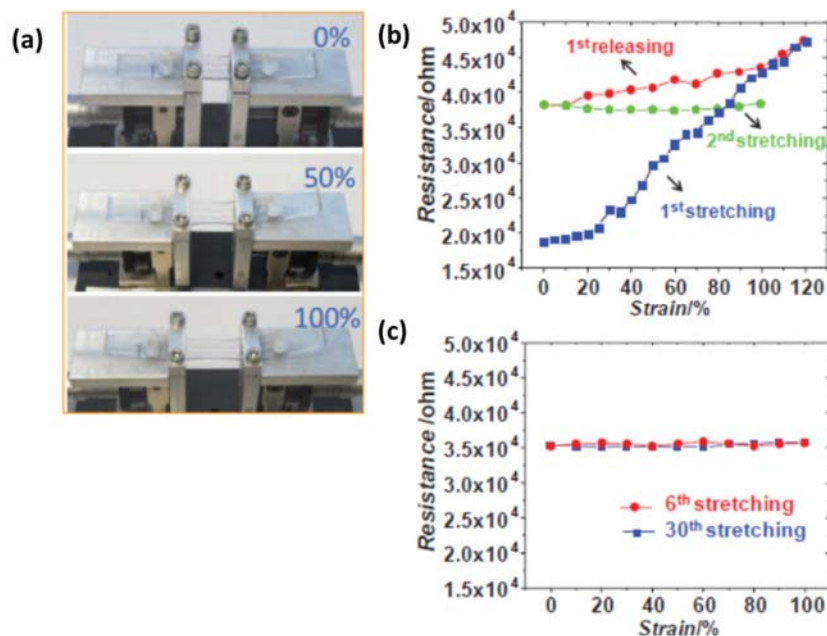


Figure II.5 (a) Photographs CNT/PDMS film under tensile strain of 0%, 50% and 100%, (b and c) Resistance of a CNT/PDMS versus in 1<sup>st</sup> stretching, 1<sup>st</sup> releasing and 2<sup>nd</sup> stretching 6<sup>th</sup> stretching and 30<sup>th</sup> stretching cycles [181].

Figure II.5 (a) shows the photograph of the CNT/PDMS film by applying the tensile strains of 0%, 50% and 100%. Figure II. 5(b) shows the resistance variation of the resistance of the CNT/PDMS with increase in tensile strain in the first stretching cycle, 2<sup>nd</sup> stretching cycle, 1<sup>st</sup> releasing cycle. Figure II.5 (c) shows the variation of the resistance of the CNT/PDMS with increase in tensile strain in the 6<sup>th</sup> and 30<sup>th</sup> stretching cycle.

Their bending stiffness is one of the most significant parameter [182]. The measurement of the mechanical properties of VACNTs is quite challenging due to forces of displacement involved. MWCNTs grown from CVD have one order of magnitude smaller  $E$ , and that of VACNTs are yet another order of magnitude smaller. The defects and structural differences account for the smaller Young's modulus of VACNTs [119, 183]. Rippling commences at very low curvatures. Tubes with smaller diameters have a rippling onset at higher strains compared to the ones with larger diameters. Tubes with larger defect density have a larger critical strain and larger relative post-rippling stiffness compared to the tubes with a smaller defect density. The stiffness prior to the tube rippling with a large defect density is much lower [184].

Instrumental indentation is a common method of testing the mechanical properties of VACNTs [185-186]. The properties of these materials depend on the individual characteristics of the CNTs and the collective inter-tube interactions dictated by the methods of synthesis. Variations in their micro-

---

structure have significant implications on their mechanical properties. These are the Young's modulus and the buckling strengths which range from sub-MPa to tens of MPa to GPa. They also have complete gamut of recoverability after large deformations <sup>[187-189]</sup>. Buckling enables the structures to store higher amounts of energy in a postburst structure and presumably higher amounts of energy being stored in the buckled regions <sup>[190-191]</sup>. APCVD-grown VACNT films deform by single vertical catastrophic shear-off event along the rim of the indenter tip under large displacement indentations. Buckling is progressively witnessed near the stiff underlying substrate and experiments on compression experiments of these materials show that APCVD-grown VACNT films reach their critical shear stress before buckling in indentation. This leads to the formation of catastrophic shear in their microstructure. Consequently, they will demonstrate negligible recovery in indentation relative to their almost perfect recoverability when subjected to compression <sup>[192-193]</sup>.

Aligned CNTs slide on a PDMS substrate under tension, but buckle under compression. This irreversible mechanical deformation accounts for the irreversibility in the electric resistance upon the first stretching. The resistance of buckled VACNTs does not change upon mechanical strain and this is responsible for their application in stretchable electronics, touchscreens, solar cells and sensors. These stretchable devices can be fabricated through interface-mediated buckling and could open ways for large-scale production of nanowires and other based stretchable electronics <sup>[194]</sup>. Micro-mechanical bending process of VACNTs has been done to fabricate displacement sensor. This has been done to utilize the optical property of the individual CNTs. Displacement sensor is widely used in generating positional feedback for any given closed loop motion control system. Displacement sensors are being used to measure the linear and the angular displacements. The displacement sensors which were available in the market were big in size and were marred with complexities during the process of measuring <sup>[195]</sup>. Alternative VACNTs of optically reflective and dark surface can be processed to make compact displacement sensors considering their ability to bend <sup>[196]</sup>. Micro-mechanical bending using 3-D micro-patterning technique is employed on VACNTs in the fabrication of the displacement sensor. This transforms the latter to optimal mirror from dark absorber surface. The resultant sensor is highly applauded due to its small size, flexibility, simple measuring process, less noise, contact-less measurement and cost effectiveness <sup>[197-198]</sup>. VACNT based triple-electrode ionization temperature sensor is easy to fabricate and this converts the temperature change directly into an electrical signal <sup>[199]</sup>.

## **II.5 Results and discussion**

Following sections in the present chapter focusses on the synthesis, characterization and applications of VACNTs. VACNTs are grown over Si/SiO<sub>2</sub> (600 nm) substrate by depositing aluminium thin



layer and Fe catalyst layer by e-beam evaporation technique. Also, VACNTs are grown over Si/SiO<sub>2</sub> (600 nm) substrate by depositing aluminium oxide thin layer by atomic layer deposition technique and Fe catalyst layer by e-beam evaporation technique. Characterization of the VACNTs grown over Al (10 nm) and Fe (1.6 nm) followed by the characterization of the VACNTs grown over Al<sub>2</sub>O<sub>3</sub> (30 nm) and Fe (1.2 nm) discussed here. Growth conditions of VACNTs are also optimized by changing the CVD process parameters and catalyst thickness (see the experimental section). Later various applications of the VACNTs done in collaboration with other groups are presented.

### II.5.1 Characterizations of the VACNTs grown over Al (10 nm) and Fe (1.6 nm)

Raman spectra of the VACNT is provided in figure II.6 (a). The G-band is a feature observed due to the stretching of C-C atoms in sp<sup>2</sup> hybridized carbon samples [200]. The D-band is observed when there is a symmetry-breaking perturbation on the hexagonal sp<sup>2</sup> bonded lattices for graphite and nanotubes. The presence of D-band is attributed to presence of defects in tube wall or to the presence of amorphous carbon. The G'-band corresponds to the second order Raman over tones [201]. I<sub>D</sub>/I<sub>G</sub> ratio calculated from Raman spectra is 0.169.

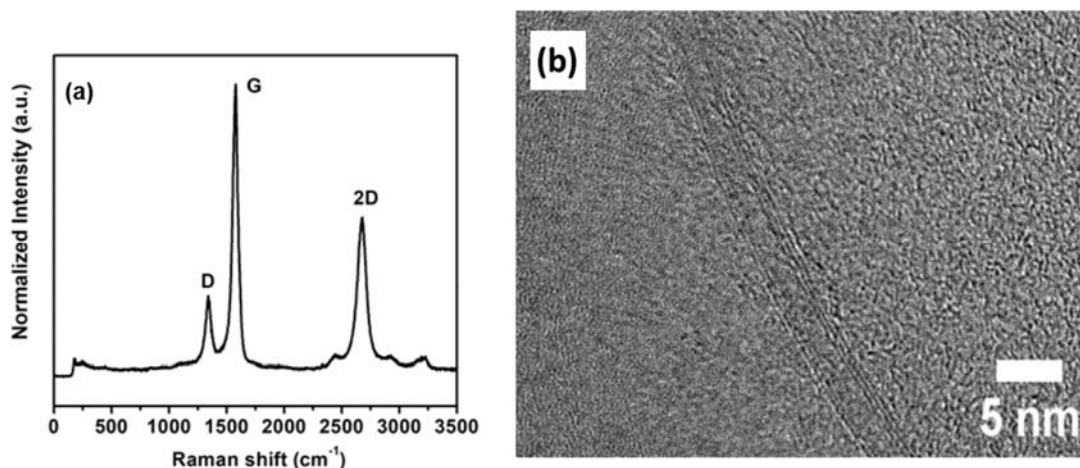


Figure II.6(a) Raman spectra of VACNTs and (b) HRTEM image of the CNT (unhinged from the VACNT arrays).

CNTs unhinged from the VACNTs bundle is ultrasonicated in high purity ethanol. Few drops of the suspension was drop-casted on the TEM grid and dried before TEM investigation. Figure II.6 (b) shows the TEM image of a typical CNT, which is unhinged from the array of VACNTs by ultrasonication. The CNTs are mostly double walled with well graphitized side walls. The diameter of the order of 2-4 nm. No catalyst impurity is observed in CNTs. Nanotubes contains defects in some section of their lengths.

Figure II.7 shows the scanning electron microscopy images of the VACNT in different magnifications. CNT arranged in regular arrays of bundles and are highly parallel. High density and van der Waals forces between the neighbouring CNTs leads to this vertical alignment. The height of the VACNTs are about 390  $\mu\text{m}$ . Nanotubes are well aligned in a direction perpendicular to the substrate. Also, the optimized VACNT growth with respect to a variety of CVD process parameters such as gas flow, water, time and catalyst thickness in order to control the length of the resultant CNT bundles is carried out ( see experimental section).

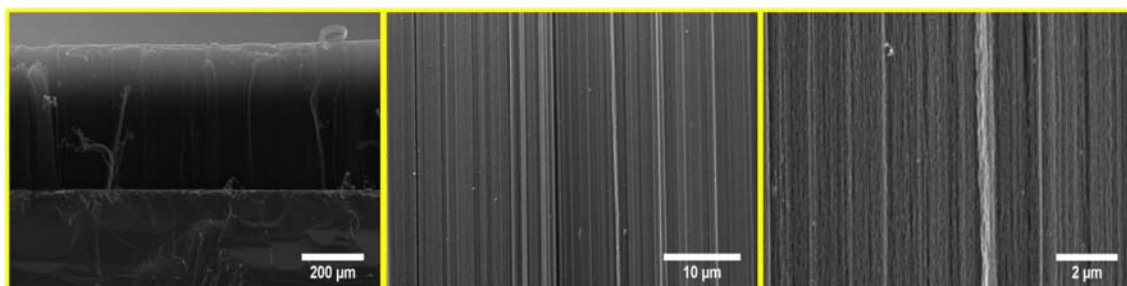


Figure II.7 SEM images of VACNTs in different magnification (scale bar=200  $\mu\text{m}$ , 10  $\mu\text{m}$ , 2  $\mu\text{m}$ ).

Figure II.8 (a) shows the nitrogen adsorption-desorption isotherms and non linear density functional theory (NLDFT) pore size distribution of the vertically aligned CNTs. The BET surface area calculated is about 515  $\text{m}^2/\text{g}$ .

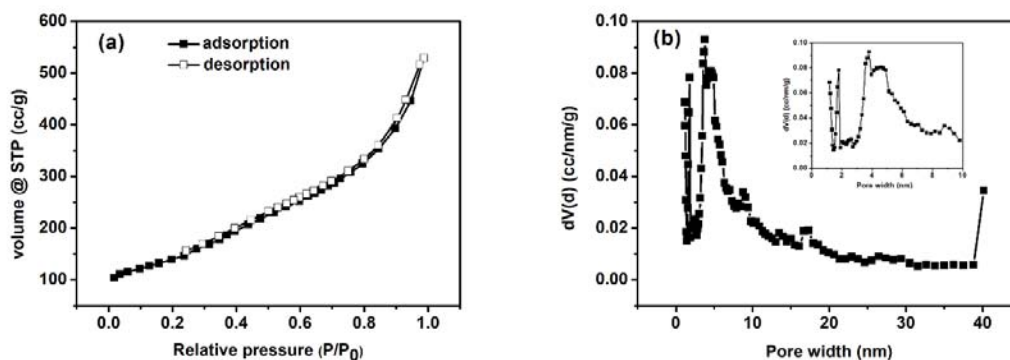


Figure II.8 (a) Nitrogen adsorption-desorption isotherm and (b) NLDFT pore size distribution of the VACNTs.

Purity of the VACNTs was determined using thermogravimetric analysis. Figure II.9 (a) shows the TGA curve for vertically aligned carbon nanotube. TGA was carried in air atmosphere in a temperature range of 35  $^{\circ}\text{C}$  to 1000  $^{\circ}\text{C}$ . The weight loss below 500  $^{\circ}\text{C}$  is associated with the removal of oxygen functional groups at dangling carbon atoms. The oxidation of CNTs starts about 500  $^{\circ}\text{C}$

and no residual mass observed after 700 °C indicates the complete burning of CNTs and the absence of the catalyst.

X-ray diffraction measurement is carried out to investigate the crystallinity of the samples. XRD patterns have been recorded VACNTs (figure II.9 (b)). The broad (002) peak indicates short range order.

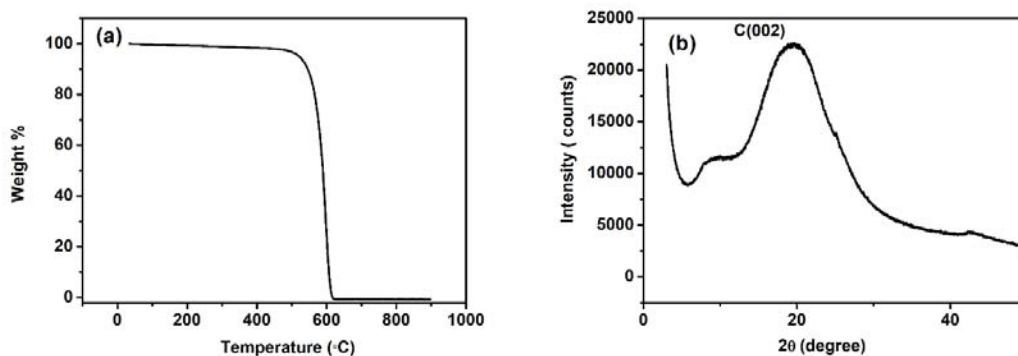


Figure II.9 (a) Thermogravimetric analysis and (b) X-ray diffraction pattern for the VACNTs.

### II.5.2 Characterizations of the VACNTs grown over Al<sub>2</sub>O<sub>3</sub> (30 nm) and Fe (1.2 nm)

Raman spectra of the VACNTs grown on aluminium oxide thickness of 30 nm and Fe thickness of 1.2 nm is shown in figure II.10 (a). The G-band is attributed to the stretching of C-C atoms in sp<sup>2</sup> hybridized carbon samples [200]. The D-band is due to the vibrations of symmetry-breaking perturbation on the hexagonal sp<sup>2</sup> bonded lattices for graphite and nanotubes. The D-band could be due to presence of defects in tube wall or due to the presence of amorphous carbon. The G'-band is due to the second order Raman over tones [201]. Intensity ratio of D-band and G-band is 0.292.

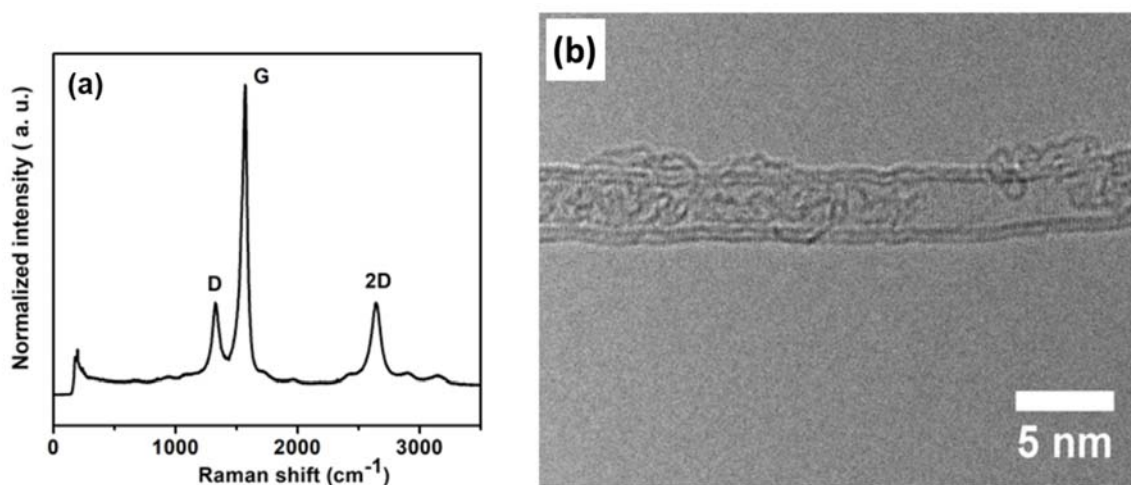


Figure II.10 (a) Raman spectra of VACNTs and (b) HRTEM image of the CNT (unhinged from the VACNT arrays).

Specimen for the TEM imaging was prepared by drop-casting the CNT dispersion on carbon coated Cu-TEM grid. High purity ethanol was used for the preparation of CNT dispersion. Figure II.10 (b) displays the TEM image of CNT, which is unhinged from the array of VACNTs. The image shows double-walled CNTs with well graphitized side walls and it has diameter of the order of 2-4 nm. CNTs are catalyst free, the outer walls contains defects in some section of their lengths and small amount of amorphous carbon.

Alignment of the CNTs was investigated using scanning electron microscopy imaging. Scanning electron microscopy images of the VACNTs recorded in different magnifications is shown in figure II.11. Nanotubes are grown perpendicular to the substrate and CNTs in the bundle shows highly parallel orientation. This vertical alignment is due to the dense packing of CNTs and van der Waals forces between the neighbouring CNTs. The influence of the Al<sub>2</sub>O<sub>3</sub> thickness and catalyst thickness in height of the VACNTs were investigated (see experimental section).

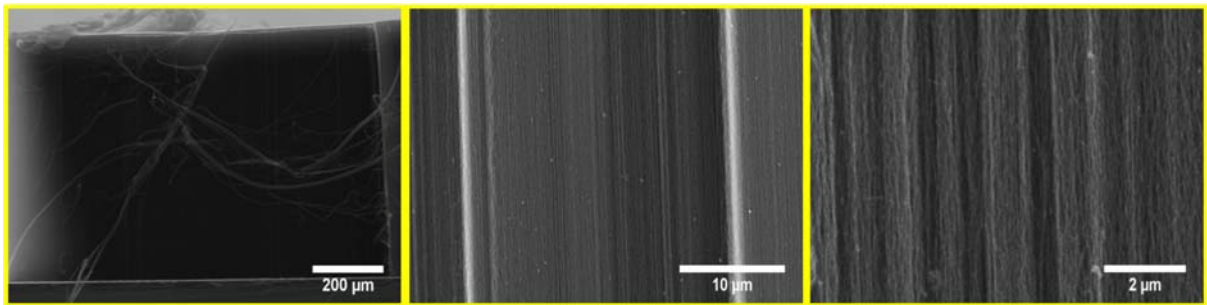


Figure II.11 SEM images of VACNT in different magnification (scale bar=200 μm, 10 μm, 2 μm).

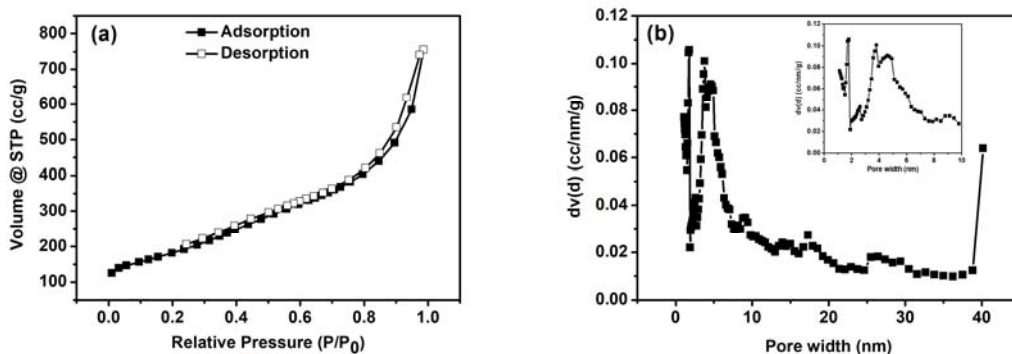


Figure II.12 Nitrogen adsorption-desorption isotherms and NLDFT pore size distribution of the VACNTs.

Nitrogen adsorption-desorption isotherms and NLDFT poresize distribution of the vertically aligned CNTs is depicted in Figure II.12 (a and b). The specific surface area calculated using BET theory is about 652 m<sup>2</sup>/g.

TGA experiment in air atmosphere was conducted to determine the purity of the VACNTs. Temperature was scanned from 35 °C to 1000 °C. Figure II.13 (a) shows the TGA curve of the vertically aligned carbon nanotubes. The sudden drop in the weight at ~500 °C is associated with the oxidation of CNTs. No residual sample after 700 °C indicates the complete oxidation of CNTs and the absence of the impurities .

X-ray diffraction pattern was recorded to investigate the crystallinity of the samples. figure II.13 (b) show the XRD pattern of VACNT and the 2θ was scanned from 5° to 50°. The broad C(002) peak indicates the short range order.

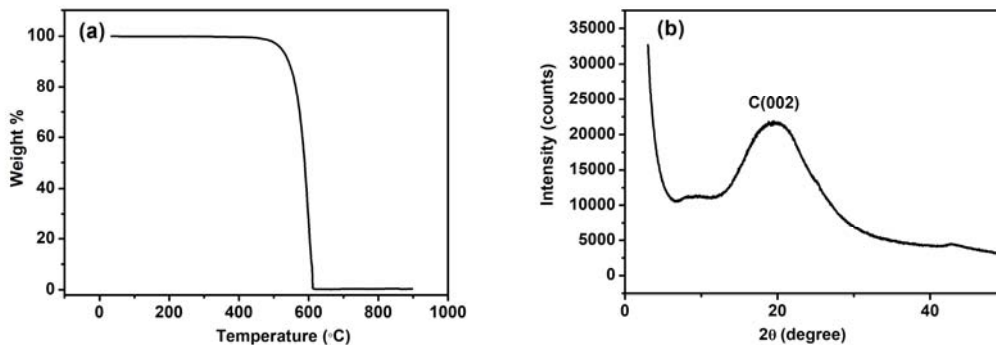


Figure II.13 (a) TGA and (b) XRD pattern for VACNTs.

### II.5.3 Application of VACNTs in microelectrode arrays

*The following works were carried out in collaboration with Prof. Dr.-Ing. Christiane Thielemann and Dr.-Ing. Nick Christoph at Hochschule Aschaffenburg, Germany and published in peer reviewed journals.*

*C. Nick, S. Yadav, R. Joshi, J.J. Schneider, C. Thielemann „Growth of Cortical Neurons Grown on Randomly Oriented and Vertically Aligned Dense Carbon Nanotube Networks“, Beilstein J. Nanotechnol., (2014), 5, 1575-1579.*

*C. Nick, S. Yadav, R. Joshi, J.J. Schneider, C. Thielemann “A three-dimensional microelectrode array composed of vertically aligned ultra-dense Carbon Nanotube Networks”, Appl. Phys. Lett., (2015), 107, 013101.*

Microelectrode array (MEA) is a device which opens a way to carry fundamental research on cells and tissues activities. The electrodes for neuron interfacing should be biocompatible, less inflammatory, mechanically stable (flexible, less stiff etc.) and highly conducting, highly porous for vascularization and cell migration and non-corrosive [202-203]. A photograph of the commercial microelectrode array with 60 electrodes (MCS GmbH) is shown in figure II.14, which contains multiple metallic sites to transfer electrical signals from cells to the output device. Intensity of the signal will be high when the cells are close to the electrodes.

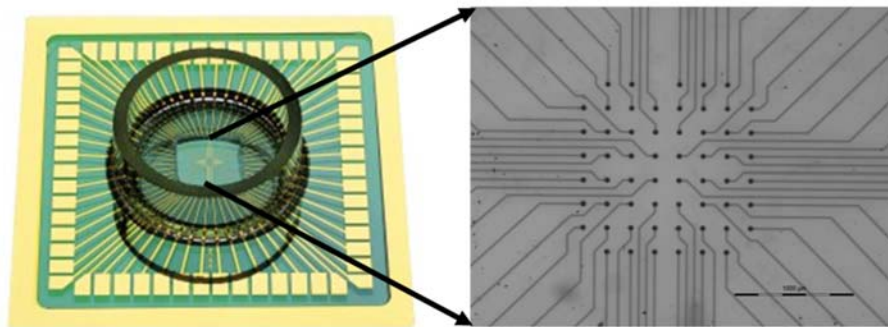


Figure II.14 MEA with 60 electrodes (MCS GmbH).

Action potential sequence in neural communication is provided in figure II.15. Nominal rest potential of a human nerve cell is  $-70$  mV. A stimulus received by the dendrites of a nerve cell open the  $\text{Na}^+$  channels, which drives the potential from  $-70$  mV to  $-55$  mV. Once the action potential is reached, more  $\text{Na}^+$  channels (voltage gated channels) opens,  $\text{Na}^+$  moves to interior of the cell and the potential reaches  $+30$  V. This stage is called depolarization. Then the  $\text{Na}^+$  channels close and  $\text{K}^+$

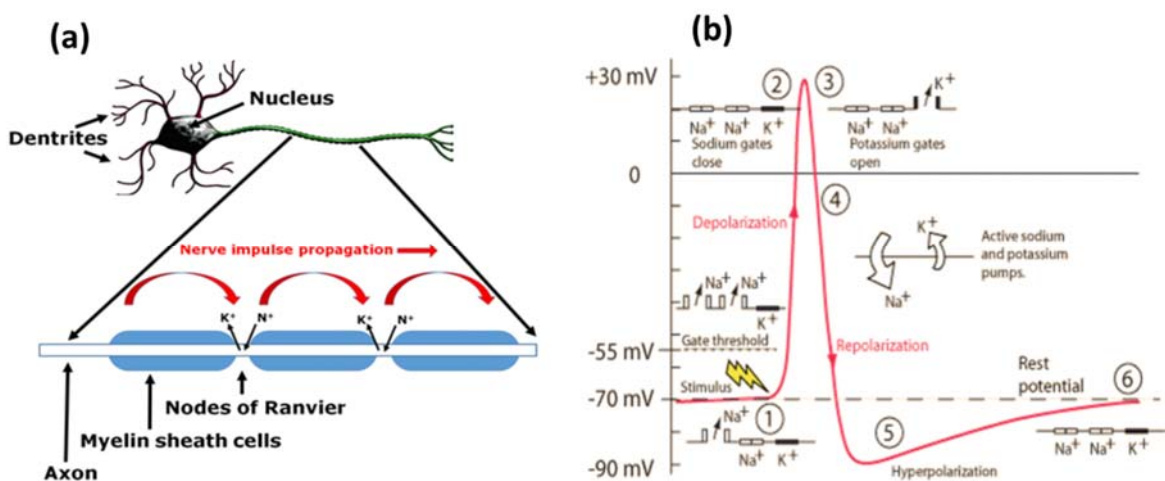


Figure II.15 Action potential sequence in neural communication [204].

channels open, the membrane begins to repolarize back to its rest potential. The repolarization brings the rest potential to about -90 mV. This stage is called hyperpolarization. Hyperpolarization helps prevents triggering the action potential in opposite direction by any stimulus sent up an axon. After hyperpolarization membrane will be back to the rest potential (-70 mV) [204].

Extra cellular recording is one of the methods used to record action potentials from the electrical activity of neurons. Extra cellular action potential from dissociated neurons was recorded initially by Pine using microelectrode array [205]. To record the action potential, size of the electrodes should be of the order of the diameter of neurons (20-50  $\mu\text{m}$ ) [206]. Electrochemical impedance is one of the technique used to investigate the electrochemical properties of the electrode. Signal to noise ratio is inversely proportional to the impedance of the electrode [207]. Microelectrode arrays with specific geometries made with highly conducting materials shows low impedance [208]. Metals (gold, platinum, tungsten and stainless steel) have high electrochemical properties and good biocompatibility used in MEA for neural recording and stimulation [209]. In order to overcome the limitations of metal electrodes such as inflammation, tissue damage and low flexibility, nonmetal based microelectrodes (polymers, carbon nanotubes etc.) are employed in neural interface and recording [207].

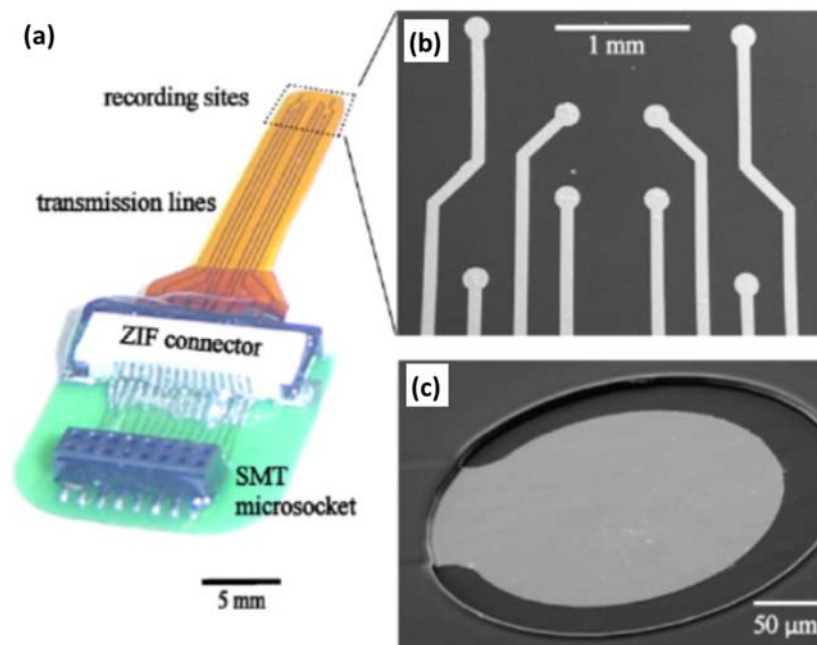


Figure II.16 (a) Channel microelectrode array. Polyimide-based array is connected via connector board consisting of a ZIF-type connector and a surface mount microsocket to the recording instrumentation, (b) A SEM micrographs of the Ti/Pt metallization layer viewed at the end of recording contacts, and (c) A SEM micrographs of the electrode opening. A thin layer of photosensitive polyimide was patterned with alignment of the metallization layer [210].

Polymers such as SU-8 [211], parylene-C [212], PEDOT:PSS [213] and polyimide [210] have been used for long term neural recording due to their excellent biocompatibility, corrosion resistance and mechanical flexibility. An eight channel microelectrode array based on polyimide is shown in figure II.16. Signal recording and communications with smallest neurons of diameter less than 300  $\mu\text{m}$  are the limitations of the polymer electrodes. Unique properties of the nanomaterials such as high electrical conductivity, high surface area, excellent chemical stability and mechanical flexibility enhance the sensitivity, response time and biocompatibility of the implanted neural interface.

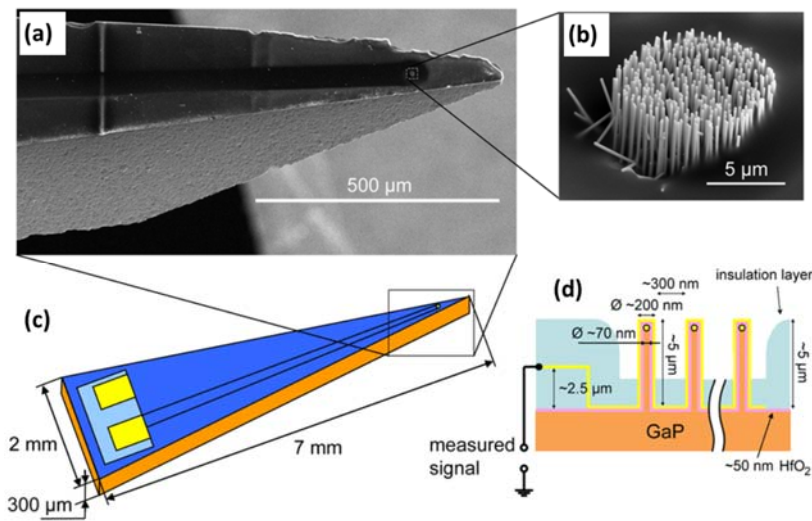


Figure II.17 Nanowire-based electrode for Acute in vivo neuronal signal recordings. (a) SEM image of the GaP based NW electrode, (b) SEM image of the HfO<sub>2</sub> coated GaP NW array for sensing, (c) Layout for the GaP NW-based electrode, and (d) Schematic for the NW geometry and the electrode layered structure [214].

Semiconducting nanowires with high aspect ratio provides low impedance interface for neural recording [214-215]. GaP nanowire array based electrode is for neuronal recording is shown figure II.17. High stiffness of the semiconducting nanowires makes stiffness mismatch between the electrodes and nerve, which is the limitation of implementing nanowires in neural communication [216].

Electrodes made up of carbon nanotubes could overcome the drawbacks of above described materials, hence it can be considered as an ideal electrode material for neuron interfacing and signal recording [217]. Figure II.18 shows the scanning electron images of a microelectrode array composed of randomly oriented CNTs and neuron cells formed on the CNT electrodes.



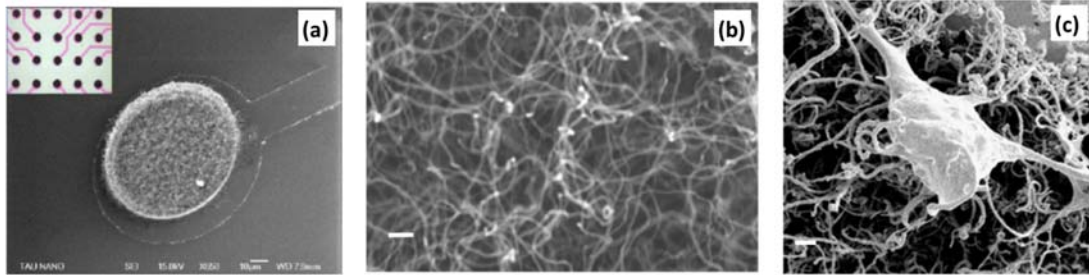


Figure II.18 CNT based microelectrode array. SEM images of a CNT island ( $80\ \mu\text{m}$ ) on a conductive titanium nitride pad ( $100\ \mu\text{m}$ ), patterned on a silicon dioxide substrate (scale bar,  $10\ \mu\text{m}$ ). Inset is the optical microscope image of array of CNT islands in MEA (scale bar,  $100\ \mu\text{m}$ ), (b) SEM image of the CNT island (scale bar,  $100\ \text{nm}$ ) and (c) SEM image of neuron cell on CNT island <sup>[218]</sup>.

Randomly oriented CNTs possess limited height and surface area. Three dimensional microelectrodes with vertically aligned carbon nanotubes overcome these limitations expanding the electrode geometry. In the present work, we demonstrate the fabrication of microelectrode array using VACNTs. The suitability of these electrodes as a sensor is tested using cyclic voltammetry and electrochemical impedance spectroscopy.

Circular microelectrodes are fabricated in a  $8 \times 8$  configuration. The diameter of the electrodes are about  $30\ \mu\text{m}$  each and the distance between the neighbouring electrodes is about  $200\ \mu\text{m}$ . A schematic of the fabrication of microelectrode with vertically aligned carbon nanotubes using photolithography and water assisted chemical vapor deposition is depicted in figure II.19.

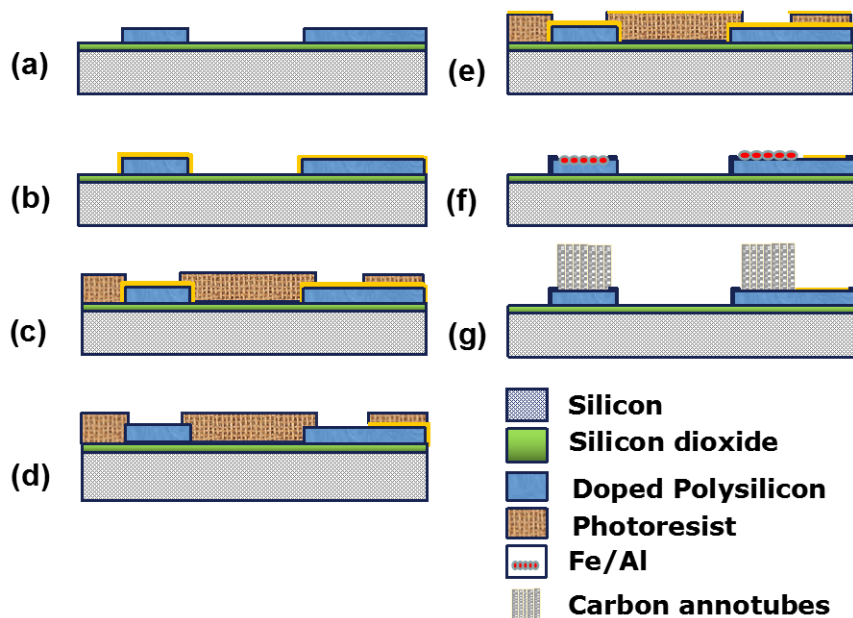


Figure II.19 Schematic of the fabrication of microelectrode with vertically aligned carbon nanotubes using photolithography and water assisted chemical vapor deposition.

In detail, SiO<sub>2</sub> (173.8± 0.6 nm) coated over Si is used as the substrate. Polysilicon of thickness 500±10 nm is coated over SiO<sub>2</sub> using chemical vapor deposition method and doped using POCl<sub>3</sub> to achieve a sheet resistance of 12.7±1 Ω (Fraunhofer Institute for Photonic Microsystems, Dresden, Germany). Then this layer is structured using photolithography technique and dry etched using reactive ion etching (step a). A primer (TI Prime, MicroChemicals GmbH) is spin coated to improve the adhesion of the photoresist. Then the photoresist (AZ 701 MIR, MicroChemicals GmbH, Ulm, Germany) is spin coated and structured using photolithography.

Reactive ion etching of polysilicon is performed using a Diener Femto RIE chamber applying a SF<sub>6</sub>/O<sub>2</sub> plasma (65% SF<sub>6</sub>+35% O<sub>2</sub> at 0.25 mbar). The photoresist is removed by acetone washing before oxidation. To insulate the electrode, an oxide layer is grown over polysilicon by thermal oxidation (step b). Dry oxidation is performed in a Carbolite chamber (GHC12/750 Carbolite GmbH, Neuhausen, Germany) at 1050 °C for about 60 min to form a SiO<sub>2</sub> layer. Then a primer (TI Prime) and photoresist is deposited and structured using photolithography (step c). After development and drying in nitrogen, residual resist or primer at the electrodes and bondpads are removed by oxygen plasma (Femto RIE, Diener electronic). In order to provide contact between CNTs and microelectrodes, oxide layer over the electrodes and outer pads are cleaned using buffered HF etching (step d). The Al (10-12 nm) and Fe (1.4-1.6 nm) are deposited using e-beam technique on the electrodes only (step e). Further, removal of the photoresist by acetone washing lift off all the unwanted metals by keeping the catalyst on the electrodes (step f). Vertically aligned carbon nanotubes are grown by water assisted chemical vapor deposition at the electrodes (step g). Procedure for the synthesis of VACNTs are discussed in experimental section. Density of carbon nanotubes over the microelectrodes is approximately 1600 VACNTs/μm<sup>2</sup>.

The ratio of overall active area compared to planar area can be calculated using the equation

$$A_{\text{ratio}} = 2\pi(r_{\text{in}} + r_{\text{out}})h\rho + 1 \quad (\text{II.1})$$

where h is the height of vertically aligned carbon nanotubes, ρ is the density of carbon nanotubes per area, r<sub>in</sub> is the inner diameter of the carbon nanotube, r<sub>out</sub> is the outer diameter of the carbon nanotube. Applying r<sub>in</sub>=2 nm, r<sub>out</sub>=2.5 nm

$$A_{\text{ratio}} = 45.24 h (\mu\text{m}) + 1 \quad (\text{II.2})$$

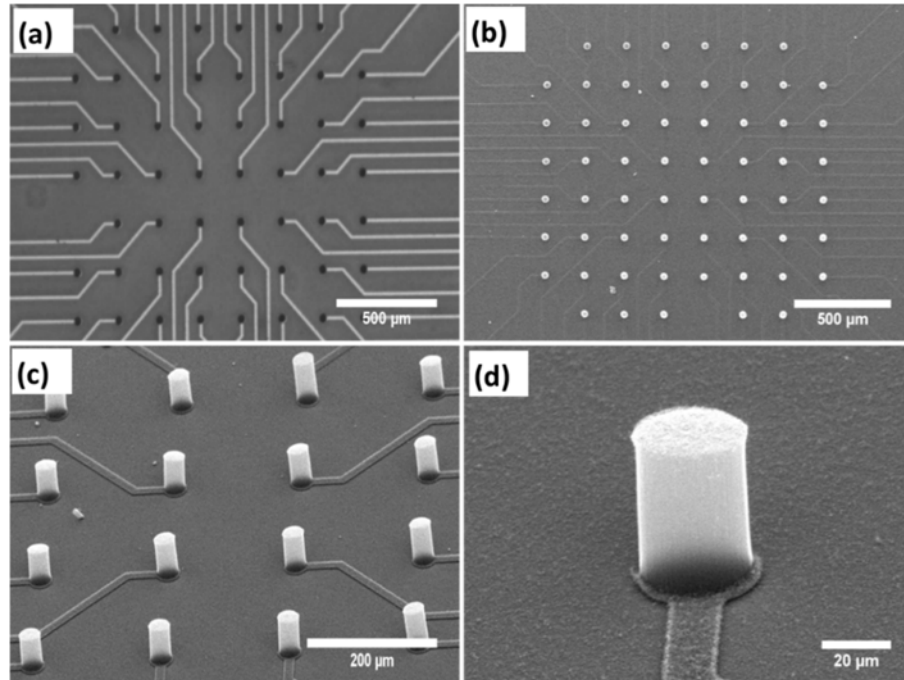


Figure II.20 SEM image of the (a) over view of the array of microelectrodes, (b, c and d) vertically aligned CNTs grown on microelectrodes in different magnifications [111].

Figure II.20 shows the SEM images of the microelectrode array made up of vertically aligned carbon nanotubes. VACNTs of height more than 100 μm can be achieved. The high aspect ratio CNTs (> 15000) shows less attachment to the substrate if no special precautions are employed in growth process. In the present study, CNTs of height about 2 μm (aspect ratio greater than 300) are used. They are mechanically more stable and can be used in electrochemical environment without destruction.

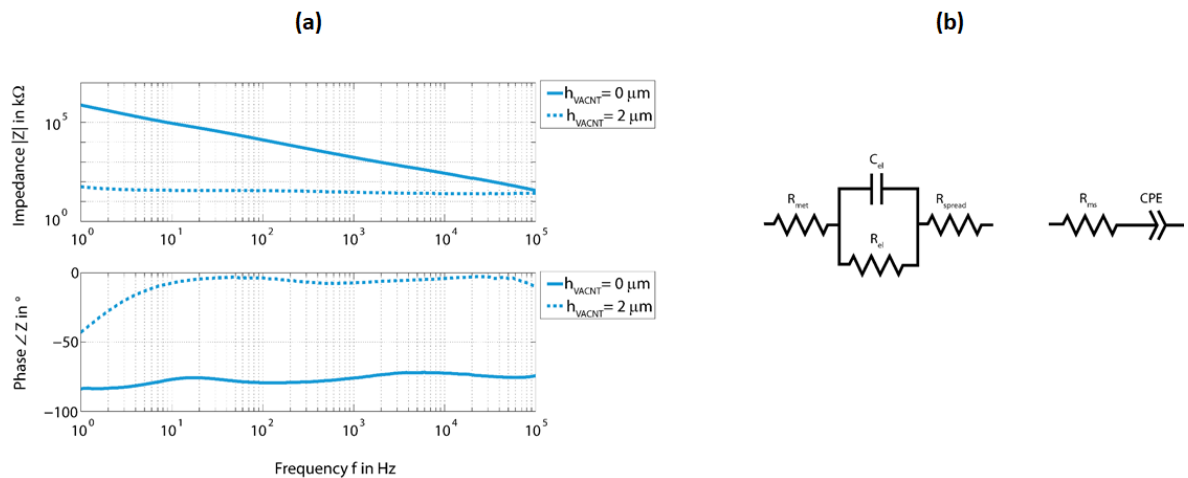


Figure II.21 (a and b) Impedance spectra and equivalent circuit of the microelectrodes and microelectrodes with vertically aligned CNTs of height 2 μm [111].

The microelectrodes were characterized using cyclic voltammetry and impedance spectroscopy. Impedance spectra is recorded using VersaSTAT 4 (Princeton Applied Research, Oak Ridge, USA) in scanning range of 1 Hz–100 kHz applying signal amplitudes of 20 mV. In order to measure the impedance spectra, a small polydimethylsiloxane (PDMS, Sylgard 184, Dow Corning, Wiesbaden, Germany) ring with a cavity filled with phosphate-buffered saline as electrolyte (PBS, Sigma-Aldrich Chemie, GmbH, Taufkirchen, Germany) is glued onto the array. Impedance spectra of plane microelectrodes and microelectrodes with vertically aligned carbon nanotubes (2  $\mu\text{m}$ ) is shown in figure II.21 (a). Figure II.21 (b) shows the electrical equivalent circuit. The electrode and electrolyte interface is described using a charge transfer resistance  $R_{el}$  and a double layer capacitor  $C_{el}$  in parallel.  $R_{met}$  and  $R_{spread}$  is attributed to the resistance of the contacts and electrolyte, which are in series.  $R_{met}$  and  $R_{spread}$  is replaced as  $R_{ms}$ .  $R_{el}$  is negligible compared to  $C_{el}$ . Then the  $C_{el}$  can be modelled as constant phase element  $Z_{CPE}=[Q(j\omega)^n]^{-1}$ . The simplified equivalent circuit is shown in figure II.21 (b). Fitting is done using the software package Zview (Scribner Associates Inc., Southern Pines, USA) and the results are summarized in Table II.1.

Table II.1 Values of  $R_{ms}$ ,  $Q$  and  $n$  by fitting the impedance spectra.

Height ( $\mu\text{m}$ )	$R_{ms}$ ( $\text{k}\Omega$ )	$Q$ ( $\mu\text{F}$ )	$n$
0		$(346\pm 54)\times 10^{-6}$	$0.845\pm 0.014$
2	$27.4\pm 8.9$	$13.5\pm 2.8$	$0.45\pm 0.11$

Cyclic voltammetry measurement is performed using three electrode set up. Vertically aligned CNTs are used the working electrode, Ag/AgCl is used as the reference electrode and platinum mesh is used as the counter electrode. The voltage is scanned from 0 to 200 mV. Cyclic voltammogram is recorded at scan rates 20, 50, 100, and 200 mV/s. 10 cycles are recorded in each scan rate. Electrodes with VACNTs show a DC-capacity of  $16.4 \pm 2.3 \text{ mF/cm}^2$  and that of polysilicon electrode is  $0.17 \pm 0.12 \text{ mF/cm}^2$ .

#### II.5.4 Application of VACNTs in neuron growth

The nervous system has two divisions: the central nervous system (CNS) and the peripheral nervous system (PNS). The brain and spinal cord are the organs of the CNS. Nervous tissue consists of two types of cells, neurons and neuroglia. Neuron or nerve cells (Figure II.22) are highly specialized to conduct impulses called action potential. Neuroglia primarily function to support and assist neurons. These nerves are made of neurons and specialized cells called Schwann cells. The Schwann cells form the myelin sheath to electrically insulate neurons. Neurons are capable of generating and

transmitting electrochemical impulses. The cell body contains the nucleus and is essential for the continuing the life of the neuron. Neurons have branched dendrites that extent from the surface of the cell body to provide a large surface area for receiving stimuli and conducting impulse to the cell body. The elongated axon conducts the impulse away from the cell body to another neuron or to an organ that responds to the impulse. A nerve impulse travels along the cell membrane of a neuron, and is electrical, but where neurons meet there is a small space called a synapse, which an electrical impulse cannot cross. At a synapse, between the axon of one neuron and the dendrite or cell body of the next neuron, impulse transmission depends upon chemicals called neurotransmitters [219]. A neuron is designed to react to stimuli, to transmit the resulting excitation rapidly to other portions of the nerve cell, and to influence other neurons, muscle cells, and glandular cells [220].

There are three major parts of the synapse: (1) a presynaptic terminal (located on axon) containing neurotransmitter, mitochondria (2) a postsynaptic terminal (located on dendrite) containing receptor sites for neurotransmitter and (3) a synaptic gap or space between the presynaptic terminal and the postsynaptic terminal [221].

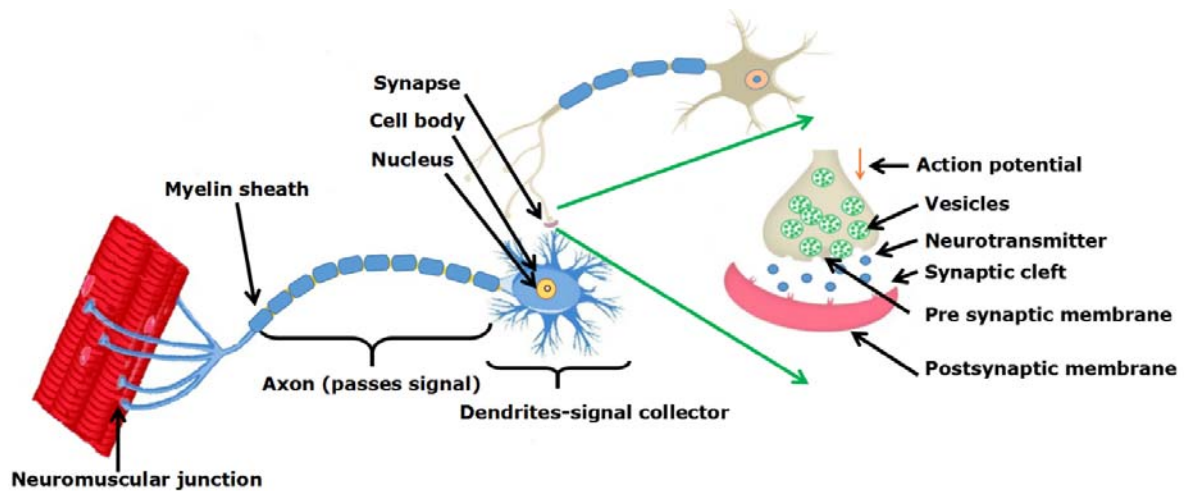


Figure II.22 Nervous system.

Carbon nanotubes have received wide interest in the biomedical field as a growth substrate for various cells [222]. Carbon nanotubes are a very promising substrate for neuron growth as well as to record and stimulate neural activity due to their excellent electrical conductivity and biocompatibility. CNTs as growth substrate is more interesting because of the form and shape of CNTs. They are similar to the extra cellular matrix. However CNTs (if conducting) may also boost activity due to short circuiting [109, 223-227]. The high intrinsic surface area and charge injection capacity makes CNTs as a promising material for neuron growth. CNTs look like extracellular

matrix due its one dimensional structure hence better adhesion of neurons is possible. Also, the surface charges and functionalization <sup>[170, 228]</sup> have an impact on the neurite growth and network formation. Neural interfacing based on vertically aligned multiwalled carbon nanotube (CNT) pillars as microelectrodes is reported. Functionalized hydrophilic CNT microelectrodes shows a high charge injection limit of 1–1.6 mC/cm<sup>2</sup> without faradic reactions <sup>[229]</sup>.

In the present study, the influence of carbon nanostructures in the growth and networking of neurons is investigated. In vitro growth of cortical neurons on randomly oriented and vertically aligned carbon nanotubes islands are presented. Randomly oriented and vertically aligned carbon nanotubes islands are structured using photolithography of the catalyst followed by water assisted chemical vapor deposition for the growth of CNTs.

Figure II.23 represents the schematic of the fabrication of islands of randomly oriented and vertically aligned CNTs using photolithography and water assisted chemical vapor deposition technique <sup>[230]</sup>. In detail, photoresist (AZ 701 MIR, Micro- Chemicals GmbH, Ulm, Germany) is coated over the substrate (Si or gold coated Si) using spin coating. Later resist is structured using photolithography (step a). Then, catalyst (Al= 10-12 nm, Fe=1.2-1.4 nm) is coated over the structured substrate by electron beam deposition technique (step b) and the photoresist is removed by acetone washing. Si substrate coated with thin layer of gold (100 nm) is used for the growth of islands of randomly oriented CNTs.

CNTs were grown using water assisted chemical vapor deposition technique <sup>[57, 64]</sup> at 780-820 °C by passing argon, hydrogen, ethene and ppm quantities of water for 2-3 minutes. Substrate with catalyst is heated to growth temperature in the presence of argon and hydrogen. At growth temperature, ethene and water is introduced into the reactor.

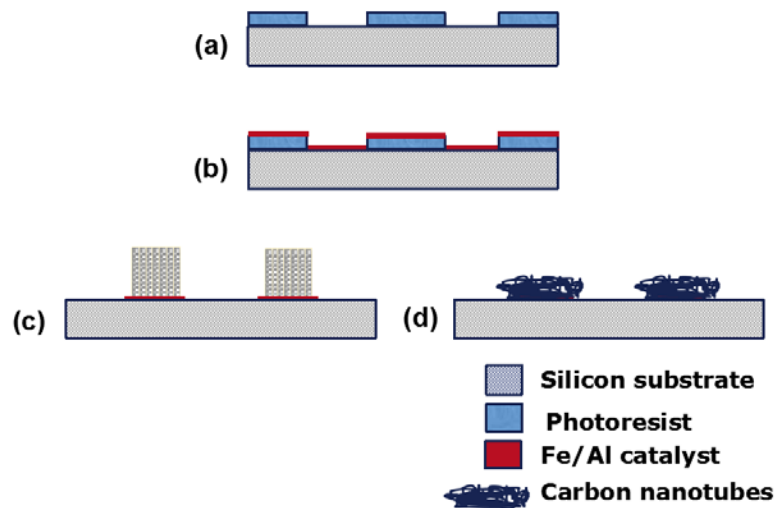


*Figure II.23 Schematic of the fabrication of islands of randomly oriented and vertically aligned CNTs using photolithography and water assisted chemical vapor deposition technique.*

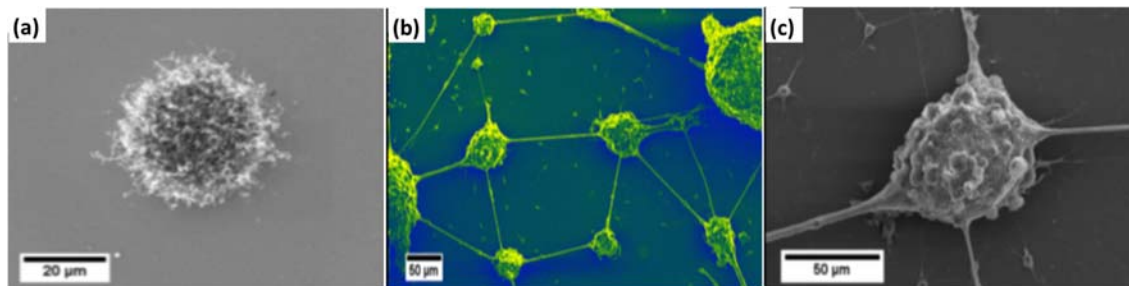


Figure II.24 (a) SEM image of a single CNT island with a diameter of  $\sim 30 \mu\text{m}$ , (b) and (c) SEM image of the neurons accumulated *in vitro* onto CNT islands after 21 days (the distance from CNT centre to CNT centre is  $200 \mu\text{m}$ ) [231].

Cryoconserved embryonic cortical rat neurons (E18 and E19) purchased from Lonza Ltd, Basel, Switzerland and were stored in liquid nitrogen until use. The substrates with CNT islands were sterilized under UV-light [232]. Preparation protocol for cell culture medium is described below. L-glutamine (2 mM) and 2% NSF-1 were added to the PNBm basal medium. NSF-1, a supplement supporting neuronal growth and survival, was aliquoted, frozen and added to the medium immediately before each use. 3mL culture medium was taken in the petridish. Neurons were thawed and cultured with a density of approximately  $500,000 \text{ cells/mm}^2$  on each substrate and incubated in a humidified atmosphere ( $37^\circ\text{C}$ , 5%  $\text{CO}_2$ , saturated atmosphere for 4 h). Half of cell culture medium was replaced twice a week and completely replaced every second week. Scanning electron microscopy imaging was done to study the growth of neurons on VACNT islands and randomly oriented CNT islands. For doing SEM investigation, the cell culture medium of the substrates was replaced with 2.5% glutaraldehyde. Glutaraldehyde was removed after 2.5 hours and all the substrates were washed in DI-water three times. Then the fixation cells were dried in ethanol (10%, 30%, 50%, 70%, 90%, 99.6% for 20 min each). Further, ethanol was replaced by hexamethyldisilazane (HMDS) and dried in air [232-234]. Prior to SEM investigation, dried fixation cells were sputter coated with 5 nm Pt/Pd. Figure II. 24 depicts that the neurons are strongly attracted by the randomly oriented CNT islands and formed clusters of cells. The islands are interconnected via cells and neurites. Figure II. 25 shows the SEM images of the growth of neurons cultivated on vertically aligned carbon nanotubes for a period of 14 days. Dense clusters of neurons observed in the vicinity of vertically aligned CNT islands after 4 hours of cultivation, which is shown in figure II.25. Also, the cell clusters are interconnected (see the arrows in figure II. 25 (a)). It was observed that the cell bridges are disappeared after two days (figure II. 25(b)) of cultivation and the cell clusters become larger. Also the cells on the Si is disappeared. Dense clusters of cells were observed after 7 days (figure II.25 (c)) of cultivation and the interconnections were not present. After 4 hours,

about  $49 \pm 15$  neural cells were observed in area of  $0.393 \text{ m}^2$  and it decreased to  $9 \pm 6$  from day 12 onwards. Clear neural connections between the CNT islands is observed after 14 days of cultivation (figure II.25 (d)).

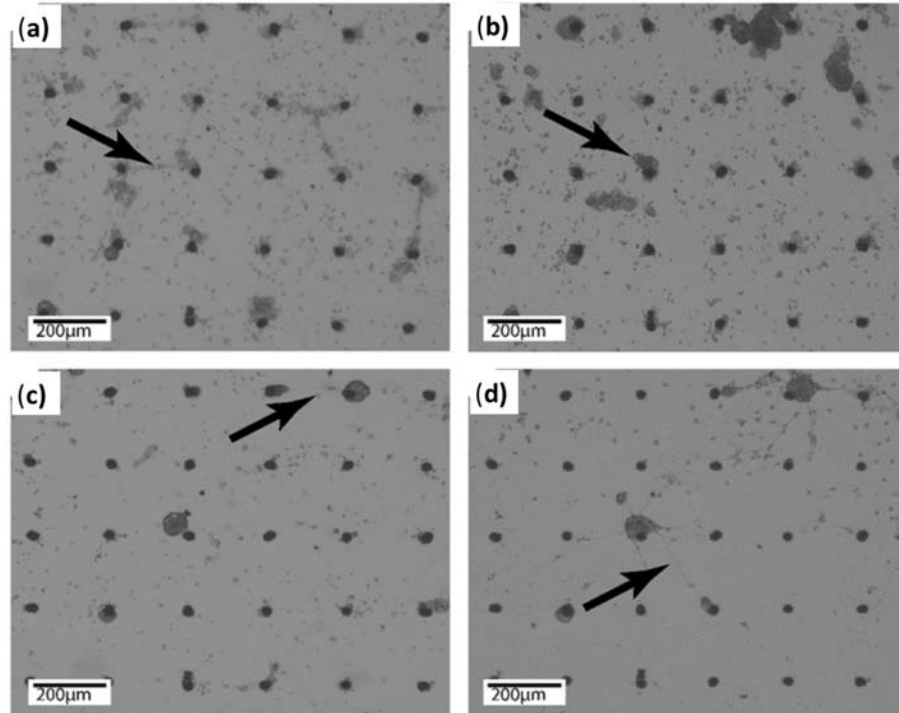


Figure II.25 Growth of cortical neurons cultured on islands of vertically aligned CNT. (a) Formation of neuron clusters after 4 h, (b) after 2 days in vitro, (c) after 7 days in vitro and (d) after 14 days in vitro. Each CNT pillar is  $30 \mu\text{m}$  in diameter and the distance between two pillars is  $200 \mu\text{m}$  (centre to centre) [231].

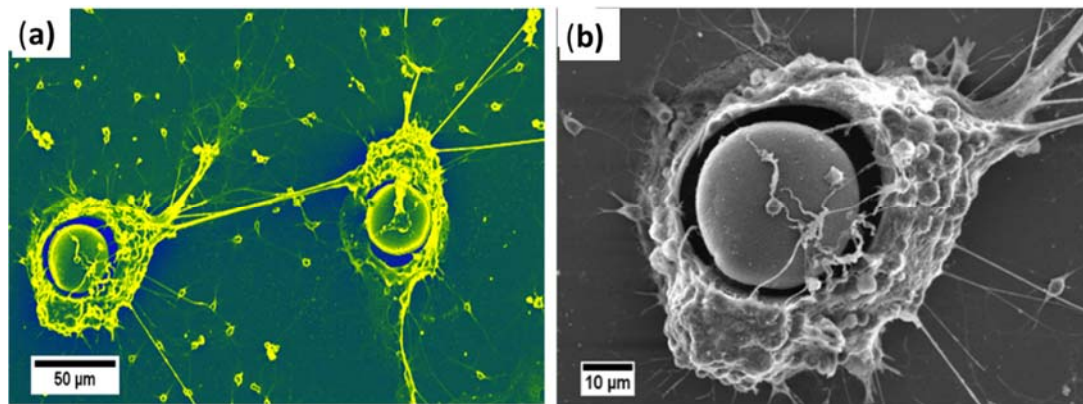


Figure II.26 SEM images of (a) two selected CNT pillar architectures with cultured cortical neurons (height about  $400 \mu\text{m}$ , diameter about  $30 \mu\text{m}$  and distance of about  $200 \mu\text{m}$  between individual CNT pillars and (b) close up view of the vicinity of the VACNTs structure and the neurons [231].



Matured neurons are observed after 21 days of cultivation (figure II.26). More cells are visible on the CNT side walls than on the top of the CNT pillars. Neurons are strongly attracted via the side walls. Though the cells are able to climb upto several micrometers, growth is not prominent on tips. This behaviour is further verified by changing the shape and size of the CNT pillars (figure II. 27). It was observed that the neurons are strongly attracted by the side walls of the CNTs.

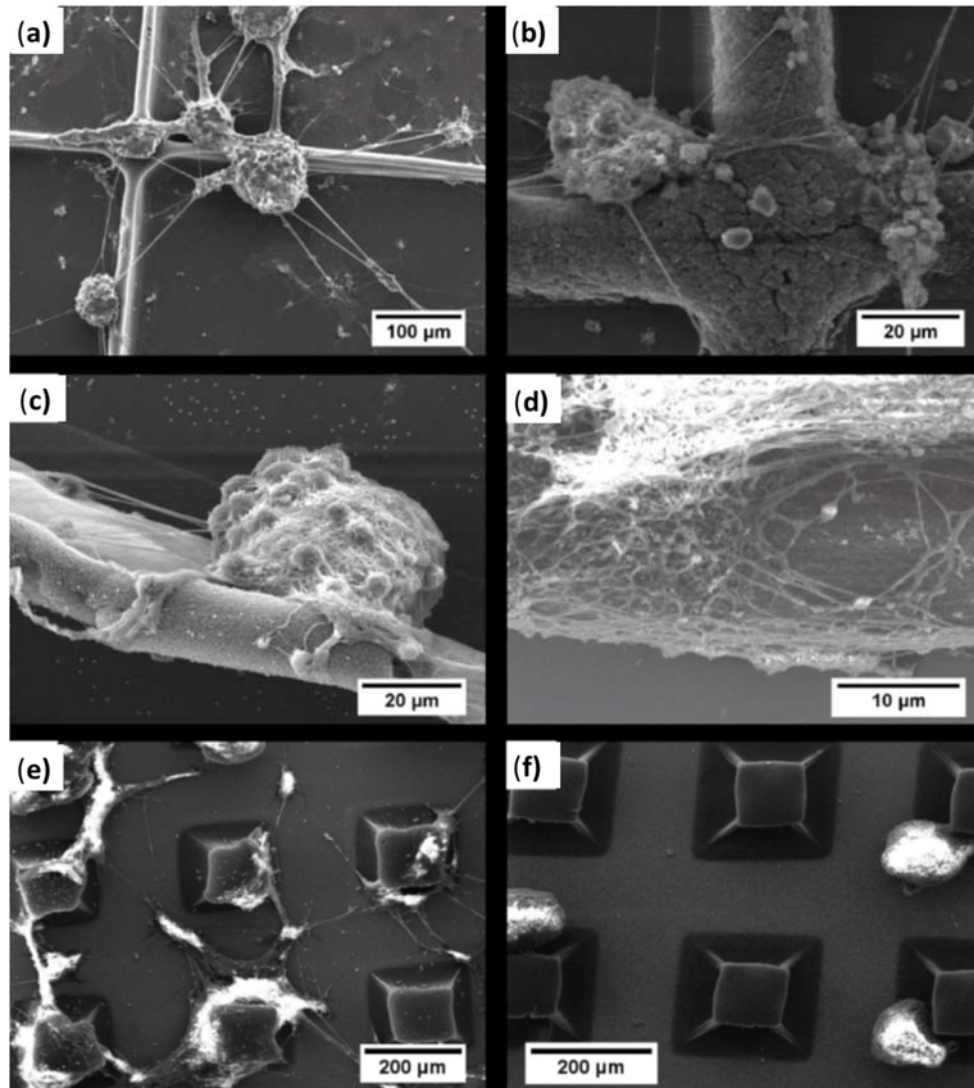


Figure II.27 SEM pictures of neuronal cell assembly on different CNT micro architectures. ((a) and (b)) Neuron growth on a cross bar structured CNT in different magnifications, (c) Higher magnified view of a neuronal cell cluster showing its preferential adherence on the side architecture of the CNT wall structure, (d) higher magnified view of a dense cell assembly on the CNT upper rim wall structure, (e) preferential cell assembly of the neuron cell line R18 (Embryonic Rat Hypothalamus Cell Line R18 (RHypoE-18)) on the CNT side walls and (f) the preferential cell assembly of a neuronal spheroid (from neurons of a chicken embryo) on the CNT side walls of CNT microstructured blocks [231].

## II.5.5 A nano-microstructured artificial-hair-cell-type sensor based on topologically graded 3D carbon nanotube bundles

*The following work was carried in collaboration with PD Dr.-Ing. habil. Oktay Yilmazoglu and M.Sc. Deniz Cicek, Department of Electrical Engineering and Information technology, TU Darmstadt and published in peer reviewed journals.*

*O. Yilmazoglu, S. Yadav, D. Cicek, J.J. Schneider “A nano-microstructured artificial hair cell type sensor based on topologically graded 3D carbon nanotube bundles”, Nanotechnology, (2016), 27, 365502.*

All organisms from bacteria to humans are mechanosensitive. The conversion of physical force or by using physical forces organisms can generate accurate 3D-structures. Hearing and touch are based on neural responses to vibration and pressure [221].

Transforming vibrational energy into an electrical signal hair cell played evolutionary role and opened door for advanced mechanosensors. Hair cells consist of hair bundle contains anywhere from 30 to a few hundred hexagonally arranged stereocilia, with one taller kinocilium (Figure II.28). Displacement of the hair bundle parallel to this plane toward the tallest stereocilia and at the limits of human hearing, hair cells can faithfully detect movements of atomic dimensions and respond in the tens of microseconds. The hair bundle movements at the threshold of hearing are approximately 0.3 nm, about the diameter of an atom of gold [235].

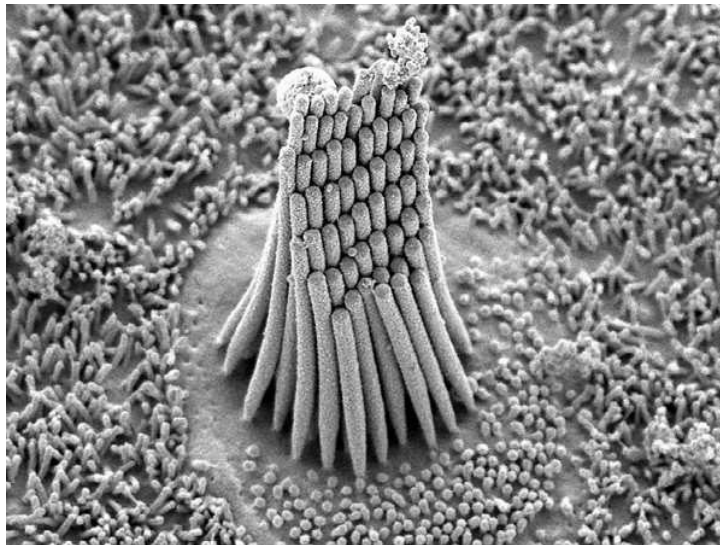


Figure II.28 A cilia hair bundle [236].

---

Cilia hair cells play vital role in functions such as hearing and balance in animals. The bending of this by the external forces such as fluid motion (motion of inner ear liquid) generates electrical signals in the inner ear. Biomimic natural hair like structures to function like cilia are already developed. Biomimetic hair flow sensors are categorized into several groups, namely thermal, piezoresistive, capacitive, magnetic, piezoelectric and optical sensors [237-240]. Engel et al. developed Artificial-hair-cell-type sensors (AHCTSs) with good sensitivity and excellent robustness using polyurethane hairs, carbon impregnated polyurethane force sensitive resistors and common MEMS processing technologies [241].

Polyvinylidene difluoride (PVDF) microfiber with a molybdenum core produced by the hot extrusion tensile method used to fabricate bionic airflow sensor [242]. Artificial hair sensors with SU-8 polymer hairs mounted on silicon nitride suspended membranes is fabricated. Electrodes on the membrane and on the substrate form variable capacitors, allowing for capacitive read-out [243]. Pillars consisting of PDMS polymer with embedded iron nanowires integrated on a GMR thin film sensor is fabricated to detect the water flow as well as air flow [244].

Carbon nanotubes are a promising material in artificial hair type sensors due to its unique properties such as high electrical conductivity, supercompressibility, bending elasticity, structural flexibility, high aspect ratio and chemical inertness. Compressive behaviour of the vertically aligned CNTs are investigated. Material properties are highly anisotropic and it possess a axial modulus of 165–275 MPa, the transverse modulus of 2.5–2.7 MPa and the out of plane shear modulus of 0.8–1.6 MPa [245]. Vertically aligned carbon nanotube shows zigzag buckles under compression and it came back to the original length upon load release [246]. This buckling behaviour was explained by employing van der Waals force among the individual nanotubes as lateral support [247]. Mechanical properties of the vertically aligned CNTs are widely studied [246, 248-253]. Electrical conductivity of the carbon nanotube block under compressive strain was investigated [248]. Vertically suspended single walled carbon nanotubes were used for electromechanical sensing [250] and vertically aligned carbon nanotubes are used as piezoresistive pressure sensor [251]. Carbon nanotube cantilever was simulated using molecular dynamics by Feng et al. [254]. Structural deformation and vibration of a CNT under fluid flow are studied using molecular dynamics simulation [255]. A typical CNT with 1 nm diameter and 1  $\mu\text{m}$  length shows sensitivity of 68  $\mu\text{m s}^{-1}$  in water. CNT coated glass fiber supported on a glass microcapillary is used as artificial hair sensor. The sensors shows piezoresistive sensitivity of 1.3% per m/s air-flow change [256].

Artificial-hair-cell-type sensor based on 3D-structured vertically aligned carbon nanotube bundles for 3D-force sensing is presented herein. The sensing is achieved by generating a lateral electrical contact between the central long CNT bundle and neighbouring shorter CNT bundles. CNT bundles

of different height is synthesized by employing a patterning technique for the CNT growth catalysts, which locally modulate the CNT growth rate [257]. The obtained hierarchical CNT structures shows excellent sensitivity and flexibility. CNT bundles with different height (topographic height variation) is a significant characteristic of our process, which mimics natural mammal cilia morphology.

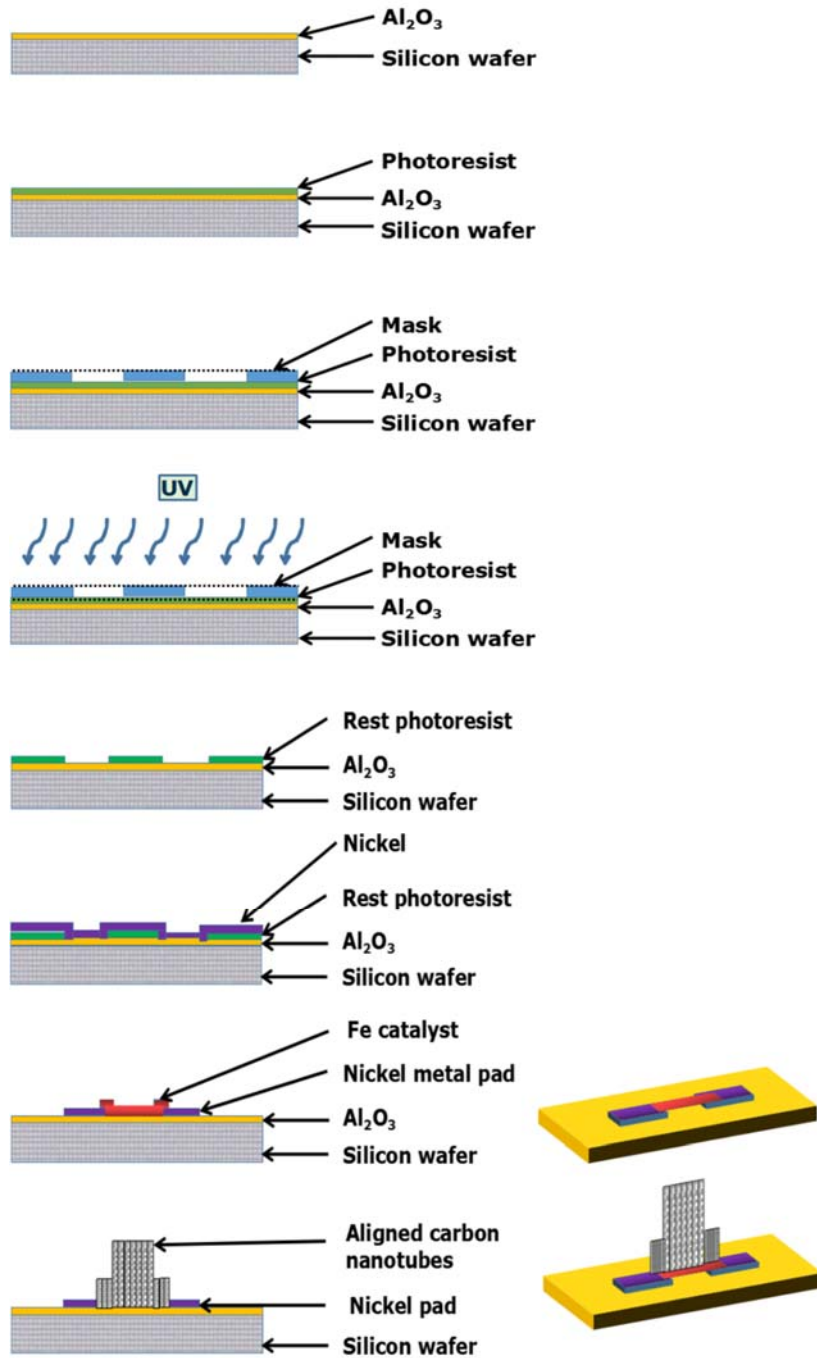


Figure II.29 Schematic of the AHCTS fabrication.

The sensor consists of 3D structured vertically aligned double-walled carbon nanotube bundles arranged in parallel. The bundles are stable due to the van der Waals interaction between the individual CNTs. The heights and width of the CNT bundles can be tuned by the fabrication process. There is a lateral contact between the longer CNT bundles and shorter CNT bundles. A schematic of the fabrication process is presented in figure II.29. In detail,  $\text{AlO}_x$  layer of thickness 30-40 nm was deposited on Si wafer or Si/SiO<sub>2</sub> (600 nm) wafer by atomic layer deposition (ALD) technique. Further, photoresist was coated over the  $\text{AlO}_x$  layer by spin coating and a chrome mask over the photoresist. Then the resulting structure was patterned using optical lithography technique and Ni contact pads of thickness 50 nm were deposited over the patterned structure by e-beam deposition technique. Rest of the photoresist is removed by acetone washing. The distance between the Ni pads (100-400  $\mu\text{m}$ ) is considered as the final width of sensor. A specially structured mask is placed on the nickel pads and Fe (1.4 -1.6 nm) is deposited. Later, the CNTs were grown using water assisted chemical vapour deposition technique at 820 °C by passing argon, hydrogen, ethene and ppm quantities of water [57, 64]. The height of the CNTs (150-1700  $\mu\text{m}$ ) are depending on the time of synthesis, catalyst design or by substrate. Width of the CNT bundles (5-100  $\mu\text{m}$ ) adjusted by the width of iron deposited.

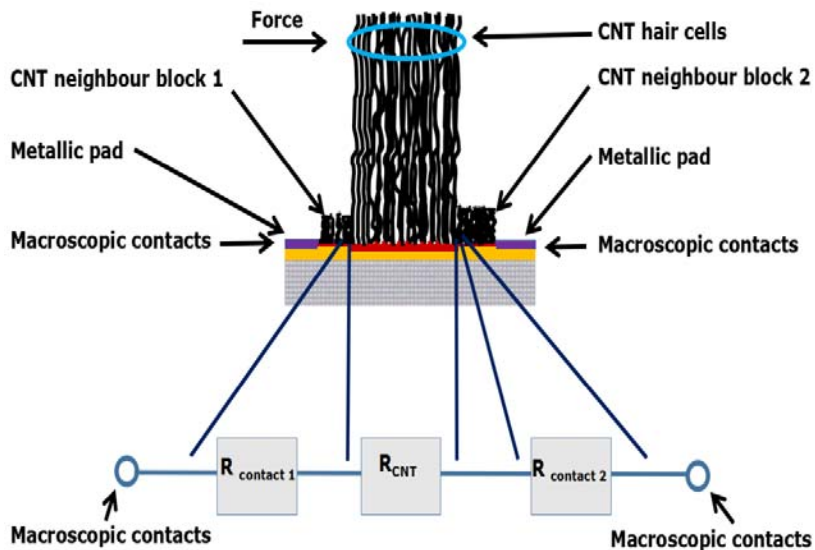


Figure II.30 Schematic of the AHCTS sensor.

Figure II.30 shows the schematic of the AHCTS with the resulting electrical resistance components of the outer CNT contact bundles to the left and right of the main CNT bundle, which detects the force impingement. The effective electrical resistance ( $R_{\text{total}}$ ) of the AHCTS device in a lateral

direction is the sum of the contact resistance of the central CNT bundle to the two neighboring CNT bundles ( $R_{\text{contact1}}$ ,  $R_{\text{contact2}}$ ) as well as the internal electrical resistance of the CNT ( $R_{\text{CNT}}$ ) within the central bundle.

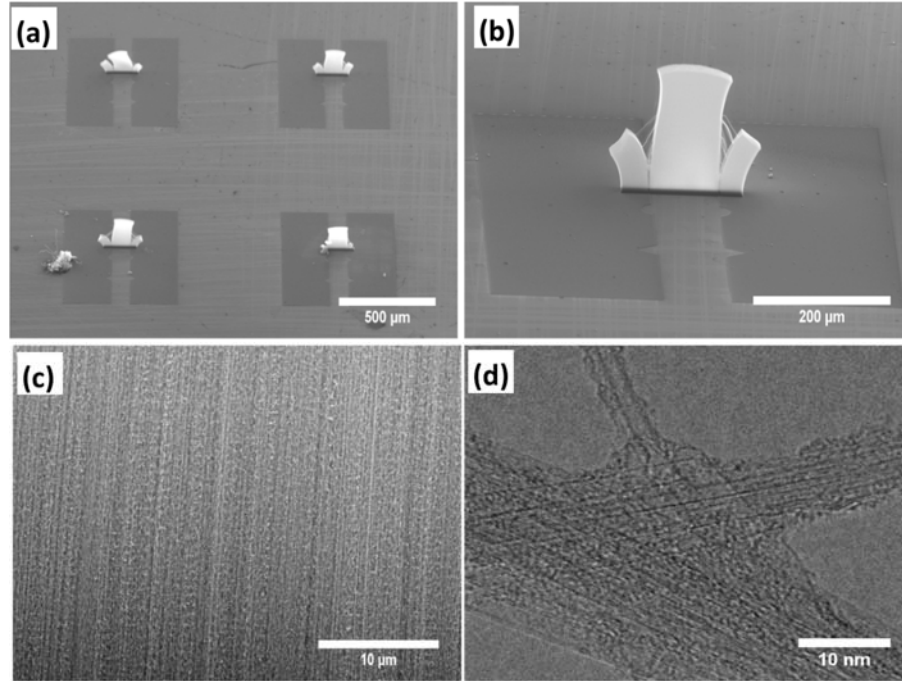


Figure II.31 ((a) and (b)) SEM image of the AHCTS with longer central CNT bundle and shorter neighbouring CNT bundle, (c) SEM image of the CNT bundle in high magnification and (d) TEM image of the CNTs unhinged from the main CNT bundle by long term ultrasonication.

Hart et al. reported strain engineered growth of bi-level CNT micropillar<sup>[257]</sup>. SEM image of the 3D AHCTS with central long CNT bundle and shorter neighbouring CNT bundles is shown in figure II.31 (a and b). The central long CNT bundle of the AHCTS device has electrical contacts with the neighboring smaller CNT bundles, which act as contact bundles. In an undeflected AHCTS device, the distance between the central CNT bundle and the two neighbouring CNT bundles is in between 1–5  $\mu\text{m}$  and increases gradually from the bottom to the top. Free-standing vertically aligned CNTs with high homogeneity is found. This special structure is achieved by patterning the catalyst by lithography technique. Each AHCTS is electrically insulated from neighbouring AHCTSs hence cross-sensitivity in the individual sensor devices is avoided. Figure II.31 (c) shows the SEM image of the central CNT bundles in high magnification, it depicts the vertical alignment of the CNTs in the bundle. The same holds true for the small bundles. Large number density of CNTs within the central CNT bundle ( $>10^9$  tubes  $\text{mm}^{-2}$ ) promotes the interaction of the central CNT bundle with the neighboring CNT bundle structures serving as contact bundles. TEM image (figure II.31 (d)) shows

that the CNTs are nearly double walled and the diameter is of the order of 3- 6 nm. The vertical electrical conductivity of these CNT bundles (thickness=100 $\mu\text{m}$ , width=200 $\mu\text{m}$ , Length=500 $\mu\text{m}$ ,  $\varnothing_{\text{CNT}}=6\text{nm}$ , and CNT density  $\sim 1 \times 10^9$  tubes  $\text{mm}^{-2}$ ) are about 1 S/cm which is close to the reported values<sup>[120]</sup>. AHCTS samples were glued onto an aluminium block in order to perform the mechanical and electrical characterization.

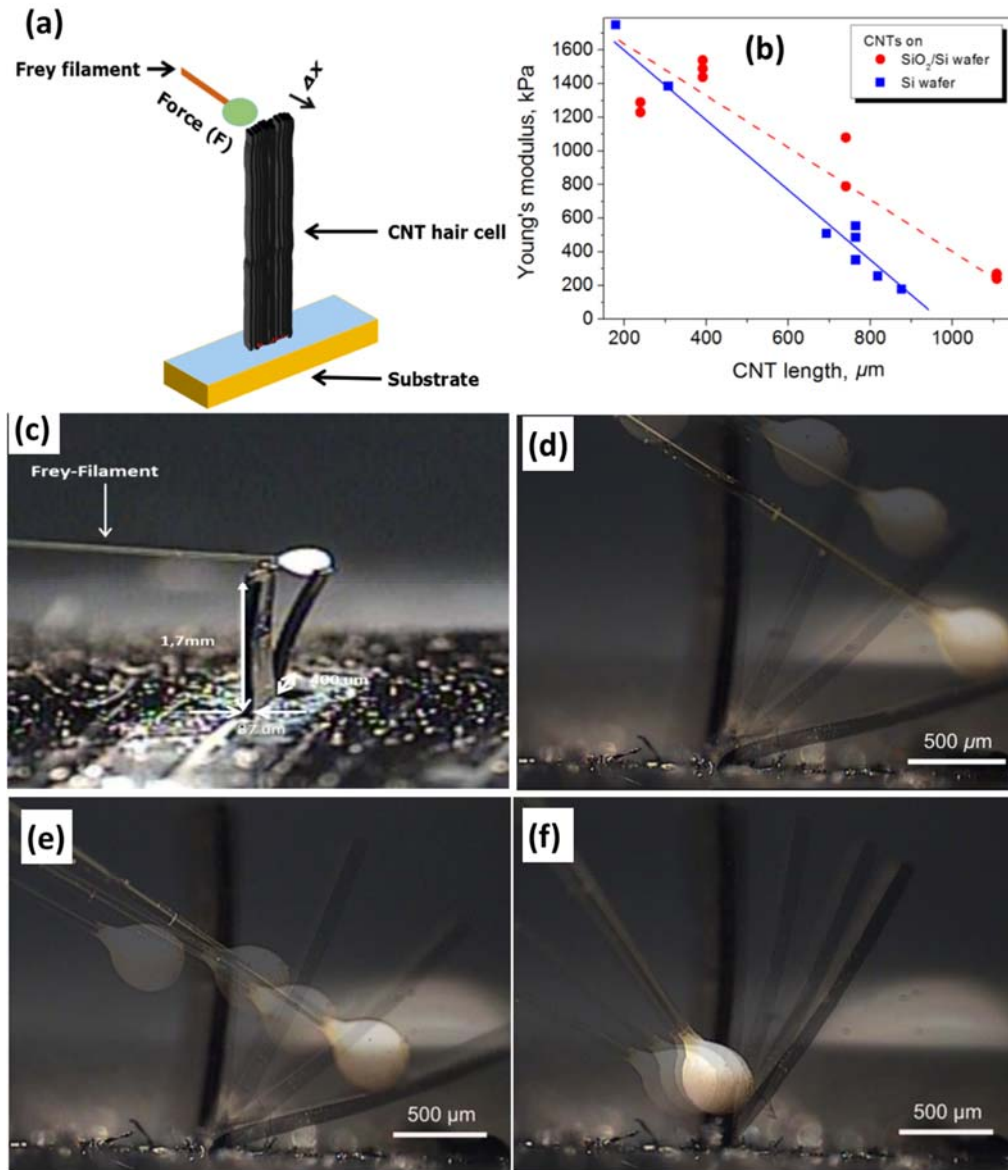


Figure II.32 (a) Schematic of the mechanical characterization of the AHCTS element with a controlled pressure load using Frey filaments, (b) the Young's modulus change with the CNT bundle length on the Si and SiO<sub>2</sub>/Si substrate, (c and d) the mechanical impingement of a Frey filament on the top, (e) middle and (f) bottom of a 3D CNT structure. The height is 1700  $\mu\text{m}$ , width is 400  $\mu\text{m}$  and the thickness is 90  $\mu\text{m}$  <sup>[110]</sup>.

### *Young's modulus and stability*

The sensitivity of the fabricated AHCTS was investigated using a camera embedded optical microscope. A home built loading platform with Frey filaments of defined force sensitivities 50  $\mu\text{N}$ , 80  $\mu\text{N}$ , 125  $\mu\text{N}$  and 200  $\mu\text{N}$  are used to deflect the CNT bundles.

They buckled at the defined force. The Young's modulus is calculated using the following formula

$$E = \frac{4Fl^3}{bd^3 \Delta x} \quad (\text{II.3})$$

where  $F$  is the lateral force applied,  $l$  is the length of the CNT bundle,  $b$  is the bundle width,  $d$  is the thickness and  $\Delta x$  is the bundle deflection.

Figure II.32 (b) shows the Young's modulus of the CNT bundles of different length grown on different substrates. The change in Young's modulus is closely related to the inherent waviness [258]. CNT bundle of length 800  $\mu\text{m}$  shows a Young's modulus about 220 kPa, which is several orders of magnitude less than the Young's modulus of single CNT (1TPa) [259]. Figure II.32 (c, d, e and f) shows the mechanical impingement of a Frey filament on the top, middle and bottom of a 3D CNT structure. The height is 1700  $\mu\text{m}$  width 400  $\mu\text{m}$ , and the thickness 90  $\mu\text{m}$ . Stable bending of up to 90° for the CNT bundle is achieved without mechanical deformation. Figure II.33 (a) shows the photograph of the side view of the CNT bundle at mechanical bending. A repeatable stable bending of the CNT bundle up to 90° could be achieved without mechanical deformation. The 3D AHCTS was bended with a home-built loading platform using a passivated GaAs wafer. The height of the CNT bundle is 300  $\mu\text{m}$ , the width is 100  $\mu\text{m}$ , and the thickness is 10  $\mu\text{m}$ .

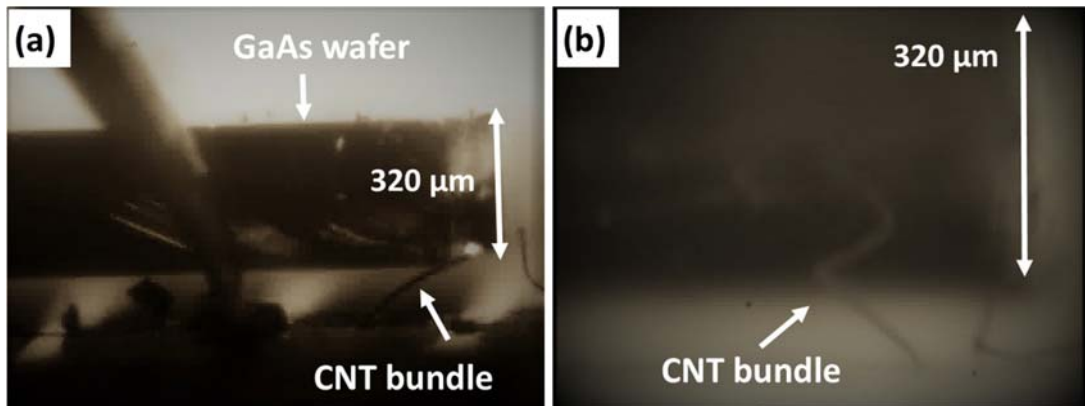


*Figure II.33 (a) Photograph of the side view of the CNT bundle at mechanical bending and (b) compression using home-built loading platform with a passivated GaAs wafer [110].*



Figure II.33 (b) shows the photograph of the side view of the CNT bundle at mechanical compression. A repeatable stable compression of the CNT bundle could be achieved without mechanical deformation. The 3D AHCTS was also compressed using the home-built loading platform with passivated GaAs wafer. The height of the CNT block is 1200  $\mu\text{m}$ , the width is 20  $\mu\text{m}$ , and the thickness is 20  $\mu\text{m}$ .

Schematic of the working principle of AHCTS sensor is provided in figure II.34. Mechanical deformation of the main bundle by applying a lateral force is shown in figure II.34 (a). Individual CNTs in the main CNT bundle touch the neighboring CNTs in this bundle. The main CNT bundle contacts the neighboring smaller CNT bundle (figure II.34(b)). Both mechanisms cause enhanced lateral cross-tube contacts, resulting in an increase in the electrical conductance to the macroscopic outer contacts.

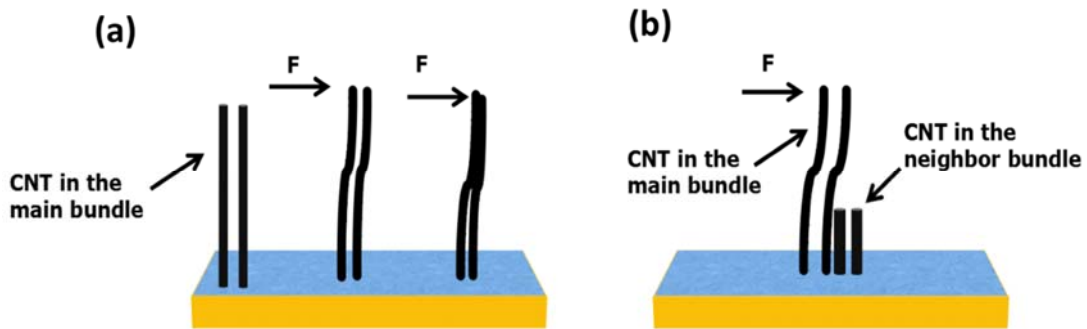


Figure II.34 Schematic of the working principle of the AHCTS sensor element. (a) under the mechanical deformation, individual CNTs in the main CNT bundle touch the neighboring CNTs in this bundle and (b) the main CNT bundle contacts the neighboring smaller CNT bundle.

A schematic of the AHCTS under loading is provided in figure II.35 (a). The nano and micro parts of the AHCTSs is connected using the Ni pads on the Si wafer. The home built loading platform uses a needle with micropositioner to measure the deflection of the CNT bundle. The displacement resolution of the micropositioner in current platform was limited to 5  $\mu\text{m}$ . The height, width and thickness of the CNT bundles used to record the resistance–deflection curves are 500, 350  $\mu\text{m}$  and 100  $\mu\text{m}$  respectively. The change in the resistance of the electrically contacted AHCTS under mechanical deformation is provided in figure II.35 (b and c). The AHCTS device shows a piezoresistivity by applying a lateral force. Mechanical deformation of the main CNT bundle decreases the lateral CNT bundle resistance. The close contact between the individual CNTs inside the lateral bundle as well as the CNT/CNT contact near to the bottom of the substrate decreases the resistance of the central CNT bundles and smaller neighbouring CNT bundles. Mechanical

deformation decreases the lateral as well as vertical resistance of the CNT sensor. The resistance decreases almost linearly with respect to the deformation. The resistance decreases about 11% at 50 $\mu\text{m}$  deflection and 20% at 30 $\mu\text{m}$  compression. There is a significant decrease in the resistance by the application of different forces. AHCTS design also works with one electrode on the Si substrate and the second electrode on the main CNT bundle. For the new design, the change in the resistance of the electrically contacted AHCTS under compression is provided in figure II.35 (d). Though the integration process is more difficult compared to the other design, the huge resistance change of  $\sim 30\%$  at 40  $\mu\text{m}$  deflection is impressive for the AHCTS. The sensor characteristics and sensitivity explicitly depends on the initial resistance of the single sensor element. The overall resistance of the fabricated AHCTS depends on the contacting dimensions, CNT dimensions and the graphitization of the CNT defined mainly by the growth conditions, like tube diameter. Resistances varies from 200  $\Omega$  to  $>2\text{ k}\Omega$  have been observed and these variation may be due to above mentioned parameters. Weaker contact of the neighboring CNT bundles is also a reason for the high initial resistance. The resistance decreases because of the additionally created current paths at an applied pressure. These lead to higher sensitivity to external mechanical stresses.

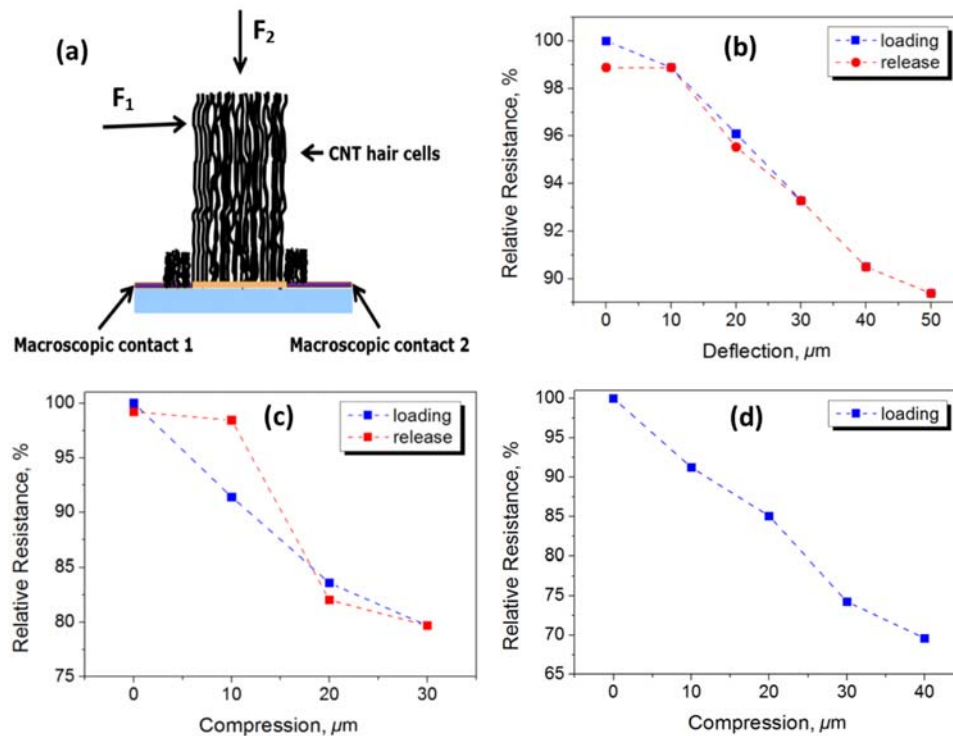


Figure II. 35 (a) A schematic of the AHCTS loading, (b) The lateral resistance change between both macroscopic contacts at lateral force  $F_1$ , (c) vertical force  $F_2$  and (d) The vertical resistance change between an outer electrode on the Si wafer and a second outer electrode on the main CNT bundle with a vertical force of  $F_2$ <sup>[110]</sup>.

### Electrostatic characterization

Figure II.36 (a) represents the schematic for the electromechanical bending of a single CNT bundle by a contactless, electrostatic method. The 3D AHCTS was deflected with a home-built loading platform using a passivated GaAs wafer. Figure II.36 (b) shows the photograph of the electromechanical bending of a long CNT bundle (length,  $l = 680 \mu\text{m}$ ). CNT bundle was deflected about  $100 \mu\text{m}$  at 2 kHz and it was mechanically stable after several hours. Stable and repeatable deflections were observed more than 10 million times. Electrostatic deflection at CNT bundle (length= $300 \mu\text{m}$ , width= $100 \mu\text{m}$  and thickness= $10 \mu\text{m}$ ) at  $f = 10 \text{ Hz}$  is shown in figure II.36 (c and d). Stable and repeatable deflections were measured.

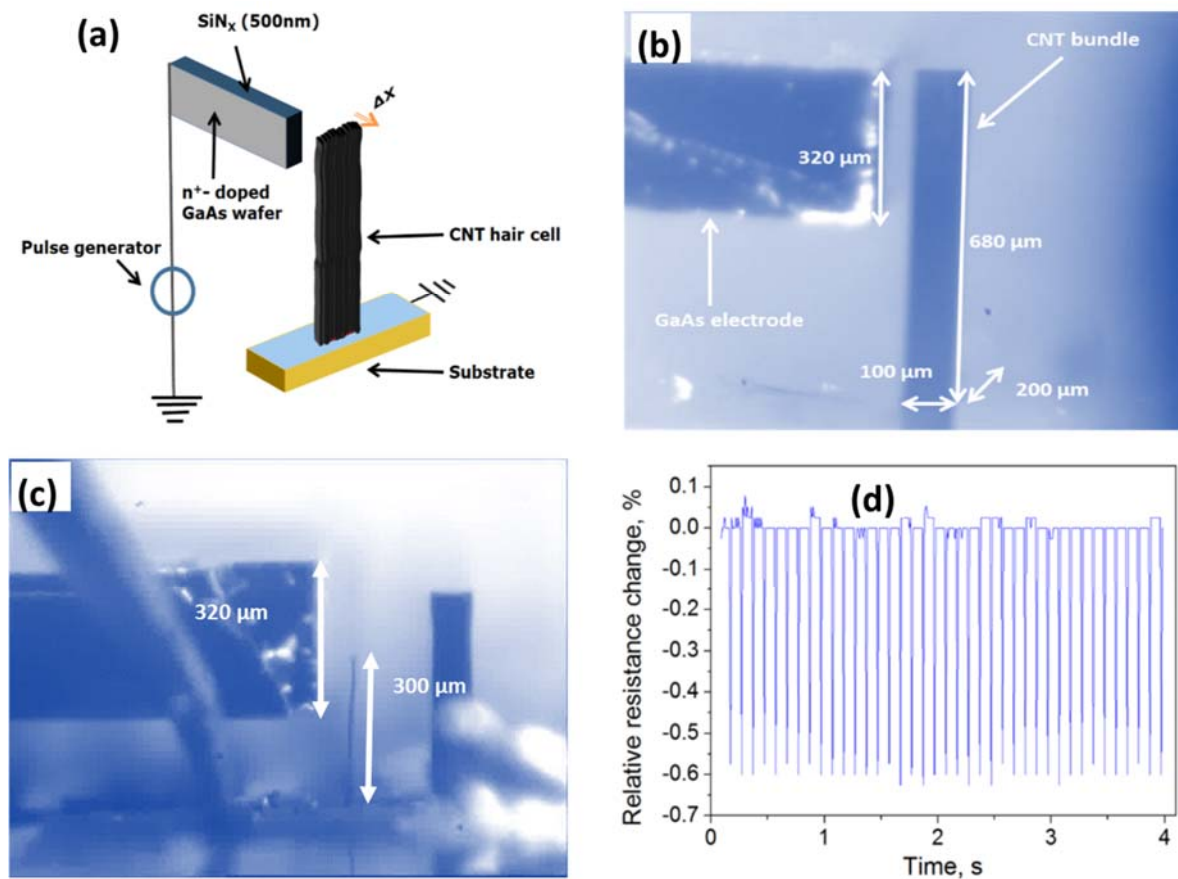
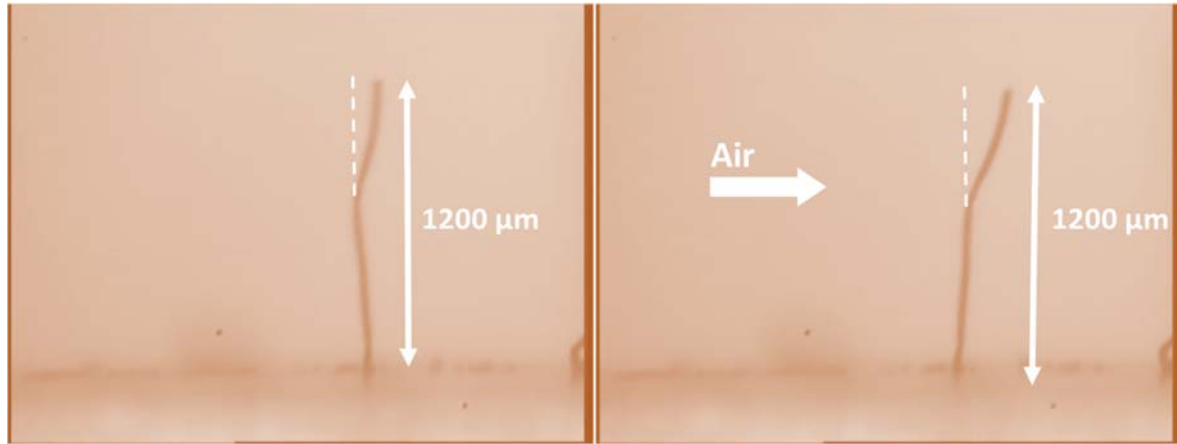


Figure II.36 The electrostatic measurements of the laterally contacted AHCTS under mechanical deformation. (a) schematic, (b, c) photograph of the contactless AHCTS loading and (d) resistance change between both lateral macroscopic contacts at 10 Hz for the CNT bundle (length= $300 \mu\text{m}$ , width= $100 \mu\text{m}$  and thickness= $10 \mu\text{m}$ )<sup>[110]</sup>

The dynamic resistance change of the CNT bundle ( $l = 300 \mu\text{m}$ ,  $w = 100 \mu\text{m}$ ,  $t = 10 \mu\text{m}$ ) was measured at 10 Hz (pulse period of 100 ms and a pulse width of 10 ms). The observed resistance change is

displayed in figure II.36 (d). The sensor showed a relative resistance change about 0.6% for a deflection of  $\sim 30 \mu\text{m}$ . Excellent repeatability is observed in the resistance change. The results shows the suitability of AHCTS to simulate multiple functions. This sensor can be used even in kHz region due to its small response/recovery time.

The bending and stability of the CNT bundle ( $l=1200 \mu\text{m}$ ,  $w=20 \mu\text{m}$ ,  $t=20 \mu\text{m}$ ) is observed under air flow (Figure II.37). Stable and repeatable deflections were measured.



*Figure II.37 Photograph of the side view of the CNT block deflected at weak air flow. The height of the CNT block is  $1200 \mu\text{m}$ , the width  $20 \mu\text{m}$ , and the thickness  $20 \mu\text{m}$  [110].*

## II.6 Conclusions

Vertically aligned carbon nanotubes are synthesized using water assisted chemical vapor deposition technique. Al/Al<sub>2</sub>O<sub>3</sub> and iron was used as the catalyst. CVD parameters are optimized for the growth of less defective VACNTs with diameter of the order of 3-6 nm. Height of the CNTs could be varied by changing the gas flow, time of synthesis and catalyst thickness. Absence of catalyst impurities were confirmed using thermogravimetric analysis and TEM.

Three dimensional microelectrodes based on vertically aligned carbon nanotubes are fabricated. These electrodes show high electrochemical active surface area, capacity and low impedance hence this could be useful in variety of sensor applications.

One dimensional structures such as randomly oriented CNTs and vertically aligned CNTs are used as the substrate for the growth of neurons. Growth of neurons dominant on side walls of the vertically aligned CNTs than on the top.

Artificial-hair-cell-type sensor (AHCTS) based on 3D structured vertically aligned carbon nanotube bundles was fabricated using chemical vapor deposition process. Their easy integration and lateral

---

electrical contacting allowed multiple mechano-electrical sensing mechanisms. The mechanical properties of the CNT bundles were investigated with respect to different substrates as well as by tuning the bundle height. More over the compression or deflection of the central CNT bundle changes the contact resistance to the shorter neighbouring bundles hence this 3D CNT sensor can detects three dimensional forces. Their easy integration and lateral electrical contacting allowed multiple mechano-electrical sensing mechanisms. The Young's modulus of the AHCTS is in between 220 kPa and 1800 kPa, which was achieved by tuning the height of the CNT bundles. The resistance decreases up to  $\sim 11\%$  at 50  $\mu\text{m}$  deflection and the detection sensitivity is as low as 1  $\mu\text{m}$ , by employing a variable load system using Frey filaments. Bending of up to 90  $^\circ$  with excellent repeatability and stability were observed. A stable deflection of AHCTS in contactless electrostatic method was observed for 10 million times. Application of AHCTS in artificial hearing technology is very promising.

---

### III SYNTHESIS, CHARACTERIZATIONS AND APPLICATIONS OF GRAPHENE OXIDE

This chapter deal with the synthesis, characterization and applications of graphene oxide.

#### III.1 Introduction

The concept of graphene was first proposed by Wallace in 1947 [260]. He used tight-binding model to study the electronic properties of graphene. The study of graphene over the previous decades has remained at theory level until 1962 when Boehm et al. synthesized few layer graphite oxide at Eduard Zintl Institute, Technical University Darmstadt and he presented the results at the Carbon Conference in Penn State University and published in germany<sup>[261-262]</sup>. Later, in 2004 Novoselov from the University of Manchester separated single graphene from graphite using a simple mechanical peeling method [263]. The physicochemical properties exhibited by graphene have attracted a substantial attention in various areas of science and technology. Graphene, one atom thick two-dimensional crystal is considered as a basic building block for all  $sp^2$  graphitic materials such as carbon nanotubes, fullerenes, and graphite. It has unique characteristics such as high electron transport capabilities, high specific surface area and high thermal conductivity. Graphene must be fabricated in order to turn graphene applications into reality. Graphene also can be obtained from graphene oxide through Brodie Method [264], Staudenmaier Method [265], Hummers' Method [266] and its modification [267] namely the Tour's Method [268] and a Microwave-assisted acid technique [269] (figure III.1).

Graphene oxide attracts interest due to the ease of access, scalability, low cost and the ease of converting to graphene. Graphene oxide is formed by the oxidation of the graphite. The interplanar spacing between the graphite layers increase during oxidation. The oxidized graphene sheets during graphene oxide preparation possess some defects which are subject to the additive quantities of the oxidant as well as the oxidizing time. The conductivity characteristics of graphene oxide depend on the amount of oxidization in the compound and the synthesis method too. Highly oxidized graphene oxide is a poor conductor of electricity. This scenario can be addressed by functionalization which entails a chemical modification of a substance that leads to development of its characteristics to conform to a specific application. The main properties altered by this process are dispersibility, hygroscopicity and toxicity. The electrical properties of graphene oxide are fundamentally altered by the functionalization process. Functionalization results to more adaptable chemically modified graphene which could have limitless range of applications [270].

Graphene oxide (GO) can be synthesized with cost-effective procedures using less costly graphite as raw material that would result to high yields. Also, GO is highly hydrophilic and is capable of

forming stable aqueous colloids which enable the collection of macroscopic structures through cheap and simple solution processes. All these are vital for the large-scale use of graphene. The properties of graphene and its structure are restored when graphene oxide is reduced and different reduction techniques result to graphene with different properties [271].

### III.2 Preparation of graphene oxide

Graphite is the precursor for the preparation of GO. Graphite consists of granules that can be obtained from both natural and synthetic sources. The natural graphite is commonly used in chemical modifications due to the presence of numerous localized defects in its  $\pi$ -structure which provide seeding points for the chemical processes to take place [272]. Figure III.1 is the schematic representation for different methods of preparation of graphene oxide. The selection of the suitable oxidizing agents for oxidizing the graphite powder is the critical point in the preparation of graphene oxide.

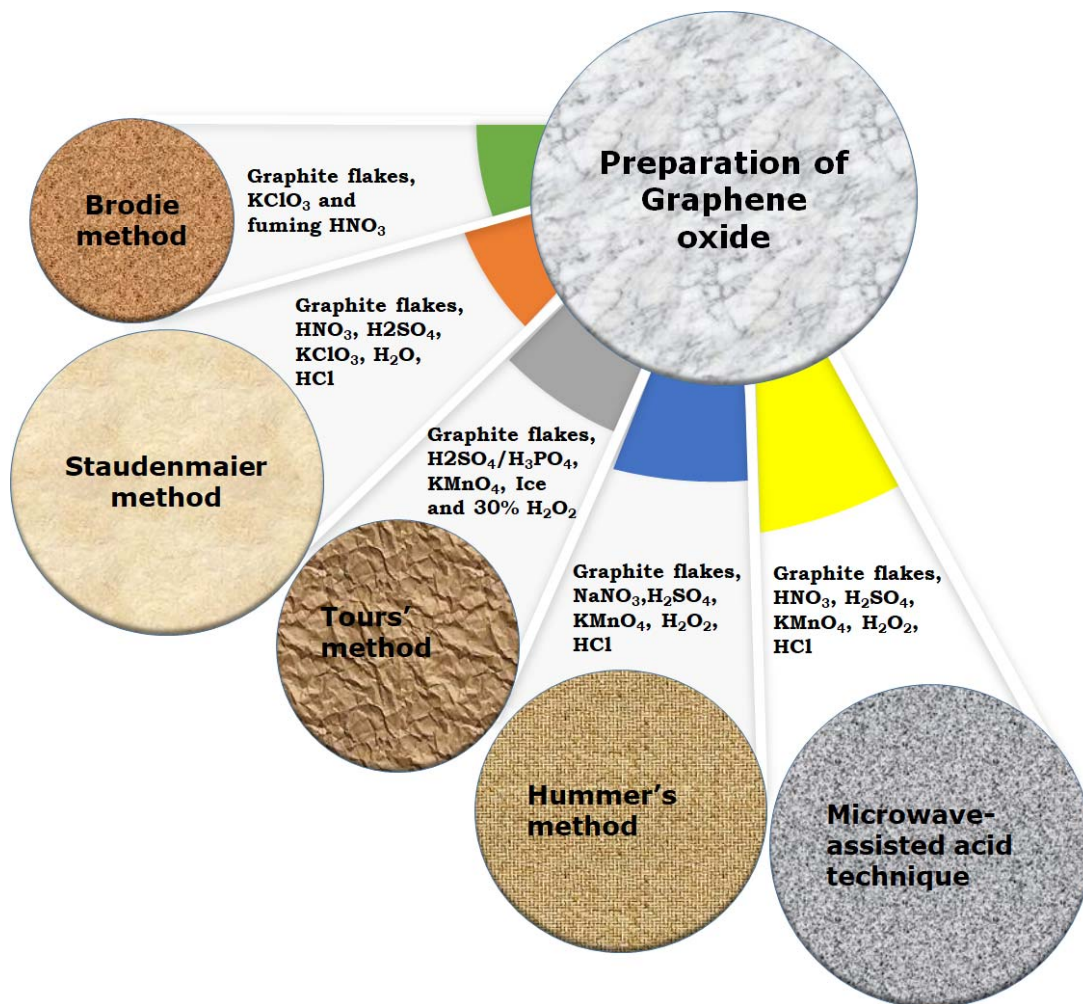


Figure III.1 Schematic of overview of preparation of graphene oxide.

### ***Brodie method***

This method was first tried by Brodie in 1859. Fuming nitric acid was added to a mixture of chlorate of potash and graphite. The percentage of carbon, hydrogen and oxygen in the oxidized product is 67.79, 1.84 and 30.37 respectively [264].

### ***Staudenmaier method***

This was a modification of the Brodie method. Here, concentrated  $H_2SO_4$  and fuming  $HNO_3$  was used as the oxidizing agents. Graphite was added to the mixture of concentrated nitric acid and sulphuric acid. Then potassium chlorate was added slowly and carefully to the mixture [265].

### ***Hummers' method***

Hummer's method was a relatively safe method of preparing graphite oxide. Graphite is oxidized using  $NaNO_3$ ,  $H_2SO_4$  and  $KMnO_4$ . The experiment was carried in a ice bath.  $KMnO_4$  was added slowly to maintain the temperature below  $15\text{ }^\circ\text{C}$ . This process could be completed within 2 hours and the temperature maintained was below  $45\text{ }^\circ\text{C}$ . [266]. A modified Hummers' method entails both oxidation of graphite and exfoliation of graphene sheets as a result of the thermal treatment of the solution [273].

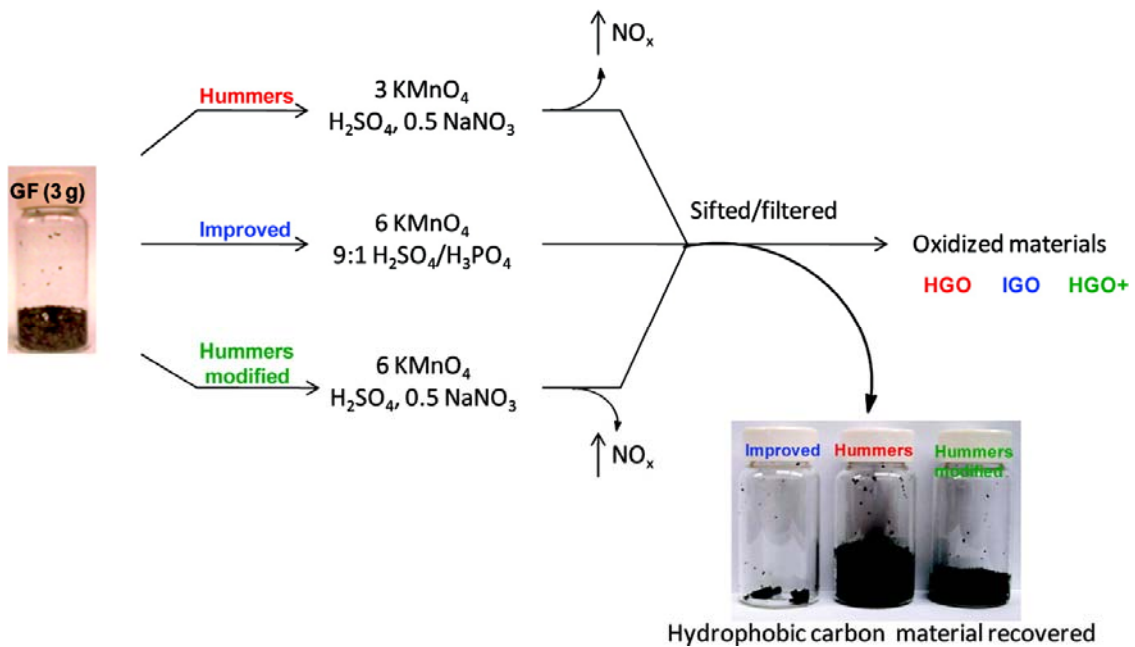


Figure III.2. Schematic representation of the oxidation of the graphite using Hummers method, Hummers modified method and improved graphene oxide synthesis method (Tour's method) [268].



---

### ***Tour's method***

This is also an improved version of Hummer's method for preparing graphene oxide. Concentrated  $\text{H}_2\text{SO}_4/\text{H}_3\text{PO}_4$  are slowly added to a mixture of graphite powder and  $\text{KMnO}_4$  [268]. Schematic representation of synthesis of graphene oxide by the oxidation of the graphite using Hummers' method, Hummers' modified method and improved graphene oxide synthesis method (the Tour's method) is shown in figure III.2

### ***Microwave-assisted acid technique***

Graphene oxide can also be prepared in acidic condition using microwave irradiation. Microwave heating replaces the traditional heating used in the Hummer's method. Natural graphite powder is mixed with  $\text{KMnO}_4$  and fuming nitric acid and the resulting mixture is magnetically stirred in a flask made of glass at room temperature. The acidic dispersion is moved to a crucible and then irradiated with microwave at a power of about 900 W for a minute. Deionized water is then used to rinse the resultant powder until it achieves a pH of 7. It is then dried at a temperature of  $110\text{ }^\circ\text{C}$  for three hours to produce expanded graphite. Conc.  $\text{H}_2\text{SO}_4$  and  $\text{KMnO}_4$  are then added to the expanded graphite for oxidation and exfoliation to take place. A green dispersion results from magnetic stirring of the mixture after half an hour. The mixture is then washed with deionized water and 10% hydrochloric acid until the pH become neutral and the resultant product is brown in colour. Graphene oxide films are obtained upon complete evaporation of water [269].

### **III.3 Reduction of graphene oxide**

Reduction of graphene oxide to reduced graphene oxide (rGO) is a key step process as it determines the quality of the rGO produced in terms of properties. Various methods of producing reduced graphene oxide from graphene oxide are chemical reduction, thermal reduction, photocatalytic reduction, electrochemical reduction, glow discharge plasma reduction and reduction based on nature-based reducing agents, which are summarized in figure III.3.

#### ***Thermal reduction***

This process is rather referred to as thermal annealing for reduction of graphene oxide. Exfoliation process is done by sudden expansion of carbon monoxide or carbon dioxide through the spaces of graphene sheets. The temperatures associated with this method are too high to decompose the oxygen-containing functional groups present in the carbon plane to liberate gases which then create

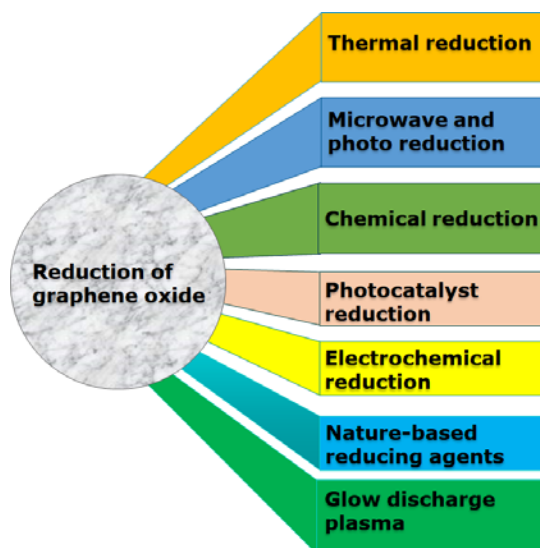


*Figure III.3 Schematic representation of reduction of graphene oxide by various reduction processes.*

enormous pressure between the piled layers. A pressure of 2.5 MPa can separate two stacked platelets of graphene oxide <sup>[274]</sup>. This thermal reduction method reduces the functionalized graphene sheets and exfoliates graphene oxide <sup>[270]</sup>. This method is a reliable one in manufacturing bulk quantities of graphene compared to the methods for production of small-sized and wrinkled sheets of graphene. In this process, the carbon atoms are removed from the carbon plane while removing the oxygen-containing groups, hence the sheets of graphene split into small pieces and the final product is with distorted carbon plane. The lattice defects in the exfoliation process of graphene oxide affects the electronic properties of the final product and hence reducing the ballistic transport path length and also bringing in the effect of scattering centers. According to Schniepp et al. <sup>[270]</sup>, C/O ratio of graphite oxide is significantly depends on the reduction temperature, which is 13 at 750 °C and 7 at 500 °C. The annealing reduction of graphene oxide is conducted either in vacuum <sup>[275]</sup> or in an inert atmosphere <sup>[276]</sup> at high temperatures. The drawback for using high temperatures is that large energy is consumed and the conditions of treatment are critical. Also, high temperatures can lead to the explosion of graphene oxide due to structure assembling. Slow heating in thermal reduction of graphene oxide makes this process to be time-consuming. For the applications which assemble graphene oxide on substrates such as carbon films, this method cannot work especially with the substrates with lower melting point like polymers and glass <sup>[271]</sup>.

### ***Microwave and photo reduction***

Microwave irradiation was devised for uniform and rapid heating of substrate. Within one minute in ambient conditions, reduced GO can produce from graphite oxide powders in a microwave oven

---

[277]. A single flash from a xenon lamp (<1cm) similar to the flashes on a camera was used to reduce free-standing films of graphite oxide by Cote et al. Rapid degassing by flash reduction expands the graphite oxide films about ten times faster. Elemental analysis says that the C/O atomic ratio in GO was 1.15 and that for flash-reduced GO was 4.23. The measured electrical conductivity of flash reduced GO films was about 1000 S/m [278] and density of flash reduced GO films was about 0.14 g/cm<sup>3</sup>. Zhang et al. [279] fabricated and patterned films of graphene oxide using femtosecond laser irradiation. The focused laser beam comprised of 120 fs pulse width, 790 nm central wave length, focused X100 objective lens and 80 MHz repetition rate. The rGO produced by this laser reduction method have highest conductivity of  $2.56 \times 10^4$  S/m.

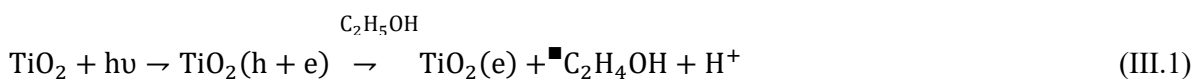
### ***Chemical reduction***

Large lateral sheets of graphene can be produced alternatively through exfoliation of graphene oxide in liquid phase. Chemical reduction of graphene oxide can be achieved through either moderate heating or at room temperature, making it a cheaper and readily available method of preparing bulk graphene quantity compared to thermal annealing method [271]. Stankovich et al. [280-281] used dimethylhydrazine and hydrazine hydrate to reduce graphite oxide by adding them to aqueous dispersion of graphite oxide. This method results agglomerated graphene-based nanosheets due to the increase of hydrophobicity. Hydrazine reduced GO shows an increased C/O ratio of about 10.3 compared to the C/O ratio of pure GO (2.7) [280]. Soluble polymers [282] are added as surfactant to retain the colloidal state of graphene oxide in water or ammonia [283] for changing the charge states of the reduced GO sheets. Simple processes like filtration can then be used to assemble the macroscopic structures in the suspended graphene sheets in the colloidal solutions [283]. Other effective and strong reducing agents of GO are metal hydrides such as aluminium hydride, sodium hydride and sodium borohydride (NaBH<sub>4</sub>). Gao et al. [284] proposed two step reduction process for reducing graphite oxide. He used concentrated sulfuric acid at a temperature of about 180 °C for dehydration after the process of deoxygenation by sodium borohydride. Fernandez-Merino et al. reported ascorbic acid as an ideal substitute for hydrazine in GO reduction process. The C/O ratio of ascorbic acid reduced GO is about 12.5 and the electrical conductivity is about 7700 S/m [285]. Other inferior reductants used for GO reduction are pyrogallol [285], hydroquinone [286], hydroxylamine [287], hot strong alkaline solutions [288].

### ***Photocatalyst reduction***

Photo-chemical reactions can be used to reduce GO through the assistance of a photocatalyst such as TiO<sub>2</sub>. Williams et al. [289] reported successful experiment of reducing graphene oxide in colloidal

state using the assistance of TiO<sub>2</sub> particles under Ultra Violet irradiation. As the reduction of GO proceeds, the color of the substance changes from light brown to dark brown to black. It has been suggested that this change in colour is a partial restoration of the  $\pi$  network in the plane of the carbon material same as in the chemical reduction process. Upon Ultraviolet irradiation, a charge separation takes place on the surfaces of the TiO<sub>2</sub> particles. Ethoxy radicals are produced in the presence of ethanol which leaves the electrons to assemble within the TiO<sub>2</sub> particles, which then interact with the graphene oxide sheets to reduce the functional groups. Through charge transfer, the hydroxyl groups can interact with carboxyl groups in the graphene oxide sheets on the surface of the TiO<sub>2</sub> particles, producing a hybrid between the two substances which can be retained after the reduction process. Some photovoltaic devices can separate electron pairs when the process is facilitated by the current collected by the rGO sheets such as dye-sensitized solar cell and photocatalysis device.



Other materials like BiVO<sub>4</sub> [290] and ZnO [291] have photocatalytic effect and have been found to achieve the process of GO reduction.

### ***Electrochemical reduction***

This method relies on removal of the oxygen functionalities electrochemically [292]. A normal three electrode electrochemical cell and aqueous buffer solution of GO at room temperature is used in the experiment. The exchange of electrons between the GO and the electrodes forms the basis of the reduction process. This method is advantageous in a way that it avoids the use of dangerous reductants such as hydrazine and its byproducts. Ramesh et al. carried reduction of GO in potassium nitrate solution using the cyclic voltammetry. The potential was scanned from 0 to -1 V with respect to a saturated calomel electrode and the scan rate maintained was 10 mV/s. The peak at -0.75 indicates reduction of GO. The resultant process is electrochemically irreversible [292]. Graphene oxide could also be reduced electrophoretic deposition at the anode which counteracts the notion that oxidation only takes place at the anode in an electrolysis cell [293].

### ***Nature-based reducing agents***

Natural antioxidants such as vitamins, amino acids and organic acids, monosaccharides such as fructose and glucose have been found to be effective reducing agents of GO due to their mild reactive

characteristic and non-toxic property. Sugars in aqueous ammonia solution acts as a good reducing agents and the ammonia acts as synergistic enhancer in the reaction rate of GO deoxygenation [294].

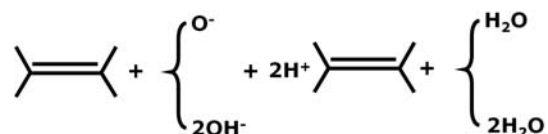
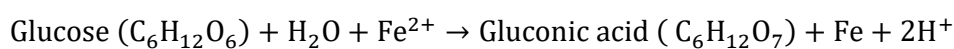
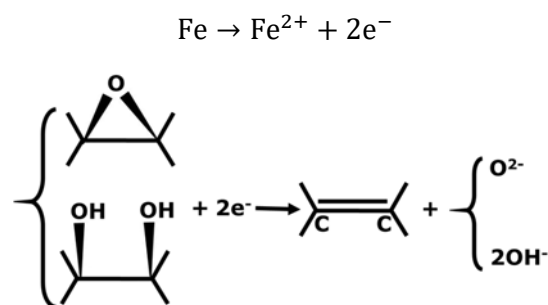


Figure III.4 Steps involved in reduction of GO using Fe foil and glucose [295].

Iron foil with glucose under neutral conditions act as a photocatalyst, which can be used to reduce GO. Fe transfers electrons to the GO and become  $\text{Fe}^{2+}$  ions. Electrons transfers to GO. Steps involved in reduction of GO using Fe foil and glucose is shown in figure III.4

Amino acids such as *L*-Cysteine, Glycine and *L*-Lysine are also natural antioxidants which can be used in the reduction of GO. *L*-Cysteine is insoluble in water and alcohol, it has thiols that can undergo redox reaction. However, the obtained reduced GO has low electrical conductivity. Glycine acts as a chemical functionalizer and effectively reduces GO to reduced GO after a span of 36 hours. *L*-Lysine works in the presence of carboxymethyl starch which acts as a stabilizer to produce reduced GO with good dispersion stability and a high C/O ratio of about 8.5. Li et al. [296] used gallic acid to reduce GO and asserted that the pyrogallol moiety (the three hydroxyl groups) in the acid induces the reduction process. Micro-organisms, hormones, proteins and peptides are also good reducing agents. For instance, Liu et al. [297] prepared bovine serum albumin (BSA)-conjugated GO and reduced GO. BSA is a protein derived from cow. Proteins have hydrophilic and hydrophobic patches in their surfaces and can well adhere to other solid surfaces making BSA a good reducing agent and stabilizer. The resultant complexes of conjugates depend on temperature and PH supplied. A schematic of decoration of BSA on GO and reduction of GO using BSA is shown in figure III.5

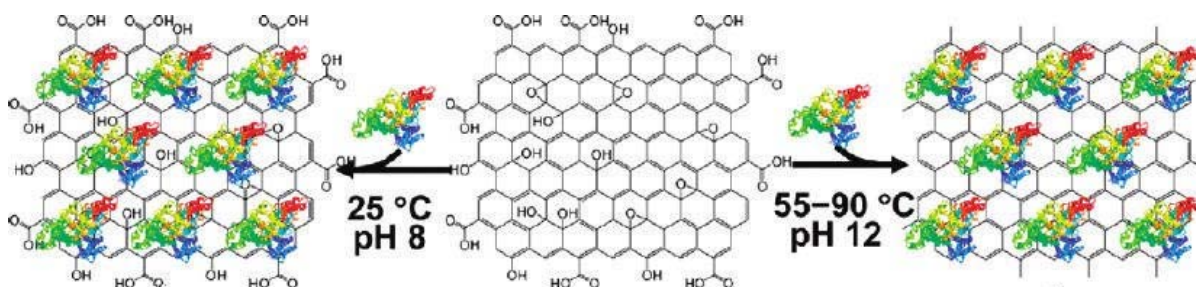


Figure III.5 BSA decoration and reduction of GO [297].

### ***Glow discharge plasma***

In this method, a glow discharge is produced and maintained between two parallel plates of graphite electrodes at a pressure of about 240 mTorr. GO is reduced by exposing it at the junction of negative-glow and Faraday-dark area for about four minutes. This is an ecofriendly and low cost method for the production of graphene in large scale. However, the direct bombardment of energetic ions in plasma removes the oxygen containing functional groups and damages the surface [298].

### **III.4 Applications of graphene oxide**

Graphene oxide and reduced graphene oxide has been widely applied in electronic devices [299-300]. Graphene thin film field effect transistors are fabricated using big size graphene oxide sheets by Wang et al.. This device shows an intrinsic carrier mobility of 5000 cm<sup>2</sup>/ (V.s). Large size GO could maintain the intrinsic structural cohesion and two-dimensional delocalized  $\pi$ -electron network needed for a functional high mobility transistor [299]. Robinson et al. used reduced graphene oxide as electrode material in high performance molecular sensor. This sensor is capable to detect chemical-warfare agents and an explosive at parts-per-billion concentrations [301]. Figure III.6 (a) shows the optical microscope image of the GO film spin casted on Si/SiO<sub>2</sub> substrate. Figure III.6 (b, c) shows the AFM images of the GO platelets film and boundary of a GO film photolithographically. Figure III.6 (d) shows the OM image showing GO film device with interdigitated Ti/Au contacts. Cai et al. [302] fabricated reduced graphene oxide based field effect transistor for biosensing. Graphene oxide is also applied in plasmonics [303-304] and metamaterials [305]. GO films are reported as better lubricant for silicon based MEMS/NEMS device [306]. Graphene oxide based nanofluids are used as coolant in nuclear reactors [307]. Graphene oxide is used as catalyst support for fuel cell [308], electrodes for supercapacitor [309-310] and batteries [311] due to their high surface area.

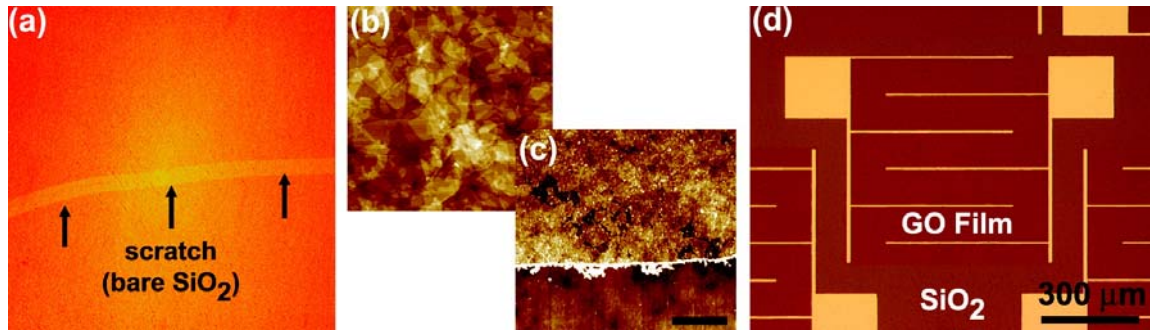


Figure III.6 (a) Optical microscope image of the (20X) showing a uniform graphite oxide film deposited via spin-casting on a 250 nm SiO<sub>2</sub>/Si substrate, (b) Atomic force microscopy (AFM) image of single overlapping GO platelets film. Platelet thickness is quantized at ~1 nm, (c) AFM image of boundary of a GO film after photolithographically processing devices from the film ( $z = 6$  nm, scale bar = 1  $\mu$ m), (d) OM image showing an electrically isolated GO device with interdigitated Ti/Au contacts [301].

Graphene oxide thinfilm was used as hole transport and electron blocking layer in organic photovoltaic cell [312-313]. A schematic of the graphene oxide based organic photovoltaic cell is shown in figure III.7 (a). The band energies of the ITO, P3HT:PCBM, and Al layers are shown in figure III.7(b). The higher work function values for GO is due to the larger electronegativity of oxygen atoms, which produce surface C<sup>δ+</sup>-O<sup>δ-</sup> dipoles *via* extraction of  $\pi$  electrons from graphene [313].

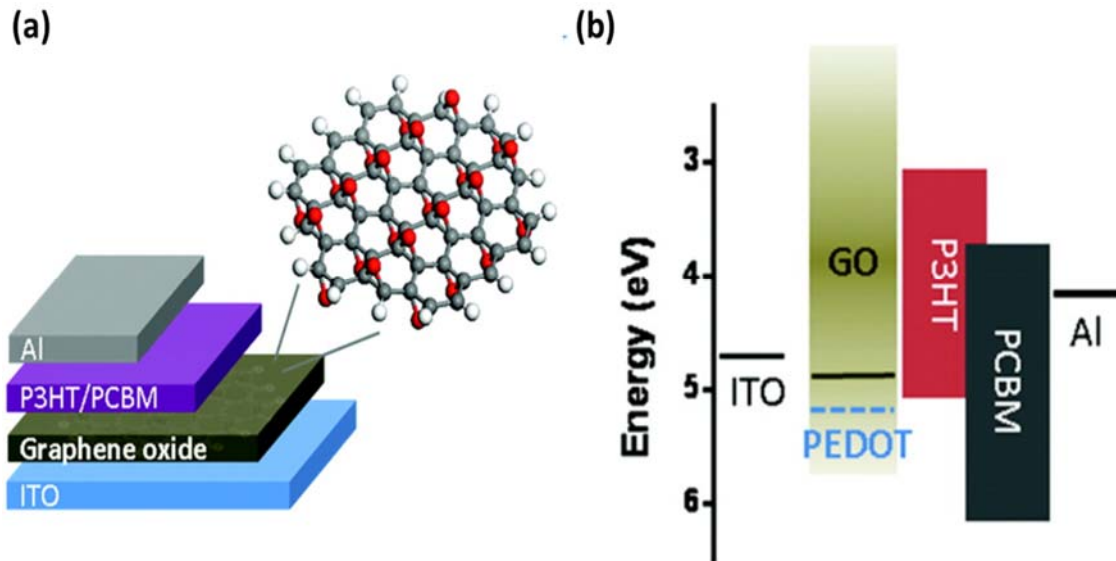


Figure III.7 (a) Schematic of the photovoltaic device structure consisting of ITO/GO/P3HT:PCBM/Al. (b) Energy level diagrams of the bottom electrode ITO, interlayer materials (PEDOT:PSS, GO), P3HT (donor), and PCBM (acceptor), and the top electrode Al [313].

GO has been used as a drug nanocarrier for the loading of a variety therapeutics, including anti-cancer drugs, poorly soluble drugs, antibiotics, antibodies, peptides, DNA, RNA and genes. [314]. Kim et al. reported that the GO modified with polyethylenimine as efficient gene delivery vector. Moreover this material could be used for bioimaging [315]. A schematic of the branched polyethylenimine-GO (BPEI-GO) hybrid material for the delivery of pDNA is shown in figure III.8. GO was used for combined therapy owing to its unique properties. Zhang et al. developed PEI-GO for the codelivery of siRNA and DOX to treat Hela cells, which shows significantly improved chemotherapy efficiency [316].

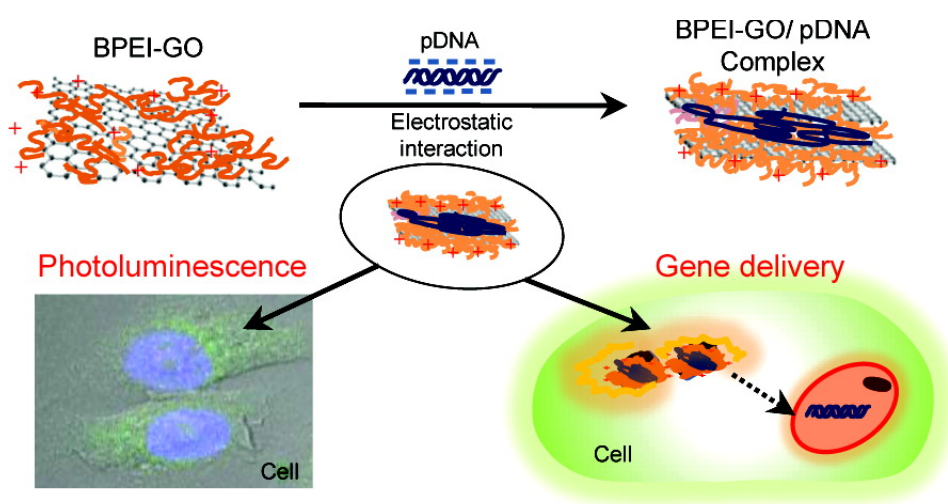


Figure III.8. Schematic of the delivery of (a) pDNA using BPEI-GO hybrid material. [315]

GO incorporated membranes are widely used for water purification and desalination [317]. Abram et al. reported tunable ion sieving using graphene oxide membranes [318], which shows 97% rejection of NaCl. A schematic representation of permeation of water and ion in the laminar direction is shown in figure III.9 (a). A photograph of the physically confined GO (PCGO) is shown in figure III.9 (b), An optical microscope image of the stacked GO laminates embedded in epoxy is shown in figure III.9 (c). Scanning electron microscopy image of the trimmed PCGO membrane is shown in figure III.9 (d). GO-polymer nanocomposites are used for bone tissue engineering application by Unnithan et al. [319]. Wan et al. used graphene oxide and cellulose hybrid aerogel for electromagnetic interference shielding. Graphene oxide binds to SO<sub>2</sub> by the means of physisorption ( $\Delta H_{ads} = 18.04 \text{ kJ mol}^{-1}$ ) [320]. Because of the layered nature of graphene oxide as well as the micropores, it promotes the conversion of SO<sub>2</sub> to SO<sub>3</sub> and this makes the graphene oxide to be good in physisorption.



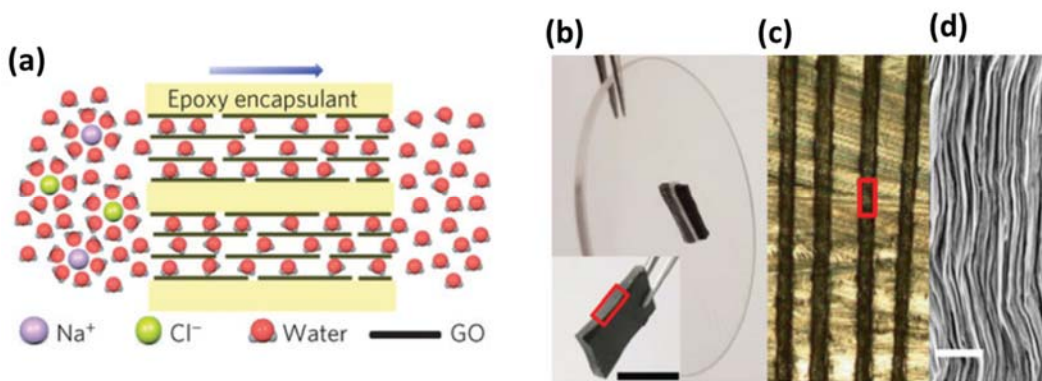


Figure III.9 (a) Schematic of the direction of ion/water permeation along graphene planes, (b) Photograph of a PCGO membrane glued into a rectangular slot within a plastic disk of 5 cm in diameter. Inset: photo of the PCGO stack before it was placed inside the slot (Scale bar, 5 mm), (c) Optical micrograph of the cross-sectional area marked by a red rectangle in figure (b), black represents 100- $\mu\text{m}$ -thick GO laminates embedded in epoxy. Epoxy is seen in light yellow with dark streaks because of surface scratches, (d) Scanning electron microscopy image from the marked region in figure (c) (Scale bar, 1  $\mu\text{m}$ )<sup>[318]</sup>.

### III.5 Results and discussion

Synthesis of graphene oxide (GO), exfoliated graphene oxide ( $\text{GO}_{\text{ex}}$ ) and reduced graphene oxide (rGO) is given in experimental section. Graphene oxide was reduced using hydrogen gas at different temperatures (200  $^{\circ}\text{C}$ -1000  $^{\circ}\text{C}$ ) and the obtained materials are named as rGO-200, rGO-400, rGO-600, rGO-800, rGO-1000. Also graphene oxide was exfoliated using liquid nitrogen and the material was named as  $\text{GO}_{\text{ex}}$ . Detailed discussion about characterization of GO,  $\text{GO}_{\text{ex}}$ , rGO-200, rGO-400, rGO-600, rGO-800 and rGO-1000 is provided in this section. Then application of bacterial cellulose and GO/rGO composites for water and oil separation is discussed.

X-ray diffraction measurement is carried out to investigate the crystallinity of the samples. XRD patterns have been recorded for graphite, GO,  $\text{GO}_{\text{ex}}$ , rGO-200, rGO-400, rGO-600, rGO-800, rGO-1000. Figure III.10 shows the X-ray diffraction pattern for graphite, GO, rGO-200, rGO-400, rGO-600, rGO-800, rGO-1000. The peak at  $2\theta \sim 26.5^{\circ}$  in graphite is attributed to the 002 plane of hexagonal graphite with a d spacing of 0.34 nm. This peak indicates the presence of long range order and crystalline nature of hexagonal graphite. When graphite is converted into GO, (002) peak shifted to  $13.16^{\circ}$ . No high intensity peaks are observed in  $\text{GO}_{\text{ex}}$ , rGO-200, rGO-400. The disappearance of the peak at  $2\theta \sim 26.5^{\circ}$  indicates the loss of long range order in  $\text{GO}_{\text{ex}}$ , rGO-200, rGO-400. The reappearance of the sharp peak at  $2\theta \sim 26.5^{\circ}$  in rGO-600, rGO-800, rGO-1000 indicates the restacking of graphene layers. Increase in crystallinity observed with increase in temperature.

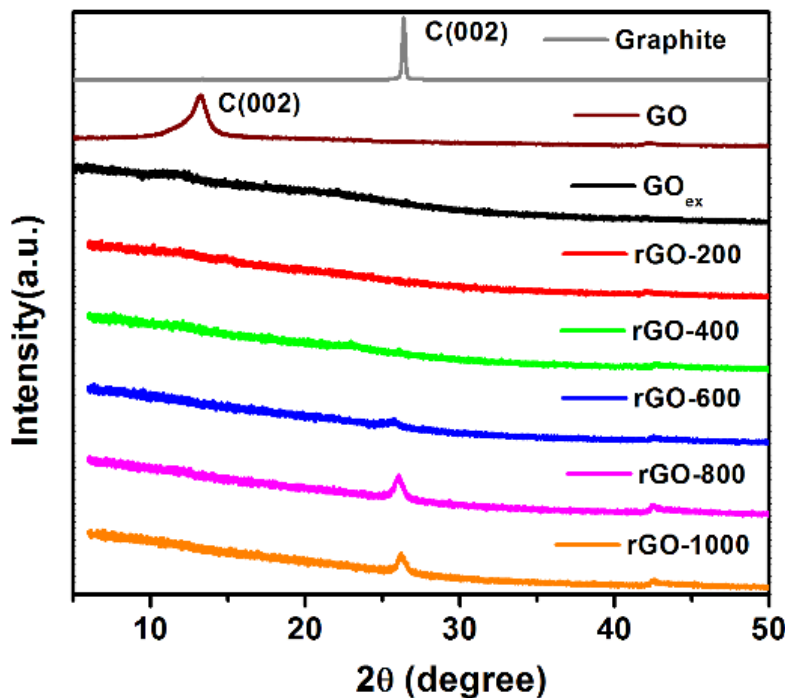


Figure III.10 X-ray diffraction patterns for graphite, GO, rGO-200, rGO-400, rGO-600, rGO-800 and rGO-1000.

Raman spectroscopy is a useful tool in characterizing molecular crystal structure, their disorder and defects in graphene oxide and reduced graphene oxide. It used to characterize graphene oxide from their other related graphene materials, other impurities or from graphene [321]. Figure III.11 shows the Raman spectra of graphite, GO, GO<sub>ex</sub>, rGO-200, rGO-400, rGO-600, rGO-800, rGO-1000 respectively. I<sub>D</sub>/I<sub>G</sub> ratio of the samples are provided in table III.1. The G peak which is observable at 1600 cm<sup>-1</sup> and 1599 cm<sup>-1</sup> for graphene oxide and reduced graphene oxide respectively. These peaks are due to scattering of first order E<sub>2g</sub> phonons of sp<sup>2</sup> C atoms. The GO spectrum of graphene oxide shows a nearly flat 2D region. The size of in-plane sp<sup>2</sup> domain affects the intensity of D band with more domains resulting to increase in the peak density. (I<sub>D</sub>/I<sub>G</sub>) is the relative intensity ratio and it's the measure of degree of disorder. It is affected by sp<sup>2</sup> clusters with the increase in clusters signifying decrease in the relative intensity ratio [321]. Defects can arise due to chemical or physical processes. Here the formation of the graphene oxide from which method affects the appearance of the spectrum. Chemically induced defects affect the 2D band with no appearance of peak in the spectrum for graphene oxide which is chemically converted from graphite [322]. This is due to highly functional groups intercalated between graphitic layers.

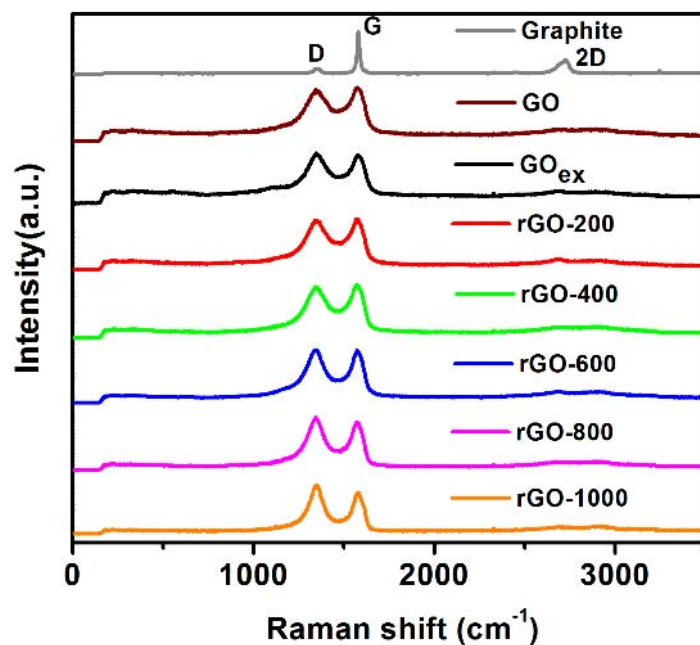


Figure III.11 Raman spectra for graphite, GO, rGO-200, rGO-400, rGO-600, rGO-800 and rGO-1000.

Table III.1  $I_D/I_G$  ratio estimated from Raman spectra of graphite, graphene oxide, exfoliated graphene oxide and reduced graphene oxide.

Sample	$I_D/I_G$
Graphite	0.136
GO	0.948
GO <sub>ex</sub>	1.0317
rGO-200	0.969
rGO-400	0.959
rGO-600	1.0165
rGO-800	1.0955
rGO-1000	1.1693

Figure III.12 shows the XPS survey spectra for GO, rGO-200, rGO-400, rGO-600, rGO-800, rGO-1000. The amount of carbon and oxygen estimated using the XPS survey spectrum of the above listed samples are provided in table III.2. The oxygen content was decreased when GO was converted to rGO. As the temperature of synthesis increased, oxygen concentration decreased in the case of rGO.

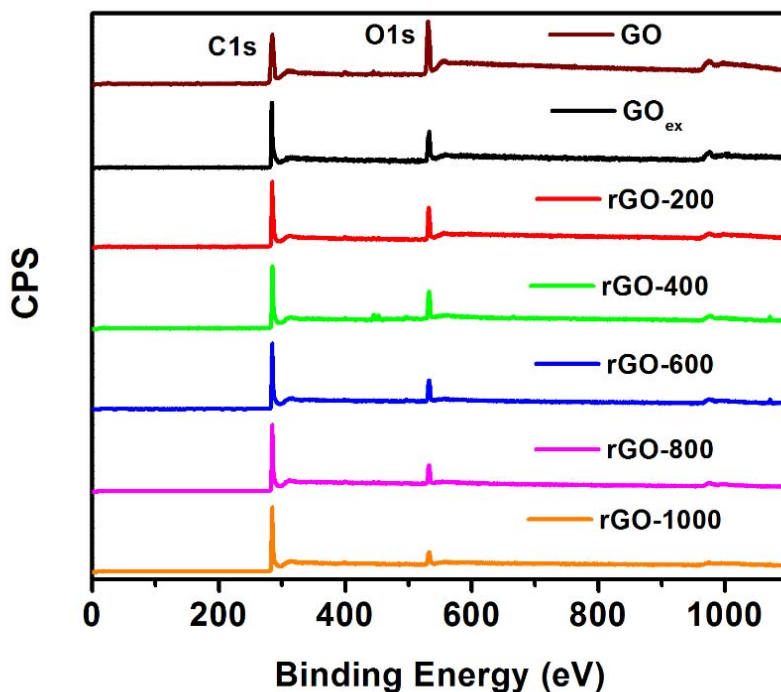


Figure III.12 XPS survey spectrum for GO, GO<sub>ex</sub>, rGO-200, rGO-400, rGO-600, rGO-800, rGO-1000.

Table III.2: Concentration of carbon and oxygen in graphene oxide, exfoliated graphene oxide and reduced graphene oxide.

Sample	At% of carbon	At% of oxygen
GO	67.293	32.307
GO <sub>ex</sub>	79.404	20.596
rGO-200	79.182	20.818
rGO-400	79.498	20.502
rGO-600	82.949	17.051
rGO-800	85.572	14.428
rGO-1000	87.636	12.364

Figure III.13 shows the deconvoluted high resolution C1s spectra for GO, rGO-200, rGO-400, rGO-600, rGO-1000. Peaks are fitted to a Gaussian-Lorentzian shape after performing Shirley background correction [323]. The deconvoluted C1s spectrum contains five peaks which are attributed to sp<sup>3</sup>C, sp<sup>2</sup>C, C-O, C=O, COOH and π-π\* transitions [324]. The peak positions and concentration of the different functional groups are provided in table III.3.

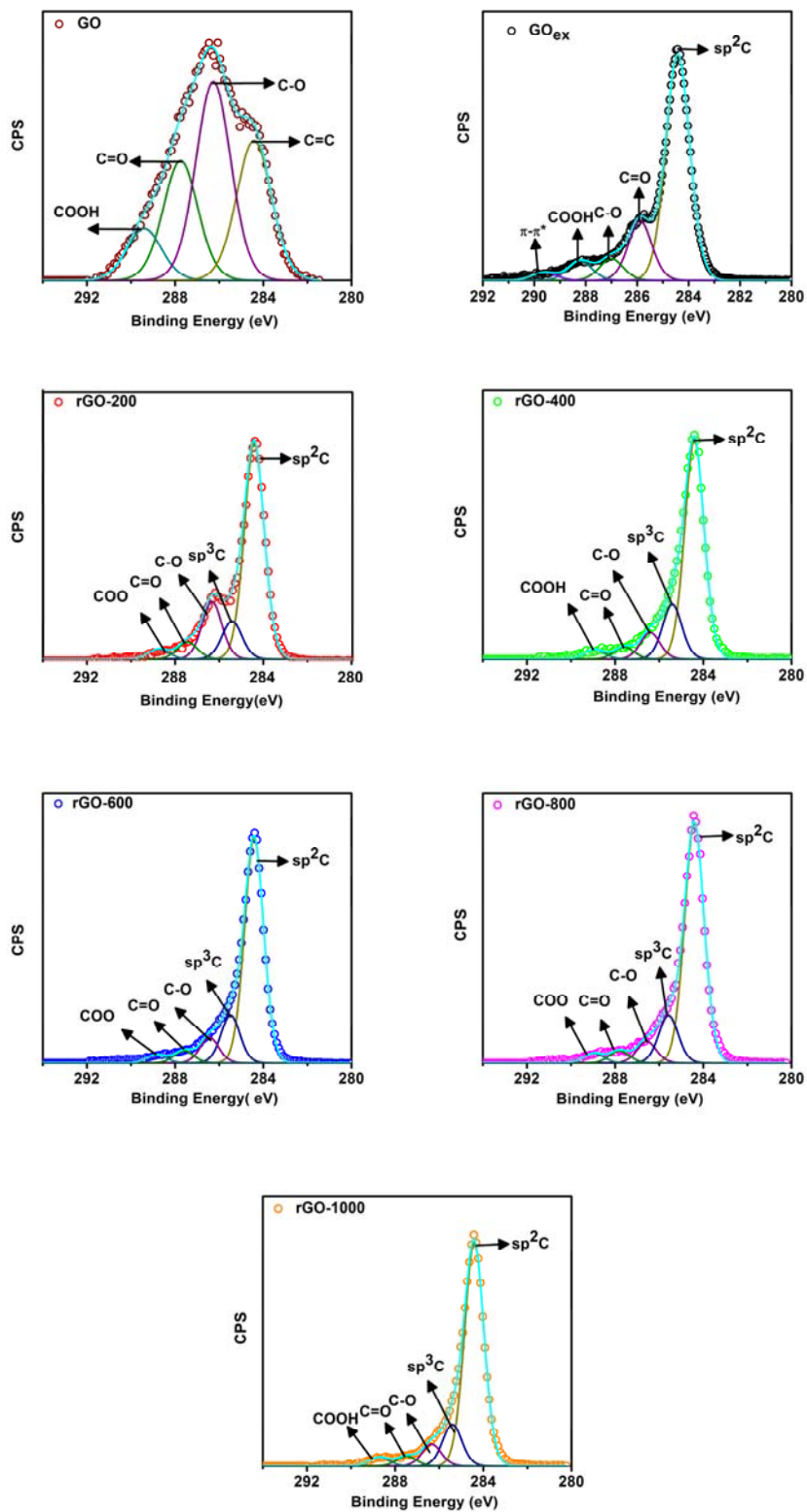


Figure III. 13 Deconvoluted high resolution C1s spectra for GO, rGO-200, rGO-400, rGO-600, rGO-800, rGO-1000.

Table III.3 Concentration of the functional groups estimated from the deconvoluted C1s spectra.

Sample	Peak position (eV)	Function groups	Concentration (%)
GO	284.43	sp <sup>2</sup> C	27.325
	286.27	C-O	38.95
	287.75	C=O	23.436
	289.39	COOH	10.288
GO <sub>ex</sub>	284.42	sp <sup>2</sup> C	67.196
	285.89	C-O	17.824
	287	C=O	6.581
	288.22	COOH	5.935
	289.62	π-π*	2.463
rGO-200	284.41	sp <sup>2</sup> C	63.371
	285.42	sp <sup>3</sup> C	11.361
	286.33	C-O	17.042
	287.44	C=O	5.149
	288.75	COOH	3.078
rGO-400	284.41	sp <sup>2</sup> C	67.495
	285.41	sp <sup>3</sup> C	17.138
	286.41	C-O	8.392
	287.59	C=O	3.833
	288.94	COOH	3.141
rGO-600	284.42	sp <sup>2</sup> C	70.356
	285.49	sp <sup>3</sup> C	14.943
	286.44	C-O	7.994
	287.6	C=O	3.981
	288.85	COOH	2.725
rGO-800	284.41	sp <sup>2</sup> C	72.295
	286.57	sp <sup>3</sup> C	6.564
	285.58	C-O	14.337
	287.8	C=O	3.775
	288.98	COOH	3.03
rGO-1000	284.41	sp <sup>2</sup> C	72.925

	285.41	sp <sup>3</sup> C	13.568
	286.34	C-O	7.161
	287.48	C=O	3.308
	288.72	COOH	3.037

The morphological features of Graphite, GO, GO<sub>ex</sub>, rGO-200, rGO-400, rGO-600, rGO-800, rGO-1000 is revealed using scanning electron microscopy imaging. Figure III.14 shows the high resolution scanning electron microscopy images Graphite, GO, GO<sub>ex</sub>, rGO-200, rGO-400, rGO-600, rGO-800, rGO-1000. The highly ordered structure visible in the SEM image of graphite. The reduced graphene oxide has a highly wrinkled architecture with few layers.

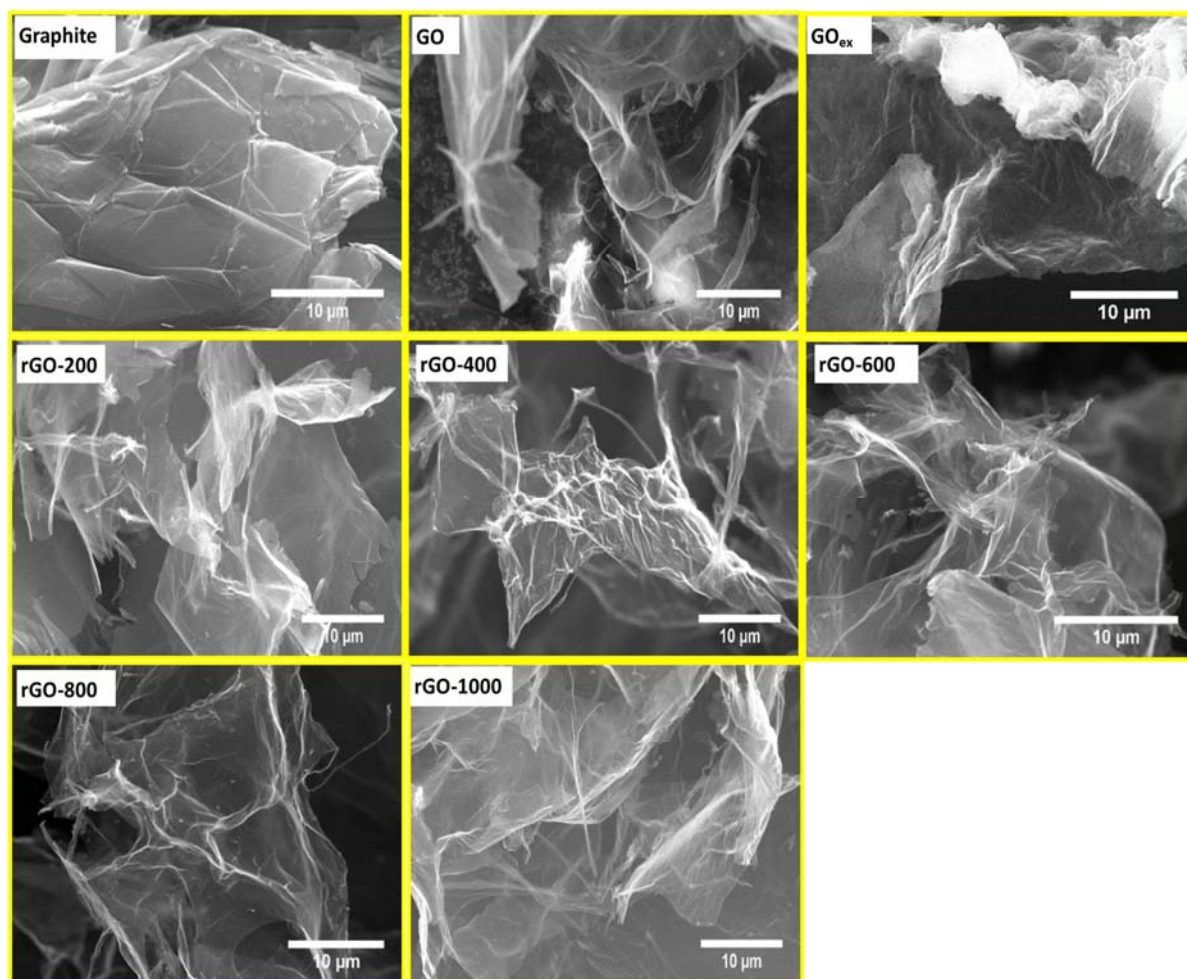


Figure III.14 SEM images for Graphite, GO, GO<sub>ex</sub>, rGO-200, rGO-400, rGO-600, rGO-800, rGO-1000.

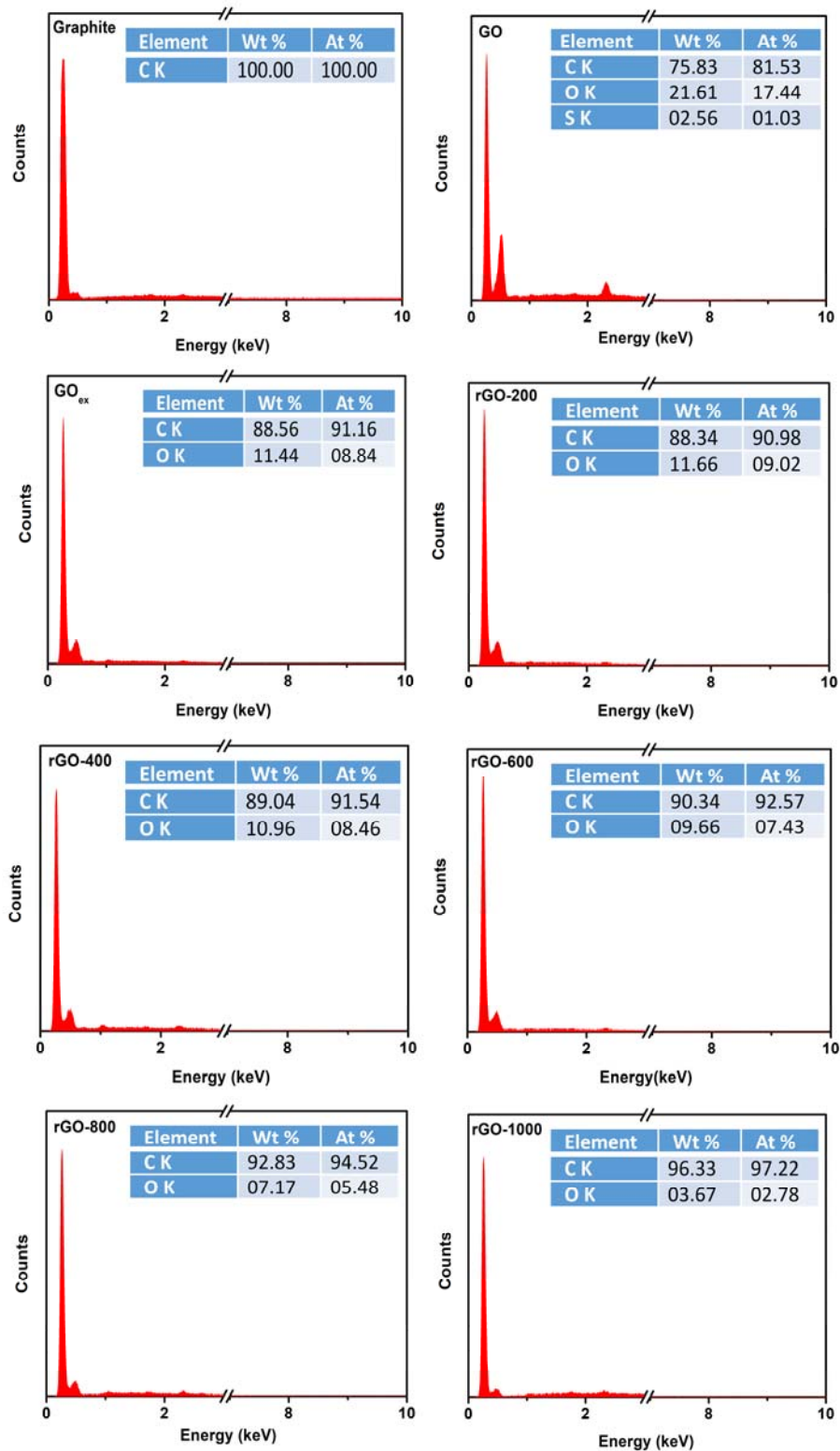


Figure III.15 EDX spectra for Graphite, GO, GO<sub>ex</sub>, rGO-200, rGO-400, rGO-600, rGO-800, rGO-1000.



---

Figure III.15 shows the EDX spectra for Graphite, GO, GO<sub>ex</sub>, rGO-200, rGO-400, rGO-600, rGO-800, rGO-1000. EDX spectra shows the presence of carbon and oxygen in Graphite, GO, GO<sub>ex</sub>, rGO-200, rGO-400, rGO-600, rGO-800 and rGO-1000. There is no oxygen present in graphite. The high oxygen content in GO indicates it is highly oxidized. After reduction/exfoliation, the amount of oxygen is drastically reduced.

### III.6 Functional application of graphene oxide

*The following work was carried in collaboration with Prof. Kai Zhang and Dr. Yonggui Wang at TU Darmstadt, Germany and published in peer reviewed journal.*

*Y. Wang, S. Yadav, T. Heinlein, V. Konjik, H. Breitzke, G. Buntkowsky, J. J. Schneider, K. Zhang “Ultra-light nanocomposite aerogels of bacterial cellulose and reduced graphene oxide for specific absorption and separation of organic liquids”, RSC Advances, (2014), 4, 21553-21558.*

Separation of water and oil spills or organic liquids becomes more relevant in recent years due to environmental, health, and economic issues such as wastewater from industries and oil spill from oil tanker or ship accidents [325-326]. Porous carbon materials such as aerogel and foam have been used for the separation of organic solvents and water [327]. Ultralight silicon aerogels have also been used as absorbents for organic oils and spills, but they suffer from the brittleness and low absorption capacity [328]. Carbon nanotube (CNT) aerogels [329], graphene [330], CNT/graphene composite [331], polyurethane sponges coated with reduced graphene oxide [332] and carbon nanofiber aerogels [333-334] showed high absorption capacity of 80-950 times of their own weights. Various methods used for the absorption of organic solvents includes separation via ultrasonication, gravity, centrifugation, membrane filtration and biological treatments [327]. The drawbacks such as slow separation, low separation efficiency and/or selectivity, recycling problems of the currently available absorbents and even pollutants released during the preparation of absorbents can be overcome by developing new green materials for separating organic pollutants and water.

Cellulose, a naturally occurring green material has been less used for the separation of oily compounds [335-336]. These works are carried by hydrophobizing the surface of cellulose fibers via deposition of silane or titanium dioxide, in order to suppress the strong interaction between cellulose and water. Also, cellulose aerogels has been used for the separation of organic compounds and oily compounds with increased volume were used due to their porous structure [335-336]. Recently, cellulose-based nanocomposite aerogels containing graphene oxide (GO) have also been used for the fabrication of superhydrophobic surface and flexible supercapacitors [337-338]. Aerogels

---

containing cellulose and GO is not suitable for the specific separation of oily compounds due to strong interaction of GO with water.

Cellulose aerogels can be made using various plant celluloses, nanocrystalline cellulose or bacterial cellulose [339-343]. Among the various cellulose, bacterial cellulose (BC) attracts more attention due to its high purity, high crystallinity and high aspect ratio [344]. Its single fibrils showed average diameter lower than 100 nm, while the length can be >100  $\mu\text{m}$  [344-345].

Herein, sustainable bacterial cellulose (BC) and graphene oxide (GO) nanocomposite aerogel were fabricated using an efficient method and it is used as a super absorbent for organic liquids. An ecofriendly freeze-drying process was used to prepare ultra-light aerogels of BC and nanocomposite BC/GO, which showed high absorption capacity to organic liquids and water. BC/rGO aerogels were prepared by reduction of BC/GO aerogels in  $\text{H}_2$  environment which exhibited specific absorption only for organic liquids.

Bacterial cellulose (BC) was prepared using *G. xylinus* culture in Hestrin-Schramm medium [346]. In detail, 20.0 g glucose, 5.0 g yeast extract, 5.0 g bacterial peptone, 2.7 g sodium phosphate dibasic ( $\text{Na}_2\text{HPO}_4 \cdot 2\text{H}_2\text{O}$ ), 1.2 g citric acid and 5.7 g magnesium sulfate ( $\text{MgSO}_4$ ) were dissolved in DI water. The pH value of the solution was adjusted to around 5 using 3 N HCl aqueous solution. Then, the growth medium was divided into 10 equal volumes of 100 ml each in a 250 ml flask. Thereafter, the initial strain solution was added into the growth medium and the solutions were incubated at 30  $^\circ\text{C}$  for 7 days. Obtained BC pellicles were purified three times in 0.1 N aqueous NaOH solution at 80 $^\circ\text{C}$ , once in 0.1 N aqueous citric acid at 80 $^\circ\text{C}$  and then washed with DI water until neutral pH. Finally, BC was freeze-dried at -50 $^\circ\text{C}$  under a vacuum of 0.1 mbar.

Dry BC was immersed in water and the suspension was stirred for 2 days in order to make BC swollen, this material was chopped firstly with a blender and then sonicated using Ultra-Turrax T25 at 18000 rpm for 30 minutes to make nanofibrillated BC. Then, the BC suspension was degassed by ultrasonication for 5 min, frozen at -65  $^\circ\text{C}$  and freeze-dried at -50  $^\circ\text{C}$  under vacuum. BC/GO aerogels were prepared by mixing 100 ml of BC suspension (1.7 g/l) and defined volume of GO suspension at 10 g/l, so that the final weight ratio of both lay at 80:20. BC/rGO aerogels were obtained by reduction of BC/GO aerogels in a HORST oven (Horst GmbH, Lorsch, Germany) at 200  $^\circ\text{C}$  for 4 h by maintaining a hydrogen flow rate of 200  $\text{cm}^3/\text{min}$ . Figure III.16 shows the photograph of the as prepared (a) GO, (b) BC aerogel, (c) aerogel of BC/GO hold by a flower and (d) BC/GO after the reduction, BC/rGO hold by a flower. Highly crystalline structure of BC was investigated using solid-state  $^{13}\text{C}$  NMR spectroscopy (Figure III.17 (a)) [347-348] and the crystallinity is found to be 84%. Figure III.17 (b) shows the FTIR spectra of BC, rBC, BC/GO and BC/rGO. The presence of peaks at 1573, 1000 and 984  $\text{cm}^{-1}$  as well as the disappearance of the signal at 1632  $\text{cm}^{-1}$  in their FTIR

spectra confirms the reduction of GO, while BC did not undergo any significant modification at 200 °C under H<sub>2</sub> flow for 4 h .

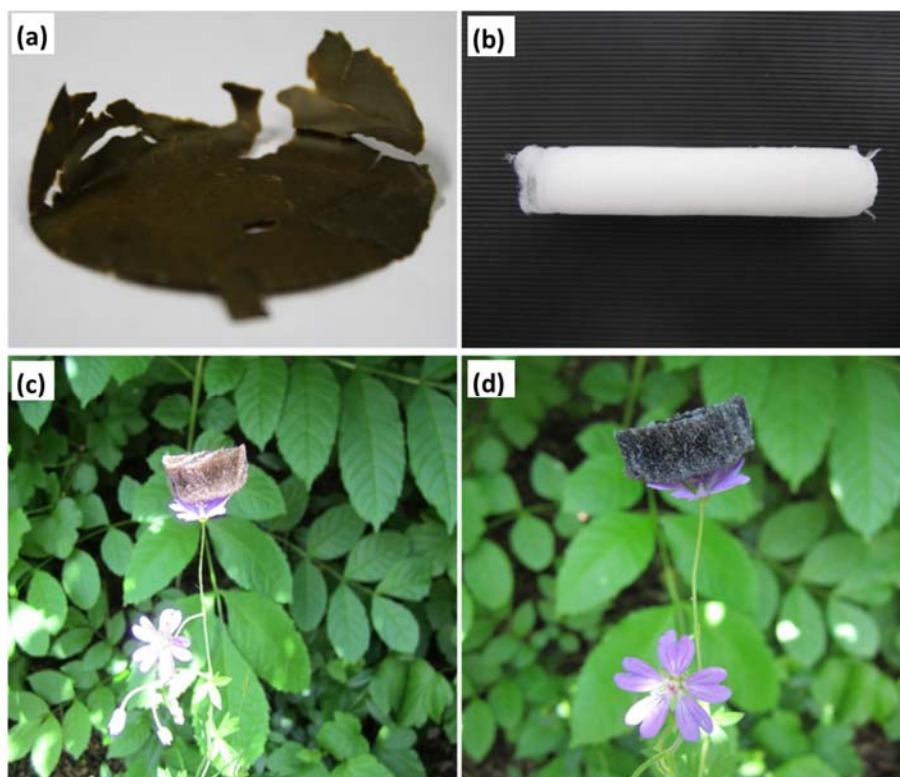


Figure III.16 Photographs (a) GO, (b) BC aerogel, (c) aerogel of BC/GO hold by a flower and (d) BC/rGO after the reduction hold by a flower.

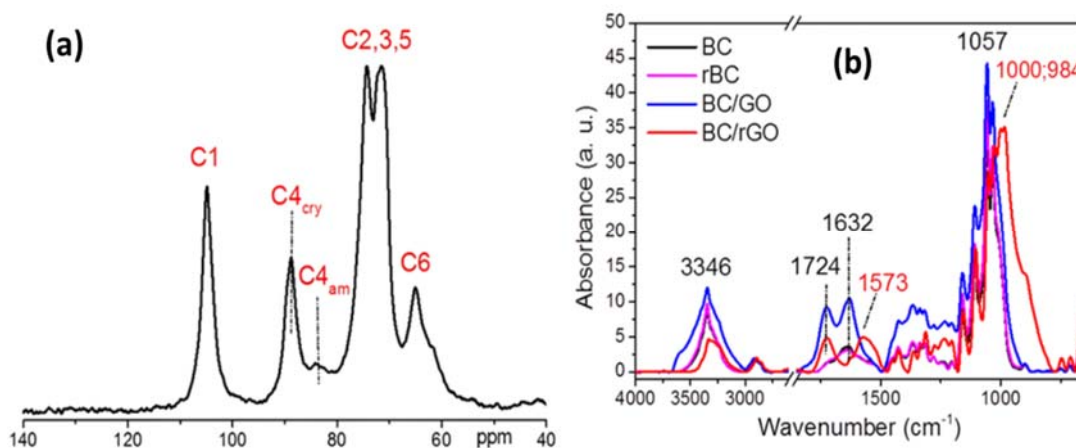
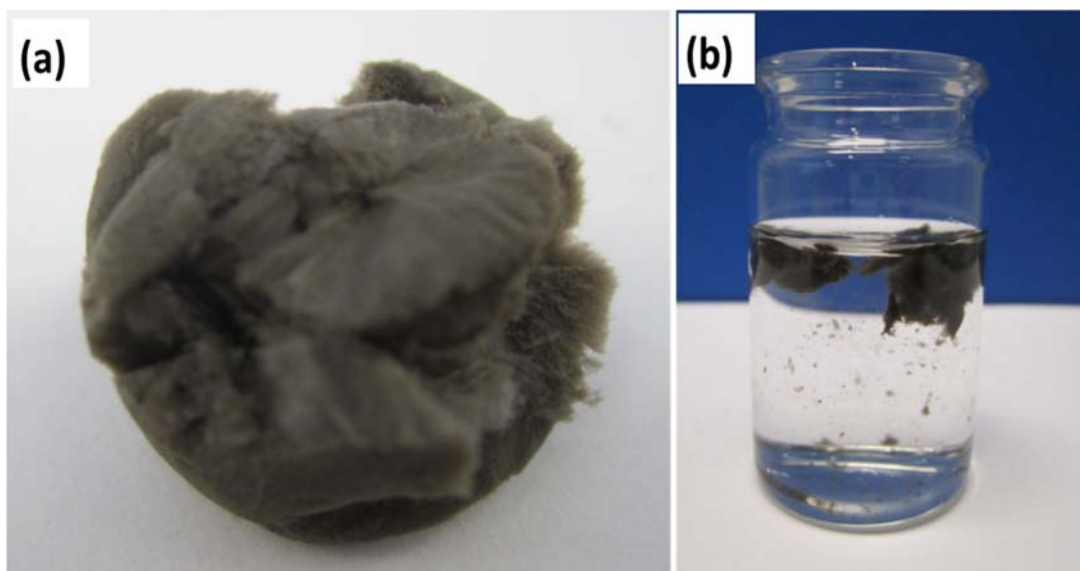


Figure III. 17 (a) solid-state <sup>13</sup>C NMR spectrum of BC and (b) FTIR spectra of BC, BC treated under H<sub>2</sub> gas at 200 °C for 4 h, BC/GO and BC/rGO [349].

Organic liquid absorption capacity of bacterial cellulose and GO based nanocomposite aerogels, bacterial cellulose and rGO based nanocomposite aerogels are examined here. Dimethylformamide (DMF) was chosen due to their polar, protic, water-miscible properties and cyclohexane was chosen due to its non-polar, aprotic, water non-miscible properties respectively. Figure III.18 (a) shows the photograph of the GO aerogel prepared using freeze-drying process and the photograph of the GO aerogel put in the organic solvent (cyclohexane) is shown in figure III.18 (b). GO aerogel could not interact with organic solvents due to its high hydrophilic nature.



*Figure III.18 (a) GO aerogel and (b) GO aerogel in cyclohexane.*

Photograph of the BC aerogel and BC/rGO aerogel (80/20) within cyclohexane and the same containing cyclohexane is depicted in figure III.19 (a, b,c,d). Absorption capacity of aerogels of BC, BC/GO (80/20), BC/GO (50/50), BC/rGO (80:20), BC/rGO (50/50) for different organic liquids are shown in figure III.19 (e) . These materials exhibited high absorption capacity for both DMF and cyclohexane. For comparison, the cyclohexane absorption capacity of BC aerogels, BC/GO aerogels and BC/rGO aerogels are high compared DMF adsorption capacity. BC aerogel absorbs up to 164 g/g own weight cyclohexane and this is due to crystalline nature of cellulose [350]. When, GO is added, the absorption capacities for both organic solvents were strongly reduced. This is probably due to enhanced hydrophilicity of GO. Further, the reduction of GO increases the absorption capacities both organic liquids. Hence, BC aerogel as well as BC/rGO nanocomposite aerogels exhibited much higher absorption capacity than those of aerogels from plant cellulose.

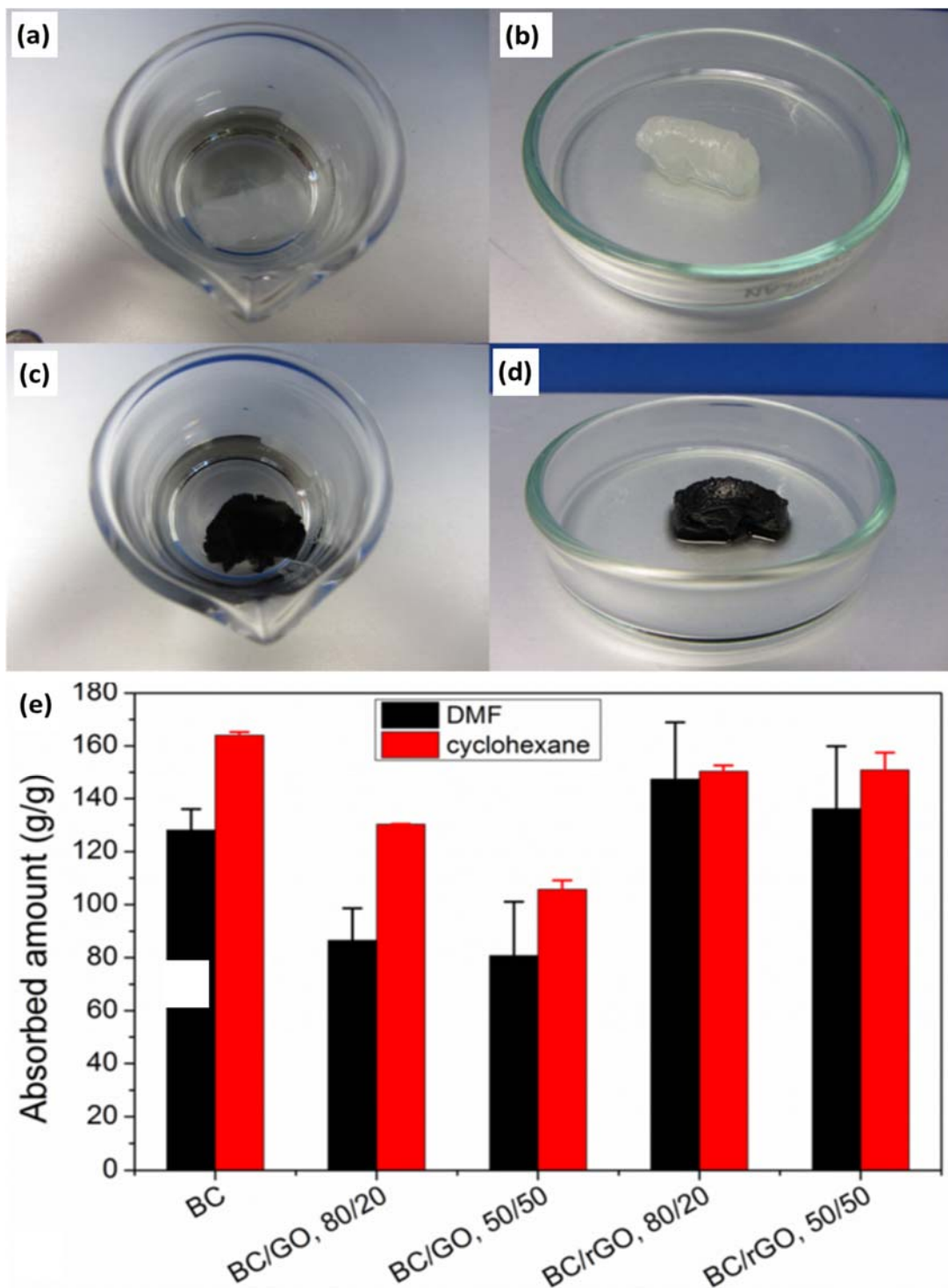


Figure III.19 Representative photo images for absorption experiment using (a) BC aerogel within cyclohexane, (b) BC aerogel containing cyclohexane, BC/rGO (80/20) aerogel, (c) BC/rGO (80/20) aerogel within cyclohexane, (d) BC/rGO (80/20) aerogels containing cyclohexane and (e) absorbed amounts of organic solvents by BC, BC/GO and BC/rGO aerogels <sup>[349]</sup>.

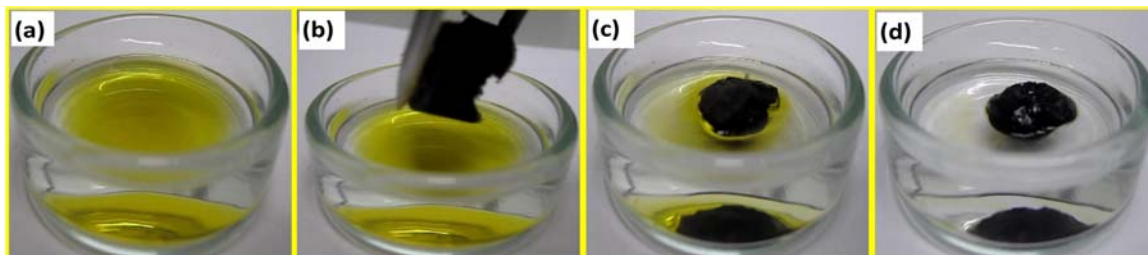


Figure III.20 Photographs of (a) dyed cyclohexane on water surface in petri dishes, (b) placement of aerogel onto the surface of the mixture, (c) absorption cyclohexane on water surface and (d) end of the absorption [349].

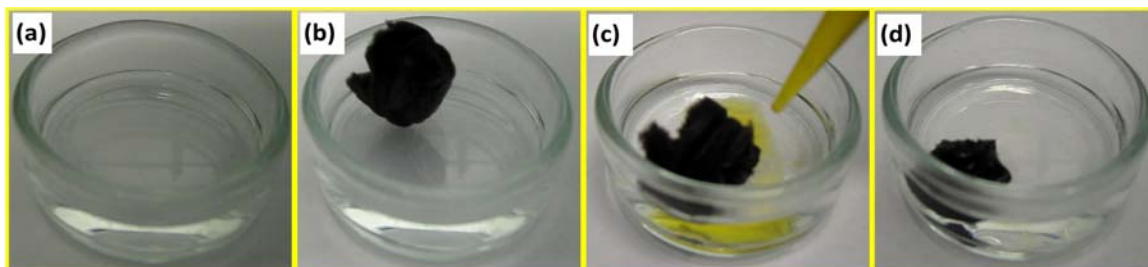


Figure III.21. Photographs of (a) pure water in petri dish, (b) placement of aerogel onto water surface, (c) begin of the addition of dyed cyclohexane and (d) end of the addition of dyed cyclohexane [349].

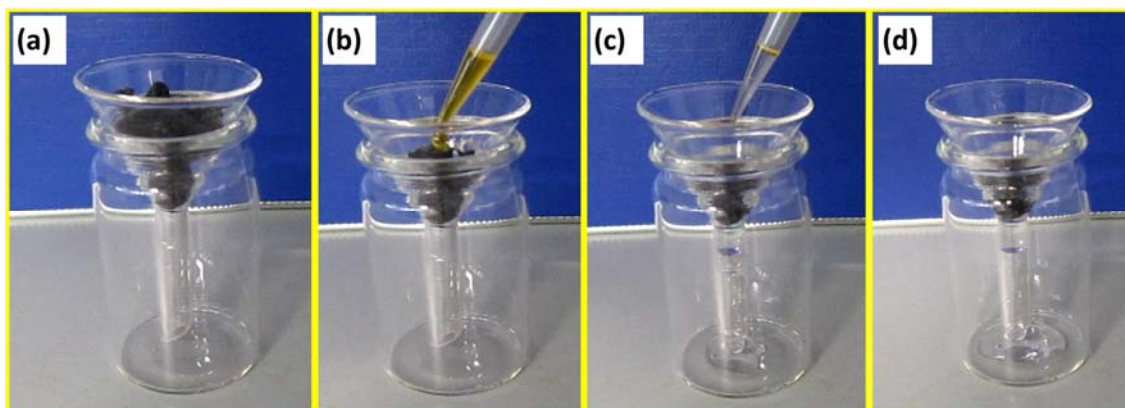


Figure III.22 (a) placement of aerogels into funnels, (b) begin of the addition of dyed cyclohexane-water-mixture, (c) end of the addition of dyed cyclohexane-water-mixture and (d) end of absorption of dyed cyclohexane [349].

Absorption of cyclohexane (dyed with Sudan I) from water surface is tested by placing the aerogels on an organic liquid-water mixture (figure III.20). It is observed that the BC/rGO (80/20) aerogels could absorb cyclohexane (dyed with Sudan I) from water surface quickly and selectively, leaving clean water (figure III.20 (d)). During the absorption, aerogels shrunk up.

Another experiment was conducted in which the aerogels are placed on the water in petri dish then the organic liquids were added BC/rGO aerogels (both 80/20) absorbed the added cyclohexane rapidly (figure III.21).

Another experiment was designed to demonstrate the online separation capability of the aerogels. Here initially, aerogels are placed on a small funnel, then the mixture of cyclohexane (dyed with Sudan I) and water was added (Figure III.22). BC/rGO aerogels absorbs cyclohexane specifically and only water flowed through the edge of BC/rGO aerogel into the vessel after the addition of the mixture of cyclohexane and water.

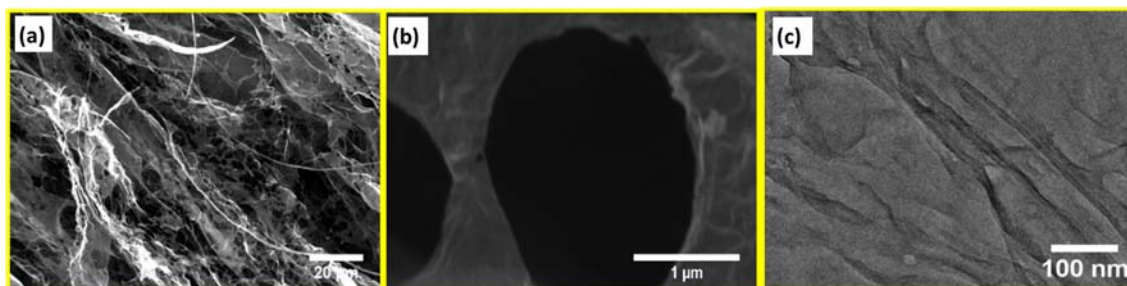


Figure III.23 (a and b) SEM images of BC/rGO aerogel (80/20) in 2 different magnifications and (c) TEM images of BC/rGO aerogel (80/20) [349].

Morphology of the nanocomposite aerogel of BC/rGO (80/20) investigated using scanning electron microscopy (Figure III.23 (a and b)), which is ascribed to the enhanced binding between BC fibrils by rGO nanosheets. Figure III.23 (c) depicts the TEM images BC/rGO composites. BC nanofibrils and rGO nanosheets were bounded together strongly during the freeze-drying, resulting in planar ultrathin sheets.

### III.7 Conclusions

Graphene oxide was successfully synthesized from graphite and reduced by heating under hydrogen environment. Graphene oxide was also exfoliated using liquid nitrogen. Formation of graphene oxide and reduction of graphene oxide is confirmed using X-ray diffraction patterns, Raman spectroscopy and X-ray photoelectron spectroscopy.

BC and BC/GO aerogels can strongly interact both with water and organic solvents. The organic liquid absorption capacity of BC or BC/GO aerogels is used to derive porosity of aerogels. BC aerogels are more non-polar than BC/GO aerogels due to the presence of individual amphiphilic nano-scaled BC fibrils. BC/rGO aerogels could specifically absorb organic solvents and thus exhibited increased non-polarity and oleophilicity than BC/GO aerogels.

## IV PHOSPHORENE AND ITS APPLICATIONS

This chapter begins with a brief introduction to two-dimensional (2D) materials. Then the synthesis and the functional properties of few layered black phosphorus in cell growth, as gas sensor and as semiconductor in a field effect transistor device is discussed.

### IV.1 Introduction

Carbon in Group 14 and phosphorus in Group 15 possess a “diagonal relationship” based on their position in the periodic system of elements (PSE) (figure IV.1). This can be due to their similar electronegativity, atomic size and polarizing power. Replacement of carbon with phosphorus sometime shows only insignificant changes in the chemical reactivity of the molecule due to the non-polar nature of the carbon-phosphorus bond <sup>[351]</sup>. Phosphorus is often called a “carbon copy” because compounds with p-p  $\pi$  bond between P and C atoms (or between two P atoms) are structurally and chemically similar to related systems with comparable multiple bonds between carbon atoms <sup>[352-353]</sup>.

	1	2	13	14	15
Period 2	Li	Be	B	C	N
Period 3	Na	Mg	Al	Si	P

Figure IV.1 Pictorial representation of elements in the PSE represents a diagonal relationship <sup>[354]</sup>.

After the discovery of graphene, semiconducting analogues of graphene such as germanane <sup>[355]</sup> and silicene <sup>[356]</sup> that exist only in the realm of theory could be synthesized. Transition metal chalcogenides with stoichiometry  $\text{MX}_2$  ( $\text{M} = \text{Ti, Zr, Hf, V, Nb, Ta, Re}$ ;  $\text{X} = \text{S, Se, Te}$ ) crystallize in to layered 2D structures. Single and few layered thick metal chalcogenides has been synthesized <sup>[357]</sup>. Color coded elements in the periodic table represents various 2D materials beyond graphene (Figure IV.2).



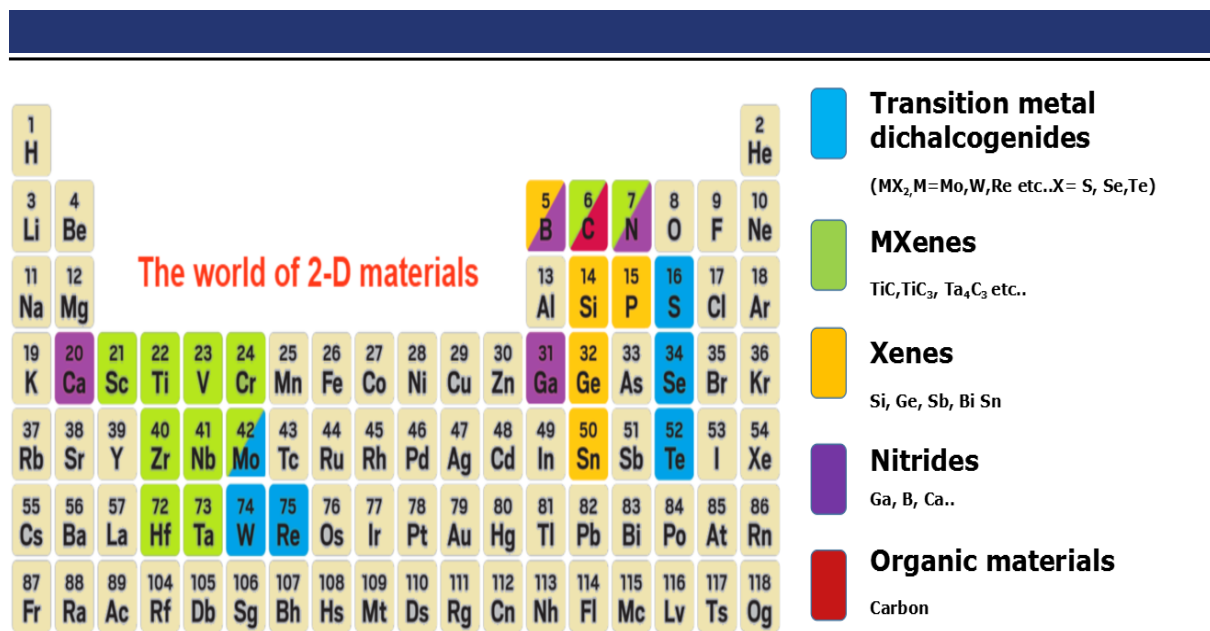
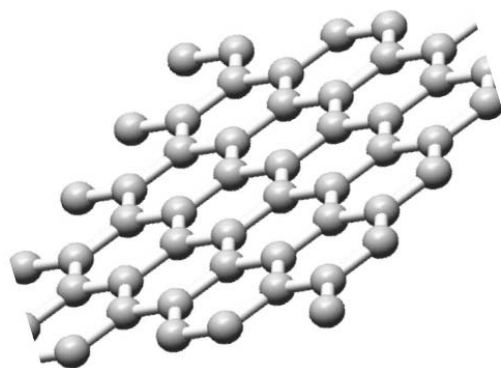


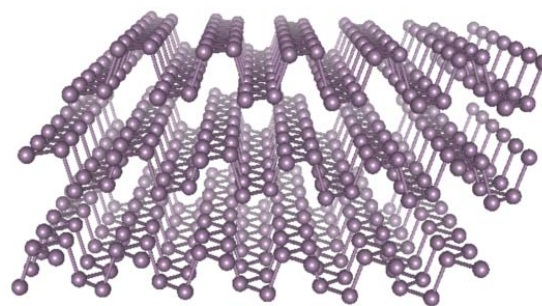
Figure IV.2 Atlas of 2D materials

Graphene has received wide attention in various application due to its superior properties such as high carrier mobility, ultrahigh surface area, excellent thermal conductivity, and quantum confinement effect [358]. The zero bandgap of graphene is limiting its wide use in electronic devices. Recently phosphorene has attracted attention in electronic devices due to its remarkable properties like its thickness-dependent band gap, strong in-plane anisotropy, and high carrier mobility [359]. A comparison of the structural and electronic properties of graphene and phosphorene is shown in figure IV.3.



**Graphene**

**Eg: 0.0 eV, High mobility**



**Phosphorene**

**Eg: 0.3 to 3.0 eV, High mobility**

Figure IV.3 Comparison of structural and electronic properties of graphene and phosphorene.

## IV.2 Phosphorene

Phosphorene is an allotrope of phosphorus and it can be viewed as black phosphorus with a single layer similar to the single layer graphene allotrope of graphite. There has been a very significant attraction in the scientific field since the discovery of phosphorene. It has been an interesting studied material for many applications such as batteries [360], transistors [361] and photovoltaic [362] because of its very unique physical and chemical properties.

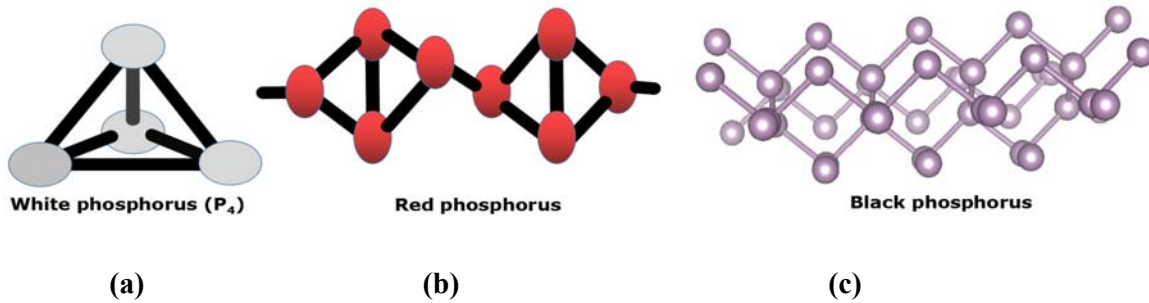


Figure IV.4 Allotropes of phosphorus (a) White phosphorus, (b) Red phosphorus and (c) Black phosphorus.

Phosphorus has various allotropes known as the solid white, red, black and the violet allotropes. Phosphorus in the gaseous state exist as di-phosphorus. White phosphorus consists of tetrahedral  $P_4$  molecules, in which each atom is bound to the other three atoms by a single bond (figure IV.4 (a)). Heating white phosphorus to  $250\text{ }^\circ\text{C}$  gives red phosphorus with polymeric chain-like structure (figure IV.4 (b)). Violet phosphorus can be produced by annealing of red phosphorus above  $550\text{ }^\circ\text{C}$  for about one day [363]. Figure IV.4 (c) shows the structure of black phosphorus, the stable allotrope of phosphorus.

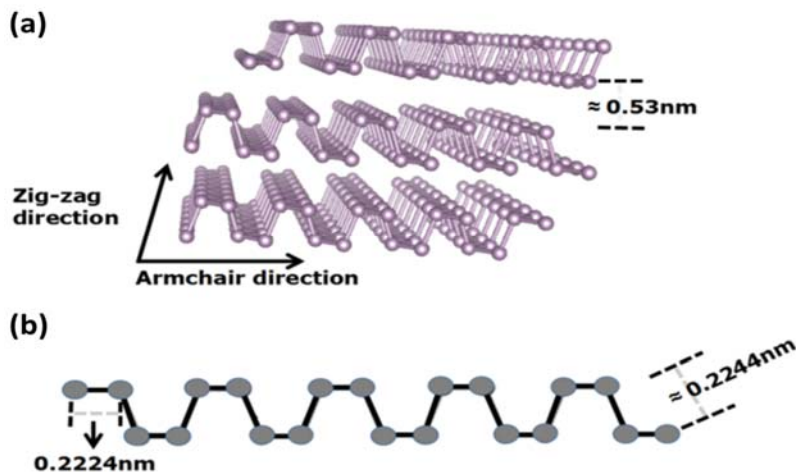


Figure IV.5 (a) Bulk black phosphorus and (b) phosphorene honey comb lattice structure.

Black phosphorus, the stable allotrope of phosphorus has a layered structure with strong in plane covalent interactions and weak van der Waals forces between the layers. The structure of bulk black phosphorus is shown in figure IV.5 (a) and the structure of single-layer phosphorene is shown in figure IV.5 (b). Phosphorene has a honeycomb lattice structure with each P atom covalently bonded to three neighbors. A single phosphorene layer forms a puckered surface due to  $sp^3$  hybridization [364].

Phosphorene can be prepared from black phosphorus via various techniques such as mechanical exfoliation, liquid phase exfoliation, shear assisted exfoliation and plasma assisted exfoliation etc. (figure IV.6) [365]. Liquid phase exfoliation has been commonly used because it is cost effective, simple, versatile, offering a useful tunnel for synthesis of these materials for research. This process involves intercalation, ion exchange and sonication so as to obtain the complete material from their liquid dispersion [366].

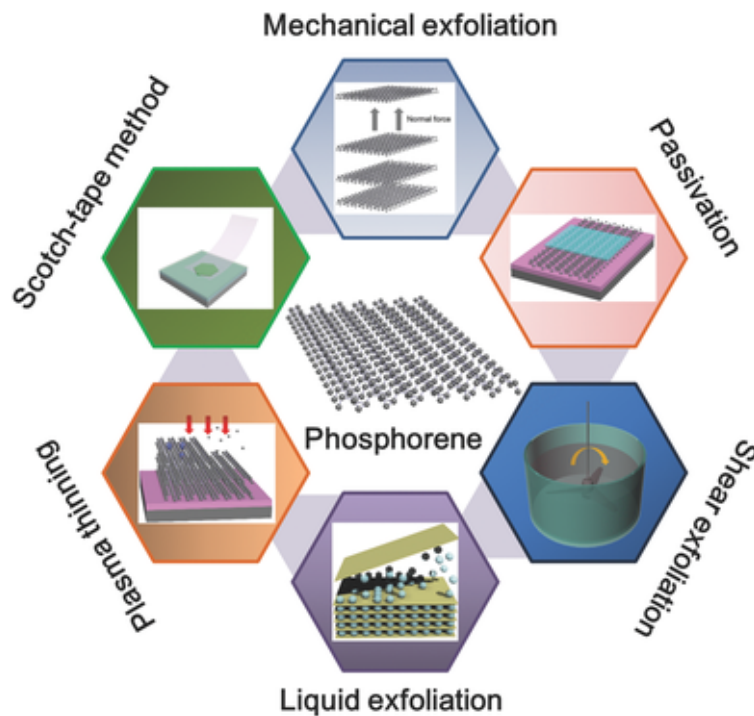


Figure IV.6 Schematic representation of different exfoliation methods for preparation of phosphorene from bulk black phosphorus [365].

Revolution of electronics through nanotechnology has led to system complexity which changes the field of nano-electronics. A transistor is a semi-conductor device used for amplification and switching of electronic signals. Saturation of the drain current is an important factor in order to reach

maximum possible operation speeds in digital and radiofrequency devices [367]. A well defined saturation behaviour is crucial in achieving high power gains. Phosphorene has received attention in electronics due to its higher carrier mobility [368] and tunable bandgap [369].

Fabrication of field-effect-transistor device with few-layer phosphorene is a useful platform for high speed field effect device applications [361]. Liu et al. reported p-type transistors of few-layer phosphorene with a high on-current of 194 mA/mm at 1.0  $\mu\text{m}$  channel length, a current on/off ratio over  $10^4$ , and a high field-effect mobility up to 286  $\text{cm}^2/\text{V}\cdot\text{s}$  at room temperature. Also they constructed 2D CMOS inverter (figure IV.7) consisting of phosphorene PMOS and  $\text{MoS}_2$  NMOS transistors, which shows the heterogeneous integration of phosphorene crystals as a channel material [369]. Phosphorene is used in the formation of radio frequency flexible thin film transistors and these device exhibit high saturation velocity  $\sim 6 \times 10^6 \text{ cm/s}$  [370].

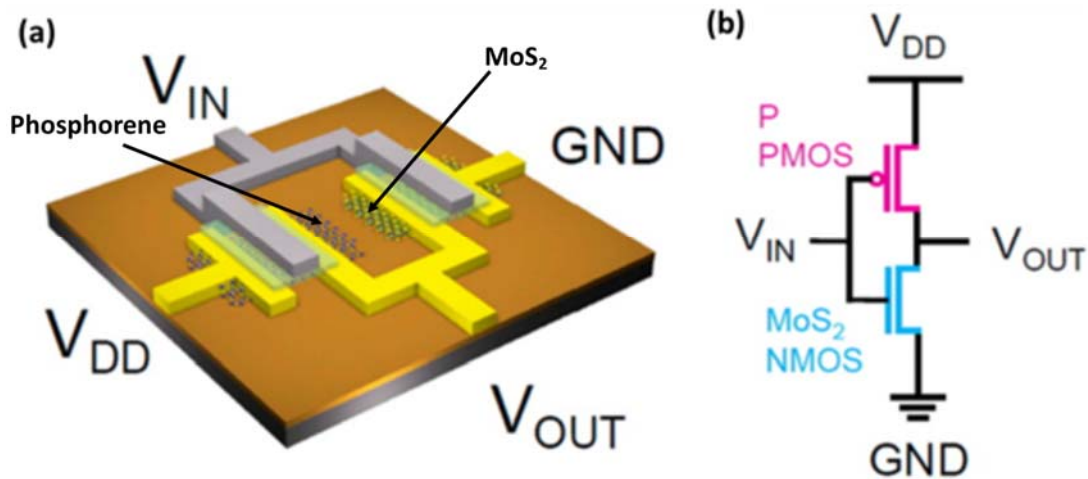


Figure IV.7 (a) Schematic view of the CMOS inverter, with  $\text{MoS}_2$  ( $\sim 5 \text{ nm}$ ) serving as the NMOS and few-layer phosphorene ( $\sim 5 \text{ nm}$ ) serving as the PMOS, (b) Circuit diagram of the CMOS inverter [369].

### IV. 3 Results and discussion

The crystal structure morphology and elemental composition of black phosphorus is investigated using powder X-ray diffraction pattern, Raman spectra, scanning electron microscopy, transmission electron microscopy and energy dispersive X-ray analysis.

Synthesis of black phosphorus is discussed in the experimental section. Black phosphorus synthesized using bismuth flux method is named as BP-1 and chemical vapor transport (CVT) reaction is named as BP-2. Black phosphorus was characterized using Raman spectroscopy. Figure IV.8 shows the Raman spectra of BP-1 and BP-2. The observed peaks are attributed to  $A_g^1$ ,  $B_{2g}$  and

$A_g^2$  vibrations [371].  $A_g^2$  to  $A_g^1$  ratio is maximum when the laser is polarized to AC direction. The crystal structure of black phosphorus with zigzag (ZZ) and armchair (AC) axes is shown in figure IV.5 (a). ZZ and AC axes correspond to the [100] and [001] direction of the orthorhombic unit cell, respectively.  $A_g^1$  is due to out of plane vibration,  $A_g^2$  and  $B_{2g}$  modes are due to inplane vibration along armchair and zigzag directions.

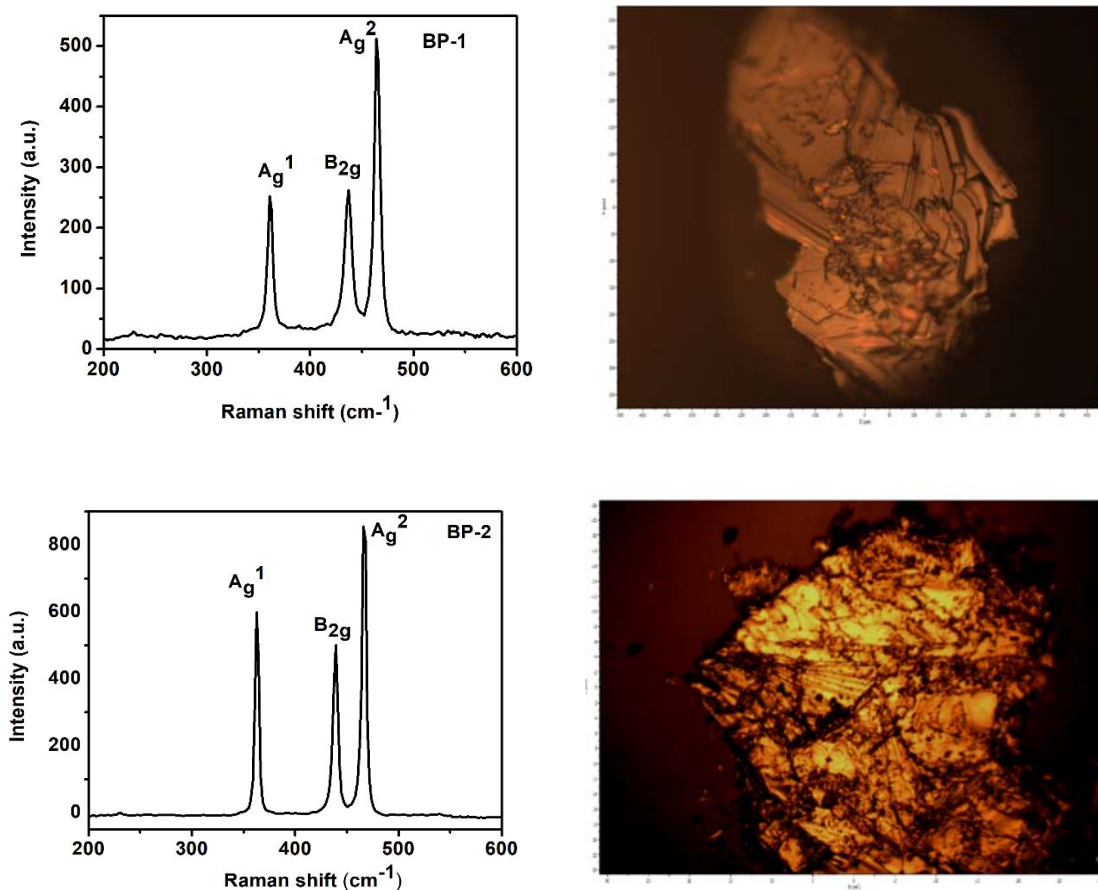


Figure IV.8 Raman spectra and optical images of BP-1 and BP-2.

Morphology of the black phosphorus is investigated using scanning electron microscopy imaging. Figure IV.9 (BP-1 and BP-2) shows the SEM image of the black phosphorous crysrallized in the form of a plate like structure.

The purity of the BP-1 and BP-2 is tested using energy dispersive X-ray analysis (figure IV.10). No bismuth impurity is observed in BP-1. The oxygen content is due to partial oxidation. No Sn and iodine from the synthesis procedure is present in BP-2.

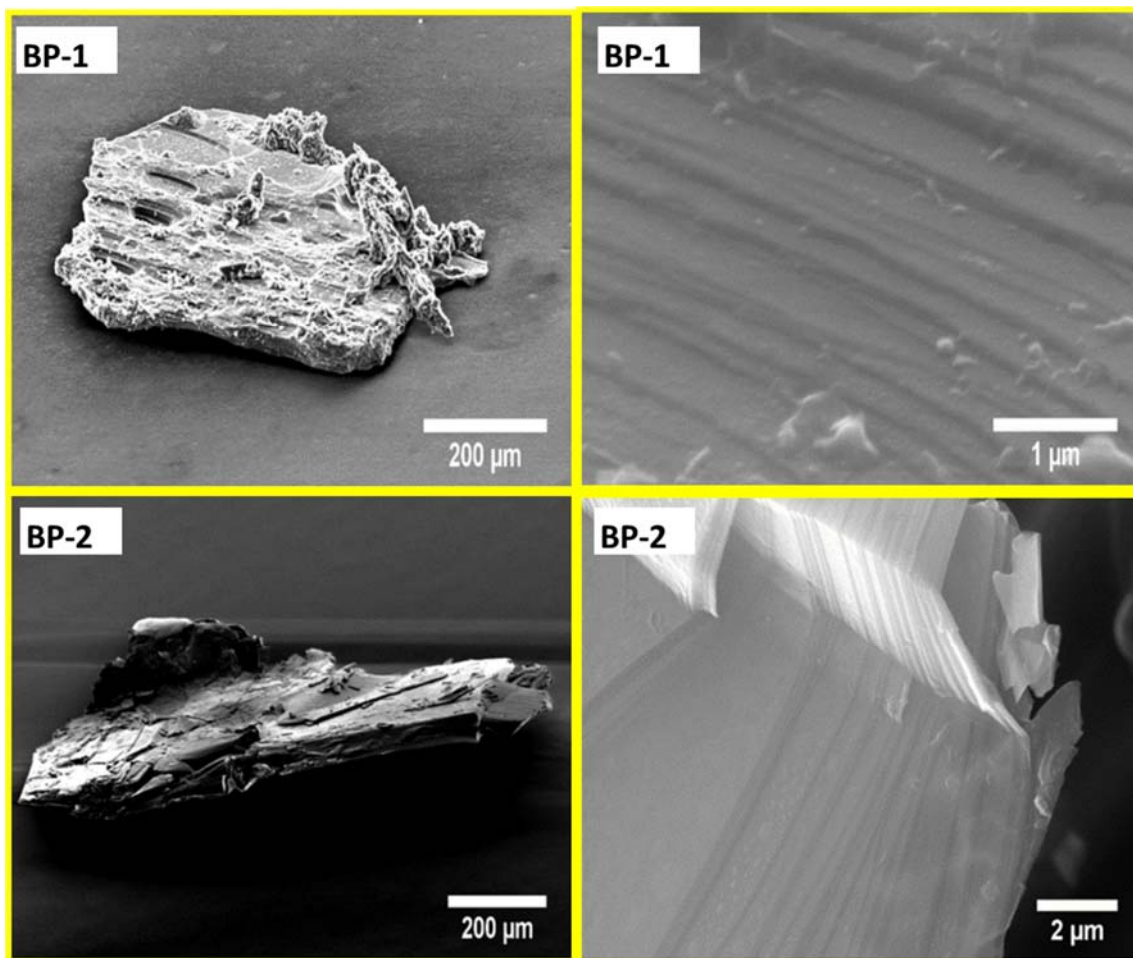


Figure IV.9 Scanning electron microscopy images of the BP-1 and BP-2.

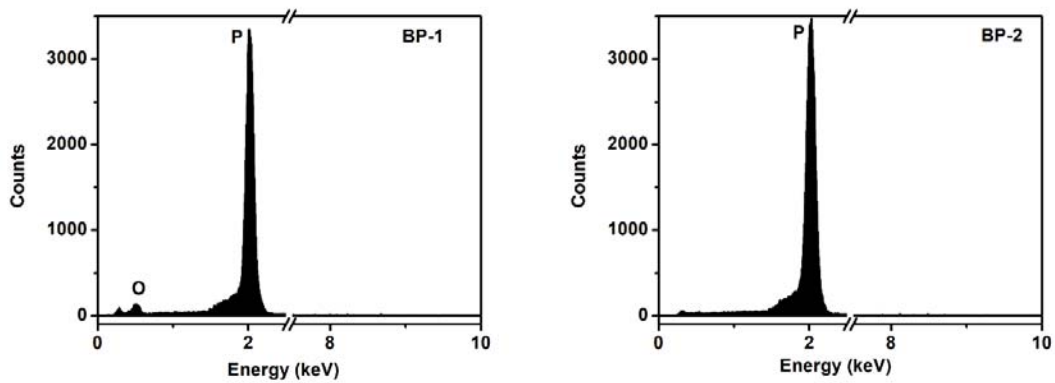
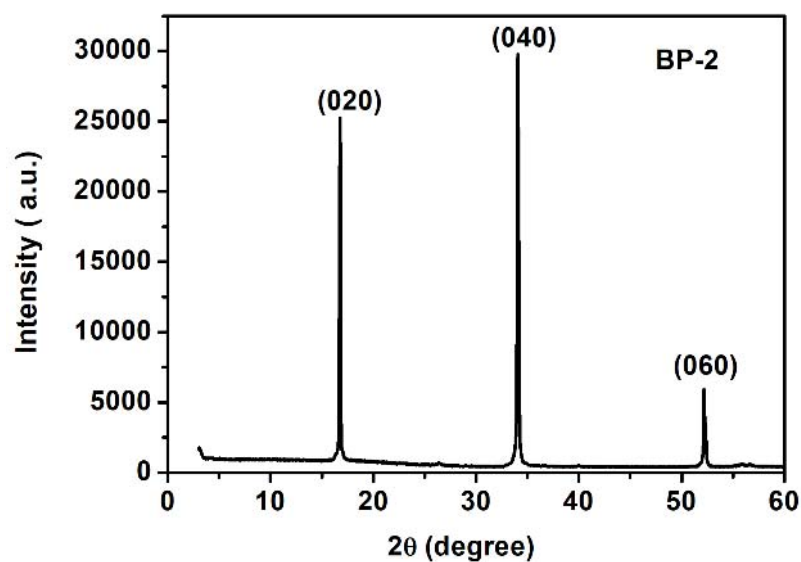
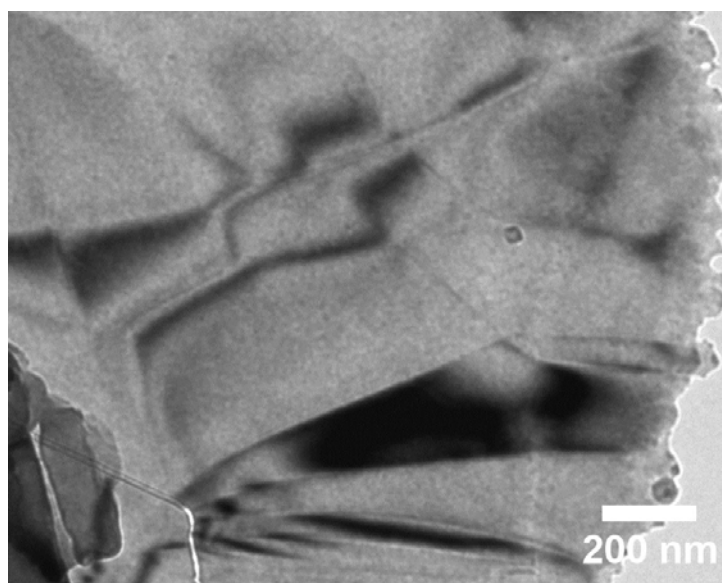


Figure IV.10 EDX spectrum of BP-1 and BP-2.



*Figure IV.11 X-ray diffraction pattern of BP-2.*

Powder X-ray diffraction pattern of the black phosphorus was recorded using Cu K $\alpha$  radiation as the X-ray source is shown in figure IV.11. The peaks are attributed to the planes BP (020), BP (040) and BP (060) and the pattern confirms the orthorhombic (Cmca) crystal structure of the exfoliated black phosphorus. The planes are oriented in (010) direction and it is due to the layered structure of material. Transmission electron microscope images of the BP-2 reveals its layered structure with wrinkles and foldings (Figure IV.12).



*Figure IV.12 TEM image of the BP-2 exfoliated in ethanol.*

## IV.4 Study towards selective functional properties of phosphorene

Fibro blast cell growth, gas sensing and field-effect-transistor device studies were carried on exfoliated black phosphorus synthesized by the CVT reaction.

### IV.4.1 Gas sensor

Graphene and related layered inorganic analogues have received great interest in gas sensing applications due to their large specific surface areas and strong surface activities [372]. Donarelli et al. studied the room temperature gas sensing properties of chemically exfoliated black phosphorus (BP) to various gases like NO<sub>2</sub>, CO<sub>2</sub>, NH<sub>3</sub>, H<sub>2</sub>, and CO gases in a dry air carrier [373]. Multilayer BP shows a detection limit of 20 ppb and 10 ppm towards NO<sub>2</sub> and NH<sub>3</sub> in dry air. Abbas et al. studied the chemical sensing capability of multilayered black phosphorus towards NO<sub>2</sub> using multilayer black phosphorus based field-effect-transistor device. The BP sensors were sensitive to NO<sub>2</sub> concentration limit of 5 ppb [374]. Herein we investigated the sensitivity of few layer black phosphorus towards NO<sub>2</sub> and NH<sub>3</sub>.

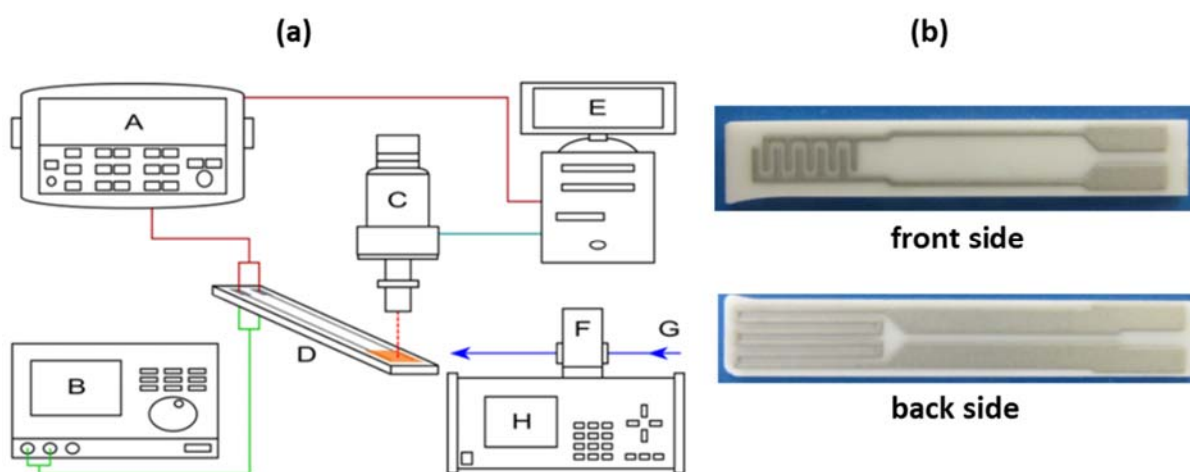


Figure IV.13 (a) Experimental setup for gas sensor measurements. A = Agilent 34972A LXI data acquisition / data logger switch unit; B = Voltcraft DPS-8003PFC power supply for temperature regulation; C = IMPAC IN 5 plus – PL pyrometer for temperature control; D = alumina sensor substrate with Pt electrodes and sensing layer on the front side and Pt heater on the back side, the sensor substrate is housed in a glass reactor; E = data analysis; F = MKS Instruments mass-flow controllers; G = gas inlet; H = MKS Instruments multi gas controller 647B.<sup>[373]</sup>, (b) Photograph of the substrate with Pt electrodes and sensing layer on the front side and Pt heater on the back side

Sensor devices were prepared on commercial alumina substrates with Pt electrodes on the front side and Pt heater on the back side. A suspension of BP-2 in ethanol was sonicated and several droplets were deposited on each of the sensor substrates. The devices were dried in air and placed separately in a glass test chamber. Before each measurement, the test chamber is evacuated, filled with dry



nitrogen and the sensor device is heated at 200 °C in a flow of 200 mL/min N<sub>2</sub> for 10 min.

The dynamic response of the sensor devices to defined concentration of NO<sub>2</sub> (10, 20, 30, 40, 50, 75, 100 ppm) and NH<sub>3</sub> (10, 20, 30, 40, 50 ppm) in dry nitrogen was measured at 30 °C. Premixed gases of NO<sub>2</sub> (Air Liquide / 0.1 Vol.-% in N<sub>2</sub>) and NH<sub>3</sub> (Air Liquide / 0.01 Vol.-% in N<sub>2</sub>) were additionally diluted with nitrogen using separate mass-flow controllers (MKS Instruments). Each 10 minutes interval of analyte gas flow is followed by purging with dry nitrogen for 50 min. The time-dependent response of the sensor is analysed by changes in resistance. The complete set-up is shown in figure IV.13.

The chemiresistors response is given as  $\Delta R/R_0 = (R-R_0)/R_0$  in which R is the time-dependent resistance and R<sub>0</sub> is the resistance measured in dry nitrogen. Plotting the dynamic response of the chemiresistors, R<sub>0</sub> is the initial resistance measured in dry nitrogen. For plotting the calibration curves, R<sub>0</sub> is recalculated for each analyte concentration by using individual baselines.

#### *Sensing properties of black phosphorus chemiresistors*

The sensing properties of black phosphorus chemiresistors to defined concentration of NO<sub>2</sub> and NH<sub>3</sub> in dry nitrogen were analysed. Figure IV.14 shows the representative dynamic response of a black phosphorus sensor device to an increasing concentration of NO<sub>2</sub> (10, 20, 30, 40, 50, 75 and 100 ppm) at 30 °C. The change in resistance is given as  $\Delta R/R_0 = (R-R_0)/R_0$ , where R is the time-dependent resistance and R<sub>0</sub> is the resistance of the initial baseline measured in dry nitrogen.

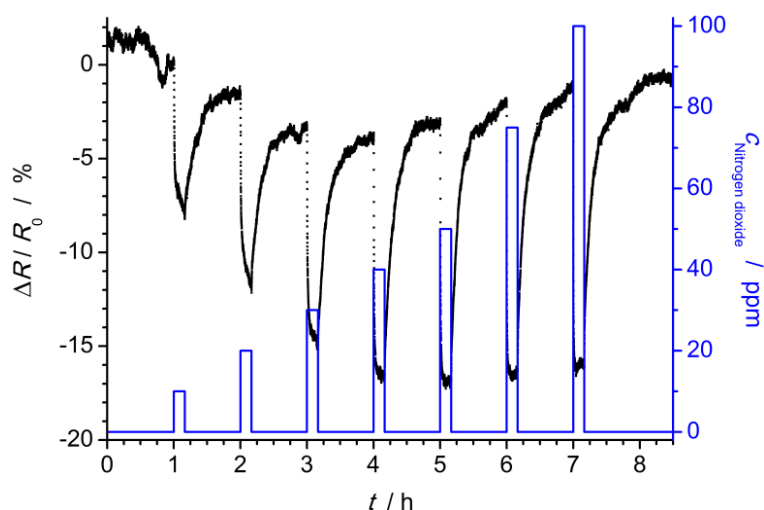


Figure IV.14 Dynamic response of chemiresistor based on black phosphorus to various concentration of NO<sub>2</sub> (10 – 100 ppm) in dry nitrogen at 30 °C. The concentration are shown as blue columns correlating to the second ordinate. The resistance decreases during the 10 min of exposure to NO<sub>2</sub> for each concentration and recovers back to the baseline when purged with dry nitrogen.

Blue columns represent intervals of exposure to  $\text{NO}_2$  and correlate to the second ordinate. The devices resistance decreases during each 10 minutes interval of exposure to  $\text{NO}_2$  and increases back to the baseline when purged with dry nitrogen for 50 min.

Figure IV.15 shows the representative dynamic response of the chemiresistor to an increasing concentration of  $\text{NH}_3$  (10, 20, 30, 40, 50 ppm) in  $\text{N}_2$  at 30 °C. The intervals of exposure to  $\text{NH}_3$  and purging with dry nitrogen are identical to the previous measurements with  $\text{NO}_2$ . The resistance remains nearly constant during intervals of purging with  $\text{N}_2$  and the baseline can only be recovered by heating the chemiresistors.

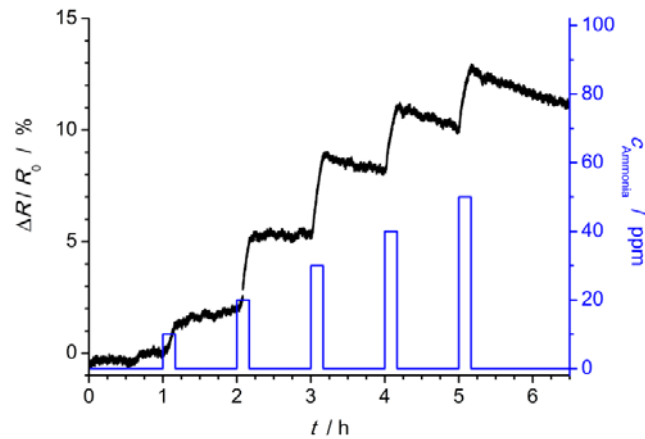


Figure IV.15 Dynamic response of black phosphorus chemiresistor to various concentration of  $\text{NH}_3$  (10 – 50 ppm) in dry nitrogen at 30 °C. The resistance increases during the 10 min of exposure for each concentration and remains nearly constant when the sensor is purged with dry nitrogen.

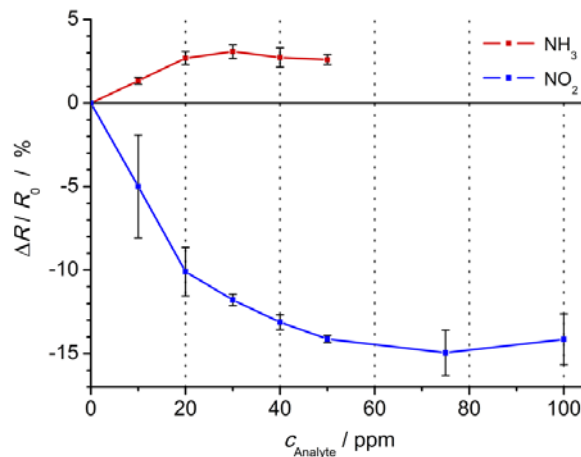


Figure IV.16 Calibration curves of black phosphorus chemiresistors in various concentration of  $\text{NH}_3$  and  $\text{NO}_2$  in dry nitrogen. The plotted response refers to changes in resistance after 10 min of exposure to analyte gas flow for each concentration.

---

Calibration curves of black phosphorus chemiresistors based on their dynamic response to NO<sub>2</sub> and NH<sub>3</sub> are shown in figure IV.16. For plotting the change in resistance  $\Delta R/R_0$  in the calibration curves, R<sub>0</sub> is recalculated using individual baselines for each analyte concentration.

As recovering the chemiresistors baseline by purging with nitrogen at 30 °C was only possible for NO<sub>2</sub> sensing, the plotted values for NH<sub>3</sub> are considered to be minimum values for the sensors response. Exposure to an increasing concentration of NO<sub>2</sub> in the range of 10 – 50 ppm results in a higher response of the devices up to -14 %. Further increasing the concentration of NO<sub>2</sub> (50 – 100 ppm) does not significantly change the chemiresistors response, showing a maximum value of -15 %. A higher sensor response to an increasing concentration of NH<sub>3</sub> can only be observed in the range of 10 – 20 ppm. The maximum value for the minimum response of black phosphorus chemiresistors to NH<sub>3</sub> (20 – 50 ppm) is 3 %.

#### **IV.4.2 Field-effect-transistor**

*The field-effect-transistor device work was carried in collaboration with Dr. Ritu Srivastav and M. Sc. Harneet Kaur at NPL Delhi, India, Dr. Om Prakash Sinha at Amity university, Noida, India and published in peer reviewed journal.*

*H. Kaur, S. Yadav, K. Srivastava, N. Singh, J.J. Schneider, O.P. Sinha, V.V. Agrawal, R. Srivastava “Large area fabrication of semiconducting phosphorene by Langmuir Blodgett assembly”, Nature Sci. Rep., (2016), 6, 34095.*

The layered structure of black phosphorus and weak van der Waals interaction between the layers made the possibility of producing phosphorene via exfoliation of black phosphorus. Fabrication of field effect transistors with few-layer phosphorene is a useful platform for the high speed field effect device applications. Liu et. al fabricated mechanically exfoliated few layer phosphorene based field-effect transistor device and found that the charge carrier mobility is thickness dependent <sup>[361]</sup>. Few layered phosphorene nanosheets were separated from black phosphorus using ultrasonication of black phosphorus in NMP and its application in a field-effect transistor device described here <sup>[376]</sup>. The band gap of the phosphorene is measured as 2.2 eV<sup>[376]</sup>, which is higher than that of bulk black phosphorus (1.9 eV). Atomic force microscopy measurements revealed that the thickness is of the order of 2-4 nm. The interlayer spacing of phosphorene in a multilayered sheet is 0.5 nm, hence this sheets consists of approximately three to seven layers <sup>[376]</sup>. Langmuir- Blodgett (LB) assembly technique is used to assemble the phosphorene sheets, detailed description can be seen in our paper <sup>[376]</sup>. A mixture of NMP and deoxygenated water is used as the subphase in LB trough due to the

strong hetero association of NMP with water. Moreover, NMP is a good solvent for suspension of phosphorene and it acts as protecting layer/ encapsulation layer to prevent degradation of the phosphorene nanosheets during assembling, hence unoxidized LB assembled nanosheets of phosphorene can be obtained.

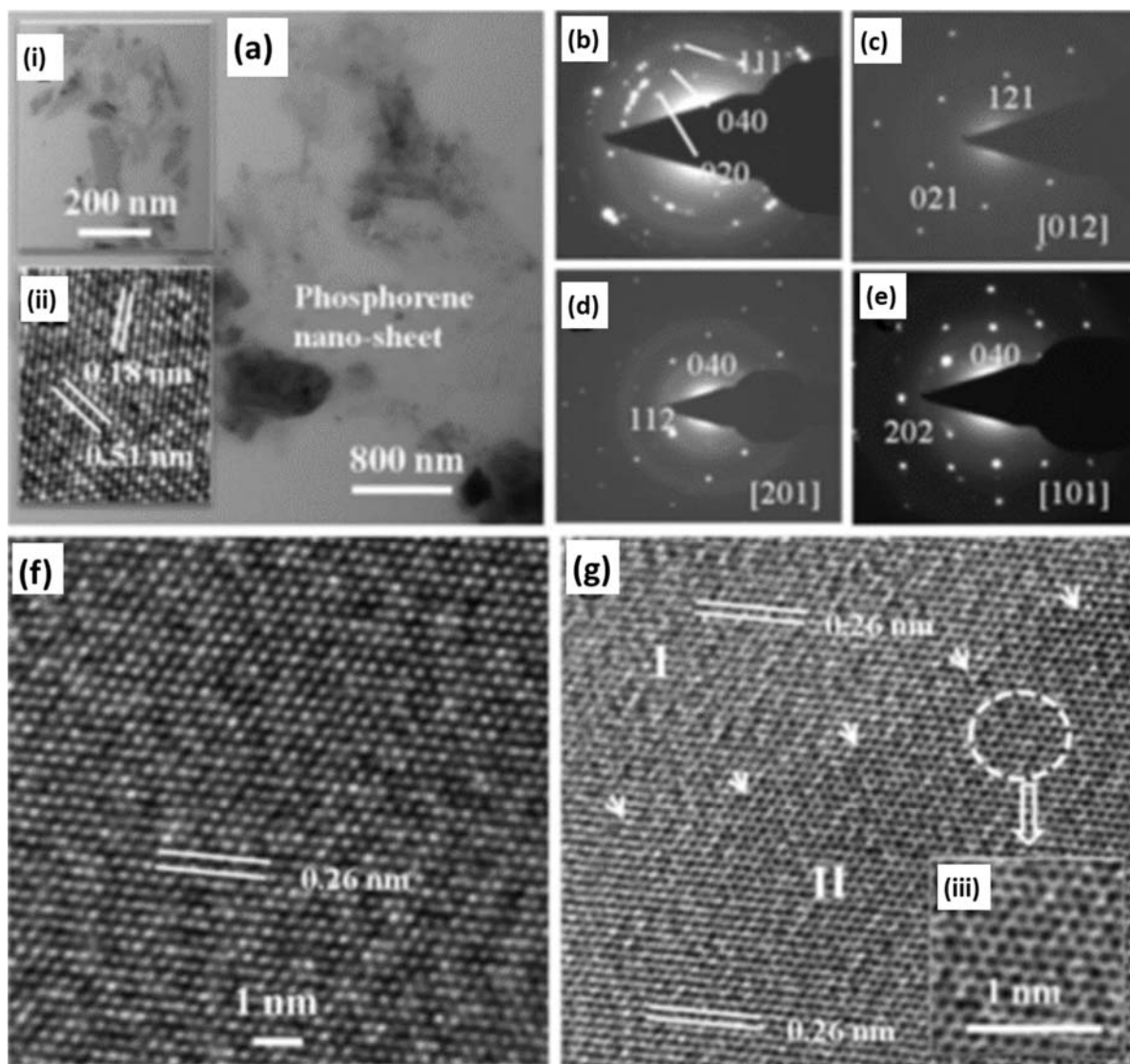


Figure IV.17 HRTEM of LB assembled phosphorene on TEM grids. (a) Thin sheets of phosphorene. Inset (i) Aggregate of thin sheets of phosphorene, (ii) Atomic scale image of nanosheets, (b–e) selected area electron diffraction patterns, (f) Atomic scale micrograph of phosphorene, (g) interface between two sheets of phosphorene, Inset (iii) Honeycomb microstructure of phosphorene [376].

High resolution transmission electron microscopy (HRTEM) is carried for the LB assembled phosphorene sheets transferred to the TEM grids (carbon coated copper grids). Phosphorene is

---

recognized by TEM imaging (Figure IV.17 (a)) and inset i shows that the phosphorene sheets are assembled. High resolution TEM image (inset ii in figure IV.17 (a)) depicts evolution of atomic plane with a regular spacing of about 0.51 nm and 0.18 nm with the miller indices ( $hkl$ ) of (020) and (112), respectively (crystal structure: orthorhombic, lattice constants:  $a = 0.331$  nm,  $b = 1.029$  nm,  $c = 0.4302$  nm, space group:  $Cmca$ , reference: JCPDS card no. 76-1961). Selective area diffraction (SAED) patterns are recorded corresponding to the image of aggregated phosphorene sheets (inset in figure IV.17 (a)) is shown in figure IV.17 (b). Figure IV.17 (b) depicts the presence of a set of Debye rings in reciprocal space and this is attributed to the important planes of orthorhombic crystal structure of phosphorene with ( $hkl$ ) indices as (020), (040), (111). A set of SAED patterns recorded for phosphorene nanosheets (Figure IV.17 (a)) is displayed in figure IV.17 (c-e). Single crystalline electron diffraction patterns with [012], [210] and [110] zone axes of orthorhombic crystal structure of phosphorene is depicted in figure IV.17 (c-e) clearly reveals that the individual sheets of phosphorene were well crystallized and atomic planes are well organized in the single crystalline nature with no evidence of structural disorder or oxidation. Figure IV.17 (f) illustrates the atomic scale image of the phosphorene with stacking of 040 plane, which corresponds to a inter-atomic separation of 0.26 nm. Figure IV.17 (g) depicts the boundary between phosphorene sheets, which is marked using arrows. Both sheets are well aligned with a inter-atomic separation of 0.26 nm. Figure IV.17 (g) inset shows the honey comb structure of phosphorene.

Semiconducting properties of the phosphorene investigated by fabricating a field-effect transistor (FET) device. The FET device was fabricated on a Si substrate with  $SiO_2$  (230 nm) layer as dielectric and gold patterning on top of the  $SiO_2$ . Si substrate acts as the gate, gold electrodes on top acts as the source and drain (Figure IV.18 (a)). A conducting channel between the gold electrodes (5  $\mu m$ ) is made by assembling phosphorene nanosheets on substrate (Figure IV.18 (b)) by Langmuir-blodgett assembly technique. Bridging between source and drain via phosphorene is shown figure IV.18 (c). Thickness of the phosphorene measure using AFM is about 4 nm. (Figure IV.18 (d)). The switching behaviour of the FET is measured at room temperature is shown in figure IV.18 (e). The back gate voltage  $V_{GS}$  was scanned from  $-10$  V to 0 V, keeping drain voltage  $V_{DS}$  as  $-1$  V. The maximum on state drain current  $I_{DS}$  is  $10^2 \mu A/\mu m$  while off-state current is  $10^{-2} \mu A/\mu m$  enabling a high on-off current modulation ratio of 104. Figure IV. 18 (f) represents the  $I_{DS}$  versus  $V_{DS}$  curve for different  $V_{GS}$  which says that current in few layer phosphorene FET can be controlled by providing a suitable gate voltage. Comparison of  $I_{on}/I_{off}$  ratio with the previous reported values <sup>[369, 377-378]</sup> gave an insight that the LB assembly is a suitable and convenient method for the fabrication of superior quality phosphorene thin films.

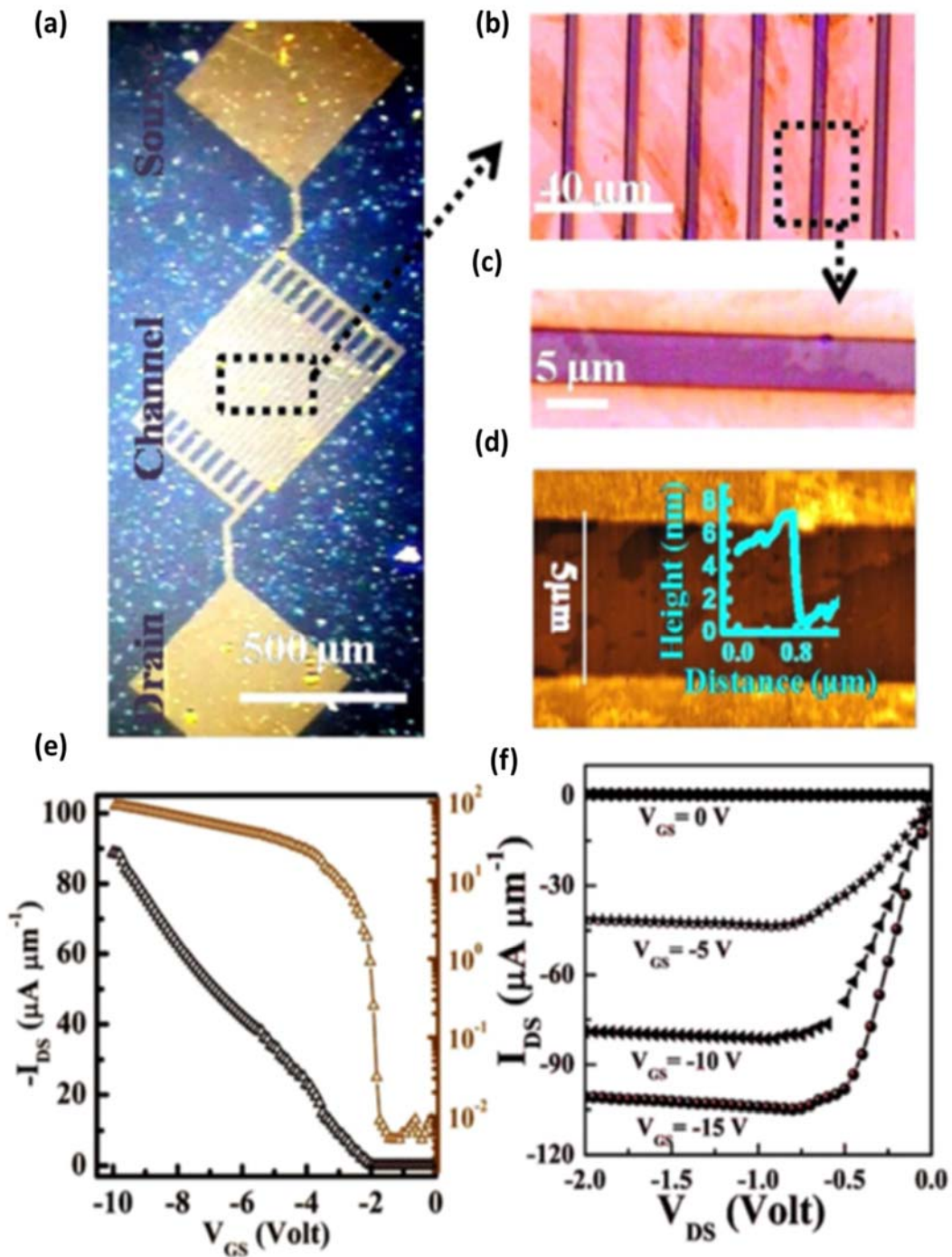


Figure IV.18 (a) Digital image of the device, (b) Optical image of channel, (c) Magnified optical image showing a connecting nanosheet between source and drain, (d) AFM of the device. Inset: Height profile of nanosheet, (e) Variation of drain current  $I_{\text{DS}}$  with gate voltage  $V_{\text{GS}}$  (left y-axis is the linear scale, and right y-axis is the logarithmic scale) and (f) Variation of drain current  $I_{\text{DS}}$  with the drain voltage  $V_{\text{DS}}$  for different gate voltages  $V_{\text{GS}}$  [376].

#### IV.4.3 Human embryonic kidney cells growth

The human embryonic kidney (HEK) cells growth work was carried in collaboration with Prof. Dr. rer. nat. Robert Stark and M. Phil. Asma Siddique at TU Darmstadt.

Stability of the BP-nanodots in human body systems permitting their use in biomedical applications [379-380]. Photodegradable character of black phosphorus to biocompatible phosphorus oxides further highlights its therapeutic potential against cancer [381]. Black phosphorus with small thickness and size have high reactivity with oxygen and water [382-384]. In the present work, HEK cells growth on exfoliated black phosphorous sheets was investigated.

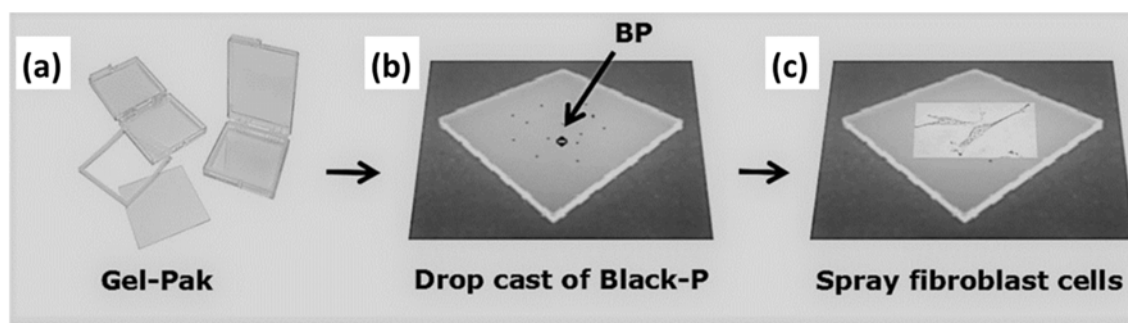


Figure IV.19 Procedure for the coating of BP-2 and fibroblast cells on PDMS gel pack.

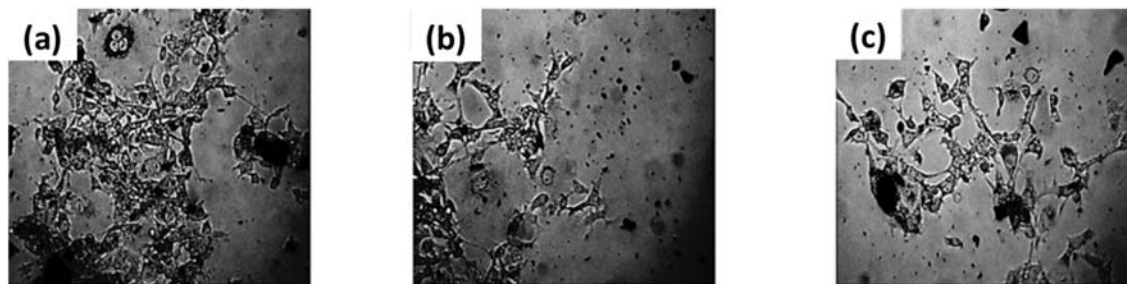


Figure IV.20 Photograph of the Fibroblast COS-7 cells cultured on black phosphorous (a) after first wash, (b) second wash and (c) third wash.

Fibroblast COS-7 cells were maintained in DMEM/Ham's growth media supplemented with 15% FCS and 1 mL Normocin (antibiotic) in Corning CellBIND tissue culture flask at 37 ° C in a CO<sub>2</sub> incubator. Black phosphorus exfoliated in ethanol was dropcasted over the gel pack. Then this was used as the substrate for the growth (figure IV.19). Cells from passage 30 were allowed to grow on the surface of material for 3 days. Then surfaces were washed with sterile phosphate-buffered saline (PBS) thrice and images were taken after washing (figure IV.20).

---

Zeiss AXIO Observer Z1 connected to a HSM Axiocam camera was used for imaging, and the images were processed using Axiovision SE64 software (Carl Zeiss Microscopy GmbH, Frankfurt, Germany). Growth of cells over the exfoliated black phosphorous is observed. The biocompatibility of this material is under investigation.

#### **IV.5 Conclusions**

Black phosphorus is successfully synthesized using bismuth flux method and chemical vapor transport reaction. The formation of black phosphorus is confirmed using Raman spectroscopy and X-ray diffraction pattern. The growth of HEK fibroblast cells on the black phosphorus confirms that it can be used as platform for different cells growth. Gas sensing application reveals the potential of black phosphorus for detection of toxic gases such as NO<sub>2</sub> and NH<sub>3</sub>. A high on-off current modulation ratio of 10<sup>4</sup> is achieved by Langmuir-Blodgett assembled phosphorene based field effect transistor. The results shows that Langmuir-Blodgett assembly is a suitable method to make phosphorene films.



---

## V SUMMARY AND OUTLOOK

The present thesis focus towards the synthesis and functional properties vertically aligned carbon nanotubes (VACNTs), graphene oxide (GO) and black phosphorus (BP) and their application in gas sensor, mechanical sensor, field-effect-transistor device and cell growth.

Water assisted chemical vapor deposition was employed for the growth of vertically aligned carbon nanotubes. Thin film deposition techniques such as atomic layer deposition and electron beam evaporation was employed for the buffer layer and catalyst layer (Al, Al<sub>2</sub>O<sub>3</sub> and Fe). CVD parameters were optimized for the growth of less defective impurity free VACNTs with diameter of the order of 4-6 nm. Height of the CNTs could be varied by changing the gas flow, time of synthesis and catalyst thickness.

VACNTs based microelectrode arrays were fabricated. Electrochemical measurements reveal a high electrochemical active surface area, capacity and low impedance, hence this could be useful in variety of sensor applications. VACNTs were used as substrate for neuron growth and the experiments reveals that the growth of neurons are dominant on side walls of the VACNTs than on the top.

Artificial hair cell type sensor (AHCTS) based on 3D structured vertically aligned carbon nanotube bundles was fabricated using chemical vapor deposition process. Their easy integration and lateral electrical contacting allowed multiple mechano-electrical sensing mechanisms. The mechanical properties of the VACNT bundles were investigated with respect to different substates as well as by tuning the bundle height. More over the compression or deflection of the central VACNT bundle changes the contact resistance to the shorter neighbouring bundles hence this 3D CNT sensor can detects the three dimensional forces. The Young's modulus of the AHCTS is in between 220 kPa and 1800 kPa, which was achieved by tuning the height of the VACNT bundles. The resistance decreases up to ~11% at 50  $\mu$ m deflection and the detection sensitivity is as low as 1  $\mu$ m, by employing a variable load system using Frey filaments. Bending of up to 90 ° with excellent repeatability and stability were observed. A stable deflection of AHCTS in contactless electrostatic method was observed for 10 million times. Application of AHCTS in artificial hearing technology is very promising.

Graphene oxide was synthesized by the oxidation of graphite. Interplanar spacing increased during oxidation due to intercalation of functional groups which is confirmed by X-ray diffraction pattern. High temperature reduction in hydrogen environment leads to the formation of reduced graphene oxide with few layers, high crystallinity and low amount of oxygen functional groups. Quantification of C/O ratio and functional groups were performed by XPS measurement.

---

Bacterial cellulose and graphene oxide composite aerogels were prepared and used for organic liquid absorption. GO aerogels can strongly interact both with water and organic solvents. The organic liquid absorption capacity of BC or BC/GO aerogels is used to derive porosity of aerogels. BC aerogels are more non-polar than BC/GO aerogels due to the presence of individual amphiphilic nano-scaled BC fibrils. BC/rGO aerogels could specifically absorb organic solvents and thus exhibited increased non-polarity and oleophilicity than BC/GO aerogels.

Black phosphorus is successfully synthesized from red phosphorus using bismuth flux method and chemical vapor transport reaction. The formation of black phosphorus is confirmed using Raman spectroscopy and X-ray diffraction pattern. The growth of HEK fibroblast cells on black phosphorus is achieved hence it can be used as platform for different cells growth. Gas sensing performance of black phosphorus towards  $\text{NH}_3$  and  $\text{NO}_2$  is studied. Exposure to an increasing concentration of  $\text{NO}_2$  in the range of 10 – 50 ppm results in a higher response of the devices up to -14 %. Further increasing the concentration of  $\text{NO}_2$  (50 – 100 ppm) does not significantly change the chemiresistors response, showing a maximum value of -15 %. A higher sensor response to an increasing concentration of  $\text{NH}_3$  can only be observed in the range of 10–20 ppm. The maximum value for the minimum response of black phosphorus chemiresistors to  $\text{NH}_3$  (20 – 50 ppm) is 3 %.

Black phosphorus was exfoliated to phosphorene using liquid exfoliation technique. High resolution TEM measurements were carried to reveal the presence of crystalline ultrathin non-oxidised phosphorene nanosheets. The Langmuir-blodgett assembly technique was used to assemble phosphorene nanosheets over large area. High on-off current modulation ratio of  $10^4$  is achieved in Langmuir-blodgett assembled phosphorene based field effect transistor. The results shows that Langmuir-blodgett assembly is a suitable method to make phosphorene films.

---

## VI EXPERIMENTAL SECTION

### VI.1 Characterization techniques

X-ray diffraction patterns were recorded using the X-ray diffractometer, STOE Stadi P, position sensitive detector with Cu K $\alpha$  line as the X-ray source ( $\lambda=1.54 \text{ \AA}$ ). The curve is recorded between  $2\theta \approx 0$  to  $80^\circ$ .

Raman spectra were recorded on Horiba LabRam HR 800 micro Raman spectrometer (Horiba Jobin Yvon, GmbH, Bensheim, Germany) equipped with an air-cooled Argon ion laser (emission line,  $\lambda=514.5 \text{ nm}$ ).

Scanning electron microscopy (SEM) performed on a Philips XL30 FEG high-resolution scanning electron microscope (HR-SEM) (SEMTECH Solutions, Inc., North Billerica, MA) operating at 2 kV, samples were coated with thin palladium/platinum film. Specimen for FESEM imaging was prepared by coating the sample on carbon tape. FESEM Imaging was carried out in high vacuum mode.

XPS measurements were performed using a K-Alpha XPS spectrometer (Thermo Fisher Scientific, East Grinstead, UK). XPS analysis was carried out by irradiating the sample by monochromated Al K $\alpha$  X-ray source. CASA XPS software was used for peak fitting and analysis.

FT IR-ATR was conducted on Spectrum One FT IR Spectrometer (PerkinElmer, Massachusetts, USA) at room temperature (RT) between 4000 and 600  $\text{cm}^{-1}$  with a resolution of 4  $\text{cm}^{-1}$ . Scans of 32 were accumulated. The spectra were baseline-corrected with 20 iterations and 200 statistical baseline points using OPUS Ver. 6.5 (Bruker Optics, Ettlingen, Germany).

N<sub>2</sub> adsorption (77 K) measurements were carried out on a Quantachrome NOVA3000e system. The samples were heated in vacuum overnight at 150 °C. Surface area was calculated by using multipoint BET method. Pore size distributions were determined by using non-local density functional theory (NLDFT) kernel assuming a slit/cylindrical pore, available in the software NOVAVin10.

High resolution transmission electron microscopy (HRTEM) measurements were carried out on a FEI Tecnai F20 G2 operated at 200 kV at ERC Jülich.

### VI.2 Thin film deposition units

#### VI.2.1 Electron beam (e-beam) evaporation unit

A schematic and photograph of the Home-made electron beam set up is shown in figure VI.1. It consists of an electron gun, high voltage power supply (G. V. Planer Ltd. England), filament current controller, vacuum system, Cressington MTM-10 thickness monitor.

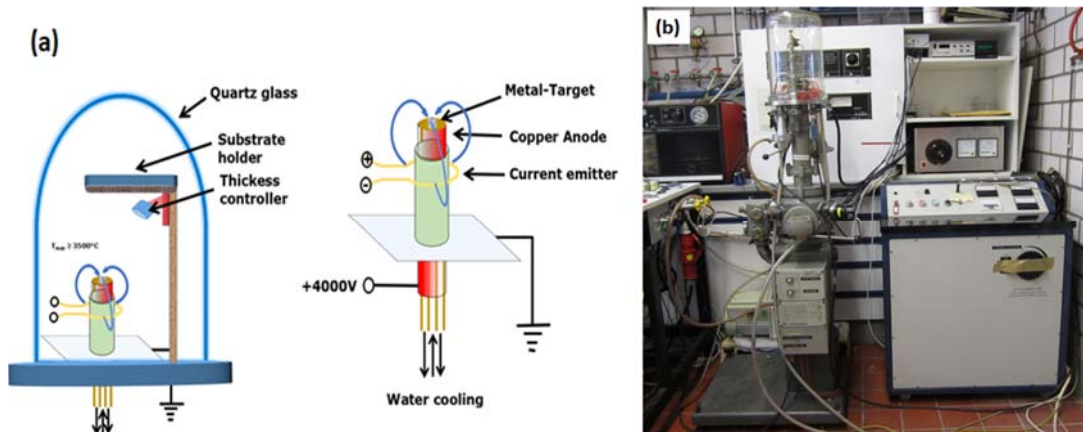


Figure VI.1 (a) Schematic and (b) photograph of the e-beam set up.

## VI.2.2 Atomic layer deposition (ALD) unit

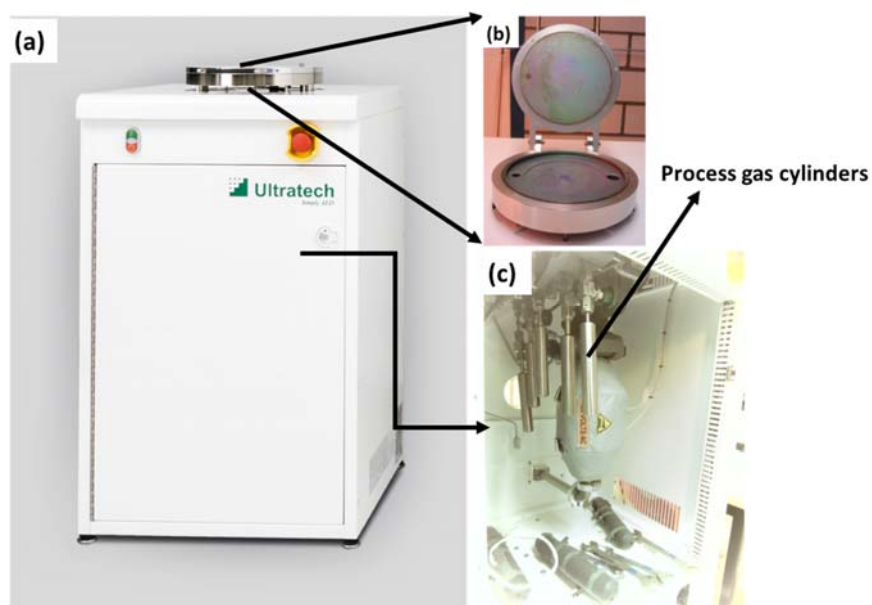


Figure VI.2 (a) photograph of the ALD unit, (b) inside view of the ALD process chamber and (c) inside view of the ALD cabinet.

A photograph of the ALD unit (Cambridge Ultratech Savannah S 100 System) is shown in figure VI.2. It consists of a process chamber (figure VI.2 (b)) and cabinet with process gas cylinders (figure VI.2 (c)). A savannah software is used to control the process.

### VI.2.3 Catalytic chemical vapor deposition (CVD) unit

The schematic and photograph of a CVD set up is shown in figure VI.3 (a and b). The furnace consists of three zones. Commercially, available mass flow controllers (MKS Instruments, 179B type flow meters with controller unit 647B) are used to flow gases. Water is allowed into the furnace by passing argon (carrier gas) through inbuilt deionized water bubbler. The water sensor displays the dew points of water. The dew point -38.5 to -39 corresponds 150 to 141 ppm of water, argon (99.996%), hydrogen (99.9990%), ethene (99.90%) and ppm quantities of water vapor passed together through a hygrometer (Easidew Dew-Point Transmitter EA2, range -100/+20, Michell Instrument) to the furnace.

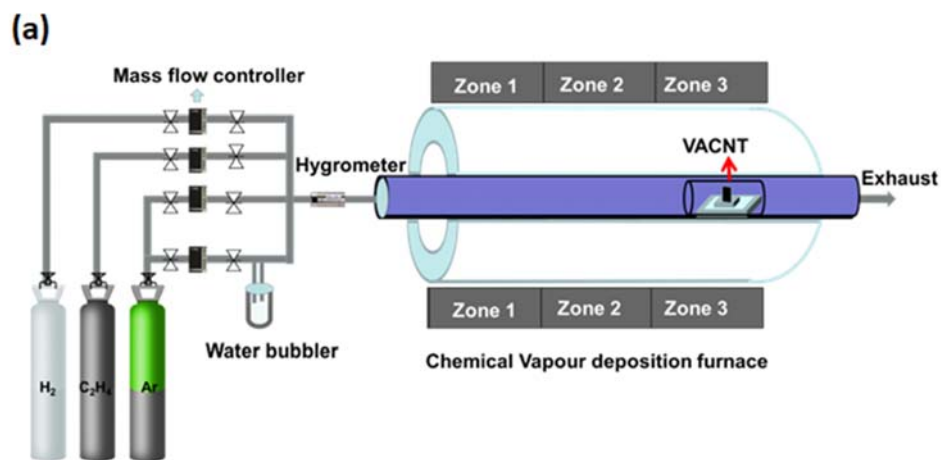


Figure VI.3 (a) Schematic and (b) photograph of the chemical vapor deposition unit.

---

### **VI.3 Vertically aligned carbon nanotubes**

Synthesis of vertically aligned carbon nanotubes using water assisted chemical vapor deposition technique is discussed below.

#### **VI.3.1 Deposition of aluminium and iron**

High purity aluminium pellets (99.999%, EVOCHEM GmbH, Germany) and iron pieces (99.999%, abcr GmbH, Germany) were deposited by e-beam evaporation technique. Aluminium thickness of 10-15 nm and Fe thickness of 0.6-1.8 nm was deposited. In detail, premelted ingot of metal (Al/Fe) was placed in the water cooled copper hearth inside the chamber and substrate was mounted to the substrate holder. Then the reaction flask is evacuated to a pressure of  $5 \times 10^{-6}$  mbar to allow the passage of electrons from electron source (tungsten filament) to metal ingot. Enter the density of the metal in the thickness monitor device. A current of 55-60 A was applied to the tungsten filament. When the filament become hot enough, it emit electrons. The electron beam generated is focussed to a spot size of a 5-8 mm diameter on the metal ingot using high voltage (~ 2kV). When the electron beam strikes the metal, kinetic energy of the electrons is converted in to thermal energy, which helps to melt the metal ingot. Then, evaporated metal atoms deposit on the substrate (Si/SiO<sub>2</sub>) to make a thin film. Thickness of the film is controlled by a Cressington MTM-10 quartz crystal thickness monitor and shutter. At the end of the deposition switch off the high voltage supply and slowly turned off the filament current.

#### **VI.3.2 Growth of VACNTs**

Vertically aligned carbon nanotubes were grown using water assisted chemical vapor deposition (WACVD) technique. The substrate used for the growth is a Si wafer with 600 nm SiO<sub>2</sub> coating on it. Further, a thin layer of Al coating was done using electron beam evaporation (e-beam) technique followed by a thin layer of iron is also coated using electron beam evaporation technique. The substrate placed on a silicon plate was inserted in to third zone of the furnace. The gas outlet valve should be connected to the fume hood. The growth temperature is about 820 °C and at this temperature, argon (99.996%), hydrogen (99.9990%), ethene (99.90%) and ppm quantities of water vapor passed together. Different steps followed for the synthesis of VACNTs are summarized in table VI.1. In step 1 (heating), switch on argon (600 sccm) and hydrogen (400 sccm). Set the temperature to 820 °C and begin the heating at a rate of 41 °C/minute. Step 2 (water). In step 2 (water), no humidity is inserted. In Step 3 (Growth), ethene (75 sccm), water (150 ppm), hydrogen (100 sccm) and argon (500 sccm) passed together for 5 minutes at 820 °C and VACNTs are grown in this step3. In step 4 (flush), hydrogen and ethene was stopped. Water was passed at 820 °C for

one minute. In step 5 (cooling), water and heating of the furnace is stopped. Argon was allowed till the temperature reaches below 200°C. Also, influence of various growth parameters such as hydrogen, ethene, water, catalyst and time is discussed below.

Table VI.1 Reaction steps in the synthesis of VACNTs

Reaction Step		Catalyst formation	H <sub>2</sub> O	Growth	Flush	Cool
Time (min.)		20		5	1	30
Temperature (°C)						
Gas (sccm)	Ar	600		500	500	250
	H <sub>2</sub>	400		100		
	C <sub>2</sub> H <sub>4</sub>			75		
	H <sub>2</sub> O				-38.5	

Influence of hydrogen in growth of VACNT is investigated by changing the flow rate of hydrogen from 0 to 300 sccm and keeping all other growth parameters such as Argon (500 sccm), ethene (100 sccm), water (150 ppm), Fe thickness (1.4 nm), Al thickness (10 nm), growth temperature (820 °C) and growth time (5 minutes) constant. Scanning electron microscopy images and Raman spectra have been recorded for all the samples is shown in figure VI.4 and VI.5 (a). I<sub>D</sub>/I<sub>G</sub> ratio estimated from Raman spectra and height is estimated from SEM images is shown in figure VI.5 (b). A low I<sub>D</sub>/I<sub>G</sub> ratio and highest height is achieved when the hydrogen flow rate was 100 sccm. When the hydrogen flow was above 100 sccm height is decreased and I<sub>D</sub>/I<sub>G</sub> ratio is increased.

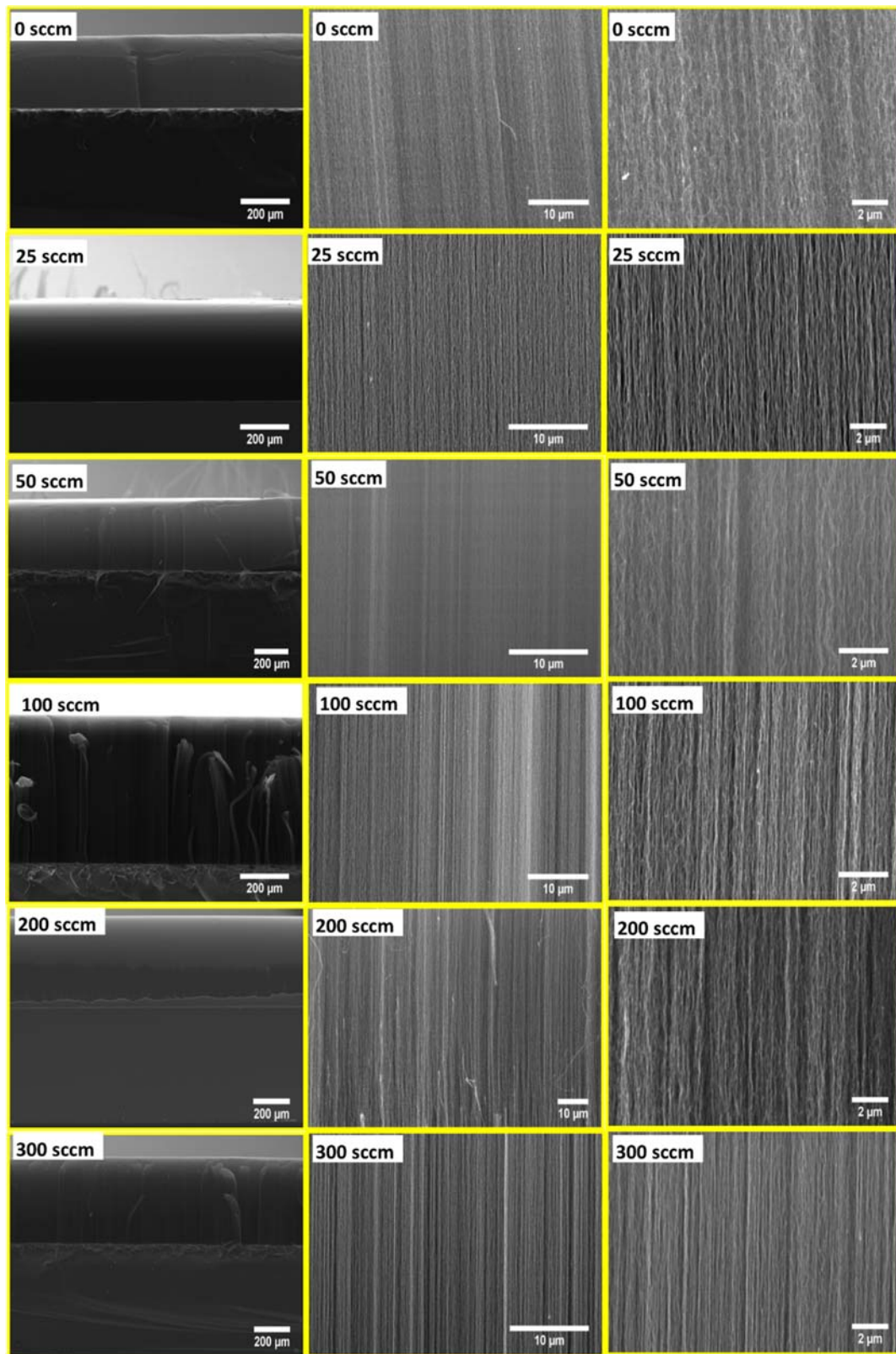


Figure VI.4 SEM images of the VACNTs grown in different hydrogen flow rate at three magnifications (scale bar=200 μm, 10 μm and 2 μm); keeping other conditions constant.



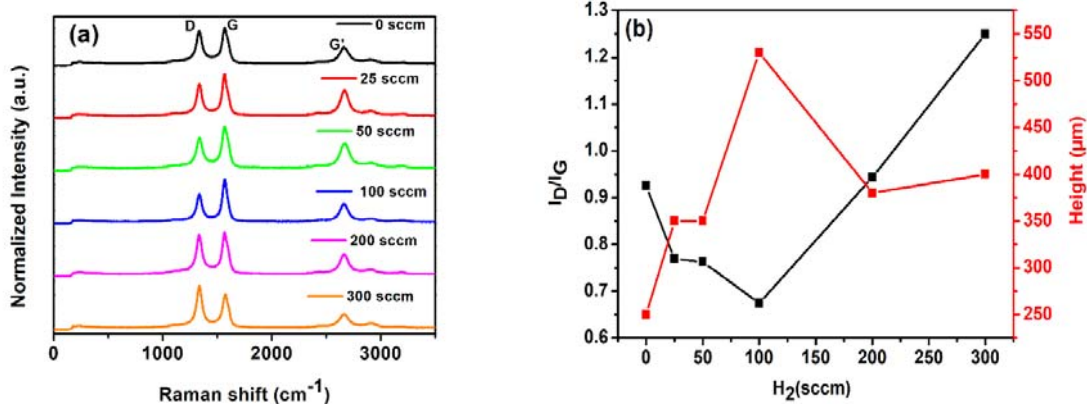


Figure VI.5 (a) Raman spectra of VACNTs with different hydrogen flow rate, (b)  $I_D/I_G$  ratio and height of the VACNTs with different hydrogen flow rate; keeping other parameters constant.

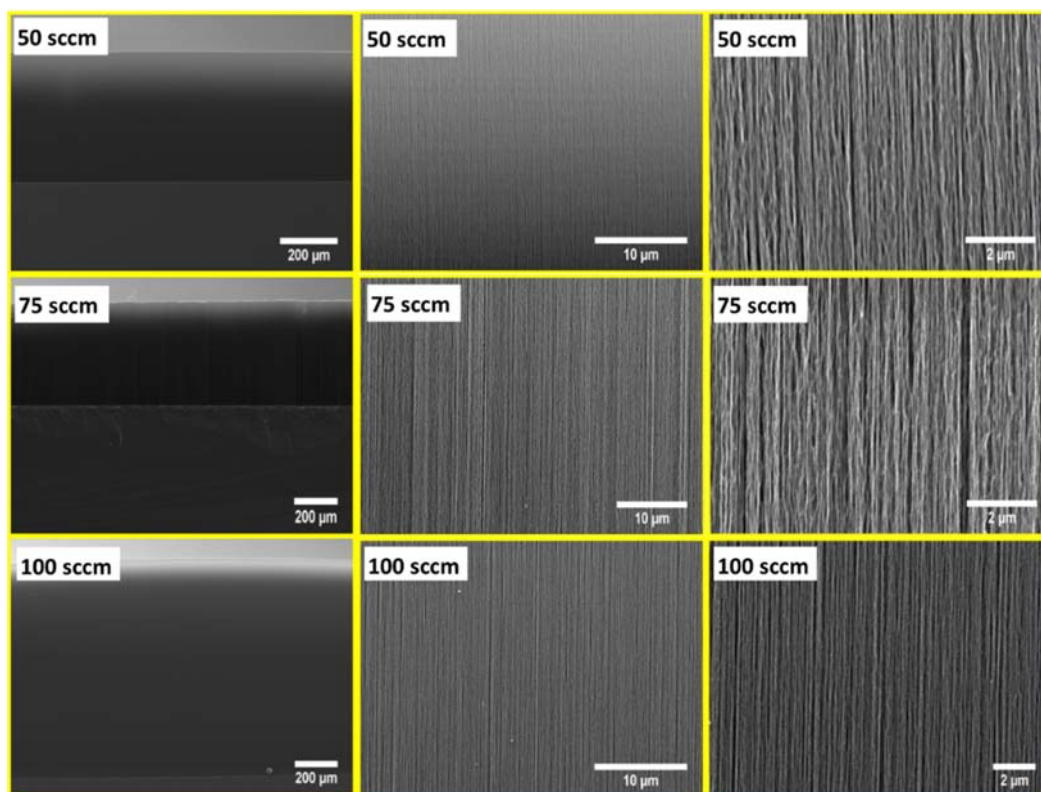


Figure VI.6 SEM images of the VACNTs grown in different ethene flow rate at three magnifications (scale bar=200 μm, 10 μm and 2 μm); keeping other conditions constant.

Hydrogen has an impact in the decomposition rate of carbon source (ethene)<sup>[158]</sup>. So an optimum hydrogen and carbon ratio is required for the growth of high quality carbon nanotubes. Influence of the flow rate of ethene is investigated by changing its flow rate from 50 to 100 sccm keeping other growth parameters such as Argon (500 sccm), hydrogen (100 sccm), water (150 ppm), Fe thickness

(1.4 nm), Al thickness (10 nm), growth temperature (820 °C) and growth time (5 minutes) constant. SEM images and Raman spectra of the samples is shown in figure VI.6 and VI.7 (a).  $I_D/I_G$  ratio estimated from Raman spectra and height is estimated from SEM images is shown in figure VI.7 (b).

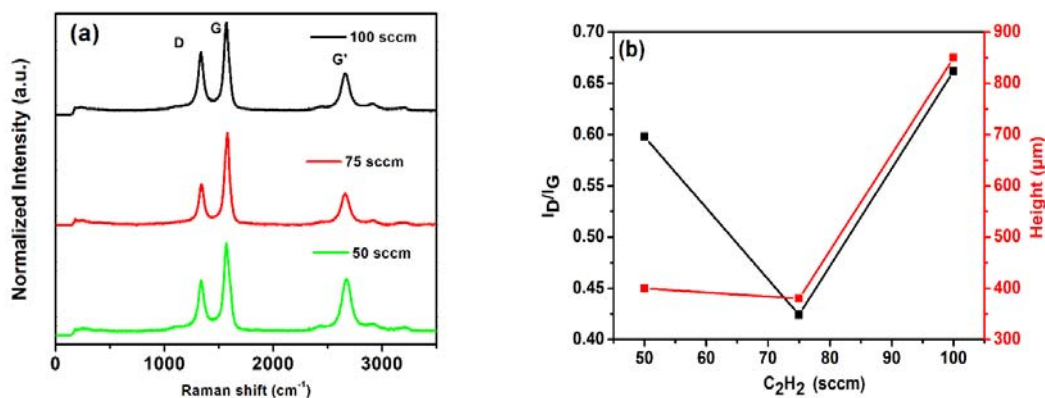


Figure VI.7 (a) Raman spectra of VACNTs with different ethene flow rate, (b)  $I_D/I_G$  ratio and height of the VACNTs with different ethene flow rate; keeping other parameters constant.

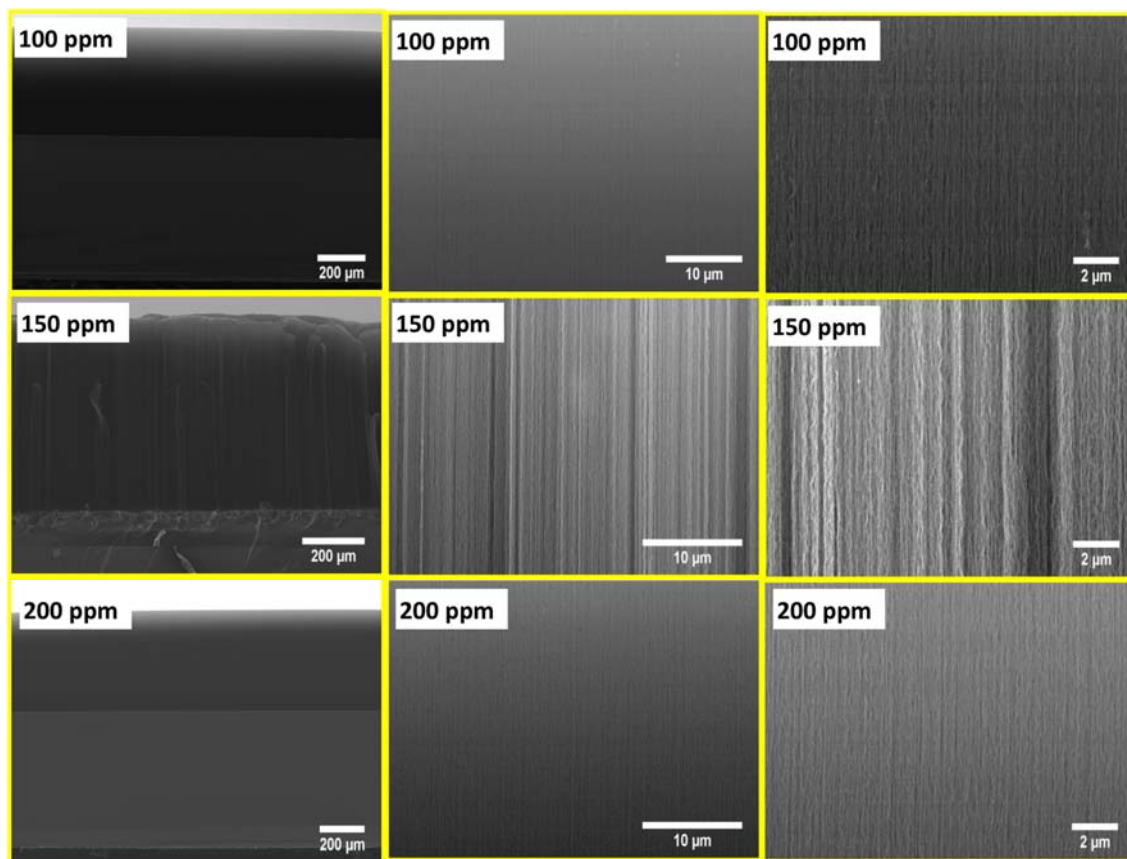


Figure VI.8 SEM images of the VACNTs grown in different water amount at three magnifications (scale bar=200  $\mu m$ , 10  $\mu m$  and 2  $\mu m$ ); keeping other conditions constant.

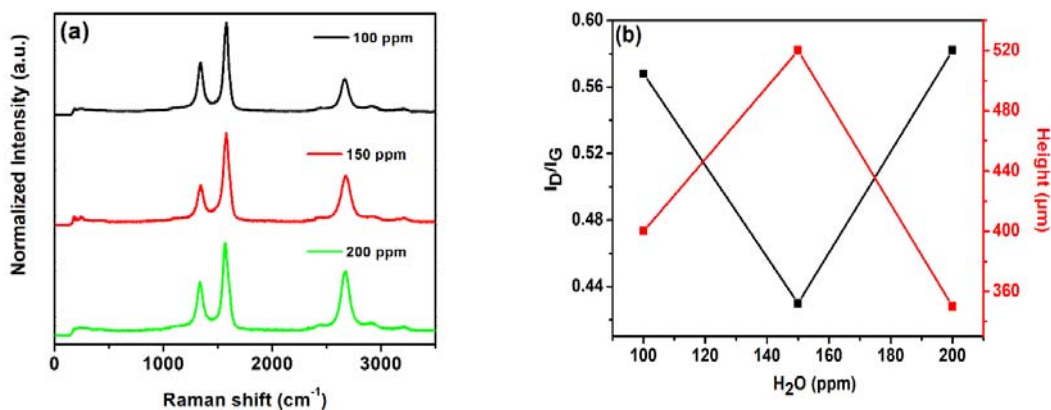


Figure VI.9 (a) Raman spectra of VACNTs with different water amount, (b)  $I_D/I_G$  ratio and height of the VACNTs with different water amount; keeping other parameters constant.

Water oxidizes the amorphous carbon deposited on the catalyst hence life time of the catalyst can be enhanced. Influence of the water is investigated by changing its water vapor amount from 100 to 200 ppm keeping other growth parameters such as Argon (500 sccm), hydrogen (100 sccm), ethene (75 sccm), Fe thickness (1.4 nm), Al thickness (10 nm), growth temperature (820 °C) and growth time (5 minutes) constant. SEM images and Raman spectra for the samples are shown in figure VI.8 and VI.9 (a).  $I_D/I_G$  ratio calculated from Raman spectra and height measured using SEM is shown in figure VI.9 (b).

Influence of catalyst (Fe) thickness is investigated by changing the it from 0.6 nm to 1.8nm with step of 0.2 nm keeping other growth parameters such as Argon (500 sccm), hydrogen (100 sccm), ethene (75 sccm), water (150 ppm), Al thickness (10 nm), growth temperature (820 °C) and growth time (5 minutes) constant. SEM images and Raman spectra of the samples is shown in figure VI.10 and VI.11 (a).  $I_D/I_G$  ratio and height of VACNTs are shown in figure VI.11 (b). Lowest  $I_D/I_G$  ratio is observed when the catalyst thickness was about 1.6 nm.

Influence of growth time is investigated by changing it from 1 minutes to 10 minutes, keeping other growth parameters such as Argon (500 sccm), hydrogen (100 sccm), ethene (75 sccm), water (150 ppm), Al thickness (10 nm), Fe thickness (1.6 nm), growth temperature (820 °C) constant. SEM images and Raman spectra of the samples are shown in figure VI.12 and VI.13 (a).  $I_D/I_G$  ratio estimated from Raman spectra and height is estimated from SEM images is shown in figure VI.13 (b). It was observed that, height of CNT increased gradually with increase in growth time. A height of 900  $\mu\text{m}$  is achieved when the growth time was 10 minutes.

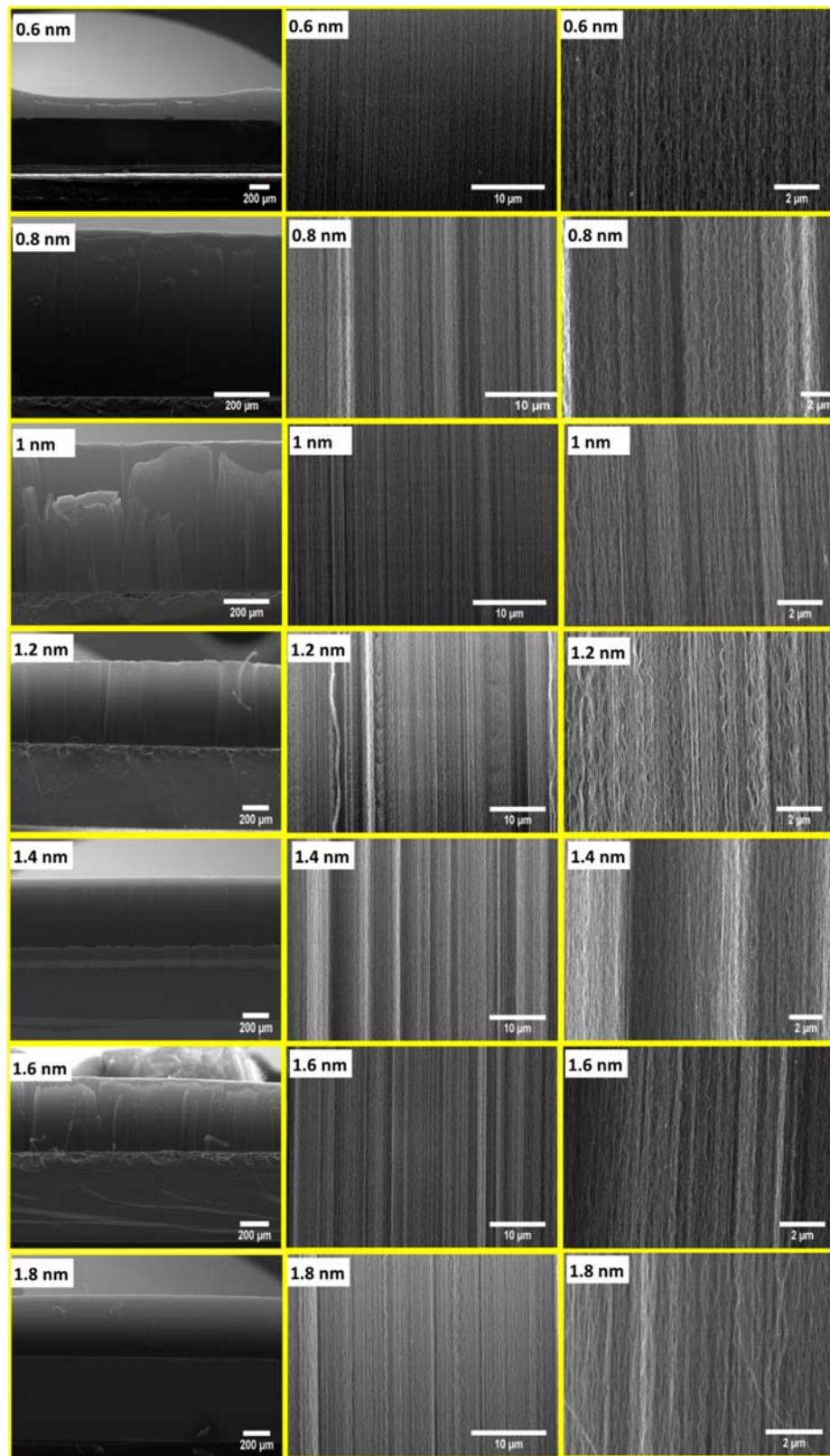


Figure VI.10 SEM images of the VACNTs grown in different catalyst thickness (Fe) at three magnifications (scale bar=200 μm, 10 μm and 2 μm); keeping other conditions constant.

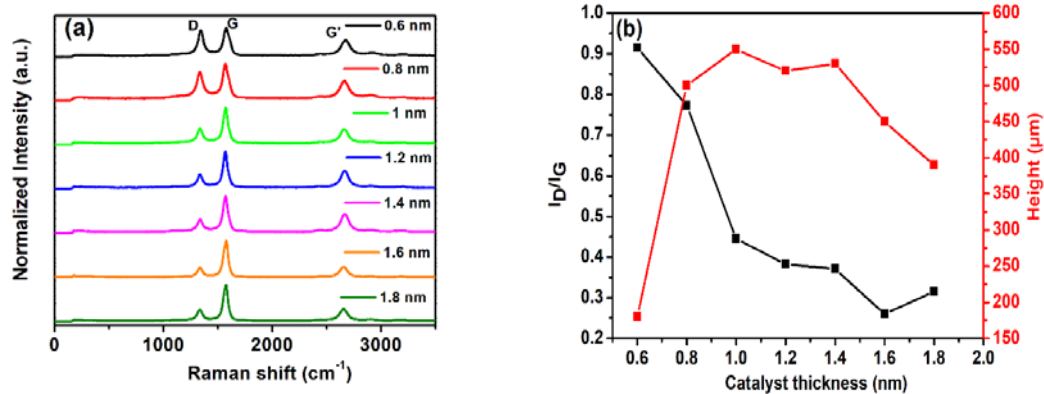


Figure VI.11 (a) Raman spectra of VACNTs with different catalyst thickness, (b)  $I_D/I_G$  ratio and height of the VACNTs with different catalyst thickness; keeping other parameters constant.

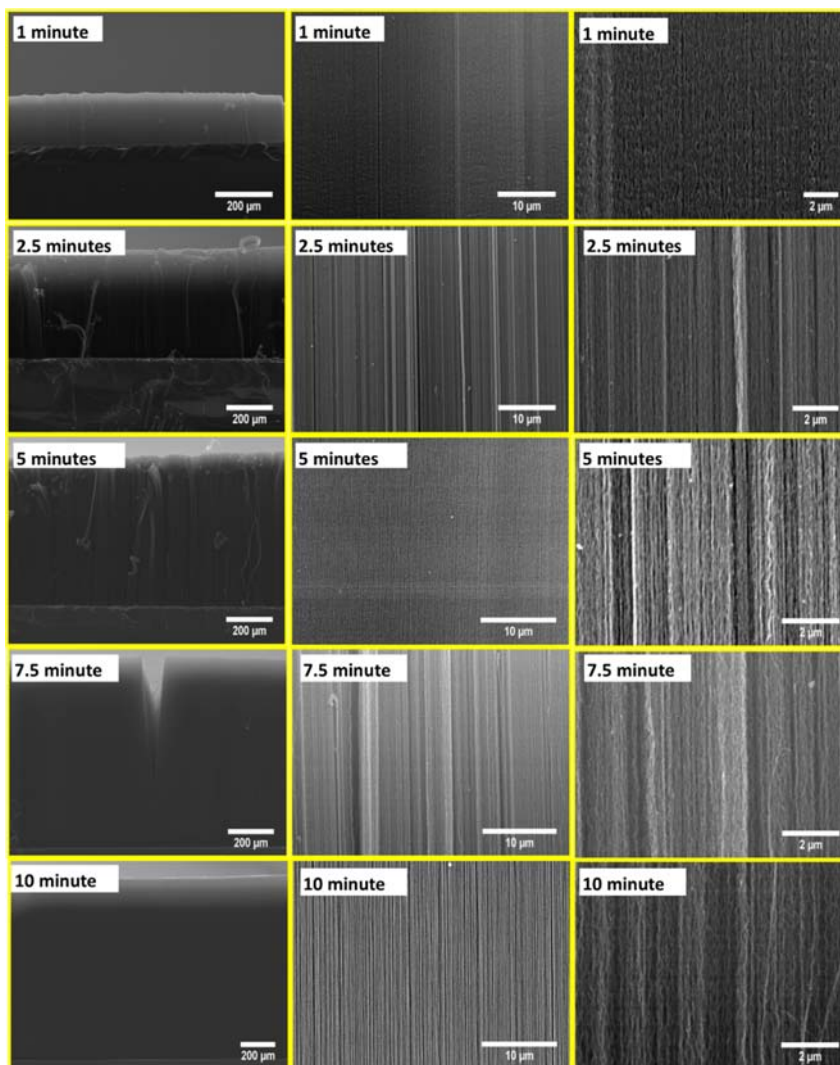


Figure VI.12 SEM images of the VACNTs grown in different growth time at three magnifications (scale bar=200 μm, 10 μm and 2 μm); keeping other conditions constant.

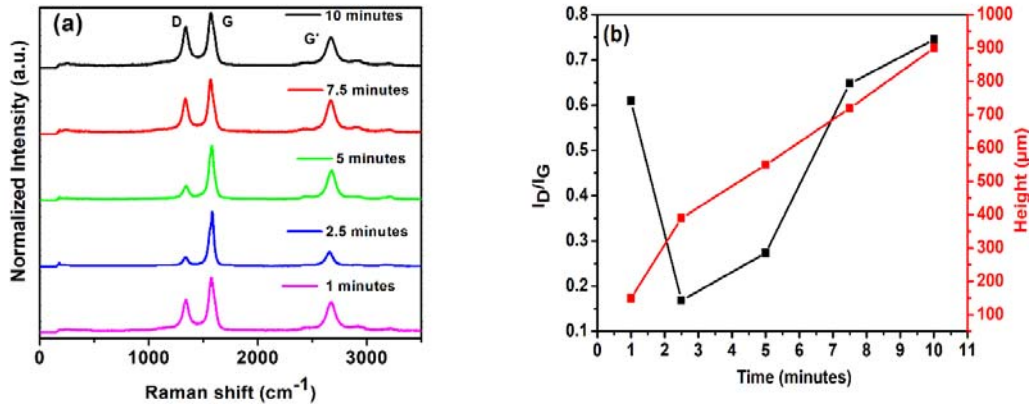


Figure VI.13 (a) Raman spectra of VACNTs with different growth time, (b)  $I_D/I_G$  ratio and height of the VACNTs with growth time; keeping other parameters constant.

### VI.3.3 Deposition of aluminium oxide

Atomic layer deposition is technique used to deposit thin films from vapor phase. Control over composition is possible in ALD compared to other physical vapour deposition technique due to sequential, self-saturating gas-surface reaction control. Thickness control is possible by layer by layer deposition. Moreover, ALD process is happening at modest temperatures ( $< 300\text{ }^\circ\text{C}$ ). High aspect ratio films can be prepared through this process. [385]

$\text{Al}_2\text{O}_3$  thin films with thickness 10-40 nm were deposited over Si/SiO<sub>2</sub> substrate using atomic layer deposition reactor (Cambridge Ultratech Savannah S 100 System). Chemicals used are Trimethylaluminium (Strem Chemicals) and Water (HPLC grade, Sigma Aldrich), Argon is from Alphagaz (99,9999 % purity). Deposition was carried at a temperature of  $200\text{ }^\circ\text{C}$  and at a pressure of less than 1 torr using water and Trimethylaluminium as the precursors. The pulse times for each Trimethylaluminium and water are 0.015 s. Purge time of Argon between the pulses is 5 seconds and the flow rate of argon is 20 sccm. Number deposition cycle varied from 100 to 400.

Figure VI.14 shows the schematic of the processing steps of aluminium oxide deposition using ALD process. Substrate with adsorbed water molecules (*substrate-O-H*) is placed in the ALD reaction chamber and Trimethylaluminium (TMA) is pulsed into the reaction chamber followed by the pulsed TMA reacts with OH groups and form methane as byproduct. This reaction continues until the whole whole surface is passivated (step 1, 2 and 3)



Further, TMA and water vapor ( $\text{H}_2\text{O}$ ) is pulsed into the reaction chamber. Reaction of  $\text{H}_2\text{O}$  with the

dangling methyl groups on the new surface results aluminum- oxygen (Al-O) bridges and hydroxyl surface groups, TMA pulse gives methane as the reaction product. (step 4,5,6)

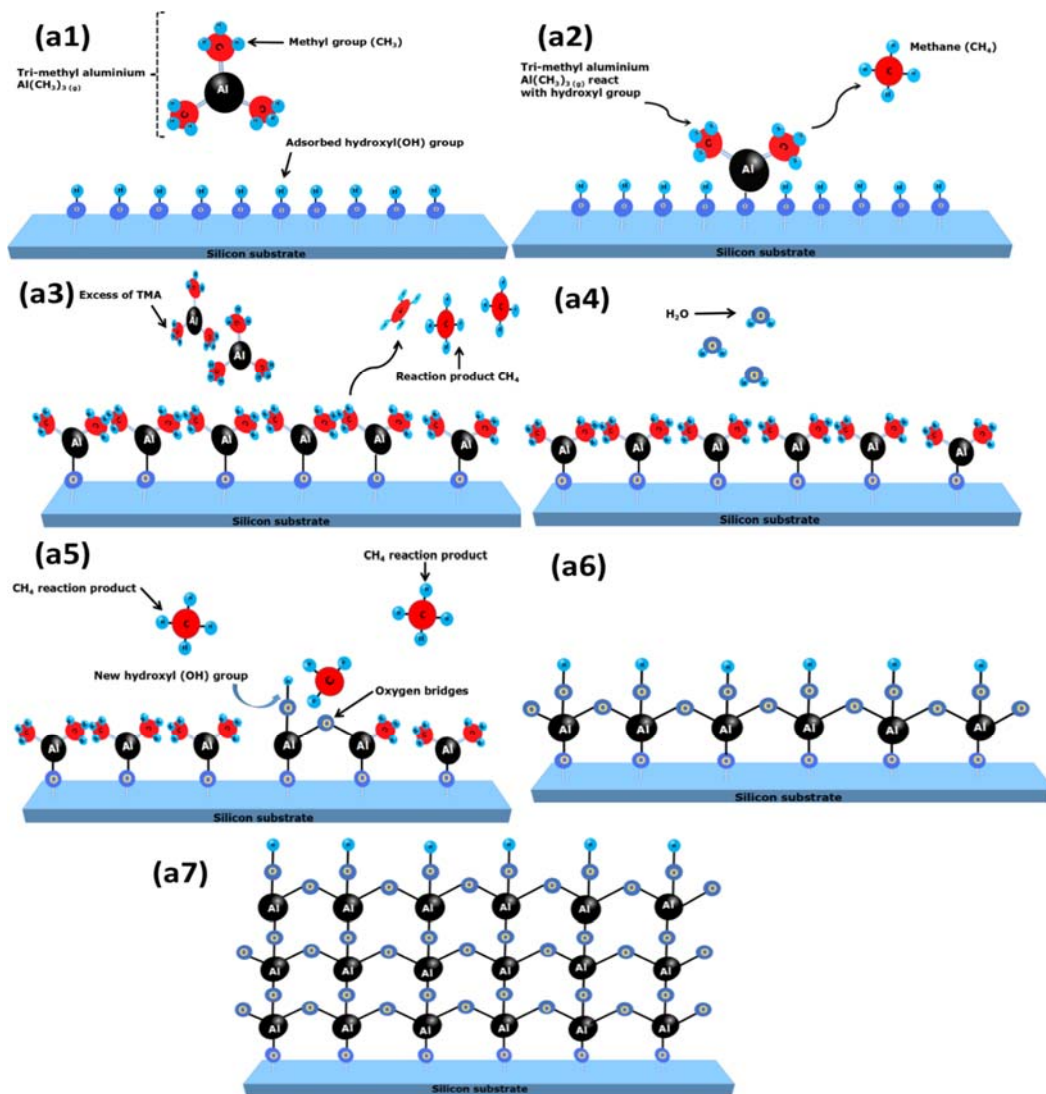
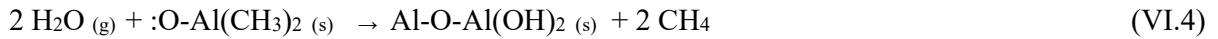
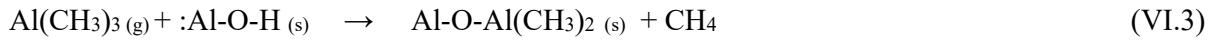
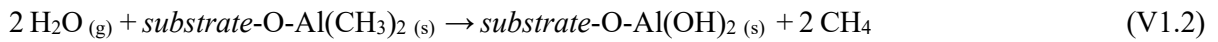


Figure VI.14 Schematic of the atomic layer deposition of  $\text{Al}_2\text{O}_3$ <sup>[386]</sup>.

### VI.3.4 Growth of VACNTs

Influence of  $\text{Al}_2\text{O}_3$  thickness deposited by ALD is investigated by changing its thickness from 10 to 50 nm and keeping other growth parameters such as Argon (500 sccm), hydrogen (100 sccm), ethene (75 sccm), water (150 ppm), Fe thickness (1.4 nm), growth temperature (820 °C) and growth time (5 minutes) constant. SEM images and Raman spectra of the samples are shown in figure VI.15 and VI.16 (a).  $I_D/I_G$  ratio height and height of VACNTs are shown in figure VI.16 (b).

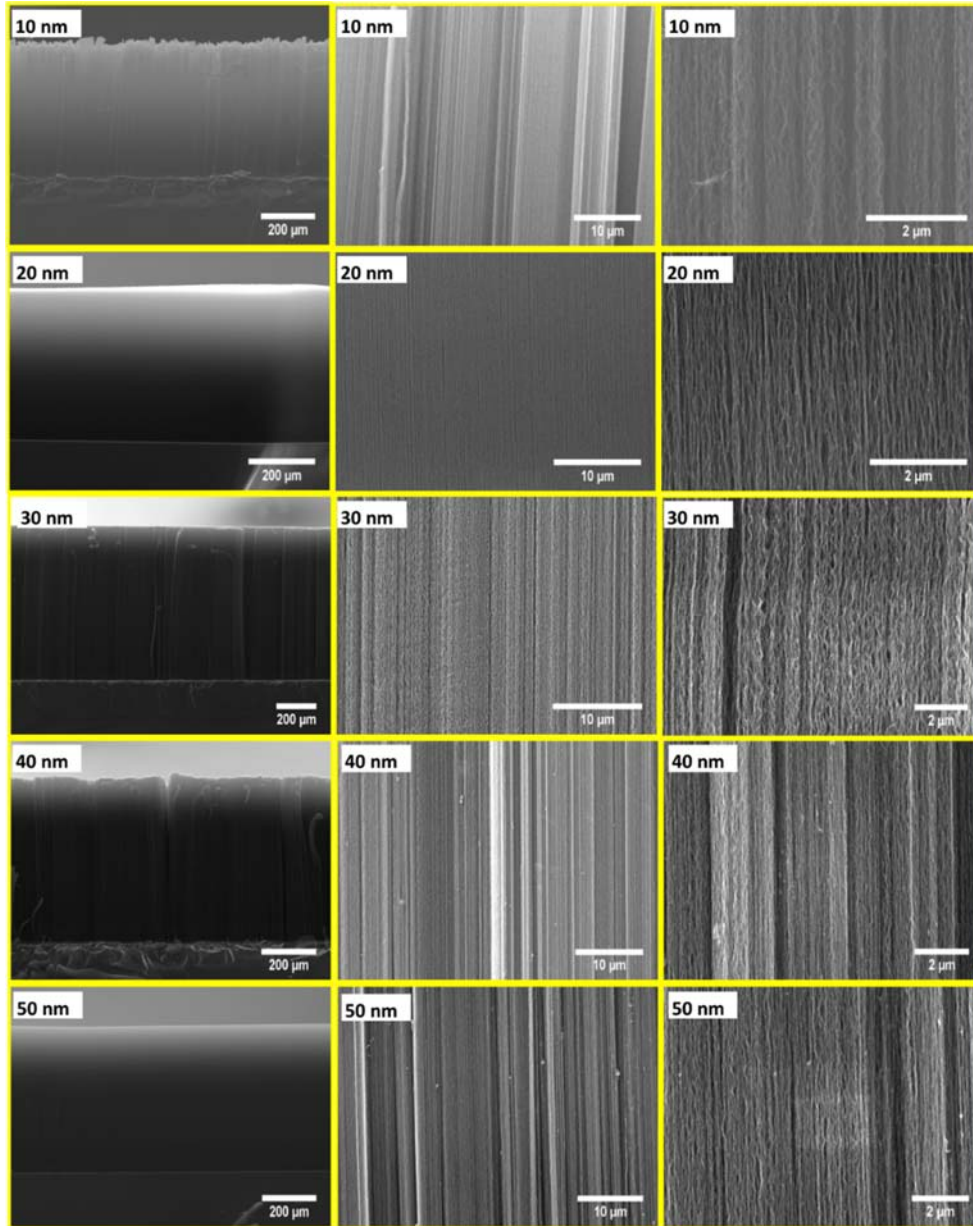


Figure VI.15 Scanning electron microscopy images of the VACNTs grown in different  $\text{Al}_2\text{O}_3$  thickness at three magnifications (scale bar=200  $\mu\text{m}$ , 10  $\mu\text{m}$  and 2  $\mu\text{m}$ ); keeping other conditions constant.



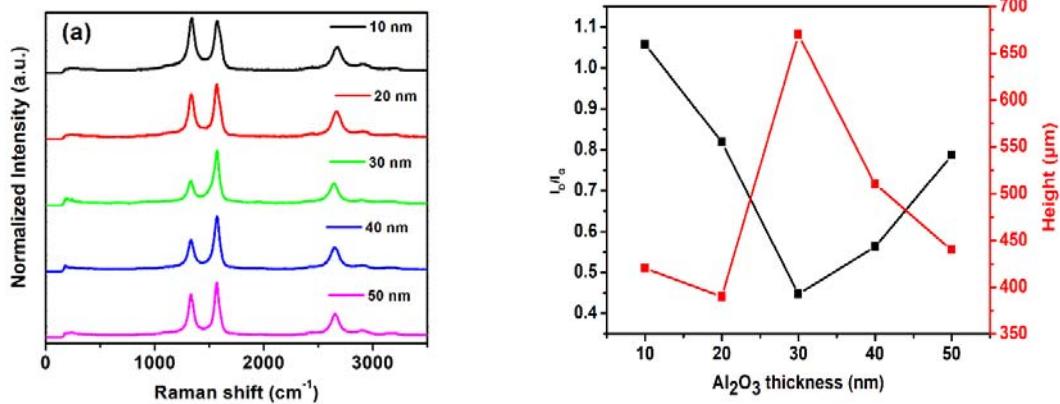


Figure VI.16 (a) Raman spectra of VACNTs with different Al<sub>2</sub>O<sub>3</sub> thickness, (b) I<sub>D</sub>/I<sub>G</sub> ratio and height of the VACNTs with different Al<sub>2</sub>O<sub>3</sub> thickness; keeping other parameters constant.

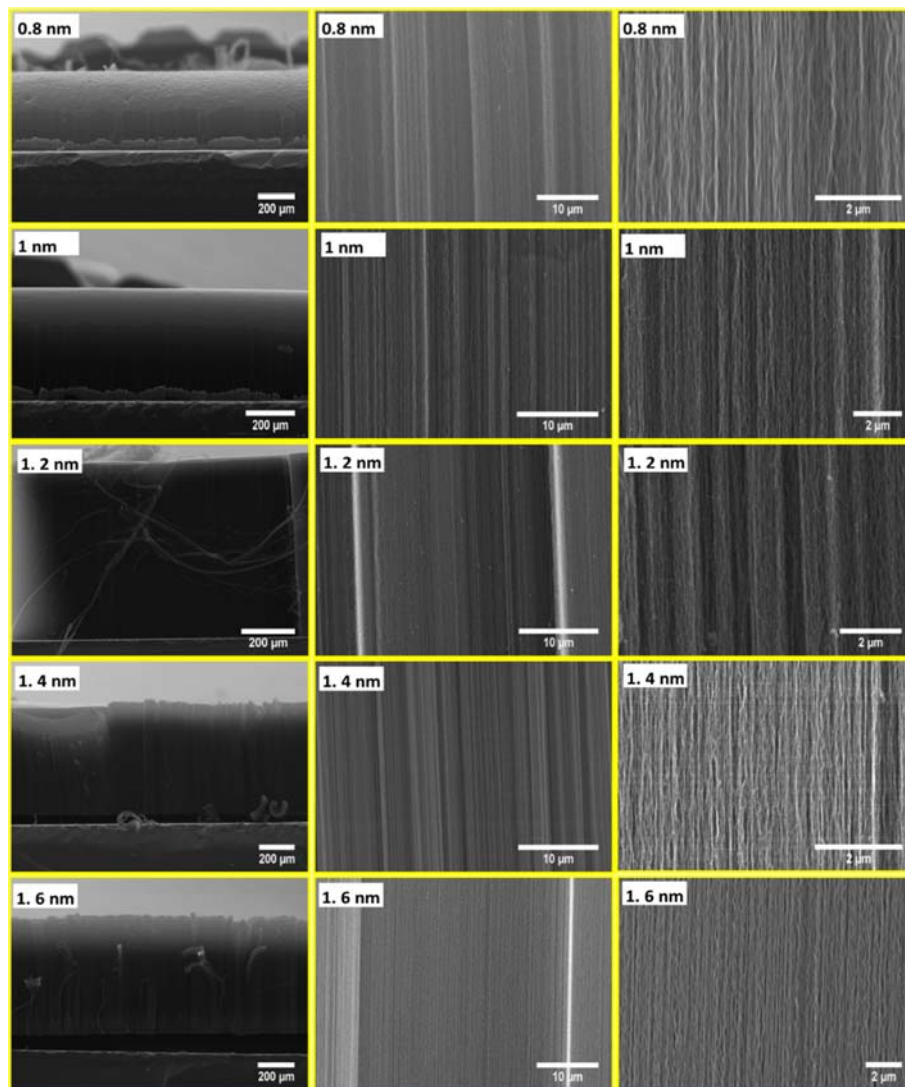


Figure VI.17 SEM images of the VACNTs grown in different catalyst thickness (Fe) at three magnifications (scale bar=200 μm, 10 μm and 2 μm); keeping other conditions constant.

Influence of iron thickness in the growth of VACNTs is investigated by varying the iron thickness from 0.8 nm to 1.6 nm with a step of 0.2 nm keeping other growth parameters like Argon (500 sccm), hydrogen (100 sccm), ethene (75 sccm), water (150 ppm), Al<sub>2</sub>O<sub>3</sub> thickness (30 nm), growth temperature (820 °C) and growth time (5 minutes) constant. SEM image and Raman spectra is shown in figure VI.17 and VI.18 (a).

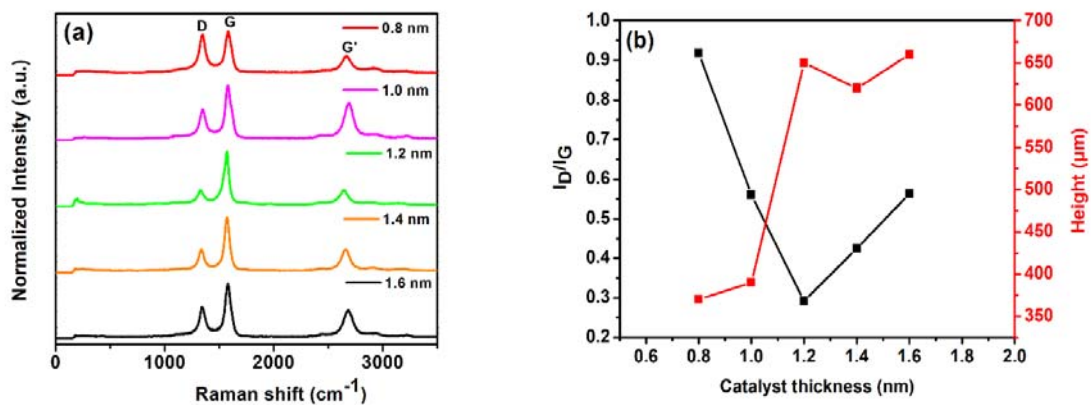


Figure VI.18 (a) Raman spectra of VACNTs with different catalyst thickness (Fe), (b)  $I_D/I_G$  ratio and height of the VACNTs with different catalyst thickness; keeping other parameters constant.

## VI.4 Graphene oxide and reduced graphene oxide

Synthesis of graphene oxide, reduction of graphene oxide and exfoliation of graphene is discussed below.

### VI.4.1 Synthesis of graphene oxide

Graphene oxide (GO) was synthesized using the improved method described by Marcano et al. [268]. A schematic of the synthesis is shown in figure VI.19. In step 1, 3g graphene flakes and 18g  $\text{KMnO}_4$  was added to 9:1 mixture of 360 ml  $\text{H}_2\text{SO}_4$  (98%) and 40 ml  $\text{H}_3\text{PO}_4$  (85%). Further, the above suspension was heated at 50 °C for 18 h and cooled down to room temperature. In step 2, the slightly lilac suspension was poured into 600 ml ice containing 3ml  $\text{H}_2\text{O}_2$  (30%). After standing at RT for 12 h, the solid was separated via centrifugation. In step 3, the precipitate was washed using 140 ml water, 140 ml aqueous HCl solution (36%), twice with 14ml ethanol (99%). In step 4, diethyl ether is used for the coagulation. Then the collected sample is dried at 80 °C get final GO. Reduced graphene oxide was prepared by exfoliation of graphene oxide (GO).

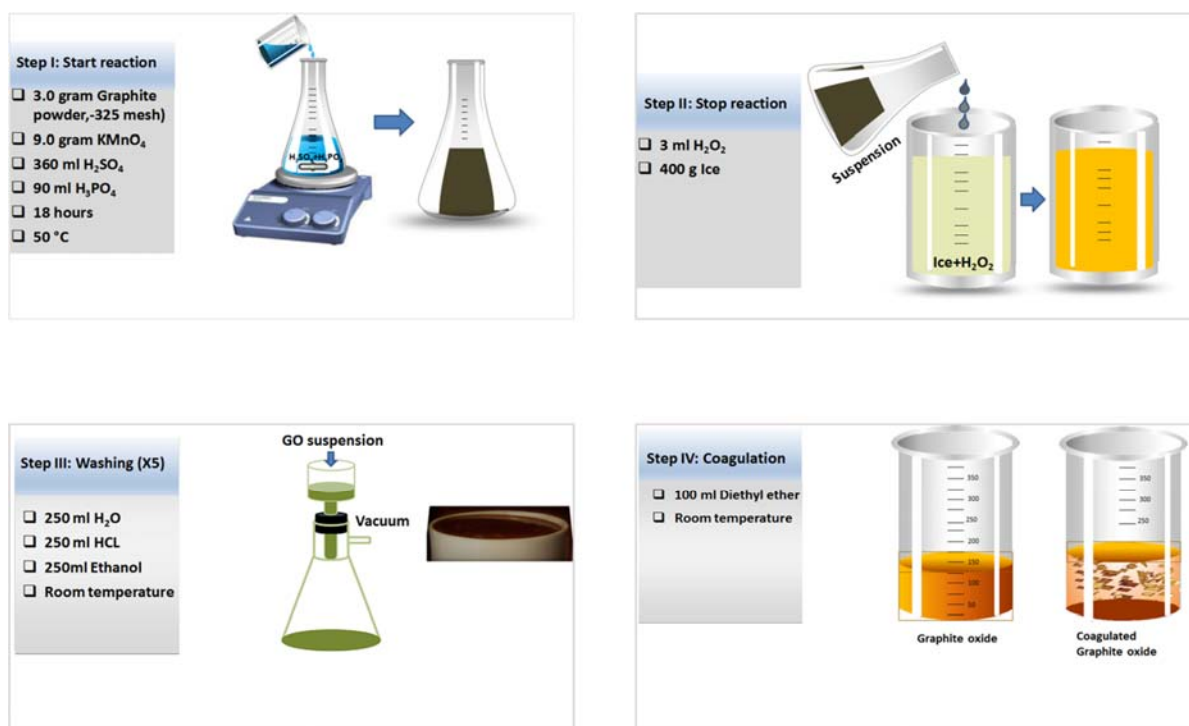


Figure VI.19 Schematic of synthesis of GO.

### VI.4.2 Exfoliation of graphene oxide ( $\text{GO}_{\text{ex}}$ )

Graphene oxide was dispersed in water via ultrasonication for 2 h. Then the above dispersion was soaked in a liquid nitrogen bath for 20-30 s. The brownish sample obtained is further sonicated and centrifuged many times, then dried at 75 °C for 24 hours. Finally the dried sample was grinded mechanically and the powder formed was sieved with 100 micron stainless steel strainer and named as  $\text{GO}_{\text{ex}}$ . A schematic of the exfoliation of graphene oxide is shown in figure VI.20.

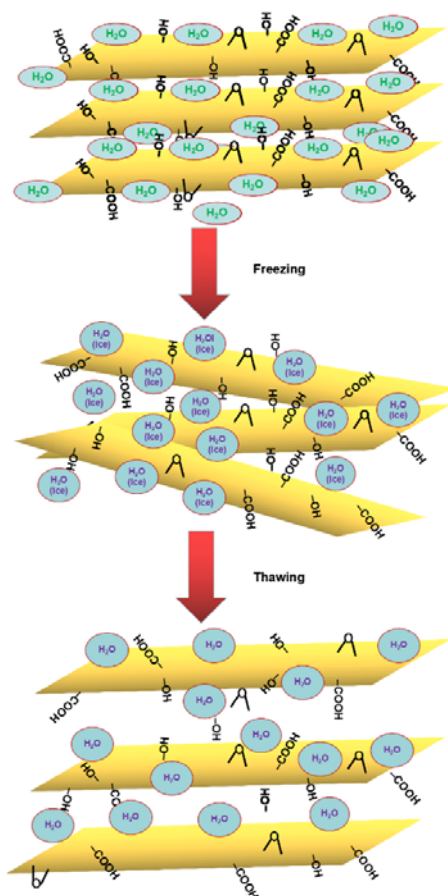
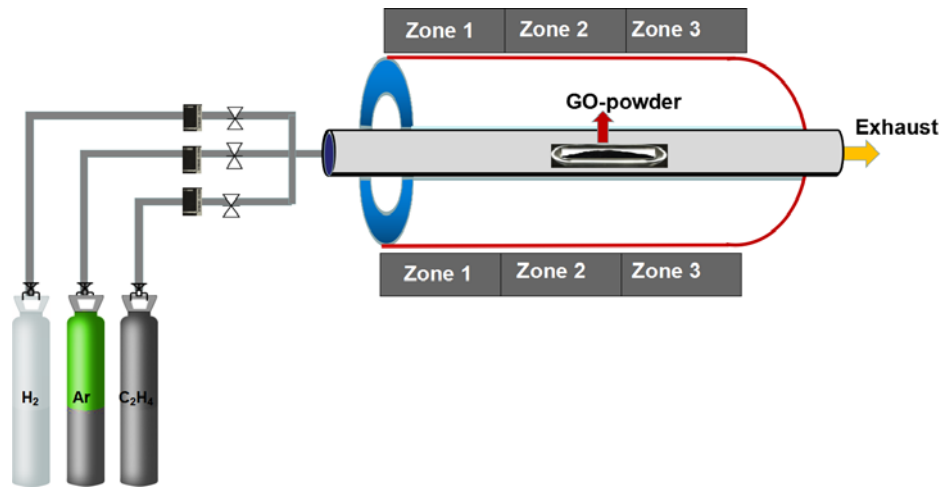


Figure VI.20 Schematic for exfoliation of graphene oxide.

### VI.4.3 Reduction of graphene oxide

Graphite oxide was reduced using hydrogen gas at different temperatures (200 °C-1000 °C). In the detailed experimental procedure, A quartz boat with GO powder is kept at the centre of a quartz tube is inserted in a tubular furnace. Both ends of the quartz tube were closed with coupling arrangements with gas flow provision (figure VI.21). Argon was allowed about 30 minutes to create an inert environment. The temperature of the furnace was increased from 200 °C to 1000 °C and hydrogen

was allowed at this temperature for the exfoliation to happen. The reduction was done for 4 hours. Then materials are labelled as rGO-200, rGO-400, rGO-600, rGO-800, rGO-1000.



*Figure VI.21 Schematic for the reduction of graphene oxide.*

---

## VI.5 Black phosphorus

Bulk black phosphorus can be prepared using two methods which are bismuth flux method<sup>[387]</sup> and chemical vapor transport reaction<sup>[388]</sup>.

### VI.5.1 Bismuth-flux method

Black phosphorus is prepared by following the bismuth flux method reported by Baba et al.<sup>[387]</sup>. Initially red phosphorus is converted to white phosphorus and black phosphorus is synthesized using white phosphorus and bismuth. Figure VI.22 depicts the schematic of preparation of black phosphorus (BP-1) crystals via bismuth flux method. In detail, A two branched quartz glass apparatus (Figure VI.22 (a)) apparatus was used for the synthesis of single crystals of BP-1. Red phosphorus granules (red-P) and bismuth (Bi) granules with purity 99.999% is received from ABCR GmbH, Germany. Red-P granules (1g) and Bi granules (20 g) were separately taken in the two branches of the quartz glass apparatus (Figure VI.22 (b)). Insertion of red-P in to the quartz-glass apparatus was performed in a glove box under argon atmosphere. Glass-quartz wool was placed above red-P in order to perform smooth evaporation of red-P. Then the apparatus was evacuated to pressure of  $10^{-3}$  mbar using diffusion pump and sealed off (Figure VI.22 (c)). Bismuth granule was fixed in the bottom of the branched tube via single time melting and resolidification. Then, temperature of the red-P was set to 480 °C using a home made CVD, transporting tube temperature was maintained as 250 °C using ribbon heater and the bismuth is at room temperature. Vaporized phosphorus transports through the transporting tube to the cold end of the tube and condense there in the form of a white liquid (Figure VI.22 (e)). During this process, a complete conversion of red-P to white phosphorus is achieved.

Later, the quartz-glass ampoule containing bismuth and white phosphorus are sealed from the main quartz-glass apparatus. Then, the quartz ampoule is immersed in oil bath of 80 °C to melt the white phosphorus, whose melting point is about 44.1°C. Liquid white phosphorus move to the opposite to bismuth and solidified there. Thereafter, bismuth is melted by heating upto 300 °C using ribbon heater and poured into the white phosphorus. Later the ampoule is immediately placed at 400 °C, shaken and rotated for 5 minutes. Then, the ampoule is placed at 400 °C for 48 hours, cooled down to 200 °C at a rate of 20°C/min and to room temperature at a rate of 10 °C/min to get needle like black phosphorus crystals (BP-1) (figure VI.22 (f)). The resulting material is taken out by breaking the ampoule and immersed in 30% nitric acid to resolve black phosphorus and Bi (figure VI.22 (g)). The final black phosphorus can be in the form of needle or sheet (figure VI.22 (h)). The disadvantages of bismuth flux method are low yield, time consuming and the size of the crystal is small.

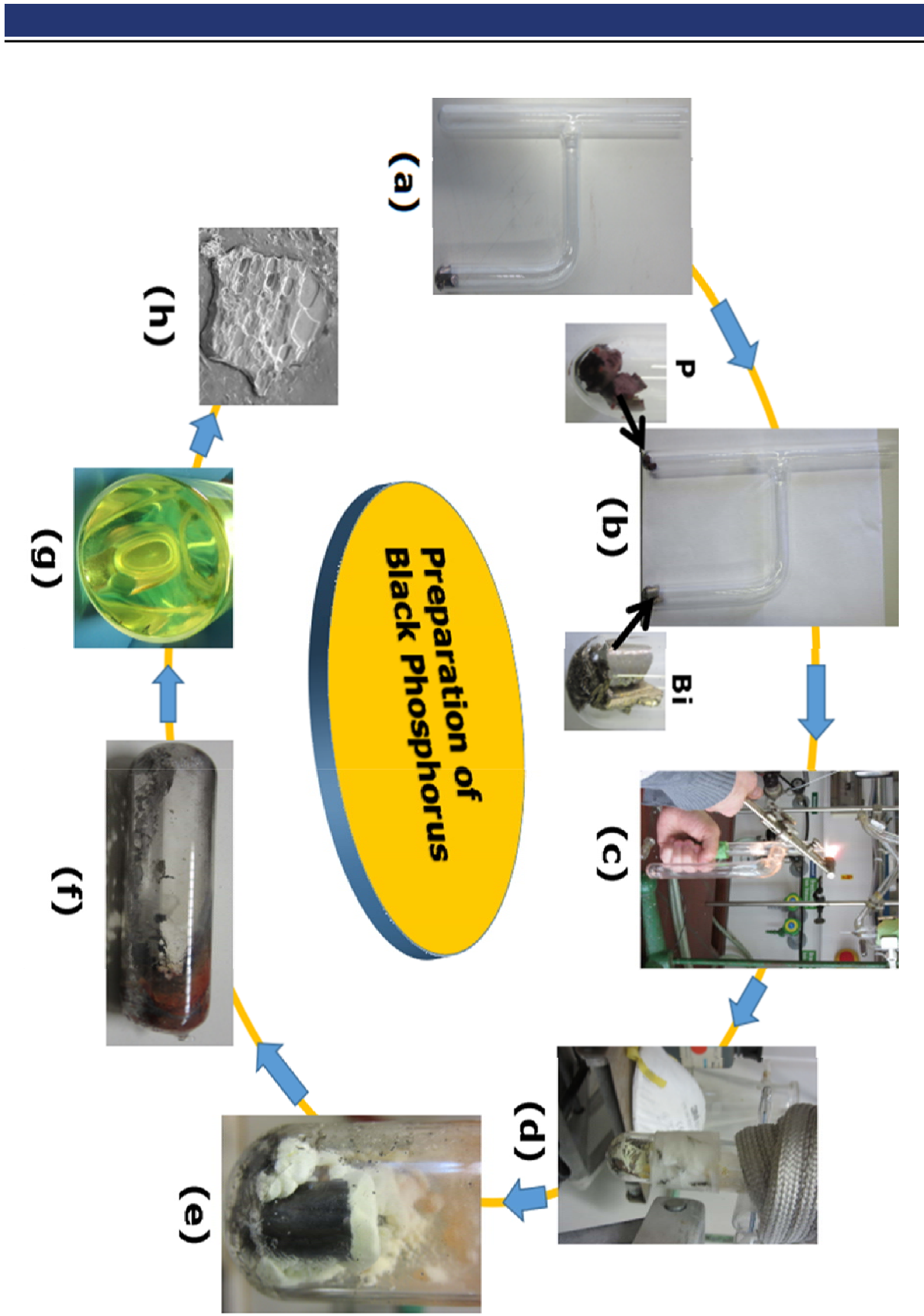
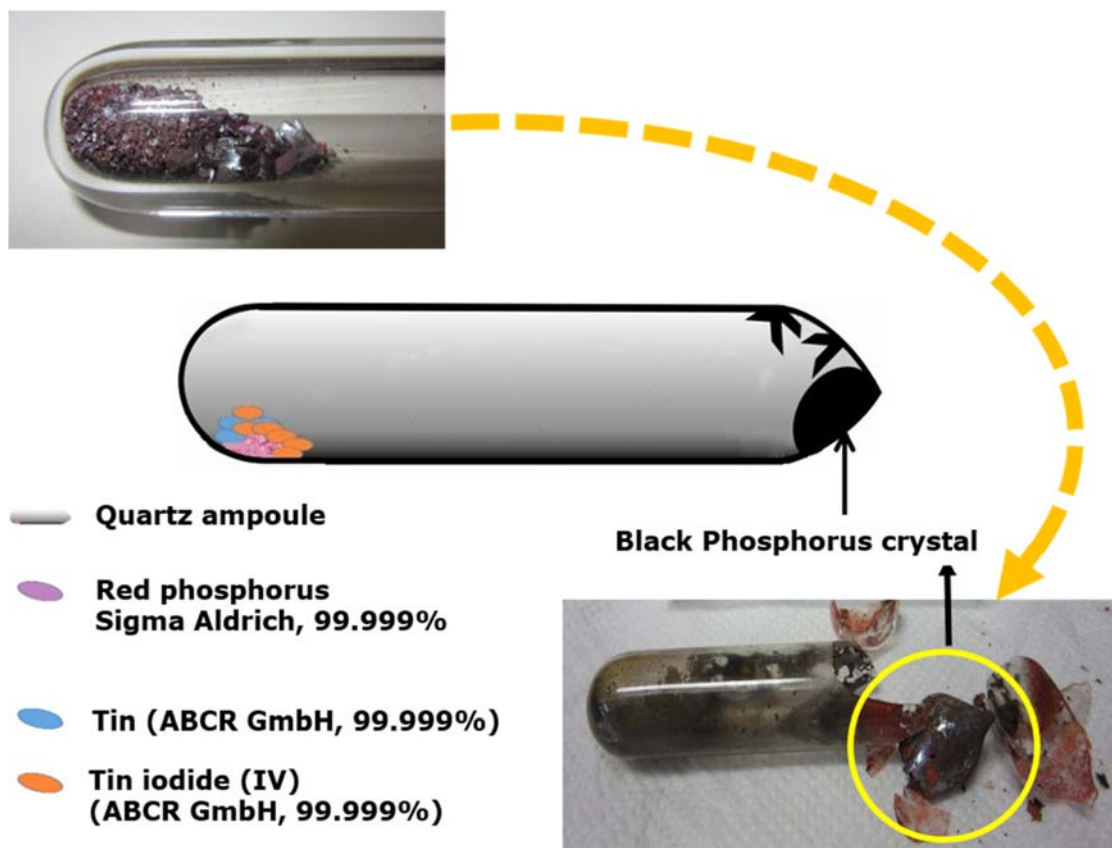


Figure VI.22 Schematic of preparation of black phosphorus via bismuth flux method.

## VI.5.2 Chemical vapor transport reaction

To synthesize black phosphorus crystals (BP-2), red phosphorus (500 mg, 99.999%, Sigma-Aldrich), Sn (20 mg, 99.999%, ABCR GmbH) and SnI<sub>4</sub> (10 mg, 99.999%, ABCR GmbH) were placed in a quartz-glass ampoule.



*Figure VI.23 Schematic of the quartz-glass ampoule with initial materials and final black phosphorus in a chemical vapor transport reaction.*

Later, the ampoule is evacuated to a pressure of  $10^{-3}$  mbar using diffusion pump. Then the ampoule is placed in a furnace such that the initial materials are in the hot region and the empty end of the ampoule in the cold region. The furnace temperature was set to 695 °C with increasing rate of 7 °C/minute and kept 6 hours, then the temperature reduced to 550 °C with slow cooling in 8 hours and kept 72 hours in 550 °C followed by cooling to room temperature done. Sn and iodine are the only side products of this synthesis. Figure VI.23 shows the schematic of the quartz-glass ampoule with initial materials for the reaction and final black phosphorous crytal. Different temperatures are applied for volatilization and crystallization.



### VI.5.3 Exfoliation of black phosphorus

Black phosphorus is exfoliated in ethanol using probe sonicator (BANDELIN SONOPLUS) to get few layer black phosphorus. Sonication was carried for 30 minutes with 40% power in continuous mode. Figure VI.24 shows the schematic of preparation of few layer black phosphorus from bulk black phosphorus by probe sonication.

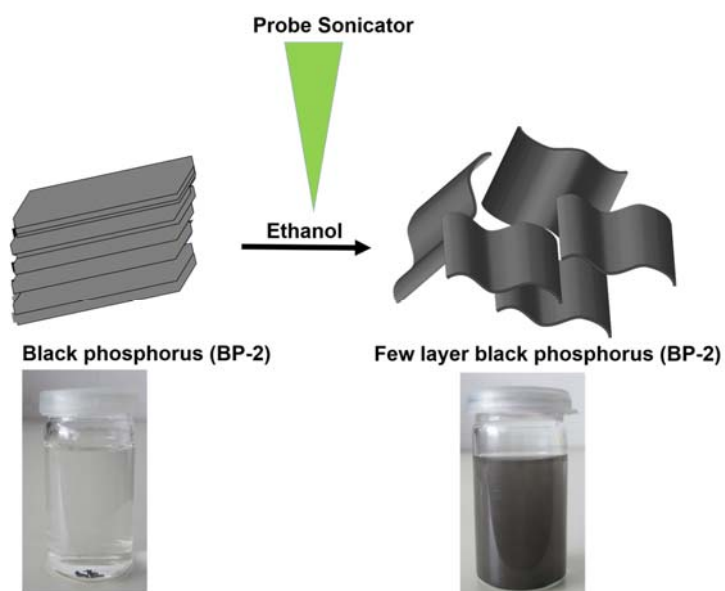


*Figure VI.24 Schematic of preparation of few layer black phosphorus.*

---

## VII REFERENCES

- [1] M. Dresselhaus, G. Dresselhaus, R. Saito, *Carbon* **1995**, *33*, 883-891.
- [2] J.-P. Issi, L. Langer, J. Heremans, C. Olk, *Carbon* **1995**, *33*, 941-948.
- [3] R. Saito, M. Fujita, G. Dresselhaus, M. S. Dresselhaus, *Applied Physics Letters* **1992**, *60*, 2204-2206.
- [4] M. S. Dresselhaus, G. Dresselhaus, P. C. Eklund, *Science of fullerenes and carbon nanotubes: their properties and applications*, Academic press, **1996**.
- [5] [www.nanotube.msu.edu](http://www.nanotube.msu.edu), 2-10-2017, 11.30 AM.
- [6] <https://en.wikipedia.org/wiki/Graphene>, 2-10-2017, 11.30 AM.
- [7] Y. Deng, S. W. Cranford, *Computational Materials Science* **2017**, *129*, 226-230.
- [8] F. Cataldo, S. Iglesias-Groth, Y. Hafez, G. Angelini, *Journal of Radioanalytical and Nuclear Chemistry* **2014**, *299*, 1955-1963.
- [9] G. Povie, Y. Segawa, T. Nishihara, Y. Miyauchi, K. Itami, *Science* **2017**, *356*, 172-175.
- [10] R. Purohit, K. Purohit, S. Rana, R. S. Rana, V. Patel, *Procedia Materials Science* **2014**, *6*, 716-728.
- [11] P. Harris, *Carbon Nanotube Science. Synthesis, Properties and Applications.*, Cambridge University Press, **2009**.
- [12] F. Wang, D. Kozawa, Y. Miyauchi, K. Hiraoka, S. Mouri, Y. Ohno, K. Matsuda, *Nature Communications* **2015**, *6*, 6305.
- [13] Z. Wu, Z. Chen, X. Du, J. M. Logan, J. Sippel, M. Nikolou, K. Kamaras, J. R. Reynolds, D. B. Tanner, A. F. Hebard, A. G. Rinzler, *Science* **2004**, *305*, 1273-1276.
- [14] M. Abe, K. Murata, K. Matsumoto, *Journal of Applied Physics* **2010**, *107*, 084504.
- [15] Z. Ting, M. Syed, V. M. Nosang, A. D. Marc, *Nanotechnology* **2008**, *19*, 332001.
- [16] R. Das, M. E. Ali, S. B. A. Hamid, S. Ramakrishna, Z. Z. Chowdhury, *Desalination* **2014**, *336*, 97-109.
- [17] D. Lee, B.-H. Lee, J. Yoon, D.-C. Ahn, J.-Y. Park, J. Hur, M.-S. Kim, S.-B. Jeon, M.-H. Kang, K. Kim, M. Lim, S.-J. Choi, Y.-K. Choi, *ACS Nano* **2016**, *10*, 10894-10900.
- [18] A. Javey, J. Guo, Q. Wang, M. Lundstrom, H. Dai, *Nature* **2003**, *424*, 654-657.
- [19] G. Girishkumar, M. Rettker, R. Underhile, D. Binz, K. Vinodgopal, P. McGinn, P. Kamat, *Langmuir* **2005**, *21*, 8487-8494.
- [20] J. Opatkiewicz, M. C. LeMieux, Z. Bao, *ACS Nano* **2010**, *4*, 2975-2978.
- [21] C.-L. Tsai, F. Xiong, E. Pop, M. Shim, *ACS Nano* **2013**, *7*, 5360-5366.
- [22] Y. Rangom, X. Tang, L. F. Nazar, *ACS Nano* **2015**, *9*, 7248-7255.

- 
- [23] A. Srivastava, O. N. Srivastava, S. Talapatra, R. Vajtai, P. M. Ajayan, *Nat Mater* **2004**, *3*, 610-614.
- [24] M. Bedewy, E. R. Meshot, H. Guo, E. A. Verploegen, W. Lu, A. J. Hart, *The Journal of Physical Chemistry C* **2009**, *113*, 20576-20582.
- [25] Y. Zhao, M. Hong, N. Bonnet Mercier, G. Yu, H. C. Choi, H. R. Byon, *Nano Letters* **2014**, *14*, 1085-1092.
- [26] S. Liatard, K. Benhamouda, A. Fournier, R. Ramos, C. Barchasz, J. Dijon, *Chemical Communications* **2015**, *51*, 7749-7752.
- [27] S. Li, Y. Luo, W. Lv, W. Yu, S. Wu, P. Hou, Q. Yang, Q. Meng, C. Liu, H.-M. Cheng, *Advanced Energy Materials* **2011**, *1*, 486-490.
- [28] Y. V. Fedoseeva, L. G. Bulusheva, A. V. Okotrub, M. A. Kanygin, D. V. Gorodetskiy, I. P. Asanov, D. V. Vyalikh, A. P. Puzyr, V. S. Bondar, **2015**, *5*, 9379.
- [29] Z. Lingbo, S. Yangyang, X. Jianwen, Z. Zhuqing, D. W. Hess, C. P. Wong, in *Proceedings Electronic Components and Technology, 2005. ECTC '05.*, **2005**, pp. 44-50 Vol. 41.
- [30] M. Yu, H. H. Funke, J. L. Falconer, R. D. Noble, *Nano Letters* **2009**, *9*, 225-229.
- [31] Y. Yao, J. N. Tey, Z. Li, J. Wei, K. Bennett, A. McNamara, Y. Joshi, R. L. S. Tan, S. N. M. Ling, C. P. Wong, *IEEE Transactions on Components, Packaging and Manufacturing Technology* **2014**, *4*, 232-239.
- [32] S. Iijima, *Nature* **1991**, *354*, 56-58.
- [33] J. Catherine, P. Matthieu, J. Vincent, *Nanotechnology* **2012**, *23*, 142001.
- [34] T. Guo, P. Nikolaev, A. Thess, D. T. Colbert, R. E. Smalley, *Chemical Physics Letters* **1995**, *243*, 49-54.
- [35] J. Prasek, J. Drbohlavova, J. Chomoucka, J. Hubalek, O. Jasek, V. Adam, R. Kizek, *Journal of Materials Chemistry* **2011**, *21*, 15872-15884.
- [36] M. Baro, D. Gogoi, A. R. Pal, N. C. Adhikary, H. Bailung, J. Chutia, *Chemical Vapor Deposition* **2014**, *20*, 161-169.
- [37] H. Liao, J. H. Hafner, *The Journal of Physical Chemistry B* **2004**, *108*, 6941-6943.
- [38] X. Xu, R. Ray, Y. Gu, H. J. Ploehn, L. Gearheart, K. Raker, W. A. Scrivens, *Journal of the American Chemical Society* **2004**, *126*, 12736-12737.
- [39] Y. Matsuzawa, Y. Takada, T. Kodaira, H. Kihara, H. Kataura, M. Yoshida, *The Journal of Physical Chemistry C* **2014**, *118*, 5013-5019.
- [40] S. Niyogi, H. Hu, M. A. Hamon, P. Bhowmik, B. Zhao, S. M. Rozenzhak, J. Chen, M. E. Itkis, M. S. Meier, R. C. Haddon, *Journal of the American Chemical Society* **2001**, *123*, 733-734.

- 
- [41] W. Kratschmer, L. D. Lamb, K. Fostiropoulos, D. R. Huffman, *Nature* **1990**, *347*, 354-358.
- [42] S. Iijima, T. Ichihashi, *Nature* **1993**, *363*, 603-605.
- [43] D. S. Bethune, C. H. Klang, M. S. de Vries, G. Gorman, R. Savoy, J. Vazquez, R. Beyers, *Nature* **1993**, *363*, 605-607.
- [44] P. M. Ajayan, J. M. Lambert, P. Bernier, L. Barbedette, C. Colliex, J. M. Planeix, *Chemical Physics Letters* **1993**, *215*, 509-517.
- [45] J. Guo, X. Wang, Y. Yao, X. Yang, X. Liu, B. Xu, *Materials Chemistry and Physics* **2007**, *105*, 175-178.
- [46] G. Xing, S. Jia, J. Xing, Z. Shi, *Plasma Science and Technology* **2007**, *9*, 770.
- [47] N. Braidy, M. A. El Khakani, G. A. Botton, *Chemical Physics Letters* **2002**, *354*, 88-92.
- [48] M. Kusaba, Y. Tsunawaki, *Thin Solid Films* **2006**, *506-507*, 255-258.
- [49] M. Yudasaka, R. Yamada, N. Sensui, T. Wilkins, T. Ichihashi, S. Iijima, *Journal of Physical Chemistry B* **1999**, *103*, 6224-6229.
- [50] A. Thess, R. Lee, P. Nikolaev, H. Dai, P. Petit, J. Robert, C. Xu, Y. H. Lee, S. G. Kim, A. G. Rinzler, D. T. Colbert, G. E. Scuseria, D. Tománek, J. E. Fischer, R. E. Smalley, *Science* **1996**, *273*, 483-487.
- [51] W. K. Maser, E. Muñoz, A. M. Benito, M. T. Martínez, G. F. de la Fuente, Y. Maniette, E. Anglaret, J. L. Sauvajol, *Chemical Physics Letters* **1998**, *292*, 587-593.
- [52] A. P. Bolshakov, S. A. Uglov, A. V. Saveliev, V. I. Konov, A. A. Gorbunov, W. Pompe, A. Graff, *Diamond and Related Materials* **2002**, *11*, 927-930.
- [53] P. Nikolaev, M. J. Bronikowski, R. K. Bradley, F. Rohmund, D. T. Colbert, K. A. Smith, R. E. Smalley, *Chemical Physics Letters* **1999**, *313*, 91-97.
- [54] K. Hernadi, A. Fonseca, J. B. Nagy, D. Bernaerts, A. A. Lucas, *Carbon* **1996**, *34*, 1249-1257.
- [55] M. Palizdar, R. Ahgabayazadeh, A. Mirhabibi, R. Brydson, S. Pilehvari, *Journal of nanoscience and nanotechnology* **2011**, *11*, 5345-5351.
- [56] T. Tomie, S. Inoue, M. Kohno, Y. Matsumura, *Diamond and Related Materials* **2010**, *19*, 1401-1404.
- [57] R. Joshi, J. Engstler, L. Houben, M. Bar Sadan, A. Weidenkaff, P. Mandaliev, A. Issanin, J. J. Schneider, *ChemCatChem* **2010**, *2*, 1069-1073.
- [58] A. L. M. Reddy, M. Shaijumon, S. Ramaprabhu, *Nanotechnology* **2006**, *17*, 5299.
- [59] B. Q. Wei, R. Vajtai, Y. Jung, J. Ward, R. Zhang, G. Ramanath, P. M. Ajayan, *Nature* **2002**, *416*, 495-496.
- [60] Z. Yong, L. Fang, Z. Zhi-hua, *Micron* **2011**, *42*, 547-552.

- 
- [61] M. Kumar, Ando, Yoshinori, *Journal of Nanoscience and Nanotechnology*, , 10, 3739-3758.
- [62] Z. Ren, Y. Lan, Y. Wang, *Aligned carbon nanotubes: physics, concepts, fabrication and devices*, Springer Science & Business Media, **2012**.
- [63] D. J. Srolovitz, S. A. Safran, *Journal of Applied physics* **1986**, 60, 247-254.
- [64] K. Hata, D. N. Futaba, K. Mizuno, T. Namai, M. Yumura, S. Iijima, *Science* **2004**, 306, 1362-1364.
- [65] D. N. Futaba, K. Hata, T. Yamada, K. Mizuno, M. Yumura, S. Iijima, *Physical Review Letters* **2005**, 95, 056104.
- [66] R. Ravindra, B. R. Bhat, *Journal of Metals, Materials and Minerals* **2011**, 21, 95-99.
- [67] H. Hou, A. K. Schaper, Z. Jun, F. Weller, A. Greiner, *Chemistry of Materials* **2003**, 15, 580-585.
- [68] D. Takagi, Y. Kobayashi, Y. Homma, *Journal of the American Chemical Society* **2009**, 131, 6922-6923.
- [69] Z. Yanli, S. Kazuyuki, S. Yahachi, *Japanese Journal of Applied Physics* **2006**, 45, 6508.
- [70] M. Reichenbacher, J. Popp, in *Challenges in Molecular Structure Determination* (Eds.: M. Reichenbacher, J. Popp), Springer Berlin Heidelberg, Berlin, Heidelberg, **2012**, pp. 63-143.
- [71] P. F. McMillan, *Annual review of earth and planetary sciences* **1989**, 17, 255-279.
- [72] T. Belin, F. Epron, *Materials Science and Engineering: B* **2005**, 119, 105-118.
- [73] A. C. Ferrari, J. Robertson, *Physical Review B* **2000**, 61, 14095-14107.
- [74] C. Thomsen, S. Reich, *Physical Review Letters* **2000**, 85, 5214-5217.
- [75] M. S. Dresselhaus, G. Dresselhaus, A. Jorio, A. G. Souza Filho, R. Saito, *Carbon* **2002**, 40, 2043-2061.
- [76] J. T. Ye, J. P. Zhai, Z. K. Tang, *Journal of Physics: Condensed Matter* **2007**, 19, 445003.
- [77] G. R. A. Jamal, S. M. Mominuzzaman, *Journal of Nanoscience and Nanoengineering* **2015**, 1, 74-83.
- [78] S. M. Bose, S. Gayen, S. N. Behera, *Physical Review B* **2005**, 72, 153402.
- [79] A. Jorio, M. A. Pimenta, A. G. Souza Filho, R. Saito, G. Dresselhaus, M. S. Dresselhaus, *New Journal of Physics* **2003**, 5, 139.
- [80] M. S. Dresselhaus, G. Dresselhaus, R. Saito, A. Jorio, *Physics Reports* **2005**, 409, 47-99.
- [81] K. Siegbahn, K. Edvarson, *Nuclear Physics* **1956**, 1, 137-159.
- [82] S. Chernov, B. I. Sumy, *Electronic States on the Clean and Oxygen-covered Molybdenum (110) Surface Measured Using Time-of-flight Momentum Microscopy*, Johannes Gutenberg University Mainz, **2016**.

- 
- [83] J. F. Moulder, W. F. Stickle, P. E. Sobol, K. D. Bomben, *Handbook of X-ray Photoelectron Spectroscopy*. Eden Prairie: Physical Electronics, Inc, **1995**.
- [84] P. Ayala, Y. Miyata, K. De Blauwe, H. Shiozawa, Y. Feng, K. Yanagi, C. Kramberger, S. R. P. Silva, R. Follath, H. Kataura, T. Pichler, *Physical Review B* **2009**, *80*, 205427.
- [85] K. D. Vernon-Parry, *III-Vs Review* **2000**, *13*, 40-44.
- [86] B. Voutou, E. C. Stefanaki, *Aristotle University of Thessaloniki, Greece* **2008**.
- [87] A. L. Mescher, L. C. U. a. Junqueira, *Junqueira's basic histology : text and atlas*, **2013**.
- [88] A. Aqel, K. M. M. A. El-Nour, R. A. A. Ammar, A. Al-Warthan, *Arabian Journal of Chemistry* **2012**, *5*, 1-23.
- [89] A. Argast, C. F. Tennis, *Journal of Geoscience Education* **2004**, *52*, 213-217.
- [90] Y. Fu, S. Chen, J. Bielecki, A. Matic, T. Wang, L.-L. Ye, J. Liu, *Materials Letters* **2012**, *72*, 78-80.
- [91] D. B. Williams, C. B. Carter, in *Transmission electron microscopy*, Springer, **2009**, pp. 3-22.
- [92] S. J. Pennycook, B. David, C. B. Williams, *Microscopy and Microanalysis* **2010**, *16*, 111.
- [93] A. Ghedjatti, F. Fossard, G. Wang, E. Flahaut, H. Amara, J. S. Lauret, A. Loiseau, in *emc 2016*, Wiley Online Library, **2016**.
- [94] J. Vonk, T. K. Shackelford, in *Oxford Library of Psychology* (Ed.: P. E. Nathan), Oxford University Press, New York, **2012**, p. 574.
- [95] M. Jafari Eskandari, M. A. Asadabad, R. Tafreshi, M. Emamalizadeh, *Inorganic and Nano-Metal Chemistry* **2017**, *47*, 197-201.
- [96] M. Lee, *MRS Bulletin* **2017**, *42*, 163-163.
- [97] K. R. Hebbar, *Basics of X-ray diffraction and its applications*, IK International Publishing House Pvt. Limited, **2007**.
- [98] W. Z. Zhu, D. E. Miser, W. G. Chan, M. R. Hajaligol, *Materials Chemistry and Physics* **2003**, *82*, 638-647.
- [99] L. Chen, J. Bai, C. Wang, Y. Pan, M. Scheer, X. You, *Chemical Communications* **2008**, 1581-1583.
- [100] <https://www.netzsch-thermal-analysis.com>, 2-10-2017, 11.45 AM.
- [101] S. Vyazovkin, in *Characterization of Materials*, John Wiley & Sons, Inc., **2002**.
- [102] K. A. Wepasnick, B. A. Smith, J. L. Bitter, D. Howard Fairbrother, *Analytical and Bioanalytical Chemistry* **2010**, *396*, 1003-1014.
- [103] M. J. Bronikowski, *Carbon* **2006**, *44*, 2822-2832.

- 
- [104] H. Chen, A. Roy, J.-B. Baek, L. Zhu, J. Qu, L. Dai, *Materials Science and Engineering: R: Reports* **2010**, *70*, 63-91.
- [105] Y. Yan, M. B. Chan-Park, Q. Zhang, *Small* **2007**, *3*, 24-42.
- [106] H. Zhang, G. Cao, Z. Wang, Y. Yang, Z. Shi, Z. Gu, *Nano Letters* **2008**, *8*, 2664-2668.
- [107] C. Nick, R. Joshi, J. J. Schneider, C. Thielemann, *International Journal of Surface Science and Engineering* **2012**, *6*, 246-255.
- [108] M. Wang, T. Li, Y. Yao, H. Lu, Q. Li, M. Chen, Q. Li, *Journal of the American Chemical Society* **2014**, *136*, 18156-18162.
- [109] L. Fan, C. Feng, W. Zhao, L. Qian, Y. Wang, Y. Li, *Nano Letters* **2012**, *12*, 3668-3673.
- [110] O. Yilmazoglu, S. Yadav, D. Cicek, J. J. Schneider, *Nanotechnology* **2016**, *27*, 365502.
- [111] C. Nick, S. Yadav, R. Joshi, J. J. Schneider, C. Thielemann, *Applied Physics Letters* **2015**, *107*, 013101.
- [112] F. Du, L. Qu, Z. Xia, L. Feng, L. Dai, *Langmuir* **2011**, *27*, 8437-8443.
- [113] V. P. Veedu, A. Cao, X. Li, K. Ma, C. Soldano, S. Kar, P. M. Ajayan, M. N. Ghasemi-Nejhad, *Nat Mater* **2006**, *5*, 457-462.
- [114] P. Liu, A. Lam, Z. Fan, T. Q. Tran, H. M. Duong, *Materials & Design* **2015**, *87*, 600-605.
- [115] S. Vaddiraju, H. Cebeci, K. K. Gleason, B. L. Wardle, *ACS Applied Materials & Interfaces* **2009**, *1*, 2565-2572.
- [116] X. Wang, Z. Z. Yong, Q. W. Li, P. D. Bradford, W. Liu, D. S. Tucker, W. Cai, H. Wang, F. G. Yuan, Y. T. Zhu, *Materials Research Letters* **2013**, *1*, 19-25.
- [117] C. Won Bong, B. Eunju, K. Donghun, C. Soodoo, C. Byung-ho, K. Ju-hye, L. Eungmin, P. Wanjun, *Nanotechnology* **2004**, *15*, S512.
- [118] O. A. Ageev, Y. F. Blinov, M. V. Il'ina, B. G. Konoplev, V. A. Smirnov, in *Intelligent Nanomaterials*, John Wiley & Sons, Inc., **2016**, pp. 361-394.
- [119] M. V. Ilina, Y. F. Blinov, O. I. Ilin, V. S. Klimin, O. A. Ageev, in *International conference on Micro- and Nano-Electronics, Vol. 10224*, **2016**, p. 102240U.
- [120] O. Yilmazoglu, R. Joshi, A. Popp, D. Pavlidis, J. J. Schneider, *Journal of Vacuum Science & Technology B, Nanotechnology and Microelectronics: Materials, Processing, Measurement, and Phenomena* **2011**, *29*, 02B106.
- [121] Q. Ye, A. M. Cassell, H. Liu, K.-J. Chao, J. Han, M. Meyyappan, *Nano Letters* **2004**, *4*, 1301-1308.
- [122] E. Reyes, A. A. Krokhin, J. Roberts, *Physical Review B* **2005**, *72*, 155118.
- [123] T. Gabay, E. Jakobs, E. Ben-Jacob, Y. Hanein, *Physica A: Statistical Mechanics and its Applications* **2005**, *350*, 611-621.

- 
- [124] A. Yoshinori, I. Sumio, *Japanese Journal of Applied Physics* **1993**, 32, L107.
- [125] B. Hornbostel, M. Haluska, J. Cech, U. Dettlaff, S. Roth, in *Carbon Nanotubes* (Eds.: V. N. Popov, P. Lambin), Springer Netherlands, Dordrecht, **2006**, pp. 1-18.
- [126] J. Chrzanowska, J. Hoffman, A. Małolepszy, M. Mazurkiewicz, T. A. Kowalewski, Z. Szymanski, L. Stobinski, *physica status solidi (b)* **2015**, 252, 1860-1867.
- [127] F. Kokai, K. Takahashi, M. Yudasaka, S. Iijima, *The Journal of Physical Chemistry B* **2000**, 104, 6777-6784.
- [128] M. Zhang, M. Yudasaka, S. Iijima, *The Journal of Physical Chemistry B* **2004**, 108, 12757-12762.
- [129] S. S. Madani, K. Zare, M. Ghoranneviss, A. Salar Elahi, *Journal of Alloys and Compounds* **2015**, 648, 1104-1108.
- [130] S. C. Lyu, B. C. Liu, S. H. Lee, C. Y. Park, H. K. Kang, C. W. Yang, C. J. Lee, *The Journal of Physical Chemistry B* **2004**, 108, 1613-1616.
- [131] W. Z. Li, S. S. Xie, L. X. Qian, B. H. Chang, B. S. Zou, W. Y. Zhou, R. A. Zhao, G. Wang, *Science* **1996**, 274, 1701-1703.
- [132] Z. F. Ren, Z. P. Huang, J. W. Xu, J. H. Wang, P. Bush, M. P. Siegal, P. N. Provencio, *Science* **1998**, 282, 1105-1107.
- [133] S. Huang, A. W. H. Mau, T. W. Turney, P. A. White, L. Dai, *The Journal of Physical Chemistry B* **2000**, 104, 2193-2196.
- [134] Y. Avigal, R. Kalish, *Applied Physics Letters* **2001**, 78, 2291-2293.
- [135] S. Fan, M. G. Chapline, N. R. Franklin, T. W. Tomblor, A. M. Cassell, H. Dai, *Science* **1999**, 283, 512-514.
- [136] R. Andrews, D. Jacques, A. M. Rao, F. Derbyshire, D. Qian, X. Fan, E. C. Dickey, J. Chen, *Chemical Physics Letters* **1999**, 303, 467-474.
- [137] V. O. Nyamori, N. J. Coville, *Organometallics* **2007**, 26, 4083-4085.
- [138] N. Chopra, P. D. Kichambare, R. Andrews, B. J. Hinds, *Nano Letters* **2002**, 2, 1177-1181.
- [139] S. Esconjauregui, M. Fouquet, B. C. Bayer, C. Ducati, R. Smajda, S. Hofmann, J. Robertson, *ACS Nano* **2010**, 4, 7431-7436.
- [140] K. Hata, D. N. Futaba, K. Mizuno, T. Namai, M. Yumura, S. Iijima, in *Digest of Papers Microprocesses and Nanotechnology 2005*, **2005**, p. 90.
- [141] C. Supriya, N. Takeshi, Y. Yuya, P. Lujun, N. Yoshikazu, *Japanese Journal of Applied Physics* **2006**, 45, L720.
- [142] C. Schünemann, F. Schäffel, A. Bachmatiuk, U. Queitsch, M. Sparing, B. Rellinghaus, K. Lafdi, L. Schultz, B. Büchner, M. H. Rummeli, *ACS Nano* **2011**, 5, 8928-8934.



- 
- [143] D. N. Futaba, K. Hata, T. Namai, T. Yamada, K. Mizuno, Y. Hayamizu, M. Yumura, S. Iijima, *The Journal of Physical Chemistry B* **2006**, *110*, 8035-8038.
- [144] P. B. Amama, C. L. Pint, L. McJilton, S. M. Kim, E. A. Stach, P. T. Murray, R. H. Hauge, B. Maruyama, *Nano Letters* **2009**, *9*, 44-49.
- [145] T. Yamada, A. Maigne, M. Yudasaka, K. Mizuno, D. N. Futaba, M. Yumura, S. Iijima, K. Hata, *Nano Letters* **2008**, *8*, 4288-4292.
- [146] T. Yamada, T. Namai, K. Hata, D. N. Futaba, K. Mizuno, J. Fan, M. Yudasaka, M. Yumura, S. Iijima, *Nat. Nanotechnol.* **2006**, *1*, 131-136.
- [147] G. Chen, R. C. Davis, D. N. Futaba, S. Sakurai, K. Kobashi, M. Yumura, K. Hata, *Nanoscale* **2016**, *8*, 162-171.
- [148] K. Hasegawa, S. Noda, *ACS Nano* **2011**, *5*, 975-984.
- [149] N. Suguru, H. Kei, S. Hisashi, K. Kazunori, Z. Zhengyi, M. Shigeo, Y. Yukio, *Japanese Journal of Applied Physics* **2007**, *46*, L399.
- [150] Y. Li, G. Xu, H. Zhang, T. Li, Y. Yao, Q. Li, Z. Dai, *Carbon* **2015**, *91*, 45-55.
- [151] Y. Zhang, J. M. Gregoire, R. B. van Dover, A. J. Hart, *The Journal of Physical Chemistry C* **2010**, *114*, 6389-6395.
- [152] H. Kimura, J. Goto, S. Yasuda, S. Sakurai, M. Yumura, D. N. Futaba, K. Hata, *Scientific Reports* **2013**, *3*, 3334.
- [153] G. Lanzani, T. Susi, P. Ayala, T. Jiang, A. G. Nasibulin, T. Bligaard, T. Pichler, K. Laasonen, E. I. Kauppinen, *physica status solidi (b)* **2010**, *247*, 2708-2712.
- [154] J. Huang, Q. Zhang, M. Zhao, F. Wei, *CHINESE SCI BULL* **2012**, *57*, 157-166.
- [155] C. N. R. Rao, A. Govindaraj, *Accounts of Chemical Research* **2002**, *35*, 998-1007.
- [156] R. Sen, A. Govindaraj, C. N. R. Rao, *Chemical Physics Letters* **1997**, *267*, 276-280.
- [157] L. Ci, J. Wei, B. Wei, J. Liang, C. Xu, D. Wu, *Carbon* **2001**, *39*, 329-335.
- [158] R. Joshi, Technische Universität **2010**.
- [159] R. A. Bell, in *Conduction in Carbon Nanotube Networks: Large-Scale Theoretical Simulations* (Ed.: R. A. Bell), Springer International Publishing, Cham, **2015**, pp. 9-24.
- [160] M. S. Dresselhaus, G. Dresselhaus, P. C. Eklund, A. M. Rao, in *The Physics of Fullerene-Based and Fullerene-Related Materials* (Ed.: W. Andreoni), Springer Netherlands, Dordrecht, **2000**, pp. 331-379.
- [161] S. M. C. N.B. Brandt, Y.G. Ponomarev, *Modern Problems in Condensed Matter Sciences* **1988**, *20*, 29-72.
- [162] T. W. Odom, J.-L. Huang, P. Kim, C. M. Lieber, *Nature* **1998**, *391*, 62-64.
- [163] J.-C. Charlier, X. Blase, S. Roche, *Reviews of modern physics* **2007**, *79*, 677.

- 
- [164] R. Saito, G. Dresselhaus, M. S. Dresselhaus, *Physical properties of carbon nanotubes, Vol. 4*, World Scientific, **1998**.
- [165] S. Berber, Y.-K. Kwon, D. Tománek, *Physical Review Letters* **2000**, *84*, 4613-4616.
- [166] D. Bom, R. Andrews, D. Jacques, J. Anthony, B. Chen, M. S. Meier, J. P. Selegue, *Nano Letters* **2002**, *2*, 615-619.
- [167] S. C. Tsang, Z. Guo, Y. K. Chen, M. L. H. Green, H. A. O. Hill, T. W. Hambley, P. J. Sadler, *Angewandte Chemie International Edition in English* **1997**, *36*, 2198-2200.
- [168] Z. Liu, S. Tabakman, K. Welsher, H. Dai, *Nano Res.* **2009**, *2*, 85-120.
- [169] A. Sucapane, G. Cellot, M. Prato, M. Giugliano, V. Parpura, L. Ballerini, *Journal of nanoneuroscience* **2009**, *1*, 10-16.
- [170] M. P. Mattson, R. C. Haddon, A. M. Rao, *Journal of Molecular Neuroscience* **2000**, *14*, 175-182.
- [171] S. Raya, G. Alon, D.-P. Moshe, A. Sarit, A. Amir, B.-J. Eshel, H. Yael, *Nanotechnology* **2009**, *20*, 015101.
- [172] B. Bhushan, D. Luo, S. R. Schricker, W. Sigmund, S. Zauscher, *Handbook of nanomaterials properties*, Springer Science & Business Media, **2014**.
- [173] J. P. Salvetat, G. A. D. Briggs, J. M. Bonard, R. R. Bacsa, A. J. Kulik, T. Stöckli, N. A. Burnham, L. Forró, *Physical Review Letters* **1999**, *82*, 944-947.
- [174] A. Krishnan, E. Dujardin, T. W. Ebbesen, P. N. Yianilos, M. M. J. Treacy, *Physical Review B* **1998**, *58*, 14013-14019.
- [175] X. Wei, Q. Chen, L.-M. Peng, R. Cui, Y. Li, *The Journal of Physical Chemistry C* **2009**, *113*, 17002-17005.
- [176] Y. Li, K. Wang, J. Wei, Z. Gu, Z. Wang, J. Luo, D. Wu, *Carbon* **2005**, *43*, 31-35.
- [177] F. Li, H. M. Cheng, S. Bai, G. Su, M. S. Dresselhaus, *Applied Physics Letters* **2000**, *77*, 3161-3163.
- [178] Z. W. Pan, S. S. Xie, L. Lu, B. H. Chang, L. F. Sun, W. Y. Zhou, G. Wang, D. L. Zhang, *Applied Physics Letters* **1999**, *74*, 3152-3154.
- [179] L. Cai, J. Li, P. Luan, H. Dong, D. Zhao, Q. Zhang, X. Zhang, M. Tu, Q. Zeng, W. Zhou, S. Xie, *Advanced Functional Materials* **2012**, *22*, 5238-5244.
- [180] K. Liu, Y. Sun, P. Liu, X. Lin, S. Fan, K. Jiang, *Advanced Functional Materials* **2011**, *21*, 2721-2728.
- [181] Y. Zhang, C. J. Sheehan, J. Zhai, G. Zou, H. Luo, J. Xiong, Y. T. Zhu, Q. X. Jia, *Advanced Materials* **2010**, *22*, 3027-3031.

- 
- [182] F. A. Ghavanini, H. Jackman, P. Lundgren, K. Svensson, P. Enoksson, *Journal of Applied Physics* **2013**, *113*, 194308.
- [183] T. Holleboom, *Modellering av elektriska och mekaniska egenskaper av kolnanorör*, **2011**.
- [184] D.-Y. Khang, J. Xiao, C. Kocabas, S. MacLaren, T. Banks, H. Jiang, Y. Y. Huang, J. A. Rogers, *Nano Letters* **2008**, *8*, 124-130.
- [185] E. P. Koumoulos, C. A. Charitidis, *Applied Surface Science* **2017**, *396*, 681-687.
- [186] H. J. Qi, K. B. K. Teo, K. K. S. Lau, M. C. Boyce, W. I. Milne, J. Robertson, K. K. Gleason, *Journal of the Mechanics and Physics of Solids* **2003**, *51*, 2213-2237.
- [187] S. Xiao, W. Hou, *Fullerenes, Nanotubes and Carbon Nanostructures* **2006**, *14*, 9-16.
- [188] B. Lukić, J. W. Seo, R. R. Bacsa, S. Delpoux, F. Béguin, G. Bister, A. Fonseca, J. B. Nagy, A. Kis, S. Jeney, A. J. Kulik, L. Forró, *Nano Letters* **2005**, *5*, 2074-2077.
- [189] S. Pathak, N. Mohan, P. P. S. S. Abadi, S. Graham, B. A. Cola, J. R. Greer, *Journal of Materials Research* **2012**, *28*, 984-997.
- [190] H. Shima, *Materials* **2012**, *5*.
- [191] R. Zhang, Q. Wen, W. Qian, D. S. Su, Q. Zhang, F. Wei, *Advanced Materials* **2011**, *23*, 3387-3391.
- [192] T.-W. Chou, L. Gao, E. T. Thostenson, Z. Zhang, J.-H. Byun, *Composites Science and Technology* **2010**, *70*, 1-19.
- [193] S. Pathak, in *Structure and Multiscale Mechanics of Carbon Nanomaterials* (Ed.: O. Paris), Springer Vienna, Vienna, **2016**, pp. 191-226.
- [194] Y. Zhu, F. Xu, *Advanced Materials* **2012**, *24*, 1073-1077.
- [195] M. A. M. Razib, T. Saleh, M. A. Hassan, *IEEE*, **2014**, pp. 1-5.
- [196] M. R. M. Asyraf, M. Rana, M. A. Hassan, T. Saleh, *International Journal of Scientific & Engineering Research*, *6*, 47-52.
- [197] M. Masud Rana, T. Saleh, M. R. Mohd Asyraf, A. G. A. Muthalif, *Cogent Engineering* **2017**, *4*.
- [198] O. Yilmazoglu, A. Popp, D. Pavlidis, J. J. Schneider, D. Garth, F. Schüttler, G. Battenberg, *Nanotechnology* **2012**, *23*, 085501.
- [199] Z. Pan, Y. Zhang, Z. Cheng, J. Tong, Q. Chen, J. Zhang, J. Zhang, X. Li, Y. Li, *Sensors* **2017**, *17*.
- [200] M. S. Dresselhaus, G. Dresselhaus, A. Jorio, *The Journal of Physical Chemistry C* **2007**, *111*, 17887-17893.
- [201] M. S. Dresselhaus, A. Jorio, M. Hofmann, G. Dresselhaus, R. Saito, *Nano Letters* **2010**, *10*, 751-758.

- 
- [202] A. Subramanian, U. M. Krishnan, S. Sethuraman, *Journal of Biomedical Science* **2009**, *16*, 108.
- [203] D. N. Heo, H.-J. Kim, Y. J. Lee, M. Heo, S. J. Lee, D. Lee, S. H. Do, S. H. Lee, I. K. Kwon, *ACS Nano* **2017**, *11*, 2961-2971.
- [204] 2-10-2017, 12.30 PM.
- [205] J. Pine, *Journal of Neuroscience Methods* **1980**, *2*, 19-31.
- [206] X. X. Yan, L. S. Jen, L. J. Garey, *Cerebral Cortex* **1996**, *6*, 524-529.
- [207] D. Khudhair, S. Nahavandi, H. Garmestani, A. Bhatti, in *Emerging Trends in Neuro Engineering and Neural Computation*, Springer, **2017**, pp. 41-59.
- [208] B. Ghane-Motlagh, M. Sawan, in *2013 2nd International Conference on Advances in Biomedical Engineering*, **2013**, pp. 38-41.
- [209] B. Ghane-Motlagh, M. Sawan, *Materials Sciences and Applications* **2013**, *Vol.04No.08*, 13.
- [210] S. Myllymaa, K. Myllymaa, H. Korhonen, J. Töyräs, J. E. Jääskeläinen, K. Djupsund, H. Tanila, R. Lappalainen, *Biosensors and Bioelectronics* **2009**, *24*, 3067-3072.
- [211] S. H. Cho, H. M. Lu, L. Cauller, M. I. Romero-Ortega, J. B. Lee, G. A. Hughes, *IEEE Sensors Journal* **2008**, *8*, 1830-1836.
- [212] R. Wang, X. Huang, G. Liu, W. Wang, F. Dong, Z. Li, *Journal of Microelectromechanical Systems* **2010**, *19*, 367-374.
- [213] D. Khodagholy, T. Doublet, M. Gurfinkel, P. Quilichini, E. Ismailova, P. Leleux, T. Herve, S. Sanaur, C. Bernard, G. G. Malliaras, *Advanced Materials* **2011**, *23*, H268-H272.
- [214] D. B. Suyatin, L. Wallman, J. Thelin, C. N. Prinz, H. Jörntell, L. Samuelson, L. Montelius, J. Schouenborg, *PLoS ONE* **2013**, *8*, e56673.
- [215] J. T. Robinson, M. Jorgolli, A. K. Shalek, M.-H. Yoon, R. S. Gertner, H. Park, *Nat Nano* **2012**, *7*, 180-184.
- [216] S. B. Jun, in *Smart Sensors for Health and Environment Monitoring* (Ed.: C.-M. Kyung), Springer Netherlands, Dordrecht, **2015**, pp. 75-105.
- [217] C. Nick, C. Thielemann, *BioNanoScience* **2014**, *4*, 216-225.
- [218] G. Tamir, B.-D. Moti, K. Itshak, S. Raya, R. A. Ze'ev, B.-J. Eshel, H. Yael, *Nanotechnology* **2007**, *18*, 035201.
- [219] V. C. Scanlon, T. Sanders, *Essentials of anatomy and physiology*, FA Davis, **2014**.
- [220] C. R. Noback, N. L. Strominger, R. J. Demarest, D. A. Ruggiero, *The human nervous system: structure and function*, Springer Science & Business Media, **2005**.
- [221] G. Perea, M. Navarrete, A. Araque, *Trends in neurosciences* **2009**, *32*, 421-431.
- [222] L. P. Zanello, B. Zhao, H. Hu, R. C. Haddon, *Nano Letters* **2006**, *6*, 562-567.

- 
- [223] V. Lovat, D. Pantarotto, L. Lagostena, B. Cacciari, M. Grandolfo, M. Righi, G. Spalluto, M. Prato, L. Ballerini, *Nano Letters* **2005**, *5*, 1107-1110.
- [224] M. K. Gheith, T. C. Pappas, A. V. Liopo, V. A. Sinani, B. S. Shim, M. Motamedi, J. P. Wicksted, N. A. Kotov, *Advanced Materials* **2006**, *18*, 2975-2979.
- [225] Y. Hanein, L. Bareket-Keren, *Frontiers in Neural Circuits* **2013**, *6*.
- [226] A. Bédrier, F. Seichepine, E. Flahaut, I. Loubinoux, L. Vaysse, C. Vieu, *Langmuir* **2012**, *28*, 17363-17371.
- [227] E. Ben-Jacob, Y. Hanein, *Journal of Materials Chemistry* **2008**, *18*, 5181-5186.
- [228] H. Hu, Y. Ni, V. Montana, R. C. Haddon, V. Parpura, *Nano Letters* **2004**, *4*, 507-511.
- [229] K. Wang, H. A. Fishman, H. Dai, J. S. Harris, *Nano Letters* **2006**, *6*, 2043-2048.
- [230] C. Nick, R. Joshi, J. J. Schneider, C. Thielemann, *Biointerphases* **2012**, *7*, 58.
- [231] C. Nick, S. Yadav, R. Joshi, C. Thielemann, J. J. Schneider, *Beilstein Journal of Nanotechnology* **2014**, *5*, 1575.
- [232] C. Nick, S. Quednau, R. Sarwar, H. F. Schlaak, C. Thielemann, *Microsystem Technologies* **2014**, *20*, 1849-1857.
- [233] D. F. Bray, J. Bagu, P. Koegler, *Microscopy Research and Technique* **1993**, *26*, 489-495.
- [234] F. Braet, R. De Zanger, E. Wisse, *Journal of Microscopy* **1997**, *186*, 84-87.
- [235] M. Marc W. Halterman, PhD, *Neuroscience, 3rd Edition*, **2005**.
- [236] <http://www.askaop.com/blog/post/regenerating-inner-ear-hair-cells.html>, 2-10-2017, 12.55 PM.
- [237] T. Junliang, Y. Xiong, *Smart Materials and Structures* **2012**, *21*, 113001.
- [238] Z.-g. Zhou, Z.-w. Liu, *Journal of Bionic Engineering* **2008**, *5*, 358-365.
- [239] F. Rizzi, A. Quattieri, T. Dattoma, G. Epifani, M. De Vittorio, *Microelectronic Engineering* **2015**, *132*, 90-97.
- [240] A. R. Studart, *Angewandte Chemie International Edition* **2015**, *54*, 3400-3416.
- [241] J. M. Engel, J. Chen, L. Chang, D. Bullen, *Journal of Microelectromechanical Systems* **2006**, *15*, 729-736.
- [242] Y. Bian, R. Liu, S. Hui, *Functional Materials Letters* **2016**, *09*, 1650001.
- [243] J. M. K. Gijs, D. Marcel, J. v. B. John, S. S. Siripurapu, J. K. Winfred, J. H. d. B. Rik, A. Dominique, S. J. L. Theo, W. Remco, *Nanotechnology* **2006**, *17*, S84.
- [244] A. Alfadhel, B. Li, A. Zaher, O. Yassine, J. Kosel, *Lab on a Chip* **2014**, *14*, 4362-4369.
- [245] M. R. Maschmann, G. J. Ehlert, S. Tawfick, A. J. Hart, J. W. Baur, *Carbon* **2014**, *66*, 377-386.

- 
- [246] A. Cao, P. L. Dickrell, W. G. Sawyer, M. N. Ghasemi-Nejhad, P. M. Ajayan, *Science* **2005**, *310*, 1307.
- [247] Y. Li, H.-i. Kim, B. Wei, J. Kang, J.-b. Choi, J.-D. Nam, J. Suhr, *Nanoscale* **2015**, *7*, 14299-14304.
- [248] V. L. Pushparaj, L. Ci, S. Sreekala, A. Kumar, S. Kesapragada, D. Gall, O. Nalamasu, A. M. Pulickel, J. Suhr, *Applied Physics Letters* **2007**, *91*, 153116.
- [249] C. P. Deck, J. Flowers, G. S. B. McKee, K. Vecchio, *Journal of Applied physics* **2007**, *101*, 023512.
- [250] B. Y. Lee, K. Heo, J. H. Bak, S. U. Cho, S. Moon, Y. D. Park, S. Hong, *Nano Letters* **2008**, *8*, 4483-4487.
- [251] A. Bsoul, M. S. M. Ali, K. Takahata, *Electronics Letters* **2011**, *47*, 807-808.
- [252] C. M. Lin, L. Y. Lin, W. Fang, in *2010 IEEE 23rd International Conference on Micro Electro Mechanical Systems (MEMS)*, **2010**, pp. 55-58.
- [253] Y. Abdi, A. Ebrahimi, S. Mohajerzadeh, M. Fathipour, *Applied Physics Letters* **2009**, *94*, 173507.
- [254] E. H. Feng, R. E. Jones, *Physical Review B* **2011**, *83*, 195412.
- [255] C. Chen, Z. Xu, *Nanoscale* **2011**, *3*, 4383-4388.
- [256] M. R. Maschmann, G. J. Ehlert, B. T. Dickinson, D. M. Phillips, C. W. Ray, G. W. Reich, J. W. Baur, *Advanced Materials* **2014**, *26*, 3230-3234.
- [257] M. De Volder, S. Park, S. Tawfick, A. J. Hart, **2014**, *5*, 4512.
- [258] N. J. Ginga, W. Chen, S. K. Sitaraman, *Carbon* **2014**, *66*, 57-66.
- [259] J.-P. Salvetat, A. J. Kulik, J.-M. Bonard, G. A. D. Briggs, T. Stöckli, K. Méténier, S. Bonnamy, F. Béguin, N. A. Burnham, L. Forró, *Advanced Materials* **1999**, *11*, 161-165.
- [260] P. R. Wallace, *Physical Review* **1947**, *71*, 622-634.
- [261] A. C. H. P. Boehm, G. O. Fischer, U. Hofmann, *Z. Naturforsch.* **1962**, *B 17*, 150-153.
- [262] H.-P. Boehm, *Angewandte Chemie International Edition* **2010**, *49*, 9332-9335.
- [263] K. S. Novoselov, A. K. Geim, S. V. Morozov, D. Jiang, Y. Zhang, S. V. Dubonos, I. V. Grigorieva, A. A. Firsov, *Science* **2004**, *306*, 666-669.
- [264] B. C. Brodie, *Philosophical Transactions of the Royal Society of London* **1859**, *149*, 249-259.
- [265] L. Staudenmaier, *Berichte der deutschen chemischen Gesellschaft* **1898**, *31*, 1481-1487.
- [266] W. S. Hummers, R. E. Offeman, *Journal of the American Chemical Society* **1958**, *80*, 1339-1339.
- [267] J. Chen, B. Yao, C. Li, G. Shi, *Carbon* **2013**, *64*, 225-229.

- 
- [268] D. C. Marcano, D. V. Kosynkin, J. M. Berlin, A. Sinitskii, Z. Sun, A. Slesarev, L. B. Alemany, W. Lu, J. M. Tour, *ACS Nano* **2010**, *4*, 4806-4814.
- [269] M. M. Viana, M. C. Lima, J. C. Forsythe, V. S. Gangoli, M. Cho, Y. Cheng, G. G. Silva, M. S. Wong, V. Caliman, *Journal of the Brazilian Chemical Society* **2015**, *26*, 978-984.
- [270] H. C. Schniepp, J.-L. Li, M. J. McAllister, H. Sai, M. Herrera-Alonso, D. H. Adamson, R. K. Prud'homme, R. Car, D. A. Saville, I. A. Aksay, *The Journal of Physical Chemistry B* **2006**, *110*, 8535-8539.
- [271] S. Pei, H.-M. Cheng, *Carbon* **2012**, *50*, 3210-3228.
- [272] J. Li, X. Zeng, T. Ren, E. van der Heide, *Lubricants* **2014**, *2*.
- [273] B. Paulchamy, G. Arthi, B. D. Lignesh, *Journal of Nanomedicine & Nanotechnology* **2015**, *6*, 1.
- [274] M. J. McAllister, J.-L. Li, D. H. Adamson, H. C. Schniepp, A. A. Abdala, J. Liu, M. Herrera-Alonso, D. L. Milius, R. Car, R. K. Prud'homme, I. A. Aksay, *Chemistry of Materials* **2007**, *19*, 4396-4404.
- [275] H. A. Becerril, J. Mao, Z. Liu, R. M. Stoltenberg, Z. Bao, Y. Chen, *ACS Nano* **2008**, *2*, 463-470.
- [276] X. Wang, L. Zhi, K. Müllen, *Nano Letters* **2008**, *8*, 323-327.
- [277] Y. Zhu, S. Murali, M. D. Stoller, A. Velamakanni, R. D. Piner, R. S. Ruoff, *Carbon* **2010**, *48*, 2118-2122.
- [278] L. J. Cote, R. Cruz-Silva, J. Huang, *Journal of the American Chemical Society* **2009**, *131*, 11027-11032.
- [279] Y. Zhang, L. Guo, S. Wei, Y. He, H. Xia, Q. Chen, H.-B. Sun, F.-S. Xiao, *Nano Today* **2010**, *5*, 15-20.
- [280] S. Stankovich, D. A. Dikin, R. D. Piner, K. A. Kohlhaas, A. Kleinhammes, Y. Jia, Y. Wu, S. T. Nguyen, R. S. Ruoff, *Carbon* **2007**, *45*, 1558-1565.
- [281] S. Stankovich, D. A. Dikin, G. H. B. Dommett, K. M. Kohlhaas, E. J. Zimney, E. A. Stach, R. D. Piner, S. T. Nguyen, R. S. Ruoff, *Nature* **2006**, *442*, 282-286.
- [282] S. Stankovich, R. D. Piner, X. Chen, N. Wu, S. T. Nguyen, R. S. Ruoff, *Journal of Materials Chemistry* **2006**, *16*, 155-158.
- [283] D. Li, M. B. Muller, S. Gilje, R. B. Kaner, G. G. Wallace, *Nat Nano* **2008**, *3*, 101-105.
- [284] W. Gao, L. B. Alemany, L. Ci, P. M. Ajayan, *Nat Chem* **2009**, *1*, 403-408.
- [285] M. J. Fernández-Merino, L. Guardia, J. I. Paredes, S. Villar-Rodil, P. Solís-Fernández, A. Martínez-Alonso, J. M. D. Tascón, *The Journal of Physical Chemistry C* **2010**, *114*, 6426-6432.

- 
- [286] G. Wang, J. Yang, J. Park, X. Gou, B. Wang, H. Liu, J. Yao, *The Journal of Physical Chemistry C* **2008**, *112*, 8192-8195.
- [287] X. Zhou, J. Zhang, H. Wu, H. Yang, J. Zhang, S. Guo, *The Journal of Physical Chemistry C* **2011**, *115*, 11957-11961.
- [288] X. Fan, W. Peng, Y. Li, X. Li, S. Wang, G. Zhang, F. Zhang, *Advanced Materials* **2008**, *20*, 4490-4493.
- [289] G. Williams, B. Seger, P. V. Kamat, *ACS Nano* **2008**, *2*, 1487-1491.
- [290] Y. H. Ng, A. Iwase, A. Kudo, R. Amal, *The Journal of Physical Chemistry Letters* **2010**, *1*, 2607-2612.
- [291] G. Williams, P. V. Kamat, *Langmuir* **2009**, *25*, 13869-13873.
- [292] G. K. Ramesha, S. Sampath, *The Journal of Physical Chemistry C* **2009**, *113*, 7985-7989.
- [293] S. J. An, Y. Zhu, S. H. Lee, M. D. Stoller, T. Emilsson, S. Park, A. Velamakanni, J. An, R. S. Ruoff, *The Journal of Physical Chemistry Letters* **2010**, *1*, 1259-1263.
- [294] S. Thakur, N. Karak, *Carbon* **2015**, *94*, 224-242.
- [295] O. Akhavan, E. Ghaderi, S. Aghayee, Y. Fereydooni, A. Talebi, *Journal of Materials Chemistry* **2012**, *22*, 13773-13781.
- [296] J. Li, G. Xiao, C. Chen, R. Li, D. Yan, *Journal of Materials Chemistry A* **2013**, *1*, 1481-1487.
- [297] J. Liu, S. Fu, B. Yuan, Y. Li, Z. Deng, *Journal of the American Chemical Society* **2010**, *132*, 7279-7281.
- [298] Z. Bo, J. Qian, Z. J. Han, L. Duan, K. Qiu, K. Ostrikov, J. Yan, K. Cen, *Review of Scientific Instruments* **2015**, *86*, 056101.
- [299] S. Wang, P. K. Ang, Z. Wang, A. L. L. Tang, J. T. L. Thong, K. P. Loh, *Nano Letters* **2010**, *10*, 92-98.
- [300] G. Eda, M. Chhowalla, *Advanced Materials* **2010**, *22*, 2392-2415.
- [301] J. T. Robinson, F. K. Perkins, E. S. Snow, Z. Wei, P. E. Sheehan, *Nano Letters* **2008**, *8*, 3137-3140.
- [302] B. Cai, S. Wang, L. Huang, Y. Ning, Z. Zhang, G.-J. Zhang, *ACS Nano* **2014**, *8*, 2632-2638.
- [303] Y. H. Jang, A. Rani, L. N. Quan, V. Adinolfi, P. Kanjanaboos, O. Ouellette, T. Son, Y. J. Jang, K. Chung, H. Kwon, D. Kim, D. H. Kim, E. H. Sargent, *ACS Energy Letters* **2017**, *2*, 117-123.
- [304] H. Zhang, Y. Sun, S. Gao, J. Zhang, H. Zhang, D. Song, *Small* **2013**, *9*, 2537-2540.



- 
- [305] V. G. Kravets, O. P. Marshall, R. R. Nair, B. Thackray, A. Zhukov, J. Leng, A. N. Grigorenko, *Optics Express* **2015**, *23*, 1265-1275.
- [306] H. Liang, Y. Bu, J. Zhang, Z. Cao, A. Liang, *ACS Applied Materials & Interfaces* **2013**, *5*, 6369-6375.
- [307] S. D. Park, S. W. Lee, S. Kang, S. M. Kim, I. C. Bang, *Nuclear Engineering and Design* **2012**, *252*, 184-191.
- [308] B. Seger, P. V. Kamat, *The Journal of Physical Chemistry C* **2009**, *113*, 7990-7995.
- [309] S. Wang, N. Liu, J. Su, L. Li, F. Long, Z. Zou, X. Jiang, Y. Gao, *ACS Nano* **2017**, *11*, 2066-2074.
- [310] F. T. Johra, W.-G. Jung, *Applied Surface Science* **2015**, *357*, 1911-1914.
- [311] G. Ali, A. Mehmood, H. Y. Ha, J. Kim, K. Y. Chung, **2017**, *7*, 40910.
- [312] D. Chen, H. Zhang, Y. Liu, J. Li, *Energy & Environmental Science* **2013**, *6*, 1362-1387.
- [313] S.-S. Li, K.-H. Tu, C.-C. Lin, C.-W. Chen, M. Chhowalla, *ACS Nano* **2010**, *4*, 3169-3174.
- [314] J. Liu, L. Cui, D. Losic, *Acta Biomaterialia* **2013**, *9*, 9243-9257.
- [315] H. Kim, R. Namgung, K. Singha, I.-K. Oh, W. J. Kim, *Bioconjugate Chemistry* **2011**, *22*, 2558-2567.
- [316] L. Zhang, Z. Lu, Q. Zhao, J. Huang, H. Shen, Z. Zhang, *Small* **2011**, *7*, 460-464.
- [317] H. M. Hegab, L. Zou, *Journal of Membrane Science* **2015**, *484*, 95-106.
- [318] J. Abraham, K. S. Vasu, C. D. Williams, K. Gopinadhan, Y. Su, C. T. Cherian, J. Dix, E. Prestat, S. J. Haigh, I. V. Grigorieva, P. Carbone, A. K. Geim, R. R. Nair, *Nat Nano* **2017**, *12*, 546-550.
- [319] A. Rajan Unnithan, A. Ramachandra Kurup Sasikala, C. H. Park, C. S. Kim, *J. Ind. Eng. Chem.* **2017**, *46*, 182-191.
- [320] D. J. Babu, F. G. Kuhl, S. Yadav, D. Markert, M. Bruns, M. J. Hampe, J. J. Schneider, *RSC Advances* **2016**, *6*, 36834-36839.
- [321] G. Sobon, J. Sotor, J. Jagiello, R. Kozinski, M. Zdrojek, M. Holdynski, P. Paletko, J. Boguslawski, L. Lipinska, K. M. Abramski, *Optics express* **2012**, *20*, 19463-19473.
- [322] I. Childres, L. A. Jauregui, W. Park, H. Cao, Y. P. Chen, *New developments in photon and materials research* **2013**, 1-20.
- [323] D. Yang, A. Velamakanni, G. Bozoklu, S. Park, M. Stoller, R. D. Piner, S. Stankovich, I. Jung, D. A. Field, C. A. Ventrice, *Carbon* **2009**, *47*, 145-152.
- [324] P. Ok-Kyung, C. Yong-Mun, H. Jun Yeon, Y. Cheol-Min, K. Tea-Wook, Y. Nam-Ho, K. Hye Young, L. Joong Hee, K. Bon-Cheol, G. Munju, *Nanotechnology* **2013**, *24*, 185604.

- 
- [325] L. Feng, Z. Zhang, Z. Mai, Y. Ma, B. Liu, L. Jiang, D. Zhu, *Angewandte Chemie* **2004**, *116*, 2046-2048.
- [326] J. Yuan, X. Liu, O. Akbulut, J. Hu, S. L. Suib, J. Kong, F. Stellacci, *Nat Nano* **2008**, *3*, 332-336.
- [327] Z. Xue, Y. Cao, N. Liu, L. Feng, L. Jiang, *Journal of Materials Chemistry A* **2014**, *2*, 2445-2460.
- [328] A. Venkateswara Rao, N. D. Hegde, H. Hirashima, *Journal of Colloid and Interface Science* **2007**, *305*, 124-132.
- [329] X. Gui, J. Wei, K. Wang, A. Cao, H. Zhu, Y. Jia, Q. Shu, D. Wu, *Advanced Materials* **2010**, *22*, 617-621.
- [330] Y. Zhao, C. Hu, Y. Hu, H. Cheng, G. Shi, L. Qu, *Angewandte Chemie International Edition* **2012**, *51*, 11371-11375.
- [331] H. Sun, Z. Xu, C. Gao, *Advanced Materials* **2013**, *25*, 2554-2560.
- [332] Y. Liu, J. Ma, T. Wu, X. Wang, G. Huang, Y. Liu, H. Qiu, Y. Li, W. Wang, J. Gao, *ACS Applied Materials & Interfaces* **2013**, *5*, 10018-10026.
- [333] H. Bi, Z. Yin, X. Cao, X. Xie, C. Tan, X. Huang, B. Chen, F. Chen, Q. Yang, X. Bu, X. Lu, L. Sun, H. Zhang, *Advanced Materials* **2013**, *25*, 5916-5921.
- [334] Z.-Y. Wu, C. Li, H.-W. Liang, J.-F. Chen, S.-H. Yu, *Angewandte Chemie International Edition* **2013**, *52*, 2925-2929.
- [335] N. T. Cervin, C. Aulin, P. T. Larsson, L. Wågberg, *Cellulose* **2012**, *19*, 401-410.
- [336] J. T. Korhonen, M. Kettunen, R. H. A. Ras, O. Ikkala, *ACS Applied Materials & Interfaces* **2011**, *3*, 1813-1816.
- [337] A. Javadi, Q. Zheng, F. Payen, A. Javadi, Y. Altin, Z. Cai, R. Sabo, S. Gong, *ACS Applied Materials & Interfaces* **2013**, *5*, 5969-5975.
- [338] K. Gao, Z. Shao, J. Li, X. Wang, X. Peng, W. Wang, F. Wang, *Journal of Materials Chemistry A* **2013**, *1*, 63-67.
- [339] J. Cai, S. Liu, J. Feng, S. Kimura, M. Wada, S. Kuga, L. Zhang, *Angew Chem Int Ed Engl* **2012**, *51*, 2076-2079.
- [340] J. Innerlohinger, H. K. Weber, G. Kraft, *Macromolecular Symposia* **2006**, *244*, 126-135.
- [341] F. Liebner, E. Haimer, M. Wendland, M. A. Neouze, K. Schluffer, P. Miethe, T. Heinze, A. Potthast, T. Rosenau, *Macromolecular bioscience* **2010**, *10*, 349-352.
- [342] R. T. Olsson, M. A. S. A. Samir, G. Salazar-Alvarez, L. Belova, V. Strom, L. A. Berglund, O. Ikkala, J. Nogues, U. W. Gedde, *Nature nanotechnology* **2010**, *5*, 584-588.
- [343] C. B. Tan, B. M. Fung, J. K. Newman, C. Vu, *Advanced Materials* **2001**, *13*, 644-646.

- 
- [344] D. Klemm, D. Schumann, U. Udhardt, S. Marsch, *Prog Polym Sci* **2001**, *26*, 1561-1603.
- [345] C. H. Haigler, A. R. White, R. M. Brown, Jr., K. M. Cooper, *The Journal of cell biology* **1982**, *94*, 64-69.
- [346] S. Hestrin, M. Schramm, *Biochemical Journal* **1954**, *58*, 345.
- [347] P. T. Larsson, K. Wickholm, T. Iversen, *Carbohydrate Research* **1997**, *302*, 19-25.
- [348] P. T. Larsson, E. L. Hult, K. Wickholm, E. Pettersson, T. Iversen, *Solid state nuclear magnetic resonance* **1999**, *15*, 31-40.
- [349] Y. Wang, S. Yadav, T. Heinlein, V. Konjik, H. Breitzke, G. Buntkowsky, J. J. Schneider, K. Zhang, *RSC Advances* **2014**, *4*, 21553-21558.
- [350] W. G. Glasser, R. H. Atalla, J. Blackwell, R. Malcolm Brown, W. Burchard, A. D. French, D. O. Klemm, Y. Nishiyama, *Cellulose* **2012**, *19*, 589-598.
- [351] G. Rayner-Canham, *Foundations of Chemistry* **2011**, *13*, 121-129.
- [352] M. C. Simpson, J. D. Protasiewicz, *Pure and Applied Chemistry* **2013**, *85*, 801-815.
- [353] F. Mathey, J. F. Nixon, K. Dillon, *Phosphorus: the carbon copy*, Wiley, New York, **1998**.
- [354] [https://en.wikipedia.org/wiki/Diagonal\\_relationship](https://en.wikipedia.org/wiki/Diagonal_relationship), 2-10-2017, 1.00 PM.
- [355] E. Bianco, S. Butler, S. Jiang, O. D. Restrepo, W. Windl, J. E. Goldberger, *ACS Nano* **2013**, *7*, 4414-4421.
- [356] B. Lalmi, H. Oughaddou, H. Enriquez, A. Kara, S. Vizzini, B. Ealet, B. Aufray, *Applied Physics Letters* **2010**, *97*, 223109.
- [357] S. Z. Butler, S. M. Hollen, L. Cao, Y. Cui, J. A. Gupta, H. R. Gutiérrez, T. F. Heinz, S. S. Hong, J. Huang, A. F. Ismach, E. Johnston-Halperin, M. Kuno, V. V. Plashnitsa, R. D. Robinson, R. S. Ruoff, S. Salahuddin, J. Shan, L. Shi, M. G. Spencer, M. Terrones, W. Windl, J. E. Goldberger, *ACS Nano* **2013**, *7*, 2898-2926.
- [358] A. C. Ferrari, F. Bonaccorso, V. Fal'ko, K. S. Novoselov, S. Roche, P. Boggild, S. Borini, F. H. L. Koppens, V. Palermo, N. Pugno, J. A. Garrido, R. Sordan, A. Bianco, L. Ballerini, M. Prato, E. Lidorikis, J. Kivioja, C. Marinelli, T. Ryhanen, A. Morpurgo, J. N. Coleman, V. Nicolosi, L. Colombo, A. Fert, M. Garcia-Hernandez, A. Bachtold, G. F. Schneider, F. Guinea, C. Dekker, M. Barbone, Z. Sun, C. Galiotis, A. N. Grigorenko, G. Konstantatos, A. Kis, M. Katsnelson, L. Vandersypen, A. Loiseau, V. Morandi, D. Neumaier, E. Treossi, V. Pellegrini, M. Polini, A. Tredicucci, G. M. Williams, B. Hee Hong, J.-H. Ahn, J. Min Kim, H. Zirath, B. J. van Wees, H. van der Zant, L. Occhipinti, A. Di Matteo, I. A. Kinloch, T. Seyller, E. Quesnel, X. Feng, K. Teo, N. Rupesinghe, P. Hakonen, S. R. T. Neil, Q. Tannock, T. Lofwander, J. Kinaret, *Nanoscale* **2015**, *7*, 4598-4810.

- 
- [359] M. Akhtar, G. Anderson, R. Zhao, A. Alruqi, J. E. Mroczkowska, G. Sumanasekera, J. B. Jasinski, *npj 2D Materials and Applications* **2017**, *1*, 5.
- [360] W. Li, Y. Yang, G. Zhang, Y.-W. Zhang, *Nano Letters* **2015**, *15*, 1691-1697.
- [361] L. Li, Y. Yu, G. J. Ye, Q. Ge, X. Ou, H. Wu, D. Feng, X. H. Chen, Y. Zhang, *Nat Nano* **2014**, *9*, 372-377.
- [362] M. Buscema, D. J. Groenendijk, G. A. Steele, H. S. J. van der Zant, A. Castellanos-Gomez, **2014**, *5*, 4651.
- [363] S. Lin, Y. Chui, Y. Li, S. P. Lau, *FlatChem* **2017**, *2*, 15-37.
- [364] V. V. Kulish, O. I. Malyi, C. Persson, P. Wu, *Physical Chemistry Chemical Physics* **2015**, *17*, 992-1000.
- [365] S. C. Dhanabalan, J. S. Ponraj, Z. Guo, S. Li, Q. Bao, H. Zhang, *Advanced Science* **2017**, *4*, 1600305.
- [366] V. Nicolosi, M. Chhowalla, M. G. Kanatzidis, M. S. Strano, J. N. Coleman, *Science* **2013**, *340*.
- [367] F. Schwierz, *Nat Nano* **2010**, *5*, 487-496.
- [368] D. Warschauer, *Journal of Applied Physics* **1963**, *34*, 1853-1860.
- [369] H. Liu, A. T. Neal, Z. Zhu, Z. Luo, X. Xu, D. Tománek, P. D. Ye, *ACS Nano* **2014**, *8*, 4033-4041.
- [370] W. Zhu, S. Park, M. N. Yogeesh, K. M. McNicholas, S. R. Bank, D. Akinwande, *Nano Letters* **2016**, *16*, 2301-2306.
- [371] S. Lee, F. Yang, J. Suh, S. Yang, Y. Lee, G. Li, H. Sung Choe, A. Suslu, Y. Chen, C. Ko, J. Park, K. Liu, J. Li, K. Hippalgaonkar, J. J. Urban, S. Tongay, J. Wu, **2015**, *6*, 8573.
- [372] S. Yang, C. Jiang, S.-h. Wei, *Applied Physics Reviews* **2017**, *4*, 021304.
- [373] M. Donarelli, L. Ottaviano, L. Giancaterini, G. Fioravanti, F. Perrozzi, C. Cantalini, *2D Materials* **2016**, *3*, 025002.
- [374] A. N. Abbas, B. Liu, L. Chen, Y. Ma, S. Cong, N. Aroonyadet, M. Köpf, T. Nilges, C. Zhou, *ACS Nano* **2015**, *9*, 5618-5624.
- [375] J. Patzsch, I. Balog, Krau, C. W. Lehmann, J. J. Schneider, *RSC Advances* **2014**, *4*, 15348-15355.
- [376] H. Kaur, S. Yadav, A. K. Srivastava, N. Singh, J. J. Schneider, O. P. Sinha, V. V. Agrawal, R. Srivastava, **2016**, *6*, 34095.
- [377] J. Kang, J. D. Wood, S. A. Wells, J.-H. Lee, X. Liu, K.-S. Chen, M. C. Hersam, *ACS Nano* **2015**, *9*, 3596-3604.
- [378] J. Miao, S. Zhang, L. Cai, M. Scherr, C. Wang, *ACS Nano* **2015**, *9*, 9236-9243.

- 
- [379] X. Ling, H. Wang, S. Huang, F. Xia, M. S. Dresselhaus, *Proceedings of the National Academy of Sciences* **2015**, *112*, 4523-4530.
- [380] H. U. Lee, S. Y. Park, S. C. Lee, S. Choi, S. Seo, H. Kim, J. Won, K. Choi, K. S. Kang, H. G. Park, H.-S. Kim, H. R. An, K.-H. Jeong, Y.-C. Lee, J. Lee, *Small* **2016**, *12*, 214-219.
- [381] H. Wang, X. Yang, W. Shao, S. Chen, J. Xie, X. Zhang, J. Wang, Y. Xie, *Journal of the American Chemical Society* **2015**, *137*, 11376-11382.
- [382] Y. Huang, J. Qiao, K. He, S. Bliznakov, E. Sutter, X. Chen, D. Luo, F. Meng, D. Su, J. Decker, W. Ji, R. S. Ruoff, P. Sutter, *Chemistry of Materials* **2016**, *28*, 8330-8339.
- [383] Y. Huang, J. Qiao, K. He, S. Bliznakov, E. Sutter, X. Chen, D. Luo, F. Meng, D. Su, J. Decker, *arXiv preprint arXiv:1511.09201* **2015**.
- [384] J. Shao, H. Xie, H. Huang, Z. Li, Z. Sun, Y. Xu, Q. Xiao, X.-F. Yu, Y. Zhao, H. Zhang, H. Wang, P. K. Chu, **2016**, *7*, 12967.
- [385] R. W. Johnson, A. Hultqvist, S. F. Bent, *Materials Today* **2014**, *17*, 236-246.
- [386] M. U. A Tutorial by Cambridge NanoTech Inc. Cambridge, [www.cambridgenanotech.com](http://www.cambridgenanotech.com) **2005**.
- [387] B. Mamoru, I. Fukunori, T. Yuji, M. Akira, *Japanese Journal of Applied Physics* **1989**, *28*, 1019.
- [388] M. Köpf, N. Eckstein, D. Pfister, C. Grotz, I. Krüger, M. Greiwe, T. Hansen, H. Kohlmann, T. Nilges, *Journal of crystal growth* **2014**, *405*, 6-10.

---

## **Curriculum Vitae**

### **Personal Information**

Name : Sandeep Yadav  
Date of birth : 14-11-1982  
Place of birth : Uttar Pradesh, India  
Address : 006-B1, GAVANPADA, EKTA, CHS LTD,  
Vidyalaya Marg, Mulund (E),  
Mumbai-40081, Maharashtra, India

### **Education**

10/2011 – Present : Dr. rer. nat.  
Department of chemistry  
Technische Universität Darmstadt, Germany

07/2007 – 09/2009 : Master of Technology (Nanotechnology)  
Amity Institute of Nanotechnology, Amity University  
Uttar Pradesh, India

06/2004 - 10/2006 : Master of Science (Physics- Electronics)  
Mumbai University  
Mumbai, India

06/2001 – 03/2004 : Bachelor of Science ( Physics)  
Mumbai University  
Mumbai, India

